

École doctorale n° 364 : Sciences Fondamentales et Appliquées

Doctorat ParisTech

THÈSE

pour obtenir le grade de docteur délivré par

l'École Nationale Supérieure des Mines de Paris

Spécialité doctorale “Science et Génie des Matériaux”

présentée et soutenue publiquement par

Ali SAAD

le 09 février 2016

NUMERICAL MODELLING OF MACROSEGREGATION FORMED DURING SOLIDIFICATION WITH SHRINKAGE USING A LEVEL SET APPROACH

Co-directeur de thèse: **Charles-André GANDIN**

Co-directeur de thèse: **Michel BELLET**

Jury

Pr. Hervé COMBEAU,	Professeur, Ecole des Mines de Nancy, France	Rapporteur
Pr. Markus RETTENMAYR,	Professeur, Université de Jena, Allemagne	Rapporteur
Pr. Florian KARGL,	Professeur, Agence Spatiale Allemande (DLR), Allemagne	Examinateur
Dr. Charles-André GANDIN,	Directeur de recherche, CNRS, France	Examinateur
Pr. Michel BELLET,	Professeur MINES ParisTech, France	Examinateur
Dr. Frédéric COSTES,	Chef de service <i>THERCAST®</i> , TRANSVALOR S.A., France	Invité

Contents

1 General Introduction	1
1.1 Solidification notions	2
1.1.1 Solute partitioning	2
1.1.2 Dendritic growth	4
1.1.3 Mush permeability	5
1.2 Macrosegregation	6
1.2.1 Liquid thermosolutal convection	7
1.2.2 Solidification shrinkage	7
1.2.3 Movement of grains	7
1.2.4 Solid deformation	7
1.3 Other defects	8
1.4 Industrial Worries	9
1.5 Project context and objectives	10
1.5.1 Context	10
1.5.2 Objectives and outline	11
2 Modelling Review	15
2.1 Modelling macrosegregation	16
2.1.1 Macroscopic solidification model: monodomain	17
2.2 Eulerian and Lagrangian motion description	23
2.2.1 Overview	23
2.2.2 Interface capturing	23
2.3 Solidification models with level set	24
2.4 The level set method	24
2.4.1 Diffuse boundary	25
2.4.2 Mixing Laws	26
2.5 Interface motion	28
2.5.1 Level set transport	29
2.5.2 Level set regularisation	30
2.6 Mesh adaptation	33
2.6.1 Metrics and anisotropy	33
2.6.2 <i>Remesh2</i> : domains boundary remeshing	34
2.6.3 <i>Remesh4</i> : Multi-criteria remeshing	35
3 Energy balance with thermodynamic tabulations	39
3.1 State of the art	40

3.2	Thermodynamic considerations	40
3.2.1	Volume averaging	40
3.2.2	The temperature-enthalpy relationship	41
3.2.3	Tabulation of properties	41
3.3	Numerical method	44
3.3.1	Enthalpy-based approach	46
3.3.2	Temperature-based approach	46
3.3.3	Convergence	47
3.4	Validation	48
3.5	Application: multicomponent alloy solidification	48
3.5.1	Tabulations	52
3.5.2	Discussion	54
3.6	Limitations	59
4	Macrosegregation with constant metal volume	61
4.1	Introduction	62
4.2	Navier-Stokes solvers	62
4.2.1	Stable mixed finite elements	62
4.2.2	Variational multiscale (VMS)	63
4.3	Navier-Stokes solver	63
4.3.1	Strong and weak formulations	64
4.3.2	Stabilisation parameters	66
4.3.3	Implementation	67
4.4	<i>Tsolver</i> validation with fluid flow	68
4.4.1	Application to a binary alloy	68
4.4.2	Application to a multicomponent alloy	68
4.5	Macroscopic prediction of channel segregates	75
4.5.1	Introduction	75
4.5.2	Experimental work	76
4.5.3	Macroscopic scale simulations	77
4.6	Meso-Macro prediction of channel segregates	83
4.6.1	Numerical method	83
4.6.2	Configuration	85
4.6.3	Effect of vertical temperature gradient	88
4.6.4	Effect of cooling rate	90
4.6.5	Effect of lateral temperature gradient	91
5	Macrosegregation with changing metal volume	95
5.1	Solidification shrinkage	96
5.2	Choice of boundary tracking	96
5.3	Multidomain formalism	98
5.3.1	Assumptions	98
5.3.2	Metal-Air boundary definition	100
5.4	FE partitioned model	101
5.4.1	In the metal	101
5.4.2	In the air	104

5.5	FE monolithic model	106
5.5.1	Mass and momentum conservation	106
5.5.2	Energy conservation	108
5.5.3	Species conservation	109
5.6	1D application: solidification with inverse segregation	111
5.6.1	Geometry and boundary conditions	111
5.6.2	Shrinkage without macrosegregation	112
5.6.3	Shrinkage with macrosegregation	120
5.7	2D application: controlled solidification benchmark	132
5.7.1	Computational configuration	132
5.7.2	Results	134
5.7.3	Mass conservation	136
5.8	3D application: reduced-gravity solidification	141
5.8.1	Previous work	141
5.8.2	Computational configuration	143
5.8.3	Texus binary alloy	149
5.8.4	Texus ternary and quaternary alloys	155
Conclusion and Perspectives		163
Bibliography		167

Contents

List of Acronyms

Acronym	Standing for
ALE	Arbitrary Lagrangian-Eulerian
CAF D	Cellular Automata Finite Difference
CAFE	Cellular Automata Finite Element
CBB	Circumventing Babuška-Brezzi
CCEMLCC	Chill Cooling for the Electro-Magnetic Levitator in relation with Continuous Casting of steel
CEMEF	Centre de Mise en Forme des Matériaux
CFL	Courant–Friedrichs–Lewy
C.FL.	Computing and FLuids
CSF	Continuum Surface Force
DLR	Deutsches Zentrum für Luft- und Raumfahrt
DSPG	Darcy-Stabilising/Petrov-Galerkin
EML	Electromagnetic levitation
ESA	European Space Agency
FEM	Finite Element Method
FVM	Finite Volume Method
GMAW	Gas Metal Arc Welding
ISS	International Space Station
IWT	Institut für Werkstofftechnik
LHS	Left-hand side
LSIC	Least squares on incompressibility constraint
LSM	Level set method
MAC	Marker-and-cell
MD	Monolithic with low species diffusion in the air
MDA	Monolithic with low species diffusion and advection in the air
NM	Non monolithic
PF	Phase field
PSPG	Pressure-Stabilising/Petrov-Galerkin
RHS	Right-hand side
RF	Radiofrequency
RUB	Ruhr Universität Bochum
RVE	Representative Elementary Volume
SBB	Satisfying Babuška-Brezzi
SUPG	Streamline-Upwind/Petrov-Galerkin
VMS	Variational MultiScale
VOF	Volume Of Fluid

Contents

Chapter 1

General Introduction

Casting is one of the earliest production techniques created by human civilisation since the Bronze Age, dated to circa 5000 years ago. From ancient swords to nowadays Swiss Army Knives, the need for alloys has never decreased. The key phenomenon behind this technique is solidification, or the transformation of matter from liquid to solid state. With this phase change, many phenomena, not visible to the naked eye, take place with a very complex interaction, in order to form a solid. However, the combination of heat transfer (e.g. release of latent heat) and mass transfer (e.g. redistribution of chemical elements and phases), often lead to defects. *Segregation* is type of defect which can lead to uncontrolled properties of cast parts. The Latin origin of this word, *segregatus*, has the social meaning of "separating a group from the dominant majority", while in metallurgy it means a non uniform distribution of chemical species. Depending on the scale, we may speak of *microsegregation* when the heterogeneity spans some few hundred microns, whereas the term *macrosegregation* refers to a much coarser length scale, ranging from some millimetres to some meters! The solidified structure has intrinsic thermophysical and thermomechanical properties directly influenced by the segregation pattern.

In casting processes, such as continuous casting ([fig. 1.1a](#)) and ingot casting ([fig. 1.1b](#)), it is crucial to apprehend the intricate phenomena leading to macrosegregation. Its influence on intermediate processing steps (e.g. forging, coating, welding,...) to reach a manufactured product, also needs to be understood. In this introductory chapter, we give a quick overview of solidification phenomena and microstructure, then present the factors which promote segregation, on both microscopic and macroscopic scales. Aside from macrosegregation, other defects are also briefly presented.

In a continuous casting process ([fig. 1.1a](#)), the partially solidified slab is carried through a series of rolls that exert contact forces to straighten it. When a slab enters through these rolls after exiting the open copper mould, it consists of a thin solid shell that contains a mixture of solid and liquid phases known as the mushy zone, with a core still fully liquid. Enriched liquid accumulates halfway in thickness, forming a centreline macrosegregation as shown in [fig. 1.2](#). Other types of segregation patterns can be encountered while casting heavy ingots, as schematised in [fig. 1.3](#):

- a negative segregation cone promoted by the sedimentation of equiaxed crystals and settling of dendrite fragments, often seen at the bottom part of the ingot,
- positive segregation channels, known as A-segregates, form along the columnar dendritic



Fig. 1.1 – Schematics of the main steelmaking processes by (a) continuous casting and (b) ingot casting.

zones, close to the vertical contact with the mould,

- positive V-segregates can be identified in the centre of the ingot,
- a positive "hot-top" macrosegregation in the upper zone where the last rich liquid solidifies, caused by thermosolutal buoyancy forces.

Combeau et al. [2009] state that A-segregates and V-segregates formation is mainly attributed to local flow phenomena. As such, their scale is finer than macrosegregation, hence called "mesosegregates".

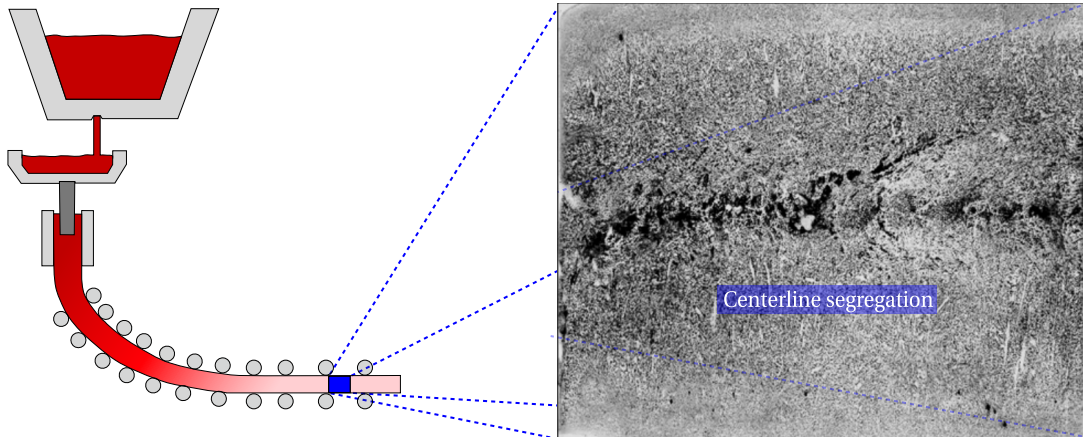


Fig. 1.2 – Zoom on a sulphur print of a continuously cast high carbon steel billet at a longitudinal section, showing high positive centreline segregation [Choudhary and Ganguly 2007].

1.1 Solidification notions

1.1.1 Solute partitioning

The simplest definition of this phenomenon is an uneven distribution of solute between the liquid and the growing solid, at the microscopic scale of the interface separating these phases.



Fig. 1.3 – (a) Sulphur print of a 65-ton steel ingot showing (b) various macrosegregation patterns and levels as well as solidification structures [Lesoult 2005].

If we consider a binary alloy, then the solubility limit is the key factor that dictates the composition at which a primary solid phase exists at equilibrium. The segregation (or partition) coefficient k determines the extent of solute rejection into the liquid during solidification:

$$k = \frac{w^{s^*}}{w^{l^*}} \quad (1.1)$$

where w^{s^*} and w^{l^*} are the solute compositions at the interface, of the solid and liquid phases respectively. When the segregation coefficient is less than unity (such is the case for most alloys during dendritic solidification), the first solid forms at the liquidus temperature, T_L , with a composition $w^{s^*} = kw^{l^*}$ less than the surrounding liquid composition, the latter being initially at the nominal composition, w_0 . Figure 1.4 illustrates a typical binary phase diagram where the real solidus and liquidus are represented by solid lines, while the possible linear approximations are in grey dashed lines. For most binary alloys, this linearisation simplifies derivation of microsegregation models, as k becomes independent of temperature.

For each phase, the relationship between the composition at the interface and that in the bulk depends on the chemical homogenisation of the phase by solute transport. The more homogeneous a phase, the closer the concentrations between the interface and the bulk, hence closer to equilibrium. It is thus essential to study the effect of homogenisation on the segregation behaviour and the subsequent effect on solidification, which is seen by a non-uniform composition through the cast product on a microscopic scale, better known as microsegregation. This phenomenon is essential in a casting process inasmuch as it affects the microstructure and grain morphology, hence the final mechanical properties of the alloy.

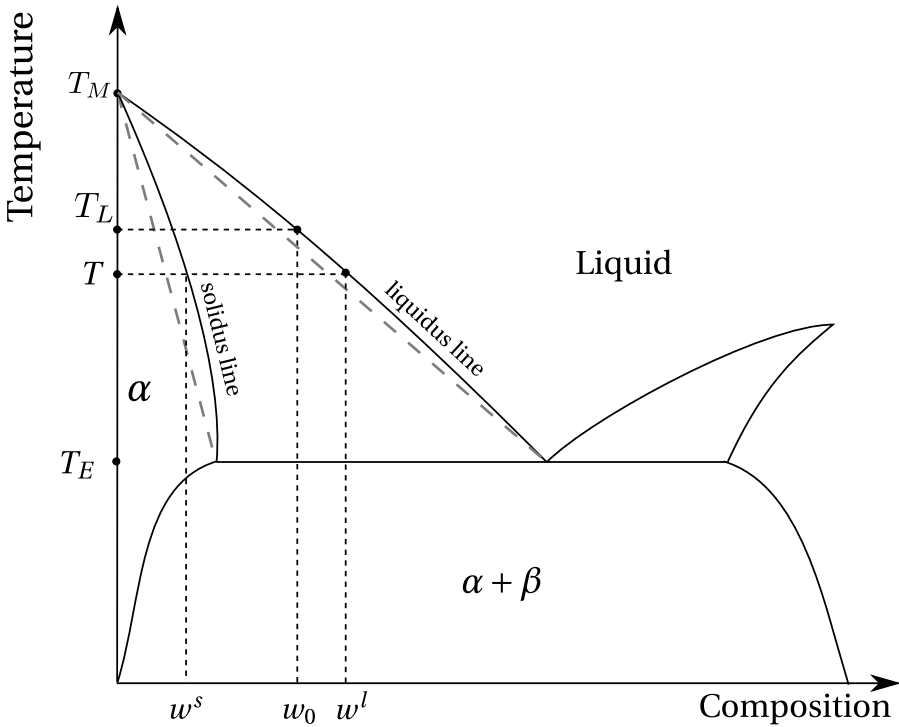


Fig. 1.4 – Typical eutectic phase diagram of a binary alloy showing the real solidus and liquidus at full equilibrium, with the corresponding linear approximations (grey dashed lines). T_M and T_E are respectively the melting point of the solvent and the eutectic temperature.

1.1.2 Dendritic growth

In a casting process, the vicinity of the chill surface where the contact between the molten alloy and the cold moulds, is the first area to solidify. Thermal gradient, G , and cooling rate, R , are two crucial parameters that define the solid-liquid interface velocity, v^* , which in turn affects the initial microstructure. Although it may not be easy to control them, their role in solidification is well established.

At low values of v^* where the interface maintains a planar shape, hence we speak of *planar growth*. With this kind of growth, a random protuberance appearing at the interface, has a low tip velocity (low driving force of solidification). As such, the rest of the interface catches up, maintaining the planar geometry. In another scenario more representative of a real casting, the interface velocity leads to its instability. The protuberance tip will grow into a liquid less rich in solute, as shown in the experimental frames of [fig. 1.5](#). The zone ahead of the solid-liquid interface is constitutionally undercooled, giving a greater driving force for the protuberance to grow in the direction of the thermal gradient.

An expression for the critical velocity is given by [Tiller et al. \[1953\]](#). As the solid-liquid interface adopts a tree-like shape, we speak of *dendritic growth*. Near the chill surface, dendrites are columnar, with a favourable growth in the $\langle 100 \rangle$ direction for alloys with cubic lattices, but different orientations are also reported in the literature [see [Dantzig and Rappaz 2009](#), p. 289]. Far from mould walls, a similar dendritic growth phenomenon occurs where temperature is uniform, but with an equiaxed morphology. [Figure 1.6](#) shows both columnar and equiaxed morphologies. Columnar dendrites are characterised by a primary spacing, λ_1 , between the

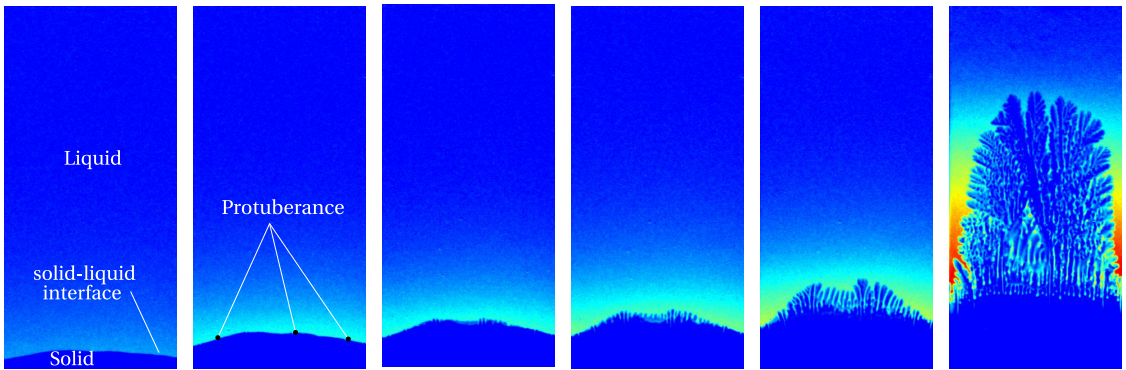


Fig. 1.5 – Experimental time evolution of a solidifying Al-4 wt.% Cu sample, showing interface destabilisation and subsequent dendritic solidification [Buffet et al. 2010]. The liquid far from the interface and having a blue colour is at nominal composition, while the one near the dendritic structure with the yellow and red colours, is richer in solute.

main trunks, and a secondary spacing, λ_2 , for the arms that are perpendicular to the trunks. It should be noted that λ_1 and λ_2 , together with the grain size, are three important microstructural parameters in the as-cast microstructure [Easton et al. 2011]. Further branching may occur but will not be discussed here.

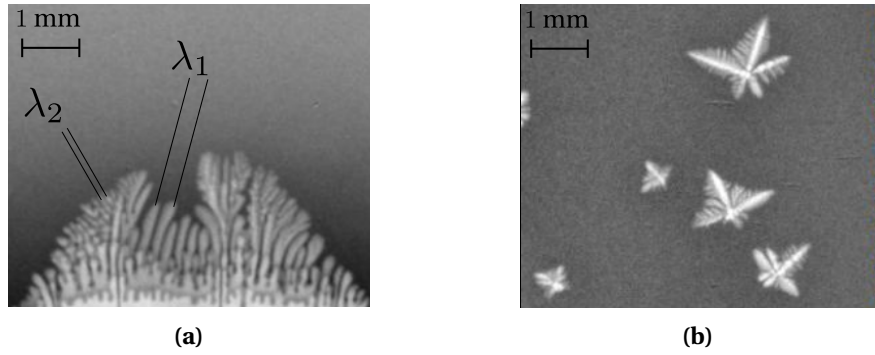


Fig. 1.6 – In situ observation by X-ray radiography of the (a) columnar microstructure for Al-4 wt.% Cu alloy [Buffet et al. 2010] and (b) equiaxed microstructure during solidification of Al-10 wt.% Cu alloy [Bogno et al. 2013].

1.1.3 Mush permeability

The dendritic geometry is crucial in solidification theory as it exhibits lower solid fraction compared to a microstructure formed by planar growth. This fact has consequences on the fluid-structure interaction in the mushy zone, namely the liquid flow through dendrites. At the chill surface, the solid grows gradually from dispersed growing nuclei to a permeable solid skeleton, until grains have fully grown at the end of phase change. In the intermediate state, the liquid flow in and out of the mushy zone through the network of dendrites is a key phenomenon from various perspectives, especially the rheological perspective .

The flow through the interdendritic liquid is damped by primary trunks and secondary dendrite arms, resulting in momentum dissipation just like in saturated porous media. The famous Darcy [1856] law relates the liquid pressure ($g^l p^l$) gradient to the average liquid velocity ($g^l \langle v \rangle^l$),

through the following equation:

$$g^l \langle v \rangle^l = -\frac{\mathbb{K}}{\mu^l} \nabla (g^l p^l) \quad (1.2)$$

where μ^l is the liquid dynamic viscosity and \mathbb{K} is the permeability tensor. Equation (1.2) do not account for the solid velocity, $\langle v \rangle^s$, assuming that the solid phase is fixed, which can occur in columnar solidification or when equiaxed grains are densely packed in later stages of solidification [Rappaz et al. 2003]. Evaluating permeability has been the subject of numerous studies that aimed to predict it from microstructural or morphological parameters. Some of these studies have started even before the first attempts to model macrosegregation by Flemings and Nereo [1967], Flemings et al. [1968], and Flemings and Nereo [1968].

Basically, all models include the solid fraction, g^s , as input to predict mush permeability along with empirical data. An instance of such models is the work of Xu and Li [1991]. Some models rely additionally on the primary dendrite arm spacing λ_1 like Blake-Kozeny [Ramirez and Beckermann 2003], or the secondary dendrite arm spacing λ_2 like Carman-Kozeny, as a meaningful parameter to determine an isotropic permeability. Other models like Poirier [1987] and Felicelli et al. [1991] derive an anisotropic permeability based on both λ_1 and λ_2 .

The present work uses a particular form of the Carman-Kozeny equation as a constitutive model for the isotropic permeability scalar (zero order tensor), depending on the secondary dendrite arm spacing, λ_2 , as follows:

$$\mathbb{K} = \frac{\lambda_2^2 g^{l^3}}{180 (1 - g^l)^2} \quad (1.3)$$

1.2 Macrosegregation

Macrosegregation generally stems from a solubility difference between a liquid phase and one or more solid phases, along with a relative velocity between these phases. While the former is responsible for local solute enrichment or depletion, the latter will propagate the composition heterogeneity on a scale much larger than just a few dendrites. This is why macrosegregation could be observed on the scale of a casting, up to several meters in length. Microsegregation may be healed by heat treatments to speed up the diffusion process and allow homogenisation. However, heterogeneities spanning on larger distances cannot be heat treated after solidification. Macrosegregation is thus an irreversible defect. Failure to prevent it, may lead to a substantial decline in the alloy's mechanical behaviour and its serviceability. Experimental investigations of macrosegregation in steels were the subject of numerous studies in the past and until now, like the work of Suzuki and Miyamoto [1973], Shah and Moore [1989], and Lesoult [2005]. They were mainly motivated by industrial research that aimed at reducing defective production caused by macrosegregation. However, steels were not the only alloys that were investigated for segregation defects. Many studies relied on other metallic alloys as a replacement recourse, for their low melting points and well-known physical and mechanical properties. Examples are aluminium-based alloys (aluminium-copper or aluminium-silicon) [Lesoult et al. 2001; Ferreira et al. 2004; Ferreira et al. 2009] and lead-tin/tin-lead alloys [Hebditch and Hunt 1974; Prescott et al. 1994; Hachani et al. 2012]. Investigating macrosegregation is also common in organic compounds like the well-known sodium chloride [Wanqi and Yaohe 1989; Sarazin and Hellawell 1992; Ludwig et al. 2012], which have the advantage of being transparent.

Four main factors can (simultaneously) cause fluid flow leading to macrosegregation: thermosolutal convection in the liquid, solidification shrinkage, solutal and thermal contraction, movement and sedimentation of equiaxed crystals and finally solid deformation.

1.2.1 Liquid thermosolutal convection

During solidification, the liquid density undergoes changes due to temperature gradients. Generally for steels, an increasing temperature results in a lighter liquid phase and vice-versa. These variations create a driving force of thermal convection in the melt, during which chemical species are redistributed by convective transport. While a uniform composition could be maintained throughout the liquid bulk where convective transport is dominant, solute gradients may appear in zones where thermal convection currents are not sufficient to homogenise the liquid solution. Similarly to thermal gradient, a solute gradient is behind liquid density variations. Nevertheless, the link between the liquid's composition and its density varies from one alloy to another. For some alloys, a positive solute gradient creates a positive density gradient, while for others the opposite is true, due to a lighter solute effect in the melt density. Whether convection is solute or temperature dominated, convection currents are important in the formation of macrosegregation, especially that the liquid phase density varies considerably upon cooling the superheated alloy to room temperature.

1.2.2 Solidification shrinkage

Solids generally have a greater density than the liquid phase ($\langle \rho \rangle^s > \langle \rho \rangle^l$), thus occupy less volume, with some exceptions such as silicon, for which the opposite is true. Upon solidification, the liquid therefore moves towards the solidification front to compensate for the volume difference caused by the phase change, as well as the phases contraction mainly due to temperature gradient. When macrosegregation is triggered by solidification shrinkage, we speak of *inverse segregation*: while one would expect negative macrosegregation near the contact with the chill due to diffusion, shrinkage-induced flow promotes the opposite phenomenon, by bringing solute-richer liquid towards the solidifying areas, thus raising their solute content, and resulting in a positively segregated region. In contrast to liquid thermosolutal convection, shrinkage flow may cause macrosegregation even without gravity.

1.2.3 Movement of grains

Globular and equiaxed dendritic grains nucleate and grow in the liquid bulk where thermal gradients are weak, or in the presence of inoculants. They are transported by the flow and can float or sediment, depending on their density [Beckermann 2002]. During their movement, the nearby liquid is driven away before the grains finally settle in the end of solidification. When the solute-rich liquid is expelled, a negative macrosegregation zone (often referred to as *negative segregation cone* in cast ingots) is detected where the grains have finally settled.

1.2.4 Solid deformation

Stresses of thermal and mechanical nature are always found in casting processes (e.g. bulging between rolls in continuous casting). Deformation of the semi-solid region located in the

mushy zone causes a relative solid-liquid flow in the inward (tensile stresses) or outward (compressive stresses) direction, leading to macrosegregation.

1.3 Other defects

Apart from macrosegregation, other defects are also encountered in industrial processes. In the casting industry, defects like pores and cracks can be disastrous causing the cast product to be rejected. If possible, the product is reheated, remelted and then cast again. Otherwise it is scrapped. From an economic point view, these operations are very expensive.



Fig. 1.7 – Three instances of solidification-related defects found in cast products: (a) internal crack in continuous casting [Arcelormittal] (b) surface cavities in ingot casting [Carlson et al. 2002] and (c) freckle in the form of a chain of equiaxed crystals in Ni-base superalloy investment casting [Giamei and Kear 1970].

Hot tearing

Hot tearing, also denoted solidification cracking or hot cracking, occurs in the mushy zone at high solid fractions when a failure or crack appears in the cast part. They refer to liquid regions enclosed in the solid, where feeding stops. Preferential sites for crack initiation are localised in regions where liquid feeding is difficult. The volume change combined with thermal stresses or external strains, may lead to cracks as shown in [fig. 1.7a](#). The temperature range in which the steel is vulnerable to hot tearing is known as the brittle temperature range, where the solid fraction is typically greater than 90%.

Porosity

Porosity is a void defect formed inside the casting or at the outer surface. It may be attributed to two different factors. Firstly, we speak of *shrinkage porosity*, when a void forms as a result of density differences between the liquid and its surrounding dendritic solid network, the latter being generally denser than the former. After solidification is complete, the casting surface may look like [fig. 1.7b](#). The second factor is the presence of dissolved gaseous phases in the melt, and is referred to as *gas porosity*. According to [Dantzig and Rappaz \[2009\]](#), these gases may be initially in the melt, or created by the reaction between the metal and water found in the air or trapped in grooves at the moulds surface. Providing sufficient cooling and pressure drop in the liquid, the latter becomes supersaturated. The nucleation of a gaseous phase is then triggered.

Freckles or segregated channels

The origin of this defect, shown in [fig. 1.7c](#), is a combined effect of microsegregation, buoyancy forces and fragmentation of the dendritic network. For a solute species that preferentially segregates into the liquid (partition coefficient less than unity) and locally reduce the liquid density, a solutal driving force is created inside the mushy zone, generating convection currents, with "plume" shapes as often reported in the literature [[Sarazin and Hellawell 1992](#); [Schneider et al. 1997](#); [Saad et al. 2015](#)]. Temperature gradient is often an additional force of convection as the liquid density is also temperature-dependent, the resulting driving force being thus qualified as "thermosolutal".

Equiaxed grains shown in [fig. 1.7c](#), are the growth result from free floating dendrite fragments in the solute-rich liquid channel. As solute accumulates in these areas, the thermosolutal convection is sustained, hence the channel solidification is delayed. This leads to the formation of a distinct crystal chain pattern, the so-called *freckle*, once the segregated channel completely solidifies.

1.4 Industrial Worries

Steel production has continuously increased over the years to meet the industrial needs. [Figure 1.8](#) shows this increase between 1980 and 2013 with a clear rise of the Chinese production. Quality constraints have also increased where specific grades of steel are needed in critical applications such as mega-structures in construction and heavy machinery. Other domains like the nuclear, are good examples showing the relevance of macrosegregation studies in developing nuclear components for the new generation Evolutionary Power Reactor, manufactured by Areva. Therefore, alloys with defects are considered vulnerable and should be avoided as much as possible during the casting process. As such, steel makers have been investing in research, with the aim of understanding better the phenomena leading to casting problems, and improve the processes when possible.

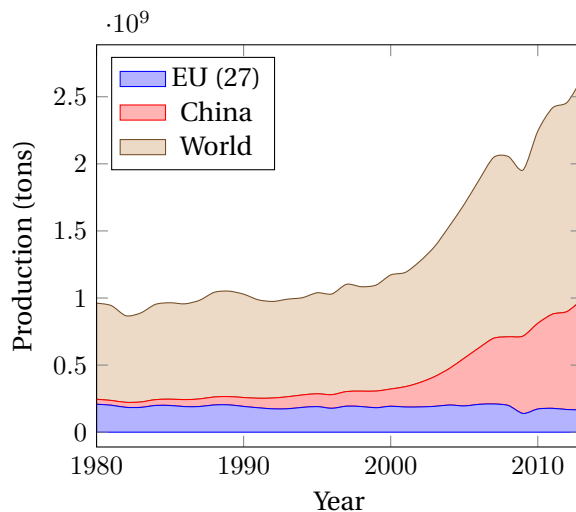


Fig. 1.8 – Evolution curves of crude steel worldwide production from 1980 to 2013 [[WSA 2014](#)].

Simulation software dedicated to alloy casting is one of the main research investments under-

taken by steelmakers. These tools originating from academic research, are actively used to optimize the process. However, few are the tools that take into account the casting environment. For instance, the continuous casting process, is a chain process where the last steps involve rolling, heat treatments, forging, etc. The continuous casting machine itself not only consists of an open mould where solidification starts, but also includes rolls, water sprays and other components. A dedicated software is one that can provide the geometric requirements with suitable meshing capabilities, as well as respond to metallurgical and mechanical requirements, mainly by handling:

- moulds and their interaction with the alloy (thermal resistances ...)
- alloy filling and predicting velocity in the liquid and mushy zone
- thermomechanical stresses in the solid
- multicomponent alloys and predicting macrosegregation
- microstructure and phases
- finite solute diffusion in solid phases
- real alloy properties (not just constant thermophysical/thermomechanical properties)
- ..., etc

1.5 Project context and objectives

1.5.1 Context

The European Space Agency (ESA) has been actively committed, since its foundation in 1975, to research. It covers not only exclusive space applications, but also fundamental science like solidification. This thesis takes part in the ESA project entitled *CCEMLCC*, abbreviating "Chill Cooling for the Electro-Magnetic Levitator in relation with Continuous Casting of steel". The three-year project from late 2011 to late 2014 denoted *CCEMLCC II*, was preceded by an initial project phase, *CCEMLCC I*, from 2007 to 2009. The main focus is studying containerless solidification of steel under microgravity conditions. A chill plate is used to extract heat from the alloy, simulating the contact effect with a mould in continuous casting or ingot casting. A partnership of 7 industrial and academic entities was formed in *CCEMLCC II*. Here is a brief summary of each partner's commitment:

Academic partners

- Center for Material Forming (CEMEF) - France: numerical modelling of microgravity chill cooling experiments
- Deutsches Zentrum für Luft- und Raumfahrt (DLR or German Aerospace Centre) and Ruhr Universität Bochum (RUB) university - Germany: preparation of a chill cooling device for electromagnetic levitation (EML), microgravity testing and investigation of growth kinetics in chill-cooled and undercooled steel alloys
- University of Alberta - Canada: impulse atomization and spray deposition of the D2 tool steel

- University of Bremen - Institut für Werkstofftechnik (IWT) institute - Germany: study of D2 tool steel melt solidification in atomization processing

Industrial partners

- ARCELORMITTAL (France): elaboration of a series of steel grades used in microgravity and ground-based studies and characterisations.
- METSO Minerals Inc. (Finland): material production with D2 tool steel for spray forming
- TRANSVALOR (France): development and marketing of the casting simulation software *THERCAST®*

CEMEF, as an academic partner, contributed to the work by proposing numerical models in view of predicting the chill cooling of steel droplets. A first model was developed by Rivaux [2011]. The experimental work by DLR considered various facilities and environments to set a droplet of molten alloy in levitation: EML (fig. 1.9) for ground-based experiments, microgravity during parabolic flight or sounding rockets and last, microgravity condition on-board the International Space Station (ISS).

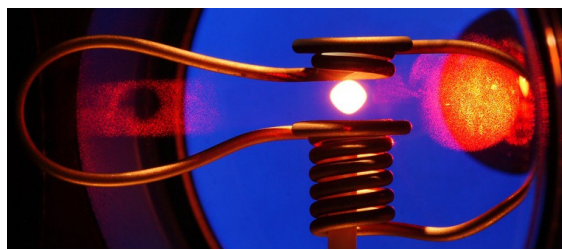


Fig. 1.9 – Electromagnetic levitation [DLR 2014].

1.5.2 Objectives and outline

The main focus of the present thesis is predicting macrosegregation with liquid dynamics assuming a fixed solid phase, i.e. no account of solid transport (e.g. equiaxed crystals sedimentation) and no account of solid deformation. At CEMEF, this scope has been adopted in previous studies by Gouttebroze [2005], Liu [2005], Mosbah [2008], Rivaux [2011], and Carozzani [2012]. Nevertheless, many modelling features evolved with time such as going from two-dimensional to three-dimensional modelling, resolution schemes for each of the conservation equations: energy, chemical species and liquid momentum, Eulerian or Lagrangian descriptions, modelling of grain structure and others. In this thesis, we propose a numerical model that takes into account i) the energy conservation in a temperature formulation based on a thermodynamic database mapping, ii) the liquid momentum conservation with thermosolutal convection and solidification shrinkage as driving forces, iii) solute mass conservation with solidification shrinkage to predict inverse segregation and iv) solidification paths at full equilibrium for multicomponent alloys. Moreover, all equations are formulated in a pure Eulerian description while using the level set method to keep implicitly track of the interface between the alloy and the surrounding gas.

To the author's knowledge, this work combining macrosegregation prediction using the level set methodology to track the metal-air interface during shrinkage has no precedent in casting

and solidification literature. The model couples in a weak fashion, all four conservation equations presented in [fig. 1.10](#), showing on the one hand, that microsegregation is an essential common link between these equations, while on the other hand, the level set interacts with conservations equations by giving the interface position.

Numerical tools

The current thesis developments are done using C++ language as a part of the in-house code, known as *CimLib* [[Digonnet et al. 2007](#); [Mesri et al. 2009](#)]. It's a finite element library with an object-oriented hierarchy consisting of global finite element solvers for physical differential equations, also point-wise and element-wise solvers for preprocessing and post-processing the finite element solution. It is also designed with a highly parallel architecture with MPICH2, which makes it possible to handle large meshes with heavy operations like mesh partitioning and adaptation. Side utilities for plotting and analysis are also developed, using python language.

Content outline

This manuscript consists of 5 chapters. In **chapter 2**, a short review introduces the state-of-art in the literature of macroscopic modelling of solidification with transport of energy, species, mass and momentum. **Chapter 3** provides details of the energy conservation equation and introduces a new temperature-based solver compatible with thermodynamic databases, **Chapter 4** focuses on the mass and momentum conservation equations and their derivation in the context of a single metallic domain (i.e. without the level set method) where the solid is assumed a fixed and rigid body. As an application, this chapter shows a breakthrough comparison between purely macroscopic and mesoscopic-macroscopic approaches in predicting the hydrodynamic instabilities that lead to channel segregation. The derived energy, mass and momentum equations for the monodomain model are revisited in **chapter 5** in the context of the level set method to take into account solidification shrinkage. The influence of shrinkage on macrosegregation is then studied in two different applications.



Fig. 1.10 – A graphical representation of the main elements of the numerical approach, for a macrosegregation model with the level set methodology, when no solid deformation or movement are considered. The dashed lines represent the interactions between the various components.

Résumé chapitre 1

Dans ce premier chapitre d'introduction, on introduit les notions de base en solidification. On s'intéresse particulièrement aux notions de ségrégation se produisant à l'échelle des structures de solidification et que l'on appelle *microségrégation*. Ce phénomène est directement lié à la différence de solubilité des espèces chimiques aux interfaces séparant les phases présentes dans l'alliage qui subit la transformation. Plusieurs facteurs, qu'ils soient relatifs au procédé de solidification ou inhérents aux phénomène de changements de phase, peuvent être à l'origine d'un mouvement des phases. Ainsi, toute vitesse relative entre ces phases est à l'origine d'un transport des espèces chimiques et donc une redistribution à l'échelle des pièces coulées. On parle alors de *macroségrégation*.

Les ségrégations à l'échelle miroscopique peuvent être homogénéisées par le biais des traitements thermiques favorisant le transport par diffusion chimique. Cependant, la macroségrégation est souvent irréversible et donc la cause de rebut de pièces produites. Ce défaut, rencontré dans des procédés de coulé continue ou coulée en lingot, est appréhendé par les sidérurgistes qui investissent dans la recherche afin de mieux contrôler leur production.

La présente thèse s'inscrit dans le cadre de l'étude de la macroségrégation, notamment quand la cause en est le mouvement de la phase liquide par convection thermosolutale et/ou par retrait à la solidification, tout en supposant que les différentes phases solides sont fixes et rigides.

Dans le **chapitre 2**, nous présentons un modèle de solidification basé sur la résolution des équations de conservation moyennées sur l'ensemble des phases, en utilisant la prise de moyenne sur des volumes élémentaires représentatifs. Ces équations comportent la conservation de la masse, l'énergie, la masse des espèces chimiques et la quantité de transport dans la phase liquide. Ce modèle est enrichi dans le **chapitre 3**, en proposant une nouvelle méthode de résolution de l'équation de la conservation d'énergie, avec la température comme variable principale. Cette méthode utilise des propriétés à l'équilibre thermodynamique tabulés à partir d'une base de données dédiée, donnant accès à des valeurs qui évoluent selon la composition de l'alliage. Dans le **chapitre 4**, on emploie cette méthode pour l'énergie, avec les autres équations de conservation, pour prédire la ségrégation en canaux produite par convection thermosolale, sans aucun changement de volume à la solidification. Comme cela nécessite d'avoir un suivi d'interface métal-air, une méthode implicite de suivi d'interface est intégrée au modèle de solidification dans le **chapitre 5**. Le modèle final permet donc de prédire la macrosérgation produite par retrait à la solidification et par convection thermosolutale avec suivi de front métal.

Chapter 2

Modelling Review

Contents

2.1	Modelling macrosegregation	16
2.1.1	Macroscopic solidification model: monodomain	17
2.2	Eulerian and Lagrangian motion description	23
2.2.1	Overview	23
2.2.2	Interface capturing	23
2.3	Solidification models with level set	24
2.4	The level set method	24
2.4.1	Diffuse boundary	25
2.4.2	Mixing Laws	26
2.5	Interface motion	28
2.5.1	Level set transport	29
2.5.2	Level set regularisation	30
2.6	Mesh adaptation	33
2.6.1	Metrics and anisotropy	33
2.6.2	<i>Remesh2</i> : domains boundary remeshing	34
2.6.3	<i>Remesh4</i> : Multi-criteria remeshing	35

2.1 Modelling macrosegregation

Microsegregation models

Solid formation depends greatly on the ability of chemicals species to diffuse within each of the solid and liquid phases. Furthermore, chemical diffusion like all other diffusional processes, is a time-dependent phenomenon. One can thus conclude that two factors influence the amount of solid formation: cooling rate and diffusion coefficients. However, convection and other mechanical mixing sources, homogenise the composition much faster than atomic diffusion. Considering that $\langle D \rangle^l / \langle D \rangle^s \approx 10^3 - 10^4$ for species within the solidification interval, *complete mixing* in the liquid is often an acceptable assumption, regardless of the solidification time. Thus, we speak of infinite diffusion in the liquid. Diffusion in the solid, also known as *back diffusion*, is the only transport mechanism with very low diffusion coefficients. Therefore, chemical species require a long time, i.e. low cooling rate, to completely diffuse within the solid. The difference in diffusional behaviour at the scale of a secondary dendrite arm, is summarised by two limiting segregation models of perfect equilibrium and non-equilibrium, which are the lever rule and Gulliver-Scheil models, respectively. Afterwards, models with finite back diffusion are presented.

Lever rule

The lever rule approximation considers ideal equilibrium in and between all phases. It requires a long solidification time, i.e. extremely slow cooling rate, hence phase compositions are homogeneous ($w^{l*} = w^l$ and $w^{s*} = w^s$) at all times as a consequence of complete mixing. These compositions are given by:

$$w^l = w^{l*} = k^{-1} w^{s*} = k^{-1} w^s \quad (2.1)$$

$$w^s = w^{s*} = \frac{k w_0}{k f^s + (1 - f^s)} \quad (2.2)$$

where w^l and w^s are the phase compositions and w^{l*} and w^{s*} are values at the solid-liquid interface in the liquid and solid phases, respectively. At the end of solidification, if a single solid phase forms, its composition is equal to the nominal composition, $w^s = w_0$.

Gulliver-Scheil

The other limiting case is the absence of diffusion in the solid or its limitation due to fast cooling. For a segregation coefficient less than unity, the consequence is a steady increase of the homogeneous liquid composition upon cooling while the solid composition continuously increases and becomes non-uniform. Compared to a full equilibrium approach, higher fractions of liquid will remain. In eutectic systems, liquid may exist until another solid structure forms, e.g. upon reaching the eutectic composition, triggering a eutectic solidification, that is the appearance of the lamellar eutectic microstructure. Assuming phase equilibrium is still valid,

i.e. $w^l = k^{-1}w^s$, the phase compositions are given by:

$$w^l = w^l = k^{-1}w^s \quad (2.3)$$

$$w^s = kw_0(1 - f^s)^{k-1} \quad (2.4)$$

$$w^s = \int_0^{f^s} w^s \mathrm{d}f^s \quad (2.5)$$

Finite back diffusion

The assumption of a negligible back diffusion overestimates the liquid composition and the resulting eutectic fraction. Therefore, many models studied the effect of limited diffusion in the solid. One of the earliest models is the Brody-Flemings models [Brody and Flemings 1966] that is based on a differential solute balance equation for a parabolic growth rate, as follows:

$$w^l = w^l = k^{-1}w^s \quad (2.6)$$

$$w^s = kw_0 [1 - (1 - 2\mathrm{Fo}^s k) f^s]^{\frac{k-1}{1-2\mathrm{Fo}^s k}} \quad (2.7)$$

where Fo^s is the dimensionless *Fourier number* for diffusion in the solid [Dantzig and Rappaz 2009]. It can be defined using the solid diffusion coefficient $\langle D \rangle^s$, solidification time t_s and the secondary dendrite arm spacing, λ_2 , as follows:

$$\mathrm{Fo}^s = \frac{\langle D \rangle^s t_s}{(\lambda_2/2)^2} \quad (2.8)$$

Several other models were since suggested and used. The interested reader is referred to the following non exhaustive list of publications: Clyne and Kurz [1981], Kobayashi [1988], Ni and Beckermann [1991], Wang and Beckermann [1993], Combeau et al. [1996], Martorano et al. [2003], and Tourret and Gandin [2009]. It is noted that some of these publications consider also a finite diffusion in the liquid phase. It is also noted that dealing with some aspects (e.g. multicomponent equilibrium phase diagrams, cross-diffusion of species, ...) is generally difficult and received a limited number of studies in the aim of determining a multicomponent segregation model, thus numerical approaches are favoured.

2.1.1 Macroscopic solidification model: monodomain

In this section, we will present the macroscopic conservation equations that enable us to predict macrosegregation in single multiphase metal system.

Volume averaging

It is crucial for a solidification model to represent phenomena on the microscale, then scale up to predict macroscopic phenomena. Nevertheless, the characteristic length of a small scale in solidification may be represented by a dendrite arm spacing, for instance for the mushy zone permeability, as it may also be represented by an atomic distance if one is interested, for instance in the growth competition between diffusion and surface energy of the solid-liquid interface. Modelling infinitely small-scale phenomena could be prohibitively expensive in computation time, if we target industrial scales. Therefore, the common volume averaging

approach alleviates these difficulties by making assumptions on intermediate scales. This technique allows bypassing this barrier by averaging small-scale variations on a so-called *representative volume element* (RVE) [Dantzig and Rappaz 2009] of volume V_E , with the following dimensional constraints: the element should be large enough to "see" and average microscopic fluctuations whilst being smaller than the scale of macroscopic variations.

Solid and liquid may exist simultaneously in the RVE, but we may also consider that no gas phase could be added (i.e. volume saturation with $V^s + V^l = V_E$). Moreover, temperature is generally assumed uniform and equal for all the phases. The formalism, introduced by Ni and Beckermann [1991], introduces a phase indicator function for any phase ϕ in the multiphase system:

$$\chi^\phi = \begin{cases} 1 & \text{in } \phi \\ 0 & \text{otherwise} \end{cases} \quad (2.9)$$

Then the approach suggests the following equations for any physical quantity ψ in system containing solid (s) and liquid (l) phases:

$$\langle \psi \rangle = \frac{1}{V_E} \int_{V_E} \psi \, d\Omega = \langle \psi^s \rangle + \langle \psi^l \rangle \quad (2.10)$$

where $\langle \psi \rangle^s$ and $\langle \psi \rangle^l$ are phase averages of ψ . Then, for any phase ϕ , one can introduce the *phase intrinsic average* of ψ , denoted $\langle \psi \rangle^\phi$, by writing:

$$\langle \psi^\phi \rangle = \langle \chi^\phi \psi \rangle = \frac{1}{V_E} \int_{V_E} \chi^\phi \psi \, d\Omega \quad (2.11a)$$

$$= \frac{1}{V_E} \int_{V^\phi} \chi^\phi \psi \, d\Omega \quad (2.11b)$$

$$= \frac{V^\phi}{V_E} \left(\frac{1}{V^\phi} \int_{V^\phi} \chi^\phi \psi \, d\Omega \right) \quad (2.11c)$$

$$= g^\phi \langle \psi \rangle^\phi \quad (2.11d)$$

where g^ϕ is the volume fraction of phase ϕ with $g^\phi = V_\phi/V_E$. The transition from eq. (2.11a) to eq. (2.11b) is the consequence of eq. (2.9). To finalize, the averaging is applied to temporal and spatial derivation operators:

$$\langle \frac{\partial \psi^\phi}{\partial t} \rangle = \frac{\partial \langle \psi^\phi \rangle}{\partial t} - \int_{\Gamma_{l-s}} \psi^\phi \mathbf{v}^* \cdot \mathbf{n}^\phi \, dA \quad (2.12)$$

$$\langle \nabla \cdot \psi^\phi \rangle = \nabla \cdot \langle \psi^\phi \rangle + \int_{\Gamma_{l-s}} \psi^\phi \cdot \mathbf{n}^\phi \, dA \quad (2.13)$$

where \mathbf{v}^* is the local relative interface velocity and Γ_{l-s} is the solid-liquid interface, while \mathbf{n}^ϕ is the normal to Γ_{l-s} , directed outwards. The surface integral terms in eqs. (2.12) and (2.13) are *interfacial averages* that express exchanges between the phases across the interface. The previous equations will be used to derive a set of macroscopic conservation equations.

Macroscopic equations

A monodomain macroscopic model relies on four main conservation equations to predict macrosegregation in a single alloy where the latter is considered without any direct representation of interactions with another domain (moulds, air, ...). The general form of such a macroscopic conservation equation is given by:

$$\frac{\partial \psi}{\partial t} + \nabla \cdot \psi \mathbf{v} + \nabla \cdot \mathbf{j}_\psi = Q_\psi \quad (2.14)$$

where the first LHS term is non-stationary, the second LHS term represents the convective transport of the quantity ψ while the third LHS term is diffusive transport of ψ . The RHS term is a source term. To determine an general averaged macroscopic equation, we must write a phase-averaged conservation equation, for any volumetric physical quantity ψ using the phase indicator function χ^ϕ for phase ϕ as follows:

$$\langle \chi^\phi \frac{\partial \psi}{\partial t} \rangle + \langle \chi^\phi \nabla \cdot \psi \mathbf{v} \rangle + \langle \chi^\phi \nabla \cdot \mathbf{j}_\psi \rangle = \langle \chi^\phi Q_\psi \rangle \quad (2.15)$$

We may then write each averaged macroscopic conservation equation as the sum of local conservation equations for each phase in the RVE using the interfacial average terms previously defined in [eqs. \(2.12\)](#) and [\(2.13\)](#). For instance, if we replace ψ by ρ for each phase $\phi \in \{l, s\}$, [eq. \(2.15\)](#) gives two phase-averaged mass balances, with interfacial terms:

$$\frac{\partial}{\partial t} (g^l \langle \rho \rangle^l) + \nabla \cdot (g^l \langle \rho \rangle^l \langle \mathbf{v} \rangle^l) = \int_{\Gamma_{l-s}} \langle \rho \rangle^l \mathbf{v}^{l*} \cdot \mathbf{n} \, dA - \int_{\Gamma_{l-s}} \langle \rho \rangle^l \mathbf{v}^* \cdot \mathbf{n} \, dA \quad (2.16a)$$

$$\frac{\partial}{\partial t} (g^s \langle \rho \rangle^s) + \nabla \cdot (g^s \langle \rho \rangle^s \langle \mathbf{v} \rangle^s) = - \int_{\Gamma_{l-s}} \langle \rho \rangle^s \mathbf{v}^{s*} \cdot \mathbf{n} \, dA + \int_{\Gamma_{l-s}} \langle \rho \rangle^s \mathbf{v}^* \cdot \mathbf{n} \, dA \quad (2.16b)$$

where \mathbf{v}^{l*} and \mathbf{v}^{s*} are respectively, the liquid and solid phase velocity at the interface and \mathbf{v}^* is the previously introduced solid-liquid interface velocity, while vector \mathbf{n} is the the normal to the solid-liquid interface, with $\mathbf{n} = \mathbf{n}^s = -\mathbf{n}^l$. Summing equations [\(2.16a\)](#) and [\(2.16b\)](#), results in the overall mass balance in the RVE:

$$\begin{aligned} \frac{\partial}{\partial t} (g^l \langle \rho \rangle^l + g^s \langle \rho \rangle^s) + \nabla \cdot (g^l \langle \rho \rangle^l \langle \mathbf{v} \rangle^l + g^s \langle \rho \rangle^s \langle \mathbf{v} \rangle^s) = \\ \int_{\Gamma_{l-s}} (\langle \rho \rangle^l \mathbf{v}^{l*} - \langle \rho \rangle^s \mathbf{v}^{s*}) \cdot \mathbf{n} \, dA - \int_{\Gamma_{l-s}} (\langle \rho \rangle^l - \langle \rho \rangle^s) \mathbf{v}^* \cdot \mathbf{n} \, dA \end{aligned} \quad (2.17)$$

where the RHS cancels to zero as shown by [Ni and Beckermann \[1991\]](#). Moreover, the authors show that with their averaging technique, interfacial exchanges for energy, chemical species and momentum cancel out as they are equal in absolute value but opposite in sign. Regarding

the LHS terms, their sum is defined along other variables as follows:

$$\langle \rho \rangle = g^l \langle \rho \rangle^l + g^s \langle \rho \rangle^s \quad (2.18)$$

$$\langle \rho \mathbf{v} \rangle = g^l \langle \rho \rangle^l \langle \mathbf{v} \rangle^l + \cancel{g^s \langle \rho \rangle^s \langle \mathbf{v} \rangle^s} \quad (2.19)$$

$$\langle \rho h \rangle = g^l \langle \rho \rangle^l \langle h \rangle^l + g^s \langle \rho \rangle^s \langle h \rangle^s \quad (2.20)$$

$$\langle \rho h \mathbf{v} \rangle = g^l \langle \rho \rangle^l \langle h \rangle^l \langle \mathbf{v} \rangle^l + \cancel{g^s \langle \rho \rangle^s \langle h \rangle^s \langle \mathbf{v} \rangle^s} \quad (2.21)$$

$$\langle \rho w_i \rangle = g^l \langle \rho \rangle^l \langle w_i \rangle^l + g^s \langle \rho \rangle^s \langle w_i \rangle^s \quad (2.22)$$

$$\langle \rho w_i \mathbf{v} \rangle = g^l \langle \rho \rangle^l \langle w_i \rangle^l \langle \mathbf{v} \rangle^l + \cancel{g^s \langle \rho \rangle^s \langle w_i \rangle^s \langle \mathbf{v} \rangle^s} \quad (2.23)$$

$$\langle \rho^l \mathbf{v}^l \rangle = g^l \langle \rho \rangle^l \langle \mathbf{v} \rangle^l \quad (2.24)$$

$$\langle \rho^l \mathbf{v}^l \times \mathbf{v} \rangle = g^l \langle \rho \rangle^l \langle \mathbf{v} \rangle^l \times \langle \mathbf{v} \rangle^l + \cancel{g^s \langle \rho \rangle^s \langle \mathbf{v} \rangle^l \times \langle \mathbf{v} \rangle^s} \quad (2.25)$$

The average diffusive fluxes are represented by $\langle \mathbf{q} \rangle$ for energy and $\langle \mathbf{j}_i \rangle$ for each solute species. They are respectively modelled using Fourier's thermal conduction law and Fick's first mass diffusion law:

$$\langle \mathbf{q} \rangle = -g^l \langle \kappa \rangle^l \nabla T - g^s \langle \kappa \rangle^s \nabla T = -\langle \kappa \rangle \nabla T \quad (2.26)$$

$$\langle \mathbf{j}_i \rangle = -g^l \langle D \rangle^l \nabla (\langle \rho \rangle^l \langle w_i \rangle^l) - \cancel{g^s \langle D \rangle^s \nabla (\langle \rho \rangle^s \langle w_i \rangle^s)} \quad (2.27)$$

In eq. (2.27), the macroscopic diffusion coefficient in the solid is neglected, by considering that for macroscopic scales, the average composition of the alloy is much more influenced by advective and diffusive transport in the liquid.

In eq. (2.26), we assume that phases are at thermal equilibrium, that is, temperature is uniform in the RVE. We also introduced the average thermal conductivity, $\langle \kappa \rangle$, defined as $\langle \kappa \rangle = g^s \langle \kappa \rangle^s + g^l \langle \kappa \rangle^l$.

Using eqs. (2.18) to (2.27) and following the same procedure done in eq. (2.17), the averaged equations for mass, energy and species conservation hence respectively write:

$$\frac{\partial \langle \rho \rangle}{\partial t} + \nabla \cdot \langle \rho \mathbf{v} \rangle = 0 \quad (2.28)$$

$$\frac{\partial \langle \rho h \rangle}{\partial t} + \nabla \cdot \langle \rho h \mathbf{v} \rangle - \nabla \cdot (\langle \kappa \rangle \nabla T) = 0 \quad (2.29)$$

$$\frac{\partial \langle \rho w_i \rangle}{\partial t} + \nabla \cdot \langle \rho w_i \mathbf{v} \rangle - \nabla \cdot (g^l \langle D \rangle^l \nabla (\langle \rho \rangle^l \langle w_i \rangle^l)) = 0 \quad (2.30)$$

As stated previously, the momentum balance in the solid phase is not taken into consideration, hence we do not sum the corresponding conservation equations. This has consequences on the advection terms in energy and species conservation, and later on we will show the consequences on the momentum conservation in the liquid.

First, the advection terms in eqs. (2.29) and (2.30) shall be redefined by considering that the fluid is incompressible ($\nabla \cdot \langle \mathbf{v}^l \rangle = 0$), which yields:

$$\nabla \cdot \langle \rho \mathbf{v} \rangle = \langle \mathbf{v}^l \rangle \cdot \nabla \langle \rho \rangle^l \quad (2.31)$$

$$\nabla \cdot \langle \rho h \mathbf{v} \rangle = \langle \mathbf{v}^l \rangle \cdot \nabla (\langle \rho \rangle^l \langle h \rangle^l) \quad (2.32)$$

$$\nabla \cdot \langle \rho w_i \mathbf{v} \rangle = \langle \mathbf{v}^l \rangle \cdot \nabla (\langle \rho \rangle^l \langle w_i \rangle^l) \quad (2.33)$$

As for the liquid momentum balance, we write:

$$\frac{\partial}{\partial t} (\langle \rho \rangle^l g^l \langle v \rangle^l) + \nabla \cdot (\langle \rho \rangle^l g^l \langle v \rangle^l \times \langle v \rangle^l) = \nabla \cdot \left(g^l \bar{\bar{\sigma}}^l \right) + g^l \mathbf{F}_v^l + \mathbf{M}^* \quad (2.34)$$

where \mathbf{F}_v^l is the vector of external body forces exerted on the liquid phase. In our case, it accounts for the fluid's weight:

$$\mathbf{F}_v^l = \langle \rho \rangle^l \mathbf{g} \quad (2.35)$$

The interfacial momentum transfer between the solid and liquid phases in eq. (2.34) is modelled by a momentum flux vector \mathbf{M}^* , consisting of hydrostatic and deviatoric parts, such that:

$$\mathbf{M}^* = \mathbf{M}_p^* + \mathbf{M}_{\mathbb{S}}^* \quad (2.36)$$

$$\mathbf{M}_p^* = p^{l*} \nabla g^l = p^l \nabla g^l \quad (2.37)$$

$$\mathbf{M}_{\mathbb{S}}^* = -g^{l2} \mu^l \mathbb{K}^{-1} (\langle v \rangle^l - \langle v \rangle^s) \quad (2.38)$$

where p^{l*} is the pressure at the interface, considered to be equal to the liquid hydrostatic pressure p^l , \mathbb{K} is a permeability scalar (isotropic) computed using eq. (1.2) and μ^l is the liquid's dynamic viscosity. The general form of the Cauchy liquid stress tensor in eq. (2.34) is decomposed as follows:

$$\langle \bar{\bar{\sigma}}^l \rangle = g^l \bar{\bar{\sigma}}^l = -(\langle p^l \rangle - \lambda \nabla \cdot \langle v^l \rangle) \bar{\bar{\mathbf{I}}} + \langle \bar{\bar{\mathbb{S}}}^l \rangle \quad (2.39)$$

where λ is a dilatational viscosity [Dantzig and Rappaz 2009] and $\bar{\bar{\mathbb{S}}}^l$ is the liquid strain deviator tensor.

In the literature, the coefficient λ is taken proportional to the viscosity: $\lambda = \frac{2}{3} \mu^l$. However, as we consider an incompressible flow, the divergence term vanishes, thus rewriting eq. (2.39) as follows:

$$\langle \bar{\bar{\sigma}}^l \rangle = -\langle p^l \rangle \bar{\bar{\mathbf{I}}} + \langle \bar{\bar{\mathbb{S}}}^l \rangle \quad (2.40a)$$

$$\langle \bar{\bar{\sigma}}^l \rangle = -\langle p^l \rangle \bar{\bar{\mathbf{I}}} + 2\mu^l \langle \bar{\bar{\dot{\epsilon}}}^l \rangle \quad (2.40b)$$

where the transition from eq. (2.40a) to eq. (2.40b) is made possible by assuming a Newtonian behaviour for the liquid phase. The strain rate tensor, $\langle \bar{\bar{\dot{\epsilon}}}^l \rangle$, depends on the average liquid velocity:

$$\langle \bar{\bar{\dot{\epsilon}}}^l \rangle = \frac{1}{2} \left(\bar{\bar{\nabla}} \langle v^l \rangle + \bar{\bar{\nabla}}^t \langle v^l \rangle \right) \quad (2.41)$$

Finally, we obtain the final form of momentum conservation in the liquid phase coupled with

the averaged mass balance, by injecting eqs. (2.35), (2.37), (2.38), (2.40b) and (2.41) in eq. (2.34):

$$\begin{aligned} \frac{\partial}{\partial t} (\langle \rho \rangle^l \langle \mathbf{v}^l \rangle) + \frac{1}{g^l} \nabla \cdot (\langle \rho \rangle^l \langle \mathbf{v}^l \rangle \times \langle \mathbf{v}^l \rangle) = \\ - g^l \nabla p^l - \mu^l \nabla \cdot (\overline{\nabla} \langle \mathbf{v}^l \rangle + \overline{\nabla^t} \langle \mathbf{v}^l \rangle) - g^l \mu^l \mathbb{K}^{-1} \langle \mathbf{v}^l \rangle + g^l \langle \rho \rangle^l \mathbf{g} \end{aligned} \quad (2.42)$$

where we intentionally employed the *superficial velocity*, $\langle \mathbf{v}^l \rangle = g^l \langle \mathbf{v} \rangle^l$, as the main unknown, together with the liquid pressure p^l . This system, when modelled in 3D, has a total of 4 unknowns (velocity vector and pressure) and 3 equations (X, Y and Z projections for the velocity vector). A fourth equation provided by the mass balance (eq. (2.28)) is therefore added for closure, giving the following system of equations :

$$\left\{ \begin{array}{l} \frac{\partial}{\partial t} (\langle \rho \rangle^l \langle \mathbf{v}^l \rangle) + \frac{1}{g^l} \nabla \cdot (\langle \rho \rangle^l \langle \mathbf{v}^l \rangle \times \langle \mathbf{v}^l \rangle) = \\ - g^l \nabla p^l - \mu^l \nabla \cdot (\overline{\nabla} \langle \mathbf{v}^l \rangle + \overline{\nabla^t} \langle \mathbf{v}^l \rangle) - g^l \mu^l \mathbb{K}^{-1} \langle \mathbf{v}^l \rangle + g^l \langle \rho \rangle^l \mathbf{g} \\ \nabla \cdot \langle \mathbf{v}^l \rangle = 0 \end{array} \right. \quad (2.43)$$

Last, the Boussinesq approximation allows taking a constant density in the inertial terms of eq. (2.43) while the variations responsible for buoyancy forces can be deduced from temperature and liquid concentration using thermodynamic databases or directly using known thermal and solutal expansion coefficients, respectively β_T and $\beta_{\langle w_i \rangle^l}$, and the reference density value ρ_0^l :

$$\langle \rho \rangle^l = \rho_0^l \left(1 - \beta_T (T - T_0) - \sum_i \beta_{\langle w_i \rangle^l} (\langle w_i \rangle^l - \langle w_i \rangle_0^l) \right) \quad (2.44)$$

Hence, the final set of equations is better known as the incompressible *Navier-Stokes* equations, applied to a solidifying melt:

$$\left\{ \begin{array}{l} \rho_0^l \left(\frac{\partial \langle \mathbf{v}^l \rangle}{\partial t} + \frac{1}{g^l} \nabla \cdot (\langle \mathbf{v}^l \rangle \times \langle \mathbf{v}^l \rangle) \right) = \\ - g^l \nabla p^l - \mu^l \nabla \cdot (\overline{\nabla} \langle \mathbf{v}^l \rangle + \overline{\nabla^t} \langle \mathbf{v}^l \rangle) - g^l \mu^l \mathbb{K}^{-1} \langle \mathbf{v}^l \rangle + g^l \langle \rho \rangle^l \mathbf{g} \\ \nabla \cdot \langle \mathbf{v}^l \rangle = 0 \end{array} \right. \quad (2.45)$$

To sum up, when solidification occurs at constant volume, i.e. when solid and liquid densities are equal and if the solid is considered fixed ($\langle \mathbf{v} \rangle^s = 0$), the multiphase system can be modelled by the four average conservation equations, for mass (eq. (2.28)), energy (eq. (2.29)), chemical species (eq. (2.30)) and liquid momentum (eq. (2.45)).

2.2 Eulerian and Lagrangian motion description

2.2.1 Overview

In mechanics, it is possible to describe motion using two well-known descriptions: Eulerian and Lagrangian. To start with the latter, it describes the motion of a particle by attributing a reference frame that moves with the particle. In other words, the particle itself is the centre of a reference frame moving at the same speed during time. The position vector, denoted by \mathbf{x} , is hence updated as follows:

$$\mathbf{x}^{(t+1)} = \mathbf{x}^{(t)} + \mathbf{v}\Delta t \quad (2.46)$$

As such, the total variation of any physical quantity ψ related to the particle can be found by deriving with respect to time, $\frac{d\psi}{dt}$. In contrast to the Lagrangian description, the Eulerian description considers a fixed reference frame and independent of the particle's trajectory. The total variation of ψ cannot be simply described by a temporal derivative, since the particle's velocity is not known to the reference frame, and thus the velocity effect, namely the advective transport of ψ , should also be considered as follows:

$$\frac{D\psi}{Dt} = \frac{\partial\psi}{\partial t} + \underbrace{\mathbf{v} \cdot \nabla \psi}_{\text{Advection}} \quad (2.47)$$

In this case, the LHS term is also known as *total* or *material derivative*. The importance of these motion descriptions is essential to solve mechanics, whether for fluids or solids, using a numerical method like the finite element method (FEM). One of the main steps of this method is to spatially discretise a continuum into a grid of points (nodes, vertices ...), where any physical field shall be accordingly discretised. Now, if we focus on a node where velocity has a non zero value and following the previously made analysis, two outcomes are possible: either the node would be fixed (Eulerian) or it would move by a distance proportional to the prescribed velocity (Lagrangian). In the latter case, points located on the boundaries constantly require an update of the imposed boundary conditions.

From these explanations, one can deduce that an Eulerian framework is suited for fluid mechanics problems where velocities are high and may distort the mesh points, whereas the Lagrangian framework is better suited for solid mechanics problems where deformation velocities are relatively low and should well behave when predicting strains.

Another motion description has emerged some decades ago, [Hirt \[1971\]](#) call it the Arbitrary Langrangian-Eulerian (ALE) method. ALE combines advantages from both previous descriptions as it dictates a Lagrangian behaviour at "solid" nodes where solid is deforming, and an Eulerian behaviour at "fluid" nodes.

2.2.2 Interface capturing

As no solid deformation is considered in this work, the Eulerian framework is a convenient choice. Solidification shrinkage is to be considered in our current scope, so it will deform the alloy's outer surface in contact with the air. We intend to track this interface and its motion over time via a numerical method. A wide variety of methods accomplish this task while they

yield different advantages and disadvantages.

Such methods fall into two main classes, either interface tracking or interface capturing, among which we cite: marker-and-cell (MAC) [Harlow and Welch 1965], volume of fluid (VOF) [Hirt and Nichols 1981], phase field methods (PF) [Karma and Rappel 1996; Beckermann et al. 1999], level set method (LSM) [Osher and Sethian 1988], coupled level set - VOF method and others. The interested reader may refer to quick references by Prosperetti [2002] and Maitre [2006] about these methods.

In the past years, the level set method received a considerable attention in many computational fields. For this reason, we will focus on this method henceforth, giving a brief literature review and technical details in the next sections.

2.3 Solidification models with level set

In classic solidification problems, the need to track an interface occurs usually at the solid-liquid interface, that is why the phase field method [Karma and Rappel 1996; Boettinger et al. 2002] and the level set method [Chen et al. 1997; Gibou et al. 2003; Tan and Zabaras 2007] were applied at a microscale to follow mainly the dendritic growth of a single solid crystal in an undercooled melt. In our case however, when we mention "solidification models using LSM", we do not mean the solid-liquid interface inside the alloy, but it is the alloy(liquid)-air interface that we intend to track, assuming that microscale phenomena between the phases within the alloy, are averaged using the previously defined technique in [section 2.1.1](#).

Very few models were found in the literature, combining solidification and level set as stated previously. Du et al. [2001] applied it to track the interface between two molten alloys in a double casting technique. Welding research, on another hand, has been more active adapting the level set methodology to corresponding applications. Two recent works used the metal-air level set methodology in welding simulations and showed promising results: Desmaison et al. [2014] employed this methodology to simulate a hybrid arc and laser beam welding used in high thickness steel sheet welding, then later, Chen [2014] applied it to gas metal arc welding (GMAW) to predict the solidification grain structure of remelted zones. More recently, Courtois et al. [2014] used the same methodology but this time to predict keyhole defect formation in spot laser welding. The tracked interface in this case was that between the molten alloy and the corresponding vapour phase.

2.4 The level set method

Firstly introduced by Osher and Sethian [1988], this method became very popular in studying multiphase flows. It is reminded that the term *multiphase* in computational domains usually refers to multiple fluids, and thus should not be mixed with definition of a phase in the current solidification context. For disambiguation, we shall use *multifluid flow* when needed, referred to as *domains* in the present work.

The great advantage lies in the way the boundary between two fluid domains, F_1 and F_2 is implicitly captured, unlike other methods where the exact boundary/interface position is needed. In a discrete domain, the concept is to assign for each mesh node of position vector \mathbf{x} , the minimum distance $d_\Gamma(\mathbf{x})$ separating it from an interface Γ , which we prefer calling boundary, as it is a numerical approximation of the limit between multiphase domains, in which we can

find the physical interfaces. The distance function, denoted α and defined in [eq. \(2.48\)](#), is then signed positive or negative, based on the domain to which the node belongs.

$$\alpha(\mathbf{x}) = \begin{cases} d_\Gamma(\mathbf{x}) & \text{if } \mathbf{x} \in F_1 \\ -d_\Gamma(\mathbf{x}) & \text{if } \mathbf{x} \in F_2 \\ 0 & \text{if } \mathbf{x} \in \Gamma \end{cases} \quad (2.48)$$

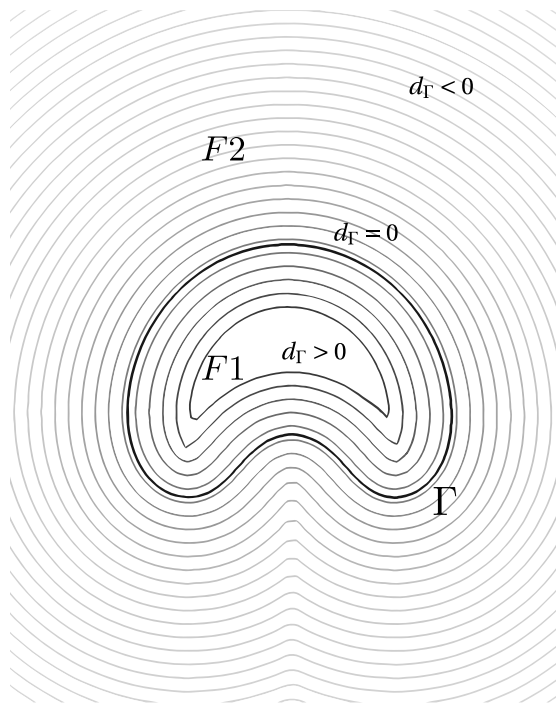


Fig. 2.1 – Schematic of the boundary Γ (thick black line) of a rising air bubble (F_1) in water (F_2). The other contours represent isovalues of the distance function around and inside the boundary contour. Those outside are signed negative whereas inside they are signed positive.

2.4.1 Diffuse boundary

The level set has many attractive properties that allows seamless implementation in 2D and 3D models. It is a continuously differentiable C^1 -function. The Heaviside function is also continuous but non differentiable, with a sharp transition from 0 to 1 across the boundary, defining the presence of domain F_1 as follows:

$$H_{\text{sharp}}^{F_1} = \begin{cases} 0 & \text{if } \alpha(\mathbf{x}) < 0 \\ 1 & \text{if } \alpha(\mathbf{x}) \geq 0 \end{cases} \quad (2.49)$$

This is better known as the non-smoothed Heaviside function relative to domain F_1 . It is established that a steep transition can lead to numerical problems, so the Heaviside function should be smoothed in a volume of fixed thickness around the boundary. Sinusoidal smoothing

in eq. (2.50) is widely used with level set formulations.

$$H^{F_1} = \begin{cases} 0 & \text{if } \alpha(\mathbf{x}) < -\varepsilon \\ 1 & \text{if } \alpha(\mathbf{x}) > \varepsilon \\ \frac{1}{2} \left(1 + \frac{\alpha(\mathbf{x})}{\varepsilon} + \frac{1}{\pi} \sin \left(\frac{\pi \alpha(\mathbf{x})}{\varepsilon} \right) \right) & \text{if } -\varepsilon \leq \alpha(\mathbf{x}) \leq \varepsilon \end{cases} \quad (2.50)$$

where the interval $[-\varepsilon; +\varepsilon]$ is an artificial boundary thickness around the zero distance.

Defining a diffuse boundary rather than a sharp one, is also a common approach in phase field methods [Beckermann et al. 1999; Sun and Beckermann 2004]. It is emphasized that the latter methods give physically meaningful analysis of a diffuse boundary and the optimal thickness by thoroughly studying the intricate phenomena happening at the scale of the boundary. However, for level set methods, there has not been a formal work leading the same type of analysis. For this reason, many aspects of the level set method lack physical meanings but remain computationally useful. In a recent paper by Gada and Sharma [2009], the authors respond partially to this problem by analysing and deriving conservation equations using a level set in a more meaningful way, but do not discuss the diffuse boundary aspect.

The Dirac delta function is also an important property to convert surface integrals to volume terms, which could turn useful when modelling surface tension effects for instance, using the *continuum surface force* method (CSF) [Brackbill et al. 1992]. A smooth Dirac function, plotted in fig. 2.2 along with the smooth Heaviside function within an interface thickness of $[-\varepsilon; +\varepsilon]$, is derived as follows:

$$\delta(\alpha) = \delta(\alpha(\mathbf{x})) = \frac{\partial H^{F_1}}{\partial \alpha(\mathbf{x})} = \begin{cases} \frac{1}{2\varepsilon} \left(1 + \cos \left(\frac{\pi \alpha(\mathbf{x})}{\varepsilon} \right) \right) & \text{if } |\alpha(\mathbf{x})| \leq \varepsilon \\ 0 & \text{if } |\alpha(\mathbf{x})| > \varepsilon \end{cases} \quad (2.51)$$

The Heaviside and delta Dirac functions can be readily processed to obtain other geometric properties from the level set, which are extremely useful. In the context of a system Ω , containing two domains F_1 separated by an interface Γ , the following properties are interesting to study [Peng et al. 1999]:

$$\text{normal vector to the boundary } \Gamma : \mathbf{n} = \frac{\nabla \alpha}{\|\nabla \alpha\|} \quad (2.52)$$

$$\Gamma \text{ boundary curvature} : \zeta = -\nabla \cdot \mathbf{n} \quad (2.53)$$

$$\text{surface area of the boundary } \Gamma : A^\Gamma = \int_{\Omega} \delta(\alpha) \|\nabla \alpha\| d\Omega \quad (2.54)$$

$$\text{volume of fluid 1} : V^{F_1} = \int_{\Omega} H^{F_1} d\Omega \quad (2.55)$$

It is reminded that for a 2D case, eq. (2.54) evaluates a length instead of the area while eq. (2.55) gives the area instead of volume. Finally, within the diffuse interface, fluids properties may vary linearly or not, depending on the mixing law, which is presented in the next section.

2.4.2 Mixing Laws

A *monolithic* resolution style, as opposed to a *partitioned* resolution, is based on solving a single set of equations for both fluids separated by an interface, as if a single fluid were considered.

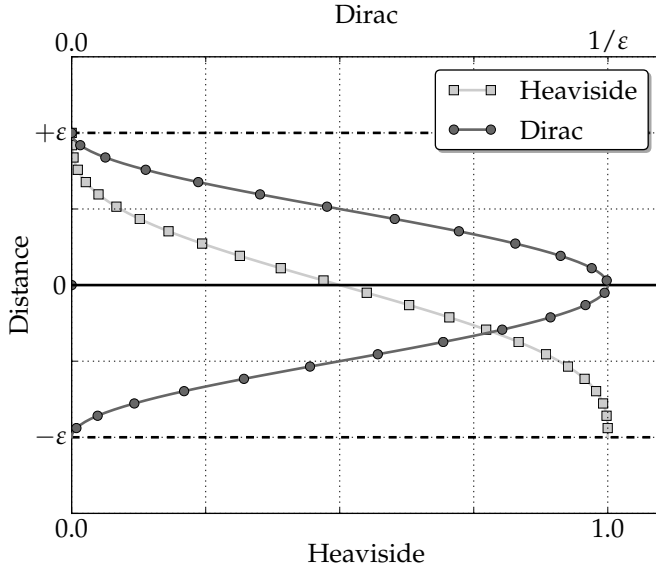


Fig. 2.2 – Schematic of two level properties inside the diffuse interface: smoothed Heaviside (lower x-axis) and Dirac delta (upper x-axis) functions. Note that the peak of the Dirac function depends on the interface thickness to ensure a unity integral of the delta function over Ω .

Level set is one among many methods that use the monolithic style to derive a single set of conservation equations for both fluids. The switch from one material to the other is implicitly taken care of by using the Heaviside function as well as mixing laws. These laws are crucial to define how properties vary across the diffuse interface in view of a more accurate resolution. The most frequently used mixing law in the literature is the arithmetic law. Other transitions are less known such as the harmonic and logarithmic mixing. The first law is maybe the most intuitive and most used for properties mixture as it emanates from VOF-based methods. If we consider any property ψ (for instance the fluid's dynamic viscosity μ) then the arithmetic law will give a mixed property $\hat{\psi}$ as follows:

$$\hat{\psi} = H^{F_1} \psi^{F_1} + H^{F_2} \psi^{F_2} \quad (2.56)$$

where $H^{F_2} = 1 - H^{F_1}$. Basically, the result is an average property that follows the same trend as the smoothed Heaviside function. As for the harmonic law, it writes:

$$\hat{\psi} = \left(\frac{H^{F_1}}{\psi^{F_1}} + \frac{H^{F_2}}{\psi^{F_2}} \right)^{-1} \quad (2.57)$$

and last, the logarithmic law writes:

$$\hat{\psi} = n^{(H^{F_1} \log_n \psi^{F_1} + H^{F_2} \log_n \psi^{F_2})} \quad (2.58)$$

where n is any real number serving as a logarithm base, which often is either the exponential e or 10.

The mixture result with this law is the same, regardless of the value of n . By looking to fig. 2.3, we clearly see that the difference between all three approaches is the property weight given to each side of the level set in the mixture. The arithmetic law, being symmetric, has equal

weights, ψ^{F_1} and ψ^{F_2} , in the final mixture. Nevertheless, the asymmetric harmonic mixing varies inside the diffuse interface with a dominant weight of one property over the other. As for the logarithmic mixture, it can be seen as an intermediate transition between the preceding laws.

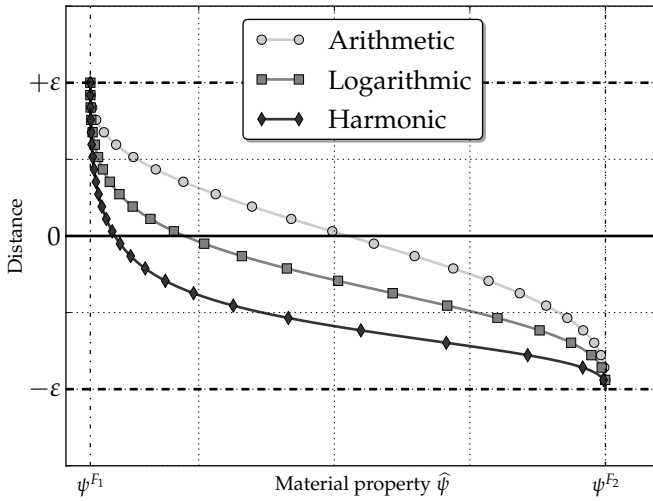


Fig. 2.3 – Three mixing laws, arithmetic, logarithmic and harmonic commonly used in monolithic formulations.

As long as the interface thickness is small enough, the choice of a mixing law should not drastically change the result, inasmuch as it depends on the discretisation resolution of the interface. This fact made the arithmetic mixing the most applied one, because it is symmetric and easy to implement (no handling of potential division problems like harmonic laws for instance). However, [Strotos et al. \[2008\]](#) claim that the harmonic law proves to conserve better diffusive fluxes at the interface. More recently, an interesting study made by [Ettrich et al. \[2014\]](#) focused on mixing thermal properties using a phase field method. They define a diffuse interface in which they separately mix the thermal conductivity, κ , and the heat capacity, c_p , then compute the thermal diffusivity as the ratio of these properties. Later, the authors compare the temperature field obtained by diffusion to a reference case in order to decide which combination of mixing laws gives the best result. Despite not being directly related to a level set method, this work gives an insight of the mixing laws possibilities and their effect on pure thermal diffusion. Otherwise, little work has been found in the literature on the broad effects of mixture types on simulation results in a level set context.

2.5 Interface motion

When a physical interface needs to have topology changes because of fluid structure interaction or surface tension for instance, the level set model can follow these changes by a transport step. The idea is to advect the signed distance function, its zero isovalue representing the interface and all other distant isovales, with velocity field as input. The motion of the interface is thus

expressed by:

$$\frac{d\alpha}{dt} = \frac{\partial\alpha}{\partial t} + \mathbf{v} \cdot \nabla\alpha = 0 \quad (2.59)$$

2.5.1 Level set transport

The finite element method gives the fully discretised weak form of [eq. \(2.59\)](#) by using a convenient set of test functions α^* belonging the Hilbertian Sobolev space:

$$\int_{\Omega} \alpha^* \frac{\partial\alpha}{\partial t} d\Omega + \int_{\Omega} \alpha^* \mathbf{v} \cdot \nabla\alpha d\Omega = 0 \quad \forall \alpha^* \in \mathcal{H}^1(\Omega) \quad (2.60)$$

The spatial discretisation of α assigns, for each of the total N nodes of a simplex, the following values:

$$\alpha = \sum_N P_j \alpha_j \quad (2.61)$$

Furthermore, with the standard Galerkin method, we replace test functions by the interpolation functions P_j , then we apply a temporal discretisation for the main unknowns by a forward (implicit) finite difference in time. Consequently, [eq. \(2.60\)](#) can be recast as follows:

$$i, j : 1 \rightarrow \text{Nnodes}$$

$$\frac{1}{\Delta t} (\alpha_j^t - \alpha_j^{t-\Delta t}) \int_{\Omega} P_i P_j d\Omega + \alpha_j^t \int_{\Omega} \mathbf{v}^t \cdot \nabla P_j d\Omega = 0 \quad (2.62a)$$

$$\left[\frac{1}{\Delta t} \int_{\Omega} P_i P_j d\Omega + \int_{\Omega} \mathbf{v}^t \cdot \nabla P_j d\Omega \right] \alpha_j^t = \frac{1}{\Delta t} \int_{\Omega} \alpha^{t-\Delta t} P_i d\Omega \quad (2.62b)$$

$$[\mathcal{M}_{ij} + \mathcal{A}_{ij}] \alpha_j^t = \mathcal{F}_i \quad (2.62c)$$

where \mathcal{M}_{ij} and \mathcal{A}_{ij} are respectively the mass (or capacity) matrix and advection matrix, both written within a local finite element, whereas \mathcal{F}_i corresponds to the RHS and is a local vector of known quantities from the previous time step. The solution of the linear system in [eq. \(2.62c\)](#) is the transported distance function.

When the convection regime becomes more dominant than diffusion (for high Peclet number), the standard Galerkin method may lead to instabilities in the solution. In this case, stabilisation is crucial to avoid these oscillations, unless very fine remeshing is done "such that convection no longer dominates on an element level", as stated by [Brooks and Hughes \[1982\]](#). The authors give a brief explanation of how numerically a convection-dominated equation can lead to oscillatory solutions with the standard Galerkin approximation. They proposed a stabilisation scheme, the Streamline Upwind Petrov-Galerkin, better known as SUPG, to stabilise advection dominated Navier-Stokes equations. Their technique applies to any convection-diffusion equation. The SUPG method consists of modifying the test functions (like a classical Petrov-Galerkin method) by adding artificial diffusion in the flow direction. The modified test function writes:

$$\alpha_{SUPG}^* = \alpha^* + \underbrace{\tau_{SUPG}^E (\mathbf{v} \cdot \nabla \alpha^*)}_{\text{upwind contribution}} \quad (2.63)$$

where the upwind contribution for each finite element E depends on a stabilisation parameter τ_{SUPG}^E that is expressed as follows:

$$\tau_{SUPG}^E = \frac{h^E}{v_{\text{flow}}^E} \quad (2.64)$$

[Equation \(2.64\)](#) shows that the SUPG parameter represents a time constant relative to an element mesh size, h^E , and an average velocity that should represent the magnitude in the flow direction. In the present work, all convection-diffusion equations are stabilised with the SUPG method, namely the conservation of mass, energy, momentum and chemical species as well as the level set transport.

2.5.2 Level set regularisation

Upon transport the distance function field, a crucial property of the level set may be partially or totally lost over the domain, which is:

$$\begin{cases} \|\nabla \alpha\| = 1 \\ \alpha(x, t) = 0 & \text{if } x \in \Gamma(t) \end{cases} \quad (2.65)$$

The closer this L^2 -norm to one, the more regular the level set. An irregular distance function induces cumulative numerical errors while transporting distance values far from the interface, resulting in wrong distance information, and loss of properties. To show one the benefit of level set regularisation, [Basset \[2006\]](#) states after showing several tests of distance function transport, that regularised distance functions transported with a standard Galerkin method (i.e. without any stabilisation) show better "quality" globally in the domain, compared to initially non-regularised ones. When the transport equation in [eq. \(2.59\)](#) is discretised in time then solved, a *regularisation* (also known as *reinitialisation*) is necessary to conserve as much as possible the property in [eq. \(2.65\)](#).

[Figure 2.4](#) shows the need of regularisation in two different simulations of the same phenomenon: rising air bubble inside water. The importance of this well studied case [[Sussman et al. 1994](#); [Hysing et al. 2009](#)] is that the interface between two fluids is highly deformable as the bubble rises because of buoyancy, and therefore the task of tracking the dynamic interface while maintaining an accurate distance function is a considerable numerical task. In the first simulation, the distance contours are squeezed against the zero-distance contour marked by the thick black line. A closer look to the interface reveals undesired distortions, with a "wavy" shape at some points. This effect is evidently an artefact of a level set transport lacking subsequent reinitialisation, inasmuch as the surface tension tends to minimise the total surface area and make it as smooth as possible. Nevertheless, the second simulation unveils much better results, especially how the interface shows no sign of destabilisation. We also note the regular spacing between contours, which is a consequence of conserving the property defined in [eq. \(2.65\)](#). This improvement is attributed to the regularization done at each time step after the transport. In the forthcoming sections, we present three regularisation methods, then show their strong and weak points.

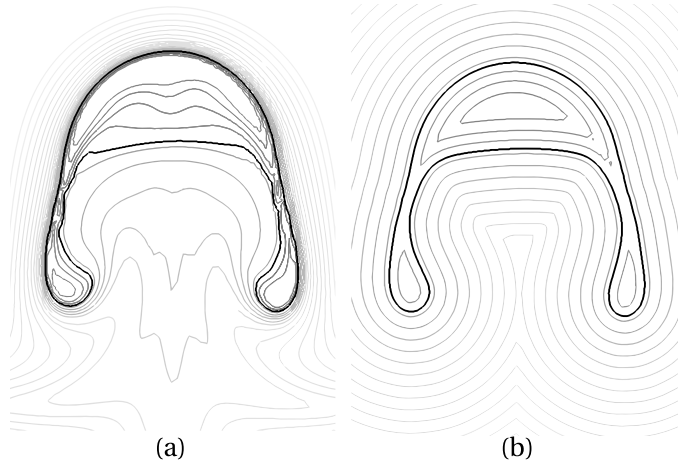


Fig. 2.4 – Schematic of the influence of level set regularisation on the distance function at the same time frame: a) without any regularisation step, the isovalue contours are distorted in the wake of the rising air bubble while being squeezed ahead of it, b) in contrast to regularising the distance function, where the contours maintain their spacing and geometric properties with respect to the tracked interface.

Classic Hamilton-Jacobi reinitialisation

In order to repair a distance function impaired by convective transport, [Sussman et al. \[1994\]](#) proposed solving a classic *Hamilton-Jacobi* equation, given in its most general form:

$$\frac{\partial \alpha}{\partial t} + \mathbb{H}(\alpha, x, t) = 0 \quad x \in \Omega, t > 0 \quad (2.66)$$

where $\alpha(x, t = 0) = \alpha_0$ is the initial value of the distance function. The term \mathbb{H} is known as the *Hamiltonian*. When the sign of the level set and its metric property ($\|\nabla \alpha\| = 1$) are considered, [eq. \(2.66\)](#) reduces to:

$$\frac{\partial \alpha}{\partial t} + S(\alpha) (\|\nabla \alpha\| - 1) = 0 \quad (2.67)$$

where $S(\alpha)$ is a step function giving the sign of the level set as follows:

$$S(\alpha) = \frac{\alpha}{|\alpha|} = \begin{cases} -1 & \text{if } \alpha < 0 \\ 0 & \text{if } \alpha = 0 \\ +1 & \text{if } \alpha > 0 \end{cases} \quad (2.68)$$

The sign function defined in [eq. \(2.68\)](#) is often smoothed to avoid numerical problems, as proposed for instance by [Sussman et al. \[1994\]](#):

$$S(\alpha) = S_\varepsilon(\alpha) = \frac{\alpha}{\sqrt{\alpha^2 + \varepsilon^2}} \quad (2.69)$$

where ε is a smoothing parameter that depends on the mesh size around the interface. However, one should be aware that within the smoothing thickness, the regularised function may suffer from local oscillations because of the reciprocal reinitialisation taking place at each side of the level set. [Peng et al. \[1999\]](#) states that this problem is more likely to happen if the initial level

set shows very weak or very steep gradients, and therefore is not regular enough. The authors eventually propose a new sign function which would reinitialise the distance function, as close as possible to the interface without modifying the latter, as follows:

$$S(\alpha) = S_\varepsilon(\alpha) = \frac{\alpha}{\sqrt{\alpha^2 + \|\nabla\alpha\|^2\varepsilon^2}} \quad (2.70)$$

Convective reinitialization

A recent work by Ville et al. [2011] introduced another concept for reinitialisation called the *convective reinitialisation*. The idea lies in combining both level set advection and regularisation in a single equation, saving resolution time. The key components of their method starts by defining a pseudo time step, $\Delta\tau$, that is linked to the main time variable through a numerical parameter λ_τ , as follows:

$$\lambda_\tau = \frac{\partial\tau}{\partial t} \quad (2.71)$$

The order of magnitude of λ_τ , which can be seen as a relaxation parameter [see Vigneaux 2007, p. 89], is close to the ratio $h/\Delta t$. Then, the classic Hamilton-Jacobi eq. (2.66) is combined into the convection step by writing:

$$\frac{\partial\alpha}{\partial t} + (\mathbf{v} + \lambda_\tau \mathbf{U}) \cdot \nabla\alpha = \lambda_\tau S(\alpha) \quad (2.72)$$

where \mathbf{U} is a velocity vector in the normal direction to the interface, defined by $\mathbf{U} = S(\alpha)\mathbf{n}$, the normal vector \mathbf{n} being previously defined in eq. (2.52). The obvious shortcoming of convective reinitialisation is that it depends on a numerical parameter λ_τ . Another limitation of the method is the use of a sinusoidal filter to modify the distance function by truncating its values beyond a thickness threshold, which is also another parameter to calibrate the resolution. The drawback of truncating the level set is the loss of information far from the interface and the inability to fully reconstruct the distance function. If we denote this threshold by E and the modified level set by $\tilde{\alpha}$ inside the thickness, then eq. (2.72) is recast as:

$$\frac{\partial\alpha}{\partial t} + (\mathbf{v} + \lambda_\tau \mathbf{U}) \cdot \nabla\alpha = \lambda_\tau S(\alpha) \sqrt{1 - \left(\frac{\pi}{2E}\tilde{\alpha}\right)^2} \quad (2.73)$$

Equation (2.73) describes the transport and partial reconstruction of the distance function α , knowing its value $\tilde{\alpha}$ inside the thickness E .

Geometric reinitialization

This category of methods go from the level set's basic geometric principle to construct a distance function, instead of solving a partial differential system of equations as in the classic Hamilton-Jacobi reinitialisation. A widely known instance of this category is the *fast marching method* developed by Sethian [1996] and influenced by the Dijkstra [1959]'s method to compute the shortest path in a network of nodes. The method aims to solve the eikonal equation in eq. (2.65) to propagate the distance function in a single direction by *upwinding*, i.e. going from low to high values of the distance function, while preserving a unitary distance gradient. *Direct reinitialisation* is another interesting method in the geometric reinitialise category. How-

ever, it has not gained noticeable attention in the literature given the terrible cost in terms of computation time and efficiency if not optimised. The main idea is very simple: reconstruct the distance function over Ω or a subset of Ω , by computing the minimum distance between each mesh node and the interface. It means that, for any point $x \in \Omega$, the following constraint should be satisfied [Osher and Fedkiw \[2003\]](#):

$$d_\Gamma(x) = \min \|x - x_\Gamma\| \quad \forall x_\Gamma \in \partial\Omega = \Gamma, \quad (2.74)$$

A efficient and optimised implementation of this method is done by [Shakoor et al. \[2015\]](#) making use of k - d trees to limit the search operations of elements and the subsequent distance evaluations in each of these elements. Moreover, the authors give a comparison of the previously stated methods on 2D and 3D cases, showing the great performance of direct reinitialisation when used with k - d trees algorithm, hence we use it in the present work.

2.6 Mesh adaptation

2.6.1 Metrics and anisotropy

The key to reduce spatial discretisation errors and obtain better results is a fine mesh. The optimal mesh resolution depends on the equations being discretised and solved on the FE grid, which consists of an array of structured triangles ([fig. 2.5a](#)), in the most basic situation. However, the potential of the Finite Element Method over other methods like the Finite Volume Method (FVM) is the use of unstructured grids. The easiest meshing solution one can choose is to create unstructured homogeneous and isotropic grid ([fig. 2.5b](#)), while respecting some constraints regarding the time step (temporal discretisation) stemming from physical or numerical conditions, e.g. diffusion shock constraint in diffusional transient equations or Courant–Friedrichs–Lewy (CFL) condition in transient advective equations. In such a case, errors due to interpolation are minimised, which guarantees good results but with expensive time cost.

Heterogeneous meshes ([fig. 2.5c](#)) that consist of fine isotropic elements in areas of interest along with coarser isotropic elements in other areas, may reduce the needed time to solve each conservation equation. Although this is an interesting alternative, it is less powerful than anisotropic meshing. In the latter ([fig. 2.5d](#)), elements adapt to a physical quantity, such as enthalpy or velocity, reducing the elemental length in the direction where the gradient is higher, while stretching the element in the orthogonal direction. This allows more accurate resolution with less elements than needed by isotropic meshing. Moreover, this type of meshing is well adapted to the context of this thesis as it allows getting a fine mesh in the normal direction to the interface, that is in its transport direction, while reducing the number of elements in other directions. Regions undergoing solidification are also important to remesh since microsegregation starts in the mushy zone, i.e. between the liquidus and solidus temperatures given by a local average composition, where fluid flow may transport species, leading eventually to macrosegregation.

Since mesh adaptation involves advanced mathematical notions, readers interested in the basics are referred to the following references: [[Coupez 1991](#); [Coupez 2000](#); [Gruau and Coupez 2005](#); [Jannoun 2014](#)].

In this study, we show and compare different remeshing methods relevant to macrosegrega-

tion prediction, and based on previous work done at CEMEF. These techniques rely on metric tensors, and some of them belong to *a posteriori* error estimators category. A metric or a metric tensor \mathcal{M} , also known as *Riemannian* metric, is a positive symmetric definite matrix that relates to an element's size in \mathbb{R}^3 via:

$$\mathcal{M} = \begin{pmatrix} M_{11} & M_{12} & M_{13} \\ M_{12} & M_{22} & M_{23} \\ M_{13} & M_{23} & M_{33} \end{pmatrix} = \mathcal{R} \begin{pmatrix} 1/h_x^2 & 0 & 0 \\ 0 & 1/h_y^2 & 0 \\ 0 & 0 & 1/h_z^2 \end{pmatrix} \mathcal{R}^T \quad (2.75)$$

where \mathcal{R} is a rotation matrix and h_x , h_y and h_z are the respective dilatation scalars defined by the metric in the (x, y, z) space, describing a three-dimensional anisotropy. The metric information is then passed to a mesh generation tool, called *MTC*, which is based on an iterative procedure of local topology optimisations. We focus hereafter on two adaptive remeshing techniques, *Remesh2* and *Remesh4*, then discuss the functional details and show some examples. Please note that these names represent only a short notation to simplify mentioning the corresponding methods easily in the text.

2.6.2 Remesh2: domains boundary remeshing

Remesh2 is an explicit h -adaptation method to compute an anisotropic metric around the zero surface of a distance function, which defines the boundary between two domains. The idea is, as mentioned previously, to reduce the elements cost in the tangential directions to level set by stretching the elements, leaving small element lengths in the normal direction, where the level

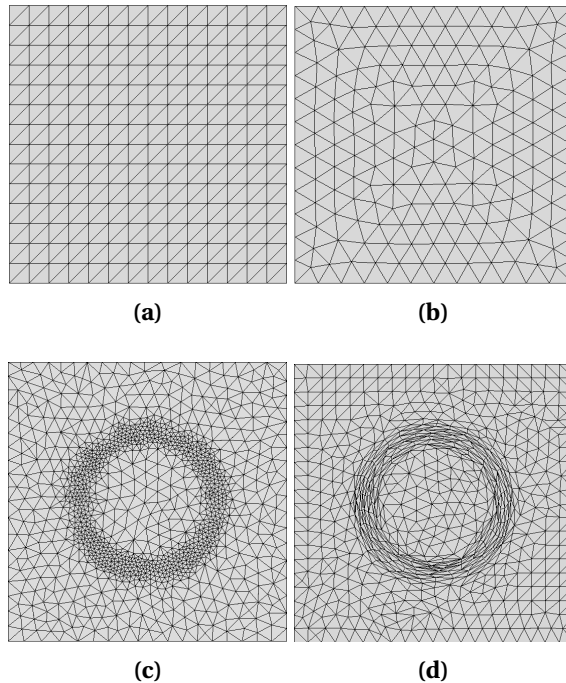


Fig. 2.5 – Alternatives for initial finite element grid generation: (a) structured homogeneous, (b) unstructured homogeneous isotropic, (c) unstructured heterogeneous isotropic and (d) unstructured heterogeneous anisotropic meshes.

set gradient is the greatest. This method is not based on error estimators, but rather on user input to choose the mesh size in normal and tangential directions to the interface, as well as the mesh size in each of the domains separated by the level set, as shown in [fig. 2.6](#). For more details about this method, the reader is referred to [Bernacki et al. 2007; Resk et al. 2009; Hitti 2011]. This remeshing technique relies on the parameter input defined in [table 2.1](#).

Table 2.1 – Summary of the mesh parameters in order to perform adaptive remeshing based on *Remesh2* technique.

Mesh parameter	Significance
ε	level set mixing thickness
h_n	mesh size in the normal direction to the level set
h_τ	mesh size in the tangential directions of the level set
h_M	mesh size in the metal
h_A	mesh size in the air
Number of nodes	resulting number of nodes after remeshing is done
Number of elements	resulting number of elements after remeshing is done

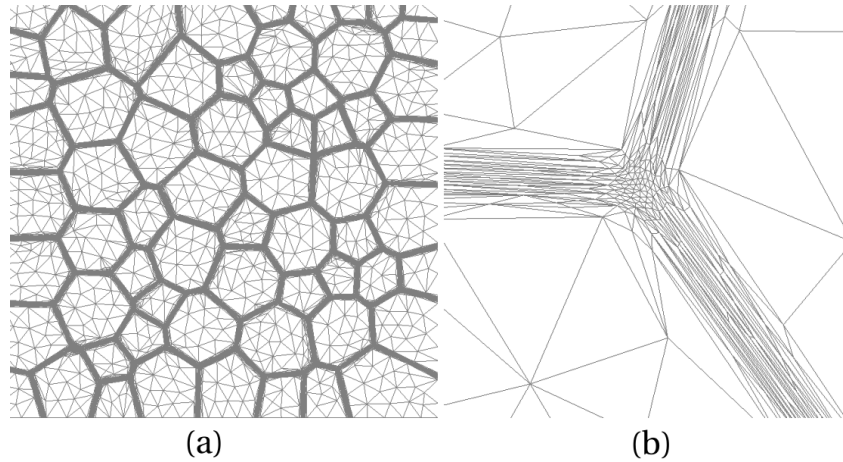


Fig. 2.6 – (a) Multiple level sets used to delimit the grains of an equiaxial polycrystal with (b) a zoom on the anisotropic mesh elements describing the grain boundaries [Hitti 2011].

2.6.3 Remesh4: Multi-criteria remeshing

It is essentially an *a posteriori* error estimator. The method consists of estimating the interpolation error for one or more nodal fields, then using a statistical concept, the so-called *length distribution tensor*, a stretching factor can be determined by solving several constraints like locally minimizing the induced error, limit the number of created nodes to a specific threshold, etc. Finally, the stretching factor is directly used to correct the edge lengths, where the latter varies in such a way to minimize the locally induced error down to a specified error limit, ε_{er} . For detailed technical information, the reader is referred to these references: [Coupez 2011; Coupez et al. 2013; El Jannoun 2014].

This method is readily compatible with multiple scalar or vector input, which results in a final metric accounting for the steepness of each quantity gradient. In solidification, such a technique is appealing since we often need to maintain a sufficiently small mesh size in areas of interest, e.g. narrow mushy zone formation caused by high thermal gradients, areas with composition variations or areas where fluid convection is a consequence to combined effects of energy-solute variations. [Figure 2.7](#) shows an example of mechanically driven flow, along with the accurate capturing of the interface using highly stretched anisotropic elements, at the edges and in the centre.

This remeshing technique relies on the parameter input defined in [table 2.2](#). Among the parameters, h_{\min} and $\varepsilon_{er.}$ are the most important. The first one sets the minimum limit for the mesh algorithm to take while topologically optimising the grid. The second parameter controls the error, and hence globally the elements shape may vary from highly anisotropic shapes (low values of $\varepsilon_{er.}$), to isotropic (high values of $\varepsilon_{er.}$). We prefer to limit this parameter by using a reasonable value, between 10 and 500, depending on the case and the final results.

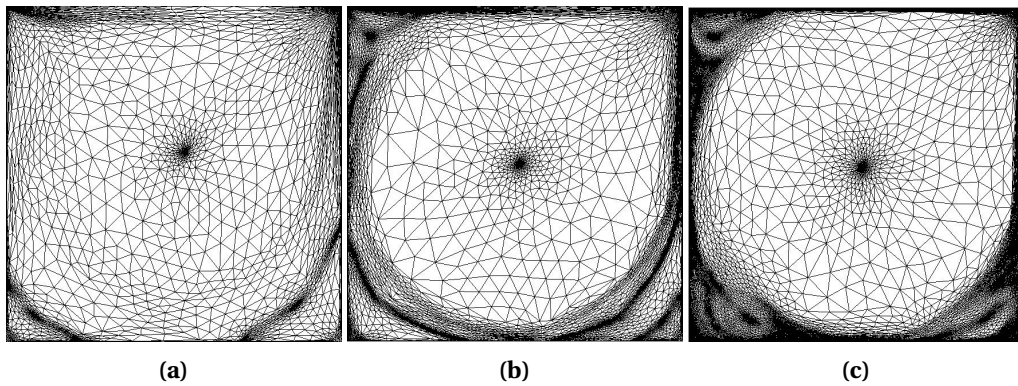


Fig. 2.7 – Edge-based anisotropic metric generation applied to a driven flow inside cavity with a Reynolds number of (a) 1000 (b) 10 000 and (c) 100 000 [[Coupez et al. 2013](#)].

Table 2.2 – Summary of the mesh parameters in order to perform adaptive remeshing based on *Remesh4* technique.

Mesh parameter	Significance
ε	level set mixing thickness
h_{\min}	minimum mesh size
$\varepsilon_{er.}$	minimum error limit
Remeshing criteria	physical quantities of interest
Number of nodes	resulting number of nodes after remeshing is done
Number of elements	imposed number of elements needed for the remesh optimisation

Résumé chapitre 2

Le second chapitre de ce manuscrit présente une revue de la littérature, concernant les aspects de modélisation utilisés dans ce travail. Au début, on présente quelques approches connues pour modéliser l'effet de la microségrégation sur la variation des fractions de phases ainsi que leurs compositions. On s'intéresse après à l'approche de prise de moyenne volumique. Celle-ci nous permet de faire des hypothèses sur des petits volumes, qualifiés de *volumes élémentaires représentatifs*, permettant d'établir des relations pour l'ensemble des propriétés des phases. En utilisant ces relations, on présente la première brique numérique de ce travail : les équations de conservation de masse, énergie, solutés et quantité de mouvement dans un contexte de solidification à volume constant, donc sans retrait. Le modèle est complété par une hypothèse de solide fixe et rigide qui permet de négliger tout mouvement des phases solides, et donc la thermomécanique de ces phases n'est pas traitée. Dans la suite du chapitre, on présente les descriptions eulérienne et lagrangienne caractérisant l'écoulement de la phase liquide. Cela s'avère nécessaire dans un contexte de solidification avec changement de volume, où l'interface entre le métal et le milieu ambiant change au cours de la transformation. Par conséquent, le choix de la méthode level set pour le suivi de cette interface est expliqué. On présente aussi des méthodes numériques pour prendre en compte le mouvement de l'interface suivie par la méthode level set, dans le contexte eulérien. Finalement, deux méthodes de remaillage adaptatif, utilisé pour l'ensemble des calculs faits pendant la thèse, sont présentés et expliqués, tout en montrant leurs avantages et leurs inconvénients.

Chapter 3

Energy balance with thermodynamic tabulations

Contents

3.1	State of the art	40
3.2	Thermodynamic considerations	40
3.2.1	Volume averaging	40
3.2.2	The temperature-enthalpy relationship	41
3.2.3	Tabulation of properties	41
3.3	Numerical method	44
3.3.1	Enthalpy-based approach	46
3.3.2	Temperature-based approach	46
3.3.3	Convergence	47
3.4	Validation	48
3.5	Application: multicomponent alloy solidification	48
3.5.1	Tabulations	52
3.5.2	Discussion	54
3.6	Limitations	59

3.1 State of the art

To model macrosegregation during solidification, a minimum of four conservation equations are necessary: conservation of mass, momentum, chemical species and energy. The phase change literature contains a wealth of numerical methods to solve energy conservation in solidifying alloys. A comprehensive overview of these methods is given by [Swaminathan and Voller \[1993\]](#).

The corresponding equation associates the total average enthalpy to the temperature via intrinsic alloy properties, such as the heat capacity of the phases and the latent heat associated with the phase transformations. However, in the course of solidification and while macrosegregation is taking place, these properties change because the average composition may vary significantly: the transformation paths are thus modified, as well as the phases' composition and heat capacity. Similarly, the latent heat of phase transformations is not a mere constant that could be distributed as a function of the phase fractions assuming only temperature-dependent phases' properties, as often found in the literature [\[Bell et al. 2009\]](#). It is thus impossible to establish a priori the dependence of the enthalpy with respect to temperature when macrosegregation alters the average composition, even in the case of full thermodynamic equilibrium between phases.

In this chapter, we discuss a suitable numerical scheme based on an enthalpy method, already used in the literature to alleviate this macrosegregation-related problem [\[Swaminathan and Voller 1993; Carozzani et al. 2013\]](#). Later on, we introduce a modified formulation, using the effective heat capacity method that increases the original scheme's efficiency.

This chapter introduces an enthalpy method that makes use of a temperature-based solver. It uses tabulated thermodynamic quantities (solidification paths, phases' enthalpy and composition) in a range of average compositions and temperatures as found in the literature [\[Doré et al. 2000; Thuinet and Combeau 2004; Du et al. 2007\]](#), with the aim of evaluating the total average enthalpy as well as the effective heat capacity. The novelty of the modified method resides in the use of thermodynamic tabulations without losing the advantages of the previous method, thus yielding faster computation times while maintaining a good accuracy.

3.2 Thermodynamic considerations

3.2.1 Volume averaging

The volume averaging technique, presented in [section 2.1.1](#), is considered when solving the energy equation in the presence of macrosegregation. The reason is that phase properties and distributions varying with the average composition, have a great impact on the average thermal properties, and hence on the overall heat transfer in the system. We recall the basic expression of the volume averaged value of a field ψ , by writing:

$$\langle \psi \rangle = \sum_{\phi} g^{\phi} \langle \psi \rangle^{\phi} \quad (3.1)$$

where g^{ϕ} denotes the volume fraction of phase ϕ in the RVE, and $\langle \psi \rangle^{\phi}$ is the intrinsic average of the quantity ψ in the RVE. It should be emphasized that the averaging technique applies to virtually all thermodynamic volumetric variables (enthalpy, density . . .). Among these variables,

the temperature is also considered to be uniform in the RVE.

Applying the volume averaging technique to the energy conservation equation along with interfacial balances between the phases, results in the following averaged equation [Rappaz et al. 2003]:

$$\frac{\partial \langle \rho h \rangle}{\partial t} + \nabla \cdot \langle \rho h v \rangle = \nabla \cdot (\langle \kappa \rangle \nabla T) + \langle \dot{Q}_V \rangle \quad (3.2)$$

where ρ stands for the density, h the mass enthalpy, v the velocity field, κ the thermal conductivity, T the temperature and \dot{Q}_V a possible volumetric heat source. Equation (3.2) is the standard averaged form of the energy conservation equation used in non-stationary phase change problems.

It is clear that the nature of the temperature-enthalpy relationship plays a central role when formulating the resolution strategy of this nonlinear equation. Generally, it is admitted that, depending on the resolution strategy, it is necessary to express enthalpy as a function of temperature or vice-versa, together with associated partial derivatives, $\frac{\partial \langle \rho h \rangle}{\partial T}$ or $\frac{\partial T}{\partial \langle \rho h \rangle}$.

It is noted that in the FEM context, the RVE is represented by a node in a finite element, so for instance the temperature in a RVE is denoted T_j henceforth, where j represents the index of the node localising the RVE.

3.2.2 The temperature-enthalpy relationship

In solidification problems, additional variables are involved in eq. (3.1) and eq. (3.2), like the transformation path that defines the history of the phase fractions, as well as the average chemical composition $\langle w_i \rangle$, i being the index of the chemical species (only the solutes are considered). The temperature-enthalpy relation averaged over the phases in a given RVE writes:

$$\langle \rho h \rangle = \sum_{\phi} g^{\phi}_{(T, \langle w_i \rangle \dots)} \langle \rho \rangle_{(T, \langle w_i \rangle^{\phi}, \dots)}^{\phi} \langle h \rangle_{(T, \langle w_i \rangle^{\phi}, \dots)}^{\phi} \quad (3.3)$$

Note that the volume average enthalpy is approximated by the product $\langle \rho h \rangle^{\phi} = \langle h \rangle^{\phi} \langle \rho \rangle^{\phi}$ in the current work. As stated in the introduction, it becomes clear from eq. (3.3) that phase properties, i.e. average phase density, $\langle \rho \rangle^{\phi}$ and enthalpy, $\langle h \rangle^{\phi}$, are temperature and composition dependent. This equation is the key to convert the average volume enthalpy to temperature (through a procedure named *H2T*) or vice-versa (*T2H*). The values of the different phase fractions g^{ϕ} (solidification path) and phase enthalpies $\langle \rho h \rangle^{\phi}$ are thus needed to close the relation.

3.2.3 Tabulation of properties

The complexity of performing a thermodynamic conversion is directly linked to the simplicity of determining the alloy properties, namely the phase fractions and both phase densities and enthalpies. In the case of binary alloys and with several assumptions with respect to the system (e.g., linear mono-variant lines in temperature-composition relationships of the phase diagram, constant heat capacity of phases and constant latent heat of transformations, equilibrium approximations between phases) analytical calculations are often used to determine the phase fractions and phase compositions. Nevertheless, analytical relations are more complex or even impossible to derive in the case of multicomponent alloys ($i > 1$), or even for binary alloys with multiple phase transformations (e.g. peritectic and eutectic reactions) with a nonlinear phase

diagram.

To overcome this problem, one can resort to thermodynamic databases and phase equilibrium calculations to tabulate the transformation paths and the phase densities and enthalpies for a given range of temperatures and average compositions. It is a handy solution for two main reasons: first, the conversion is merely a binary search in a table; secondly, it is a simple solution for coupling with macrosegregation. In this way, phase fractions g^ϕ are tabulated as functions of temperature and average composition, while for each phase ϕ the mass enthalpy, $\langle h \rangle^\phi$, and the density, $\langle \rho \rangle^\phi$, are tabulated as functions of temperature and phase intrinsic average compositions $\langle w_i \rangle^\phi$, as well as other possible parameters.

[Table 3.1](#) summarizes the steps in order to perform a temperature-to-enthalpy ($T2H$) conversion using the predefined tabulation approach. In step 1, the transformation path is acquired for each average composition, $\langle w_i \rangle$, and temperature, T , to determine the list of phases, their volume fractions g^ϕ and their intrinsic compositions $\langle w_i \rangle^\phi$, assuming full equilibrium. In step 2, the phase enthalpy $\langle h \rangle^\phi$ and density $\langle \rho \rangle^\phi$ are determined by searching for the temperature and the already known phase composition $\langle w_i \rangle^\phi$. In step 3, the average volume enthalpy is computed from the volume fraction, density and mass enthalpy of phases using [eq. \(3.3\)](#). A flowchart explaining $T2H$ conversion steps is given in [fig. 3.1](#).

The methodology to build the tabulations is straightforward. It is based on two main scans. On the one hand, intervals for the variation of the average composition $\langle w_i \rangle$ are chosen from the known alloy composition. These variations have to cover the extreme values adopted during the simulation, which are not known a priori. An interval is also selected for the variation of temperature. The latter is easier to determine as it usually starts from the initial melt temperature and goes down to the room temperature in a standard casting simulation. For each mapping of composition and temperature, a thermodynamic equilibrium state is computed. The outputs are the number of phases encountered, together with their fraction and intrinsic compositions. On the other hand, for each phase, a scan of the intrinsic composition and temperature is made to compute the intrinsic properties. The same temperature interval and step as defined earlier are used.

Regarding the enthalpy-to-temperature conversion ($H2T$) shown in the flowchart in [fig. 3.2](#), a backward iterative $T2H$ search is performed. For a known composition $\langle w_i \rangle$, denoting (τ) the iteration index to convert the enthalpy H_{input} , we start with an initial guess for temperature $T^{(\tau=0)}$ then convert it to an enthalpy $H^{(\tau=0)}$ with the $T2H$ conversion. Using an appropriate nonlinear algorithm (Brent is the most versatile in our case), we aim at minimizing the following scalar residual: $R_H = |H_{\text{input}} - H^{(\tau)}|$. Once the algorithm has converged, the temperature $T^{(\tau)}$ is the result of the $H2T$ conversion. It is inferred that the first conversion ($T2H$) is a direct one whereas the latter ($H2T$) is indirect and requires a series of iterative steps; each step being a single $T2H$ resolution. In other words, a $H2T$ conversion is a backward search for a temperature, hence it is slower. It is important to realise that this conversion's speed lag is exacerbated when tabulations increase in size (e.g. large number of temperature and composition steps) and complexity (e.g., multicomponent industrial alloys used in casting), since the search gets more complicated with the increasing number of input columns (one column for each alloying element).

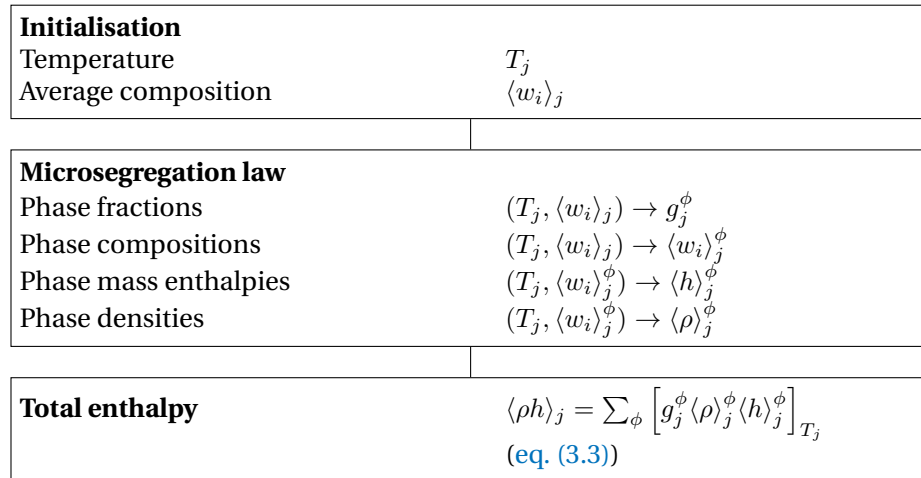


Fig. 3.1 – Algorithm for a single temperature to enthalpy (T2H) conversion at node j .

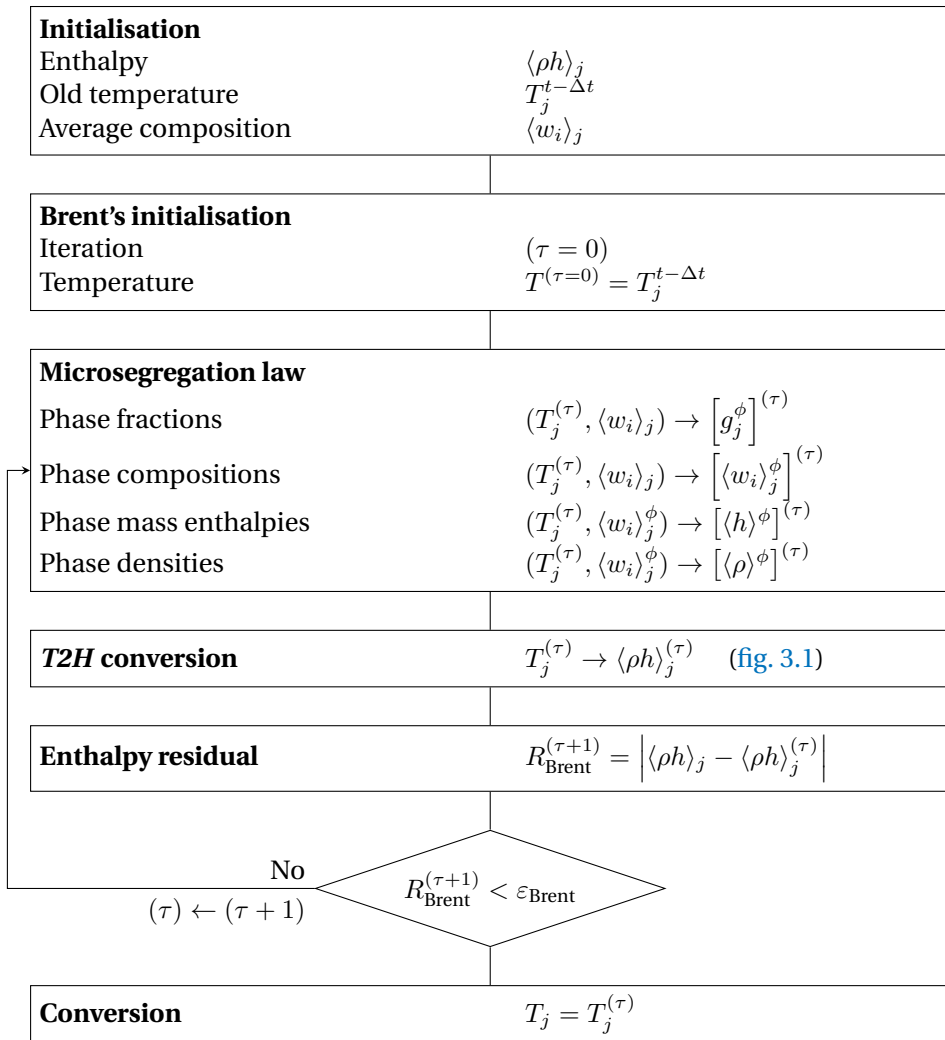


Fig. 3.2 – Algorithm for a single enthalpy to temperature (H2T) conversion at node j .

Table 3.1 – Tabulation processing for a $T2H$ procedure

Step Number	1	2	3
Inputs	$T, \langle w_i \rangle$	$T, \langle w_i \rangle^\phi$	$g^\phi, \langle \rho \rangle^\phi \langle h \rangle^\phi$
Outputs	$g^\phi, \langle w_i \rangle^\phi$	$\langle \rho \rangle^\phi, \langle h \rangle^\phi$	$\langle \rho h \rangle$ (eq. (3.3))

3.3 Numerical method

The finite element method is used to solve the energy conservation as expressed by eq. (3.2). A test function \mathcal{W} belonging to the Hilbertian Sobolev space $\mathcal{H}^1(\Omega_E)$ of continuous integrable test functions is used to formulate the integral variational form of eq. (3.2) [Süli 2000]. A Fourier boundary condition is considered on the domain boundary $\partial\Omega_E$. The domain Ω is discretised using first-order linear simplexes, Ω_E , defined by their number of local nodes, NbLoc: triangles in 2D with NbLoc=3 and tetrahedra in 3D with NbLoc=4. The outcome is a residual that we aim to minimize so that the conservation principle is satisfied.

Therefore, the weak form writes:

$$\forall \mathcal{W} \in M = \{u \in \mathcal{H}^1(\Omega_E)\} \\ \int_{\Omega_E} \mathcal{W} \frac{\partial H}{\partial t} dV + \int_{\Omega_E} \mathcal{W} \langle \mathbf{v}^l \rangle \cdot \nabla \langle \rho h \rangle^l dV - \int_{\Omega_E} \mathcal{W} \nabla \cdot (\langle \kappa \rangle \nabla T) dV - \int_{\Omega_E} \mathcal{W} \langle \dot{Q}_V \rangle dV = 0 \quad (3.4)$$

where $H = \rho h$ is a simplified notation denoting the average volumetric enthalpy, used to derive the weak formulation. Furthermore, we assume a static solid phase and an incompressible liquid phase, which allows recasting the second term of eq. (3.2) into $\langle \mathbf{v}^l \rangle \cdot \nabla \langle \rho h \rangle^l$. $\langle \rho h \rangle^l = \langle \rho \rangle^l \langle h \rangle^l$ is not main variable of the energy conservation equation's weak form, eq. (3.4). Therefore we express it as a function of temperature, which is related to the main variable via the enthalpy-temperature relation:

$$\nabla \langle \rho h \rangle^l = \nabla (\langle \rho \rangle^l \langle h \rangle^l) = \langle \rho \rangle^l c_p^l \nabla T \quad (3.5)$$

where c_p^l is the mass heat capacity of the liquid phase. Ideally, this value should be taken directly from the thermodynamic database if it is available. Otherwise, it can be derived by differentiation of the tabulated liquid mass enthalpy with respect to temperature. In this work, c_p^l is considered constant, equal to the alloy's initial mass heat capacity. The steps for discretising in time and space eq. (3.4) are well detailed in some text books like Rappaz et al. [2003]. As for enthalpy and temperature, they are spatially discretised in each simplex using interpolations functions \mathcal{P} , thus defining the nodal values H_j and T_j , respectively:

$$H = \sum_{j=1}^{\text{NbLoc}} \mathcal{P}_j H_j \quad (3.6)$$

$$T = \sum_{j=1}^{\text{NbLoc}} \mathcal{P}_j T_j \quad (3.7)$$

The Galerkin formulation gives the expression for the residual contribution at a mesh node i

(here i is not the usual solute index) for time step t in a local element Ω_E :

$$(R_i^E)^t = \mathcal{M}_{ij}^E (H_j^t - H_j^{t-\Delta t}) + \mathcal{A}_{ij}^E T_j^t + (\mathcal{K}1_{ij}^E + \mathcal{K}2_{ij}^E) T_j^t - \mathcal{F}_i^E - \mathcal{Q}_i^E = 0 \quad (3.8)$$

$i, j : 1 \rightarrow \text{NbLoc}$

where the volumetric contributions are detailed as follows:

$$\text{transient term: } \mathcal{M}_{ij}^E = \int_{\Omega_E} \frac{1}{\Delta t} \mathcal{P}_i \mathcal{P}_j dV \quad (3.9)$$

$$\text{advection term: } \mathcal{A}_{ij}^E = \int_{\Omega_E} \langle \rho \rangle^l c_p^l \mathcal{P}_i \langle \mathbf{v}^l \rangle \cdot \nabla \mathcal{P}_j dV \quad (3.10)$$

$$\text{diffusion term: } \mathcal{K}1_{ij}^E = \int_{\Omega_E} \langle \kappa \rangle \nabla \mathcal{P}_i \nabla \mathcal{P}_j dV \quad (3.11)$$

$$\text{source term: } \mathcal{Q}_i^E = \int_{\Omega_E} \mathcal{P}_i \langle \dot{Q}_V \rangle dV \quad (3.12)$$

while the surface boundary contributions are given by:

$$\text{boundary condition term 1: } \mathcal{K}2_{ij}^E = \int_{\partial\Omega_E} h_{\text{ext}} \mathcal{P}_i \mathcal{P}_j dS \quad (3.13)$$

$$\text{boundary condition term 2: } \mathcal{F}_i^E = \int_{\partial\Omega_E} h_{\text{ext}} T_{\text{ext}} \mathcal{P}_i dS \quad (3.14)$$

$$(3.15)$$

The surface integrals $\mathcal{K}2_{ij}^E$ and \mathcal{F}_i^E are related to a Fourier-type boundary condition, with h_{ext} as a coefficient of heat exchange and T_{ext} as the external temperature far from the boundary. The energy conservation principle is satisfied when the sum of the residual contributions coming from all the mesh elements is zero. In other words, the following global residual defined by the assembly of these contributions, should be minimized:

$$(R_i)^t = \mathcal{M}_{ij} (H_j^t - H_j^{t-\Delta t}) + \mathcal{A}_{ij} T_j^t + (\mathcal{K}1_{ij} + \mathcal{K}2_{ij}) T_j^t - \mathcal{F}_i - \mathcal{Q}_i = 0 \quad (3.16)$$

$i, j : 1 \rightarrow \text{NbGlob}$

where the global tensors \mathcal{M}_{ij} , \mathcal{A}_{ij} , $\mathcal{K}1_{ij}$, $\mathcal{K}2_{ij}$, \mathcal{F}_i and \mathcal{Q}_i contain respectively, after an assembly step, the contributions of the local matrices \mathcal{M}_{ij}^E , \mathcal{A}_{ij}^E , $\mathcal{K}1_{ij}^E$, $\mathcal{K}2_{ij}^E$, \mathcal{F}_i^E and \mathcal{Q}_i^E from each discretised element in the domain Ω . Accordingly, the indices i and j refer to global node numbers, where the total number of nodes is denoted by "NbGlob".

It is clear that the global residual inherits the dependence between volumetric enthalpy and temperature. This is shown in eq. (3.16) where the average volume enthalpy is a function of the temperature. It infers that this residual is a non-linear function; therefore minimizing it requires an iterative non-linear algorithm.

Our choice settles on the Newton-Raphson method, known for its quadratic convergence speed. A solidification problem can induce severe non-linearities from the release of the latent heat (which itself is temperature and composition dependent) and the variations of the average thermophysical properties of the alloy with respect to temperature, phase fraction and average composition. This algorithm could thus treat such variations. Considering the link between the properties and temperature, eq. (3.16) may be solved either for the average volumetric enthalpy

or for the temperature as the nodal unknown, hence both formulations are presented hereafter.

3.3.1 Enthalpy-based approach

The residual is re-written using a Taylor series expansion to the first order for a nonlinear iteration ($\nu - 1$) :

$$(R_i)^{(\nu)} = (R_i)^{(\nu-1)} + \left(\frac{\partial R}{\partial H} \right)_{ij}^{(\nu-1)} \Delta H_j^{(\nu-1)} + \mathcal{O}(H_j^2) \quad (3.17)$$

Neglecting the second order terms, the suggested correction at each iteration in view of cancelling the residual and giving the new value $H_j^{(\nu-1)}$, is given by the linear system in eq. (3.18) relative to what we call the *Hsolver*:

$$\left(\frac{\partial R}{\partial H} \right)_{ij}^{(\nu-1)} (H_j^{(\nu)} - H_j^{(\nu-1)}) = -R_i^{(\nu-1)} \quad (3.18)$$

where $\overline{\frac{\partial R}{\partial H}}$ is a global tangent matrix yielding the variations of the residual vector $R^{(\nu-1)}$ with respect to the volumetric enthalpy vector in the previous iteration, $H^{(\nu-1)}$. The detailed flow chart for the *Hsolver* is given in fig. 3.3. If eq. (3.8) is considered, then the contribution of an element Ω_E writes:

$$\left(\frac{\partial R^E}{\partial H} \right)_{ij}^{(\nu-1)} = \underbrace{\mathcal{M}_{ij}^E + \mathcal{A}_{ij}^E \left(\frac{\partial T}{\partial H} \right)_j^{(\nu-1)}}_{\text{no sum on } j} + \underbrace{(\mathcal{K}1_{ij}^E + \mathcal{K}2_{ij}^E) \left(\frac{\partial T}{\partial H} \right)_j^{(\nu-1)}}_{\text{no sum on } j} \quad (3.19)$$

Equation (3.19) is the core of the enthalpy-based solver. The resolution of eq. (3.18) then yields a new estimate of the vector of nodal volumetric enthalpies $H^{(\nu)}$, which are the only unknowns to be solved for. Once determined at iteration ($\nu - 1$), convergence tests are performed.

3.3.2 Temperature-based approach

Similarly to the *Hsolver*, the local residual is recast for a nonlinear iteration ($\nu - 1$), leading this time to an iterative temperature correction:

$$\left(\frac{\partial R}{\partial T} \right)_{ij}^{(\nu-1)} (T_j^{(\nu)} - T_j^{(\nu-1)}) = -R_i^{(\nu-1)} \quad (3.20)$$

where $\overline{\frac{\partial R}{\partial T}}$ is a global tangent matrix yielding the variations of the residual with respect to the temperature vector, $T^{(\nu-1)}$, at the previous iteration. This solver will be referred to as the *Tsolver*. The corresponding flow chart is given in fig. 3.4. The contribution of an element Ω_E to this tangent matrix is evaluated as:

$$\left(\frac{\partial R^E}{\partial T} \right)_{ij}^{(\nu-1)} = \underbrace{\mathcal{M}_{ij}^E \left(\frac{\partial H}{\partial T} \right)_j^{(\nu-1)}}_{\text{no sum on } j} + \mathcal{A}_{ij}^E + (\mathcal{K}1_{ij}^E + \mathcal{K}2_{ij}^E) \quad (3.21)$$

In contrast to the previous solver, eq. (3.21) is the core of the temperature-based solver. The resolution of eq. (3.20) then yields a new estimate of the vector of nodal temperatures $T^{(\nu)}$, which are the only unknowns to be solved for. Once updated for iteration $(\nu - 1)$, convergence tests are performed.

3.3.3 Convergence

The previous two sections described the iterative resolution of the same discretised energy conservation by both *Tsolver* and *Hsolver*. However, in eqs. (3.19) and (3.21), an important term emerges from the tangent matrix evaluation describing the variations between enthalpy and temperature: $\frac{\partial T}{\partial H}$ and $\frac{\partial H}{\partial T}$.

This term invokes the previously mentioned temperature-enthalpy tabulations which depend on the alloy composition. Consequently, the vector of nodal values $\frac{\partial T}{\partial H}$ (respectively $\frac{\partial H}{\partial T}$) has a great influence on the convergence of the *Hsolver* (respectively the *Tsolver*). When eq. (3.18) or eq. (3.20) is solved at iteration (ν) , this term is written using a finite difference:

$$\text{Hsolver} \quad \left(\frac{\partial T}{\partial H} \right)_j^{(\nu)} = \frac{T_j^{(\nu)} - T_j^{(\nu-1)}}{H_j^{(\nu)} - H_j^{(\nu-1)}} \quad (3.22)$$

$$\text{Tsolver} \quad \left(\frac{\partial H}{\partial T} \right)_j^{(\nu)} = \frac{H_j^{(\nu)} - H_j^{(\nu-1)}}{T_j^{(\nu)} - T_j^{(\nu-1)}} \quad (3.23)$$

For the *Tsolver*, the enthalpy vector $H^{(\nu-1)}$ is needed to evaluate eq. (3.23). In contrast, the *Hsolver* requires the values of $T^{(\nu-1)}$ vector to evaluate the corresponding eq. (3.22). In both cases, the unknown is determined by the tabulations. The indices next to the mentioned unknowns indicate that this relation is used for each iteration (ν) at each mesh node j , hence affecting the global resolution time between the two solvers. The *Hsolver* needs a *H2T* to evaluate $\frac{\partial T}{\partial H}$, whereas the *Tsolver* needs a *T2H* to evaluate the vector $\frac{\partial H}{\partial T}$. It can be seen that *Tsolver* uses solely *T2H* procedure (flowchart in fig. 3.1) and the thermodynamic tabulations to determine the volumetric enthalpy, hence the term $\frac{\partial H}{\partial T}$. On the other hand, *Hsolver* repeats the same procedure a finite number of times in order to determine a temperature output through *H2T* (flowchart in fig. 3.2) and use it to compute $\frac{\partial T}{\partial H}$. This algorithmic difference leverages the *Tsolver* in terms of computation time providing the same numerical accuracy while conserving the total system energy.

Convergence tests are necessary at the end of each iteration of the energy solver to determine the convergence status of the algorithm. In the context of the *Tsolver* for instance, the residual is re-evaluated with the newly determined temperature vector $T^{(\nu)}$ and enthalpy vector $H^{(\nu)}$ so eq. (3.16) rewrites:

$$(R_i)^{(\nu)} = \mathcal{M}_{ij} \left(H_j^{(\nu)} - H_j^{t-\Delta t} \right) + \mathcal{A}_{ij} T_j^{(\nu)} + (\mathcal{K}1_{ij} + \mathcal{K}2_{ij}) T_j^{(\nu)} - \mathcal{F}_i - \mathcal{Q}_i \quad (3.24)$$

$i, j : 1 \rightarrow \text{NbGlob}$

The norm of the current residual, $\|R^{(\nu)}\|$, is compared to a fixed small value $\varepsilon_R \approx [10^{-5}; 10^{-4}]$. The resulting temperature variation, $|T_j^{(\nu-1)} - T_j^{(\nu-1)}|$, should also respond to similar criterion between two consecutive iterations. For that purpose, we compare it to another fixed

value $\varepsilon_T \approx [10^{-3}; 10^{-2}]$. Convergence is ultimately achieved when the following criteria are simultaneously met:

$$\begin{cases} \|R^{(\nu)}\| < \varepsilon_R \\ \text{Max}_{j:1 \rightarrow \text{NbGlob}} |T_j^{(\nu)} - T_j^{(\nu-1)}| < \varepsilon_T \end{cases} \quad (3.25)$$

A comparison of both solver formulations is done in the hereafter test cases section.

3.4 Validation

The two solvers are tested in a purely diffusive case for a one-dimensional solidification configuration. Predictions with a 1D front tracking model [Gandin 2000] are used as a benchmark. They provide solutions for the temperature and solid fraction during directional solidification of a 10 cm long ingot. The nominal composition, w_0 , is Al-7 wt.% Si. The melt having a uniform initial temperature, T_0 , is cooled with a heat exchange coefficient, h_{ext} , with a fixed external temperature, T_{ext} (assuming a Fourier boundary condition) from one side, the other side being adiabatic. The initial conditions, boundary conditions and alloy properties are all listed in [table 3.2](#).

For this simple test case, we use linear temperature dependence of the intrinsic phase enthalpies, that is $\langle \rho h \rangle^s = \rho c_p T$ and $\langle \rho h \rangle^l = \rho(c_p T + l)$, where ρ is the alloy density, c_p is the heat capacity per unit mass and l_f is the latent heat per unit mass. Values for ρ , c_p and l_f , as well as for the thermal conductivities, $\kappa = \langle \kappa \rangle^l = \langle \kappa \rangle^s$, are taken constant.

A Gulliver-Scheil approximation is used to compute a single relationship between temperature and volume solid fraction, g^s , in the absence of macrosegregation. This is done assuming a linear binary phase diagram and thus requires using the properties listed in [table 3.2](#), i.e. the segregation coefficient, k , the liquidus slope, m_L , the liquidus temperature, T_L , and the eutectic temperature, T_E . [Figure 3.5](#) shows the comparison with the *Hsolver* and *Tsolver*. The cooling curves and liquid fraction results are found superimposed to the front tracking solution, thus giving validation of the implementation as well as the iterative schemes presented above to solve the energy conservation

3.5 Application: multicomponent alloy solidification

We have shown that the efficiency of the temperature-based resolution resides in its performance when combined with thermodynamic tabulations. A multicomponent alloy consists of at least two solute elements, and therefore the tabulation size increases, hence the number of search operations also increases. To demonstrate the speed-up ability of the temperature-based approach while predicting all phase transformations during macrosegregation caused solely by mass diffusion, we consider the solidification of a ternary alloy, Fe-2 wt.% C-30 wt.% Cr. In order to neglect fluid flow resolution, we assume that solidification in this case is so slow that no forces are generated inside the melt, while additionally all buoyancy forces are also neglected, so no momentum conservation is solved in this section.

As illustrated in [fig. 3.6a](#), the alloy domain has a cylinder shape close to 3-inch height \times 1-inch diameter. Exact values are reported in [table 3.3](#) with all material properties, initial and boundary conditions, as well as numerical parameters for the simulations. The steel melt is initially at

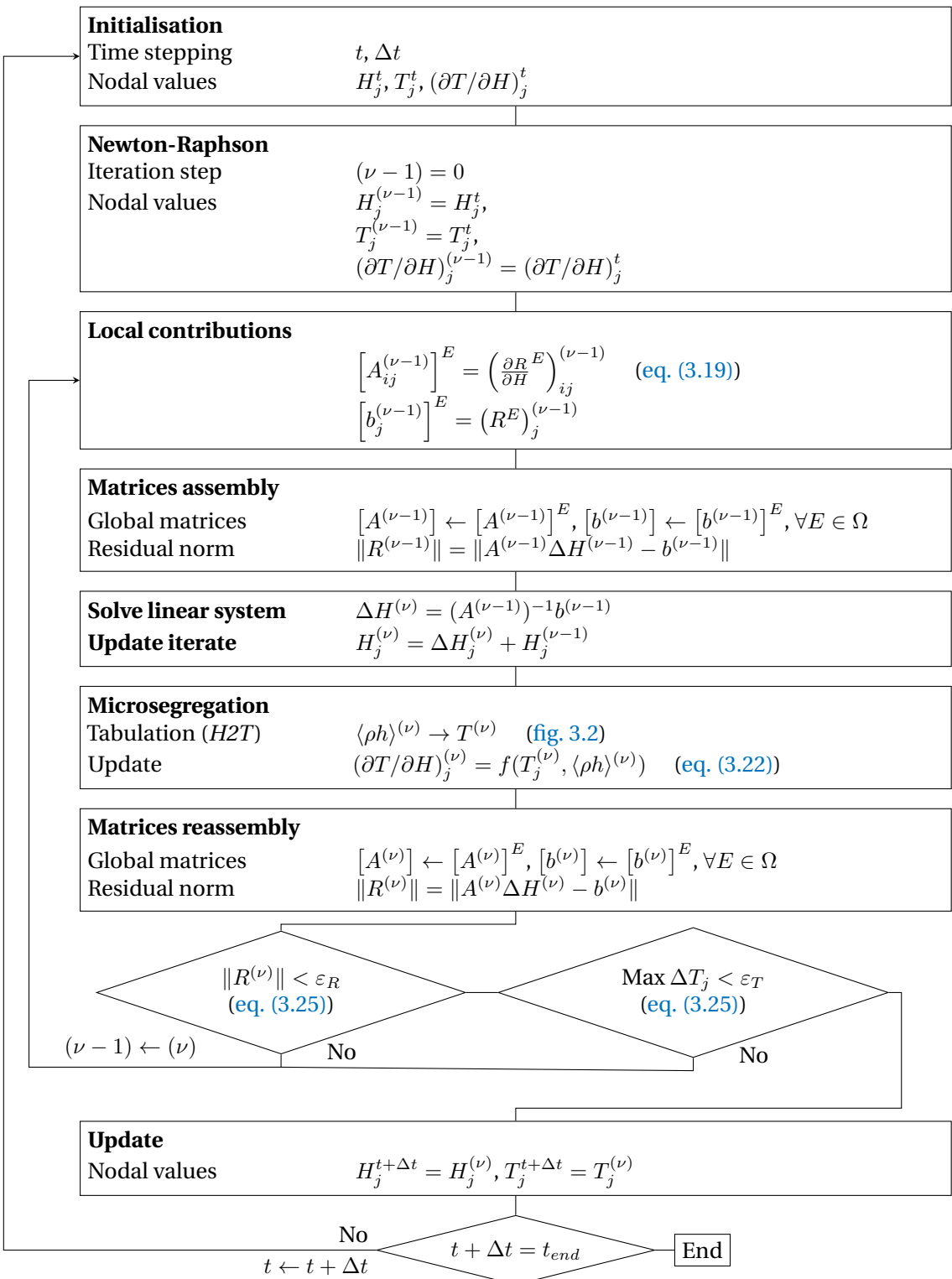


Fig. 3.3 – Resolution algorithm of the enthalpy-based solver.

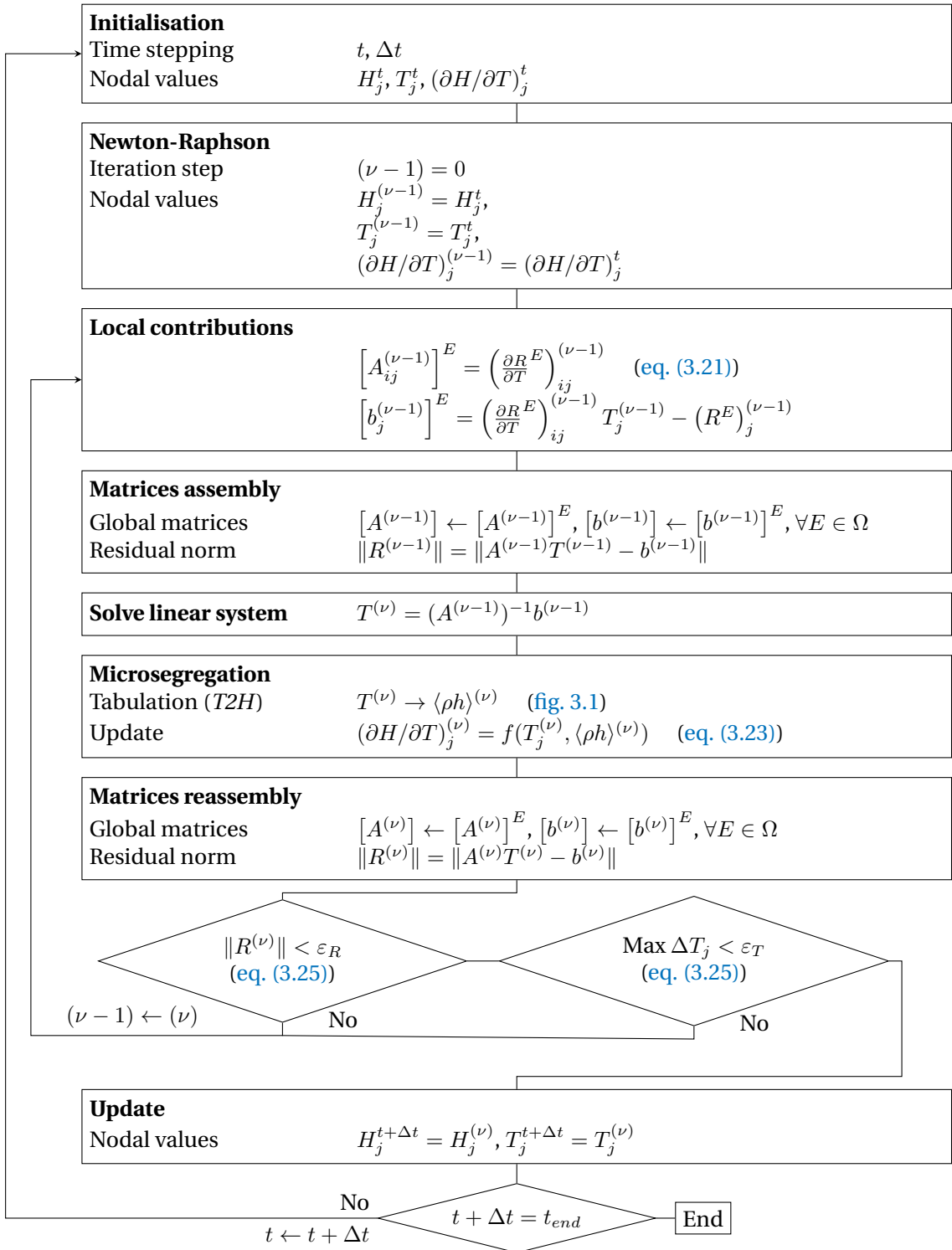


Fig. 3.4 – Resolution algorithm of the temperature-based solver.

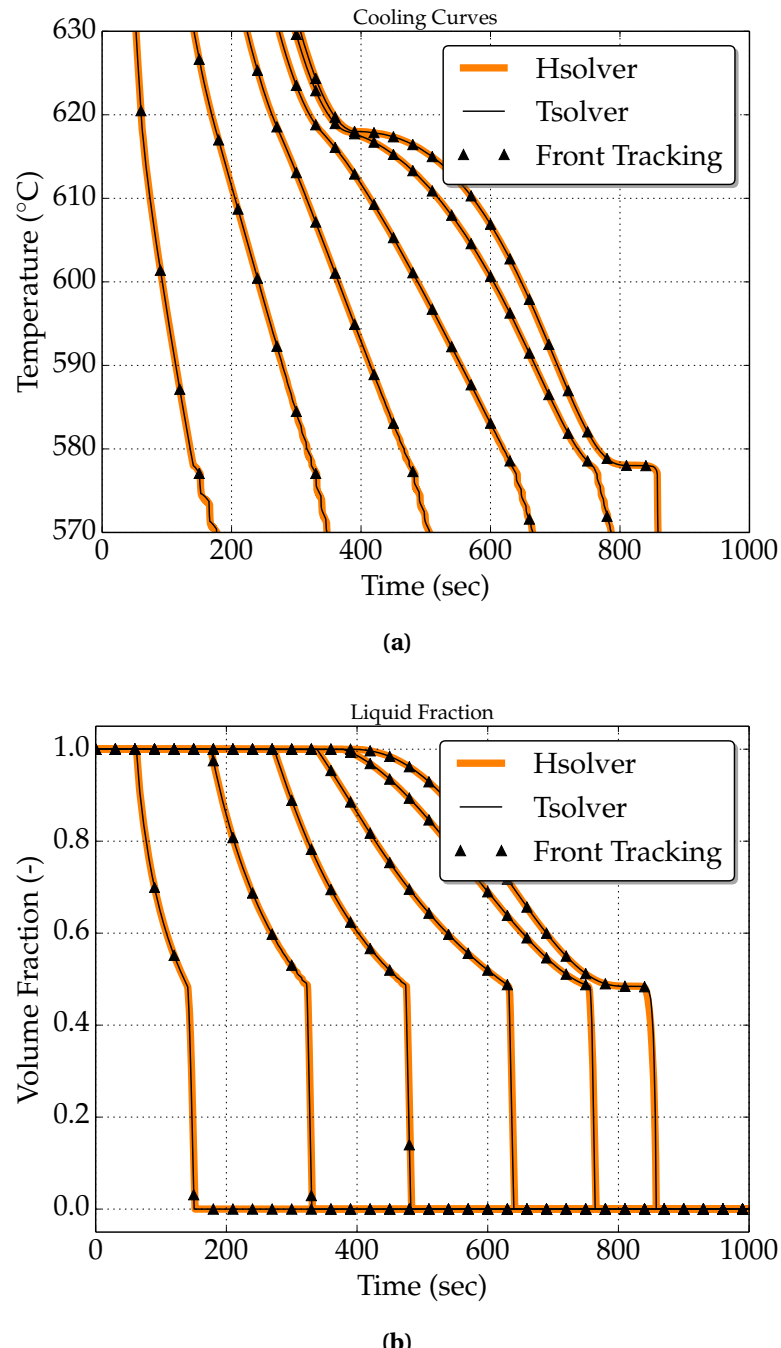


Fig. 3.5 – Computed unidirectional heat diffusion during solidification of an Al-7 wt.% Si alloy using (orange) the enthalpy method and (black) the temperature method, comparison being made for (a) cooling curves and (b) the liquid fraction history. Each curve corresponds to a position along the sample, from 0 cm (cooling side) to 10 cm (insulated side), with 2 cm spacing between the positions. The reference solution by the Front Tracking method (values in shown by the triangular markers).

Table 3.2 – Parameters for the pure diffusion test case with an Al-7 wt.% Si alloy presented in fig. 3.5

Parameter	Symbol	Value	Unit
Nominal composition	w_0	7	wt.%
Liquidus temperature	T_L	618	°C
Eutectic temperature	T_E	577	°C
Segregation coefficient	k	0.13	—
Liquidus slope	m_L	-6.5	K wt.% ⁻¹
Density	ρ	2600	kg m ⁻³
Liquid heat capacity	c_p	1000	J kg ⁻¹ K ⁻¹
Enthalpy of fusion	l_f	365 384	J kg ⁻¹
Thermal conductivity	κ	70	W m ⁻¹ K ⁻¹
Heat transfer coefficient	h_{ext}	500	W m ⁻² K ⁻¹
External temperature	T_{ext}	100	°C
Initial temperature	T_0	800	°C
Ingot length		0.1	m
FE mesh size		10 ⁻³	m
Time step	Δt	0.1	s
Convergence criterion (residual)	ε_R	10 ⁻⁶	—
Convergence criterion (temperature)	ε_T	10 ⁻²	K

1395 °C. The temperature of the bottom surface is imposed with a constant decreasing rate of 0.1 K s⁻¹ starting with 1380 °C as shown in fig. 3.6b, i.e. 40 °C higher than the nominal liquidus temperature as shown in fig. 3.7. The other surfaces are kept adiabatic.

The cylinder is held in a vertical position parallel to the gravity vector, the latter pointing downwards. fig. 3.7 also provides the transformation path of the alloy at nominal composition, i.e. assuming no macrosegregation and full thermodynamic equilibrium as computed with ThermoCalc and the TCFE6 database [TCFE6 2010; Andersson et al. 2002]. A total of 5 phases need to be handled, the characteristic temperature for their formation being reported in fig. 3.6b.

3.5.1 Tabulations

Full thermodynamic equilibrium is considered in the present case. Due to macrosegregation, the average composition is expected to continuously vary in time and space during casting. Transformation paths are thus determined a priori for a set of average compositions around the nominal value. Hence, carbon content varies in the interval [1.8,2.2]wt.% while chromium content variation is in the interval [27,33]wt.%. The offset of ± 10% with respect to the nominal composition value allows tabulating relatively small composition steps to ensure a fairly accurate mapping when compared to the corresponding ternary phase diagram.

The average composition step is 0.04 wt.% for carbon and 0.6 wt.% for chromium, thus representing 2% intervals with respect to the nominal composition. The temperature varies in the interval [100,1600]°C by 5 °C steps. For each triplet (carbon content in wt.% C, $w_{\text{C}0}$, chromium content in wt.% Cr, $w_{\text{Cr}0}$, temperature in K) corresponds a phase fraction g^ϕ and a pair of intrin-



Fig. 3.6 – Configurations for upward directional casting of (a) a 1-inch diameter × 3-inches height cylindrical domain for which (b) temperature-time conditions are imposed at its bottom surface.

sic phase composition ($\langle w_C \rangle^\phi, \langle w_{Cr} \rangle^\phi$), ϕ representing a phase. For the 5 phases listed in [fig. 3.7](#) (LIQ=liquid, BCC=ferrite, FCC=austenite, M_7C_3 =carbide, CEM=cementite), the enthalpy $\langle h \rangle^\phi$ and density $\langle \rho \rangle^\phi$, are tabulated as functions of temperature and phase intrinsic composition. If this latter input lies between two tabulated values, a linear interpolation is performed to determine the output, i.e. phase enthalpy and density. With the advancement of solidification, the liquid is enriched or depleted with solute by macrosegregation, which enables new solidification paths. It means that the primary solidifying phase is not necessarily the same as when considering the nominal composition. For this reason, the tabulation approach is interesting inasmuch as it provides phase transformation paths and values of phase properties that are compatible with the system's actual composition.

[Figure 3.8](#) summarises the tabulated thermodynamic data for two sets of average composition for the considered ternary system. Note that in the present test case, phase densities are taken constant ($\langle \rho \rangle^s = \langle \rho \rangle^l = 6725 \text{ kg m}^{-3}$). Therefore they are not tabulated. With this assumption, no shrinkage occurs upon phase change.

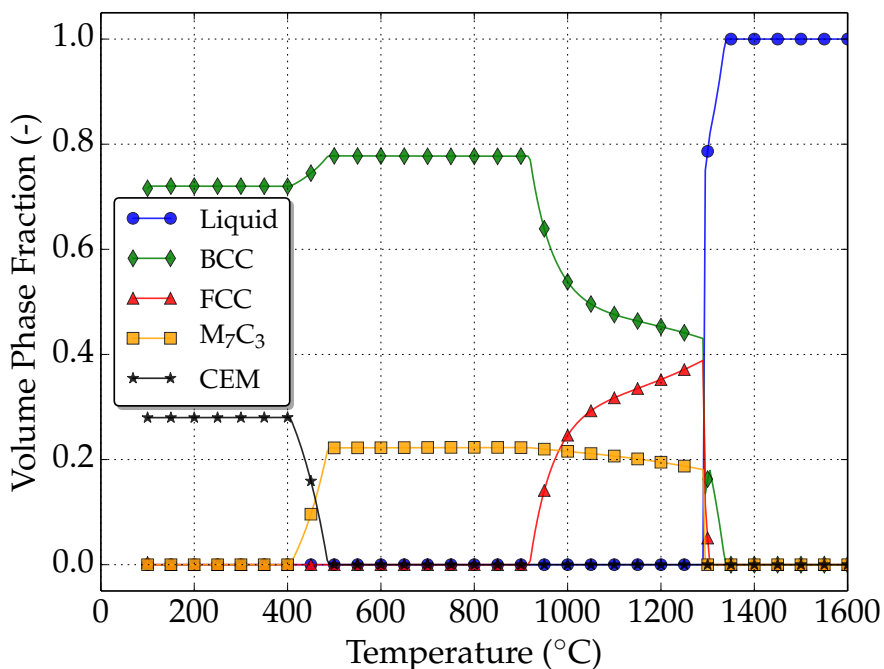


Fig. 3.7 – Thermodynamic mapping [TCFE6 2010; Andersson et al. 2002] of the transformation path for the Fe-2 wt.% C-30 wt.% Cr at nominal composition.

3.5.2 Discussion

A first case is considered without macrosegregation, that is, all mechanical driving forces are bypassed, leading to a static melt. This is achieved by nullifying the thermal and solutal expansion coefficients, which is equivalent to a constant density in space and time, i.e. no Boussinesq force is considered. This way, the average composition may only vary due to diffusion in the liquid phase.

Diffusion is significantly small in the present case and can be neglected too. The composition distribution thus maintains a homogeneous aspect throughout the sample during the

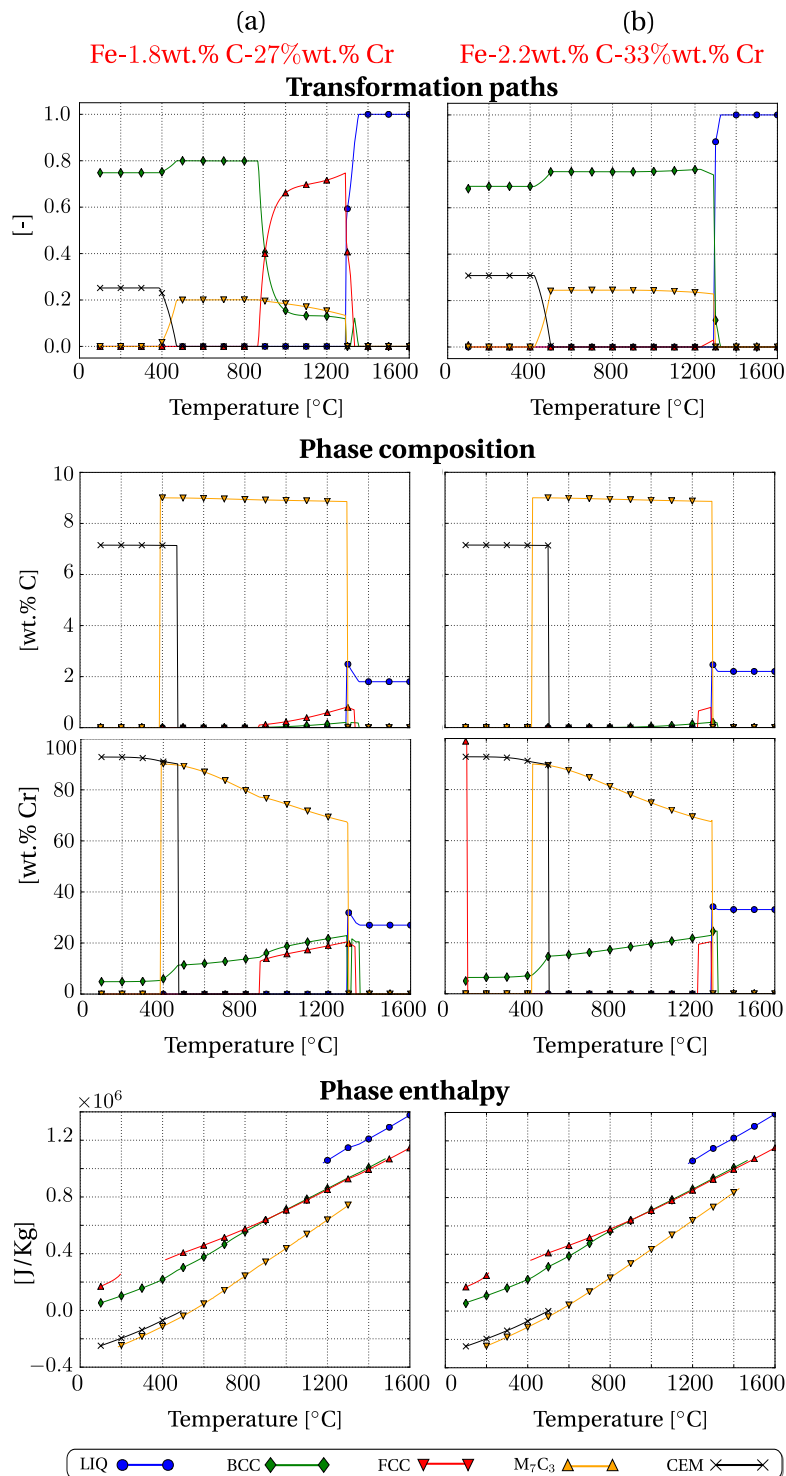


Fig. 3.8 – Tabulated thermodynamic data for the ternary system Fe-Cr alloy with software Thermo-Calc [Andersson et al. 2002] with database TCFE6 [TCFE6 2010]. The two columns represent two values of average composition, for a) low carbon and chromium content and b) high carbon and chromium content. The effect of their variation on transformation paths, phase compositions and phase enthalpies is shown in the corresponding graphs.

Table 3.3 – Solidification parameters for the Fe-2 wt.% C-30 wt.% Cr alloy.

Parameter	Symbol	Value	Unit
Nominal composition	w_{C_0}	2	wt.%
	w_{Cr_0}	30	wt.%
Characteristic temperatures	T_{bottom}	fig. 3.6b	°C
Phase fraction	g^ϕ	Tabulations fig. 3.8	–
Phase enthalpy	$\langle h \rangle^\phi$	Tabulations fig. 3.8	–
Phase composition	$\langle w_C \rangle^\phi$	Tabulations fig. 3.8	wt.%
Phase composition	$\langle w_{Cr} \rangle^\phi$	Tabulations fig. 3.8	wt.%
Diffusion coefficients	$\langle D_C \rangle^l$	15×10^{-10}	$\text{m}^2 \text{s}^{-1}$
	$\langle D_{Cr} \rangle^l$	15×10^{-10}	$\text{m}^2 \text{s}^{-1}$
Dynamic viscosity	μ^l	2×10^{-3}	Pa s
Thermal expansion coefficient	β_T	8.96×10^{-5}	K^{-1}
Solutal expansion coefficient	$\beta_{\langle w_C \rangle^l}$	1.54×10^{-3}	wt.\%^{-1}
	$\beta_{\langle w_{Cr} \rangle^l}$	1.72×10^{-2}	wt.\%^{-1}
Thermal conductivity in the solid	$\langle \kappa \rangle^s$	40	$\text{W m}^{-1} \text{K}^{-1}$
Thermal conductivity in the liquid	$\langle \kappa \rangle^l$	28	$\text{W m}^{-1} \text{K}^{-1}$
Dendrite arm spacing	λ	60×10^{-6}	m
Density	ρ_0^l	6725	kg m^{-3}
Reference composition (carbon)	$\langle w_C \rangle_{\text{ref}}^l$	2	wt.%
Reference composition (chromium)	$\langle w_{Cr} \rangle_{\text{ref}}^l$	30	wt.%
Reference temperature	$\langle w_C \rangle_{\text{ref}}^l$	1377	°C
Initial temperature	T_0	1395	°C
Ingot diameter		25×10^{-3}	m
Ingot length		75×10^{-3}	m
FE mesh size		10^{-3}	m
Time step	Δt	0.1	s
Convergence criterion (residual)	ε_R	10^{-5}	–
Convergence criterion (temperature)	ε_T	10^{-1}	K

entire cooling sequence. The phase transformations then are necessarily expected to follow the unique path shown in [fig. 3.7](#). After 407 s of cooling, the liquidus isotherm enters the bottom surface of the geometry and starts its upward propagation, marking the solidification onset.

[Figure 3.9](#) presents the simulation results at 3 successive times for the distribution of the solute species and the temperature, as well as for the fraction of phases listed in [fig. 3.7](#). At 600 s, a fully liquid region is still largely present while the mushy zone is made of liquid plus the primary solid phase (ferrite). At 10 560 s, the sample is fully solid, with fractions of ferrite and cementite that corresponds to the values read in [fig. 3.7](#) at low temperature. At the selected intermediate time, the presence of 4 phases is found. The solid region at the bottom of the cylinder is made of ferrite, austenite plus carbide, the temperature being still too high to permit the cementite to form. The mushy zone above the solid region is characterized by the presence of 3 phases due to a peritectic reaction taking place that progressively transforms ferrite into austenite in the presence of liquid.

It can be noticed that the phase fraction isovalue in [fig. 3.9](#) (at 600 s) are horizontal, owing

3.5. Application: multicomponent alloy solidification

this to two factors: the first is the temperature field, which varies unidirectionally from bottom to top, controlled by thermal diffusion, while the second is the uniform average composition throughout the sample due to the absence of convection. In fact both factors are consequences of the flow absence, which would transport heat and solute by advection, thus inevitably changing the phase distribution. The succeeding phase change is a solid-state transformation where α -ferrite and the carbide M_7C_3 react to form cementite after cooling below 490 °C, as shown in [fig. 3.6b](#). The reaction is relatively slow, ending with 28% of cementite and 72% of α -ferrite.

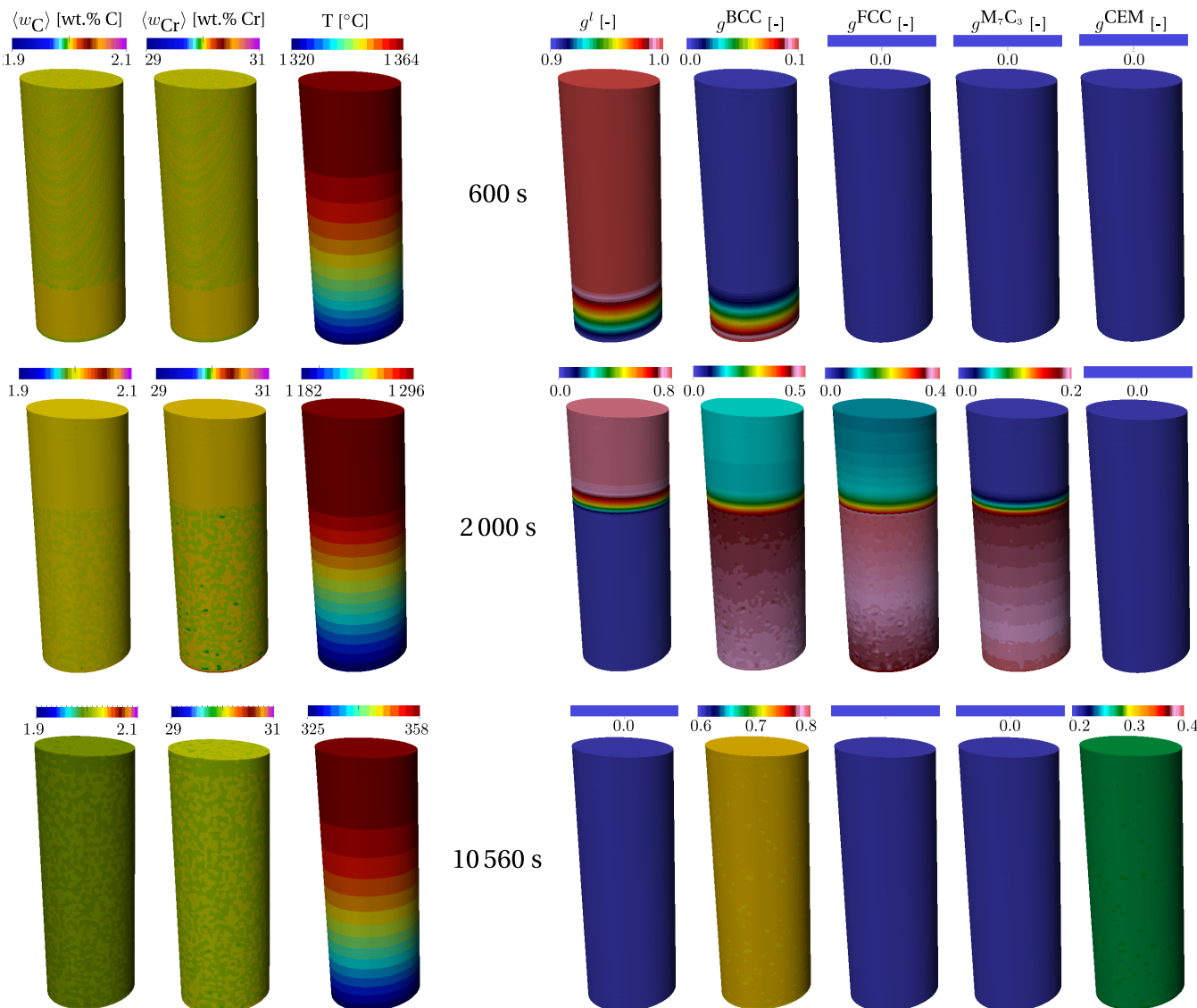


Fig. 3.9 – Upward solidification of a cylinder rod with a static liquid at 3 stages in a Fe-2 wt.% C-30 wt.% Cr. The left columns show the average composition and temperature distribution, while the right columns show the phase fractions.

3.6 Limitations

The *Tsolver* method is well suited for solidification problems with macrosegregation. In this chapter, only pure diffusion cases were simulated. The next chapter discusses the details of solving Navier-Stokes equations while predicting macrosegregation, showing thus the advantage of using the thermodynamic tabulation approach with the *Tsolver*. However, some limitations are still present and need to be explained.

First, we address the technical difficulties inherent to the solver. The previously shown algorithm in [fig. 3.4](#), showed that the Newton-Raphson method is used to linearise the energy equation then iterate on the value of the nonlinear $\frac{\partial H}{\partial T}$ term. The initial value of this term is crucial to achieve a good convergence rate, and therefore it is only manually set equal to initial phases volume heat capacity. This should evolve into an automatic initialisation based on a first evaluation given by the tabulation, making the approach more general.

The second point is the number of iterations needed by the method to converge. Although the Newton-Raphson algorithm is known for its quadratic convergence speed, imposing low convergence thresholds ([eq. \(3.25\)](#)) may easily raise the number of iterations to an average of 5 iterations before convergence can be achieved. In situations without phase change but only variable slope of enthalpy versus temperature, from 1 to 2 iterations are needed to converge. In some situations where phase change tends to be localised, i.e. taking place at some nodes, due to a local high gradient, convergence of the nonlinear system may become difficult, with residual values occasionally increasing instead of decreasing. A possible solution in such situations is to implement a line search method. It consists of interpolating the temperature between the previous temperature and the current iteration solution, in order to have a new temperature estimate, leading to a new residual estimate. This method is attractive inasmuch as it is not expensive, since no linear system is solved in the sub-iterations, only interpolations and matrices assembly to evaluate the residual.

Regarding the thermodynamic tabulations, they are only obtained by assuming full equilibrium for macrosegregation calculations. For many binary alloys, little differences are usually seen when the macrosegregation is induced by a full equilibrium and a non equilibrium solidification. It is clear however that this approximation remains limiting for multicomponent alloys. For steels, a third type of approximation is even required, named partial equilibrium, that considers equal chemical potential of interstitial elements in all phases (e.g., C), while substitutional species in the solid phases (e.g., Cr) are frozen [[Koshikawa et al. 2014](#)]. General microsegregation models coupled with thermodynamic tabulations (e.g. [[Tourret et al. 2011](#)]) for multicomponent alloys is still missing.

Résumé chapitre 3

Ce chapitre reprend les détails du solveur pour la conservation d'énergie avec changement de phase utilisé au CEMEF. Celui-ci est basé sur une méthode enthalpique, dénommée *Hsolver*, dont la variable principale est l'enthalpie moyenne volumique du système, $\langle \rho h \rangle$. Ce solveur est aussi compatible avec des données tabulées provenant de bases de données thermodynamiques, fournissant des valeurs précises pour chaque phase ϕ présente au moment de la transformation : fraction g^ϕ , composition intrinsèque $\langle w_i \rangle^\phi$, enthalpie massique $\langle h \rangle^\phi$ et densité $\langle \rho \rangle^\phi$. Avec ces données, l'équation de conservation de l'énergie est résolue dans son état nonlinéaire provenant de la dépendance de $\langle \rho h \rangle$ par rapport aux propriétés citées précédemment, sachant que celles-ci varient aussi en fonction de la composition moyenne du volume élémentaire représentatif.

Cependant, la résolution *Hsolver* nécessite une lourde recherche itérative à chaque pas de temps, consistant à convertir $\langle \rho h \rangle$ en température T pour évaluer le résidu du système nonlinéaire. Cette conversion est dénommée *H2T* et elle est compliquée du fait que les bases thermodynamiques fournissent la température comme donnée d'entrée, ce qui nous oblige de faire la recherche inverse itérative.

Dans ce chapitre, on propose de remplacer la conversion *H2T* par une autre, *T2H*. Comme son nom l'indique, on part de l'idée que la température soit la variable principale du système et on devrait alors trouver l'enthalpie moyenne volumique à chaque pas de temps. Avec ce changement, on propose donc une nouvelle formulation éléments finis, *Tsolver*, mettant en évidence les principales différences algorithmiques des deux résolutions.

Nous validons la formulation *Tsolver* dans un cas purement diffusif et comparé à des calculs faits avec la méthode *Hsolver*, ainsi qu'une comparaison avec une solution numérique obtenue par une méthode de suivi de front [GANDIN 2000]. Ensuite, nous montrons une application de solidification dirigée d'un système ternaire, Fe-0.2 wt.% C-30 wt.% Cr, en régime diffusif. Enfin, les limitations et les voies d'évolutions de la méthode *Tsolver* avec les tabulations sont détaillées.

Chapter 4

Macrosegregation with constant metal volume

Contents

4.1	Introduction	62
4.2	Navier-Stokes solvers	62
4.2.1	Stable mixed finite elements	62
4.2.2	Variational multiscale (VMS)	63
4.3	Navier-Stokes solver	63
4.3.1	Strong and weak formulations	64
4.3.2	Stabilisation parameters	66
4.3.3	Implementation	67
4.4	Tsolver validation with fluid flow	68
4.4.1	Application to a binary alloy	68
4.4.2	Application to a multicomponent alloy	68
4.5	Macroscopic prediction of channel segregates	75
4.5.1	Introduction	75
4.5.2	Experimental work	76
4.5.3	Macroscopic scale simulations	77
4.6	Meso-Macro prediction of channel segregates	83
4.6.1	Numerical method	83
4.6.2	Configuration	85
4.6.3	Effect of vertical temperature gradient	88
4.6.4	Effect of cooling rate	90
4.6.5	Effect of lateral temperature gradient	91

4.1 Introduction

Fluid flow is an important part in understanding the evolution of an alloy system undergoing phase change. It is attributed to the convective transport in fluids where the time scale is much smaller than other transport mechanisms (e.g. diffusive transport). To understand how fluid motion contributes to the heat and mass transfer, we have swiftly presented the momentum conservation equation in a solidifying liquid, [eq. \(2.45\)](#). In this chapter, we will first give a quick overview of the numerical treatment of this system of Navier-Stokes equations, then comment on some computational aspects such as the choice of a suitable time step and the conditions that impose minimum and maximum bounds on both time step and mesh size. Then, we shall present solidification applications where macrosegregation is mainly induced by thermosolutal convection without any volume change for the metal domain.

4.2 Navier-Stokes solvers

A wide array of numerical methods can be used to solve systems like [eq. \(2.45\)](#). When speaking about Navier-Stokes equations, the choice can be narrowed to two famous approaches with some similarities: stable mixed finite element method and Variational MultiScale (VMS) method. When two finite element spaces are introduced (e.g. one for velocity and another for pressure), the essential *inf-sup* condition (also known as stability condition) determined by [Babuška \[1971\]](#) and [Brezzi \[1974\]](#) should be fulfilled. It states that the formulation is ill-posed if the both spaces have the same interpolation order. For instance, a P1/P1 element (i.e. P1 for velocity / P1 for pressure) cannot guarantee the stability of the Navier-Stokes solution since velocity and pressure are both linearly interpolated at the simplex vertices. However, the major difference between the previously mentioned formulations is the way in which the inf-sup condition is accounted for. Stable mixed finite elements are stable because they directly respond to the stability condition by enriching the velocity space, hence they fall under the category of Satisfying Babuška-Brezzi (SBB) methods. In contrast, methods like VMS belong to the Circumventing Babuška-Brezzi (CBB) category [[Barbosa and Hughes 1991](#)]. CBB methods rely on equal-order interpolations with additional stabilisation that circumvents the need to satisfy the stability condition. Further details about both formulation types are given in the next subsections.

4.2.1 Stable mixed finite elements

First introduced by [Arnold et al. \[1984\]](#), the MINI element is the key ingredient of this approach. This type of element introduces an additional degree of freedom for the velocity field while keeping a linear interpolation for the pressure field, thus satisfying the Babuška-Brezzi condition with an enriched velocity space. The additional degrees of freedom are interpolated by means of the so-called *bubble* function and vanish on the element's boundary. We may therefore speak of a P1+/P1 finite element in a velocity-pressure formulation. This stable formulation has been the de facto standard for solving fluid and solid mechanics for many years at CEMEF. In *FORGE®* and *THERCAST®* codes, the P1+/P1 MINI element is used with a linear bubble function, leading to a decomposition of tetrahedra into four sub-elements to treat additional degrees of freedom for the velocity field.

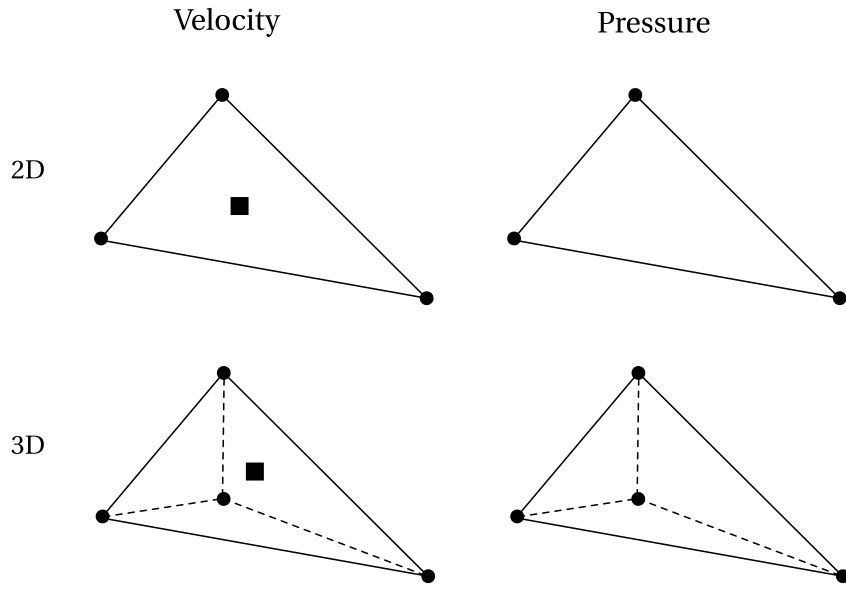


Fig. 4.1 – Schematic of 2D and 3D stable P1+/P1 finite elements, respectively triangle and tetrahedron, with velocity and pressure fields interpolation order. The dots represent the nodes while the squares represent the additional degrees, the *bubbles*.

4.2.2 Variational multiscale (VMS)

As the name indicates, this approach considers two scales of phenomena: the coarse and fine scales. Applied to our velocity-pressure formulation, these fields are decomposed according to these scales as follows:

$$\langle \mathbf{v}^l \rangle = \langle \mathbf{v}^l \rangle_h + \langle \tilde{\mathbf{v}}^l \rangle \quad (4.1)$$

$$p = p_h + \tilde{p} \quad (4.2)$$

where $\langle \mathbf{v}^l \rangle_h$ and p_h are the coarse scale velocity and pressure discretised on the finite element mesh (hence the subscript h), while the remaining terms represent the fine scale velocity and pressure that cannot be captured at the scale of the FE grid. Instead of defining a finer grid to model the effect of these terms, one can solve the fine scale equations obtained once eqs. (4.1) and (4.2) are injected in eq. (2.45) then use the output in the coarse scale equations. Further technical details about the method and the equations are found in the PhD work of [Hachem \[2009\]](#).

The added value of the VMS method is the time gain that we get by incorporating the effect of the fine scale into the coarse scale physics without discretising on a finer grid, while maintaining the ability to predict localised fluid motion such as small vortices.

4.3 Navier-Stokes solver

In the present thesis, we chose to solve the fluid momentum conservation using a stabilised P1/P1 formulation with additional element-level integrals to add stability for convection-dominated terms, transient-dominated terms and pressure terms. The stabilisation techniques include the streamline upwind/Petrov-Galerkin (SUPG), pressure stabilising/Petrov-Galerkin (PSPG)

and the least-squares on incompressibility constraint (LSIC) as a stabilisation framework introduced by Tezduyar et al. [1992]. The global approach, more commonly known as SUPG-PSPG-LSIC, prevents the classical formulation instability coming from the linear equal-order interpolation functions.

It is important to note that the P1/P1 SUPG-PSPG-LSIC approach is slightly different than a VMS approach as the derivation of stabilising terms in the latter comes from a physical interpretation of two different length scales, a resolved coarse scale and an unresolved fine scale. The incorporation of the fine-scale equation within the coarse-scale one results in additional stabilising terms, while in the current approach these terms come from a mathematical analysis based on limiting cases of diffusion or advection. The final stabilising scheme is however very similar. The Navier-Stokes solver developed by Hachem et al. [2010] and Rivaux [2011] is a convenient choice to solve a stabilised Navier-Stokes system with Darcy terms.

4.3.1 Strong and weak formulations

The solution of the strong form of eq. (2.45) consists of finding the pair $(\langle \mathbf{v}^l \rangle, p^l)$ of the previous system, when the following essential (Dirichlet type) and natural (Neumann type) boundary conditions are applied :

$$\langle \mathbf{v}^l \rangle = \mathbf{v}_0 \text{ on } \partial\Omega_{\text{Dirichlet}} \quad (4.3)$$

$$\overline{\langle \sigma^l \rangle} \cdot \mathbf{n} = \mathbf{N} \text{ on } \partial\Omega_{\text{Neumann}} \quad (4.4)$$

$$\text{with } \partial\Omega_{\text{Dirichlet}} \cup \partial\Omega_{\text{Neumann}} = \partial\Omega \quad (4.5)$$

We can comment on the strong form with the following recap points:

1. the liquid metal is Newtonian with a dynamic viscosity denoted μ^l
2. the metal is incompressible, therefore the liquid and solid densities are constant and equal (hence ρ_0^l in the inertial term) and the mass balance reduces to

$$\nabla \cdot \langle \mathbf{v}^l \rangle = 0$$
3. the Boussinesq approximation is used to compute the thermosolutal buoyancy force in the melt via the term $g^l \langle \rho \rangle^l \mathbf{g} = g^l \langle \rho \rangle^l (T, \langle w_i \rangle^l) \mathbf{g}$, where $\langle \rho \rangle^l (T, \langle w_i \rangle^l)$ can be either tabulated as a function of temperature and liquid composition for each solute i , or directly approximated by:

$$\langle \rho \rangle^l = \rho_0^l \left(1 - \beta_T (T - T_0) - \sum_{i=1}^{\text{nb species}} \beta_{\langle w_i \rangle^l} (\langle w_i \rangle^l - \langle w_i \rangle_0^l) \right) \quad (4.6)$$

where β_T and $\beta_{\langle w_i \rangle^l}$ are respectively the thermal and solutal expansion coefficients, while T_0 and $\langle w_i \rangle_0^l$ represent a reference temperature and a reference liquid composition for each chemical species, respectively.

The weak form treated by the VMS solver derives from the strong form by multiplying by test functions for velocity and pressure belonging to these functional spaces:

$$\begin{aligned} v &= \left\{ \mathbf{u}, \quad \mathbf{u} \in (\mathcal{H}^1(\Omega))^d \mid \mathbf{u} = \mathbf{v}_0 \text{ on } \partial\Omega \right\} \\ v^0 &= \left\{ \mathbf{u}, \quad \mathbf{u} \in (\mathcal{H}^1(\Omega))^d \mid \mathbf{u} = \mathbf{0} \text{ on } \partial\Omega \right\} \\ \varrho &= \{q, \quad q \in L^2(\Omega)\} \end{aligned}$$

where d stands for the space dimension. Then, based on these definitions, we write the advective upwinding stabilised test function for the velocity, \mathbf{U} :

$$\mathbf{U} = \mathbf{u} + \tau_{\text{SUPG}} \bar{\nabla} \mathbf{u} \cdot \langle \mathbf{v}^l \rangle_{\Omega_E} \quad (4.7)$$

τ_{SUPG} is an elemental stabilising parameter for advection-dominated terms and $\langle \mathbf{v}^l \rangle_{\Omega_E}$ is the superficial velocity in the element Ω_E , calculated by regular P1 interpolation:

$$\langle \mathbf{v}^l \rangle_{\Omega_E} = \frac{\sum_{i=1}^D \langle \mathbf{v}^l \rangle_i}{D} \quad (4.8)$$

Moreover, we need the following operators in order to simplify the notation of element-based variational integrals:

$$[a, b] = \int_{\Omega_E} ab \, d\Omega \quad (4.9)$$

$$[c, d]^* = \int_{\partial\Omega_E} cd \, d\Gamma \quad (4.10)$$

Finally, the SUPG-PSPG-LSIC stabilised weak formulation writes:

$$\left\{ \begin{array}{l} \forall \mathbf{u} \in v^0 \\ \left[\left(\frac{\rho_0^l}{g^l} \frac{\partial \langle \mathbf{v}^l \rangle}{\partial t} \right), \mathbf{U} \right] + \left[\left(\frac{\rho_0^l}{g^{l^2}} (\bar{\nabla} \langle \mathbf{v}^l \rangle) \langle \mathbf{v}^l \rangle \right), \mathbf{U} \right] + \left[\left(\frac{2\mu^l}{g^l} \right), \bar{\varepsilon}(\langle \mathbf{v}^l \rangle) : \bar{\varepsilon}(\mathbf{U}) \right] \\ + [(\mu^l \mathbb{K}^{-1} \langle \mathbf{v}^l \rangle), \mathbf{U}] - [(\langle \rho \rangle^l \mathbf{g}), \mathbf{U}] - [p, \nabla \cdot \mathbf{U}] - \left[\frac{\mathbf{N}}{g^l}, \mathbf{U} \right]^* \\ + [\tau_{\text{LSIC}}, (\rho_0^l \nabla \cdot \langle \mathbf{v}^l \rangle \nabla \cdot \mathbf{u})] = 0 \\ \\ \forall q \in \varrho \\ [\nabla \cdot \langle \mathbf{v}^l \rangle, q] + \\ \left[\tau_{\text{PSPG}} \frac{\nabla q}{\rho_0^l}, \left(\frac{\rho_0^l}{g^l} \frac{\partial \langle \mathbf{v}^l \rangle}{\partial t} + \frac{\rho_0^l}{g^{l^2}} (\bar{\nabla} \langle \mathbf{v}^l \rangle) \langle \mathbf{v}^l \rangle + \mu^l \mathbb{K}^{-1} \langle \mathbf{v}^l \rangle - \langle \rho \rangle^l \mathbf{g} \right) \right] = 0 \end{array} \right. \quad (4.11)$$

Replacing eq. (4.7) in eq. (4.11), we get the final weak form:

$$\left\{ \begin{array}{l} \forall \mathbf{u} \in v^0 \\ \left[\left(\frac{\rho_0^l}{g^l} \frac{\partial \langle \mathbf{v}^l \rangle}{\partial t} \right), \mathbf{u} \right] + \left[\left(\frac{\rho_0^l}{g^{l2}} (\bar{\nabla} \langle \mathbf{v}^l \rangle) \langle \mathbf{v}^l \rangle \right), \mathbf{u} \right] + \left[\left(\frac{2\mu^l}{g^l} \right), \bar{\boldsymbol{\varepsilon}}(\langle \mathbf{v}^l \rangle) : \bar{\boldsymbol{\varepsilon}}(\mathbf{u}) \right] \\ + [(\mu^l \mathbb{K}^{-1} \langle \mathbf{v}^l \rangle), \mathbf{u}] - [(\langle \rho \rangle^l \mathbf{g}), \mathbf{u}] - [p, \nabla \cdot \mathbf{u}] - \left[\frac{\mathbf{N}}{g^l}, \mathbf{u} \right]^* \\ + \left[\tau_{\text{SUPG}} \bar{\nabla} \mathbf{u} \cdot \langle \mathbf{v}^l \rangle_{\Omega_E}, \left(\frac{\rho_0^l}{g^l} \frac{\partial \langle \mathbf{v}^l \rangle}{\partial t} + \frac{\rho_0^l}{g^{l2}} (\bar{\nabla} \langle \mathbf{v}^l \rangle) \langle \mathbf{v}^l \rangle + \mu^l \mathbb{K}^{-1} \langle \mathbf{v}^l \rangle + \nabla p^l - \langle \rho \rangle^l \mathbf{g} \right) \right] \\ + [\tau_{\text{LSIC}}, (\rho_0^l \nabla \cdot \langle \mathbf{v}^l \rangle \nabla \cdot \mathbf{u})] = 0 \\ \\ \forall q \in \varrho \\ [\nabla \cdot \langle \mathbf{v}^l \rangle, q] + \\ \left[\tau_{\text{PSPG}} \frac{\nabla q}{\rho_0^l}, \left(\frac{\rho_0^l}{g^l} \frac{\partial \langle \mathbf{v}^l \rangle}{\partial t} + \frac{\rho_0^l}{g^{l2}} (\bar{\nabla} \langle \mathbf{v}^l \rangle) \langle \mathbf{v}^l \rangle + \mu^l \mathbb{K}^{-1} \langle \mathbf{v}^l \rangle + \nabla p^l - \langle \rho \rangle^l \mathbf{g} \right) \right] = 0 \end{array} \right. \quad (4.12)$$

4.3.2 Stabilisation parameters

Several expressions for τ_{SUPG} were derived by Tezduyar et al. [1992] and Tezduyar and Osawa [2000], from which we retain the following:

$$\tau_{\text{SUPG}} = \left(\frac{1}{\tau_{\text{advec}}^2} + \frac{1}{\tau_{\text{diff}}^2} + \frac{1}{\tau_{\text{trans}}^2} \right)^{-1/2} \quad (4.13)$$

where we use three parameters τ_{advec} , τ_{diff} and τ_{trans} having time as unit (s) that stabilise respectively advection-dominated, diffusion-dominated and transient-dominated regimes, given by:

$$\tau_{\text{advec}} = \frac{h_{\text{stream}}}{2\|\langle \mathbf{v}^l \rangle_{\Omega_E}\|} \quad (4.14)$$

$$\tau_{\text{diff}} = \frac{h_{\text{stream}}^2}{4\nu^l} \quad (4.15)$$

$$\tau_{\text{trans}} = \frac{\Delta t}{2} \quad (4.16)$$

where $h_{\text{stream}} = 2\|\langle \mathbf{v}^l \rangle_{\Omega_E}\| (\langle \mathbf{v}^l \rangle_{\Omega_E} \cdot \nabla \mathcal{P})$ is the element length in the stream direction, computed using the local superficial velocity and the interpolation functions \mathcal{P}_j relative to each local node j , ν^l is the liquid's kinematic viscosity ($\text{m}^2 \text{s}^{-1}$), equal to the ratio μ^l / ρ_0^l and Δt is the time step. The transient term stabilisation was initially derived for Navier-Stokes equations without Darcy term. As the latter has a significant role in the weak form eq. (4.12), it needs to be stabilised.

The current thesis is based on several past projects that either considered eq. (4.16) like Liu [2005] or modified it like Gouttebroze [2005] and Rivaux [2011] to take account the Darcy term as follows:

$$\tau_{\text{trans-darcy}} = \frac{\Delta t}{2 \left(1 + \Delta t \frac{\mu^l}{\rho_0^l \mathbb{K}} \right)} \quad (4.17)$$

In the literature, no substantial references were found to backup the formulation of eq. (4.17), it will be used in the current work though. It is worth mentioning that [Zabaras and Samanta \[2004\]](#) has invoked the necessity to stabilise Darcy terms in a generalised Navier-Stokes/Darcy P1/P1 formulation, and introduced what they call Darcy-Stabilising/Petrov-Galerkin (DSPG), using local non-dimensional numbers of Darcy (Da) and Prandtl (Pr) numbers expressing respectively the ratio of local permeability to a characteristic length L_c and the ratio of momentum diffusivity, ν^l , to heat diffusivity in the liquid, α^l :

$$\tau_{\text{darcy}} = \frac{Da}{Pr} \left(\frac{g^l}{1 - g^l} \right)^2 = \frac{\alpha^l \mathbb{K}}{\nu^l L_c^2} \left(\frac{g^l}{1 - g^l} \right)^2 \quad (4.18)$$

The definitions of the remaining stabilisation parameters are given as follows:

$$\tau_{\text{PSPG}} = \tau_{\text{SUPG}} = \left(\left(\frac{2\|\langle \mathbf{v}^l \rangle_{\Omega_E}\|}{h_{\text{stream}}} \right)^2 + \left(\frac{4\nu^l}{h_{\text{stream}}^2} \right)^2 + \left(\frac{2\left(1 + \Delta t \frac{\mu^l}{\rho_0^l \mathbb{K}}\right)}{\Delta t} \right)^2 \right)^{-1/2} \quad (4.19)$$

$$\tau_{\text{LSIC}} = \frac{h_{\text{stream}}}{2} \|\langle \mathbf{v}^l \rangle_{\Omega_E}\|^{-1} Z(Re_{\Omega_E}) \quad (4.20)$$

with $Z(Re_{\Omega_E})$ being a local Reynolds-dependant function that evaluates to:

$$Z(Re_{\Omega_E}) = \begin{cases} Re_{\Omega_E}/3 & \text{if } Re_{\Omega_E} \leq 3 \\ 1 & \text{if } Re_{\Omega_E} > 3 \end{cases} \quad (4.21)$$

and

$$Re_{\Omega_E} = \frac{\|\langle \mathbf{v}^l \rangle_{\Omega_E}\| h_{\text{stream}}}{2\nu^l} \quad (4.22)$$

4.3.3 Implementation

Time step

When solving a convective transport problem, the time step may lead to a transport inaccuracy if the so-called Courant–Friedrichs–Lewy (CFL) condition is not satisfied. The latter imposes that the optimal time step value be determined from the mesh size, h , and the velocity, $\langle \mathbf{v}^l \rangle$, over the domain as follows:

$$\Delta t \leq \Delta t_{\text{CFL}} = \min_{\Omega} \frac{h_{\text{stream}}}{\langle \mathbf{v}^l \rangle} \quad (4.23)$$

In this work, we chose to compute an initial optimal time step using eq. (4.23), but keep it constant for all simulations.

Integration order

The quadratic integrals terms in eq. (4.12) are interpolated at predefined integration points. The number of these points needed to evaluate the integrals depends on the form of finite elements as well as on the polynomial degree that we want to integrate. The higher the degree,

the more points are needed to get the most accurate results. Therefore special care should be given choosing an integrator degree to solve the previous Navier-Stokes system.

4.4 *Tsolver* validation with fluid flow

4.4.1 Application to a binary alloy

To validate the *Tsolver* with fluid flow, we consider average conservation equations already defined presented in [section 2.1.1](#). An assumption of a static and non deformable solid phase is made. Consequently, the mechanical model is reduced to the conservation of momentum in the liquid phase.

The *Tsolver*'s ability to be coupled with various physical phenomena like macrosegregation and fluid flow in porous medium is validated using an experimental solidification benchmark. The validation case consists of a 10 cm width \times 6 cm height \times 1 cm thick crucible containing a Sn-3 wt.% Pb melt. The alloy is cooled down from its two narrowest vertical sides using heat exchangers (LHE: left heat exchanger, RHE: right heat exchanger). The experiment, inspired by [Hebditch and Hunt \[1974\]](#) similar set up, has been revisited by [Hachani et al. \[2012\]](#) who performed the solidification with better controlled conditions and using an increased number of samples for composition analysis. Recently, a successful attempt to simulate the experiment was carried out by [Carozzani et al. \[2013\]](#) relying on an enthalpy resolution. All details regarding geometry, finite element discretisation, material properties and boundary conditions can be found in the latter reference.

For this computation, solidification paths, phase compositions and phase enthalpies were determined by a thermodynamic module dedicated to equilibrium calculations for binary alloys. The 3D simulation results in [fig. 4.2](#) show a satisfactory agreement with the experimental temperature measurements recorded at mid-heights of the cavity and uniformly distributed along its width.

Furthermore, simulation results with the *Tsolver* and the *Hsolver* previously obtained by [Carozzani et al. \[2013\]](#) were found to be almost superimposed. This is confirmed by a comparison made between both solvers, as shows [fig. 4.3](#), where the average composition, liquid fraction and temperature fields are extracted from a cut plane halfway through the ingot. On the same figure, if we compare the composition, we notice that the solidified part on the RHE side has basically the same segregation pattern, while the convected liquid has a slightly different solute distribution.

As for the extent of the mushy zone, we observe that liquid fraction contours are very close, indicating that temperature distributions and interdendritic segregation are also close between both solvers predictions.

Regarding the computation, the *Tsolver* resolution proves to be faster than the *Hsolver* used by [Carozzani et al. \[2013\]](#): a process time of 7000 s required a computation time of 90 hours 13 minutes compared to 114 hours 21 minutes spent by the enthalpy resolution with 32 cores on the same cluster. The gain factor is about 20%.

4.4.2 Application to a multicomponent alloy

In the previous chapter, we have considered a static melt upon solidification of multicomponent alloy. This artificial assumption is dropped in this chapter, hence taking into account

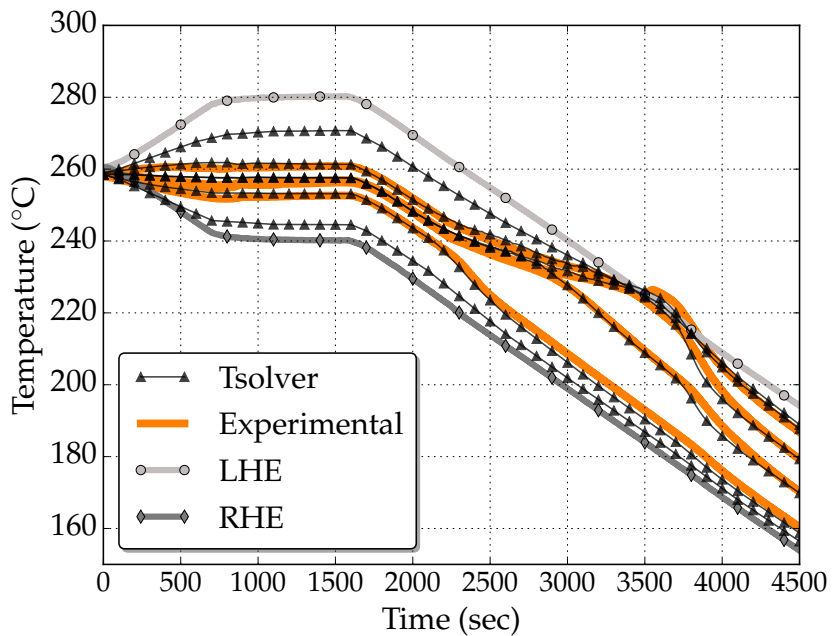


Fig. 4.2 – Results of the 3D FE convection-diffusion simulation, overlapping with the experimental cooling curves. The left (LHE) and right (RHE) heat exchangers impose the boundary temperature in the experiment.

solute transport caused by fluid motion, using realistic values of thermal and solutal expansion coefficients given in [table 3.3](#). In such conditions, the melt is in constant motion and knowing that the carbon and chromium solutes have lightening effects on the liquid at nominal composition, the density inversion resulting from the composition gradient in the interdendritic liquid, may cause flow instability (segregation plumes) at the solidification front. While the selected alloy is a steel, this application is also representative of directional cooling in a single crystal casting, e.g. for nickel-base superalloys [[Beckermann et al. 2000](#)]. Solidification of this class of alloys is carefully controlled so as to prevent any freckle-type defect to exist in the as-cast state. In this section, we consider the same simulation parameters defined in [table 3.3](#) as well as the cylindrical geometry and thermal boundary conditions previously defined in [fig. 3.6](#). Moreover, we solve the liquid momentum conservation equation, with non-slip boundary conditions on all external sides of the cylinder.

Solidification starts at 407 s when the cylinder's bottom base temperature reaches the liquidus temperature of the alloy. In fact, the solidification onset is the same as in the pure diffusion case in [fig. 3.9](#), since the average composition remains unchanged for an entirely liquid domain (assuming an initially infinite solute mixing in the melt).

As shown in [fig. 4.5](#) at 600 s, the first solid phase to form is still ferrite. We can also see solute-rich channels forming in the mushy zone and solute plumes rising in the melt above the mushy zone due to a subsequent upward flow. It is actually caused by the thermosolutal buoyancy force created by the carbon and chromium solutes.

As solidification proceeds (e.g. at 2000 s in [fig. 4.5](#)), the liquid becomes more enriched with solutes and the peritectic reaction forming the austenite phase is reached. However, for very large enriched melt, it can also be observed that primary solidification proceeds with the austenite



Fig. 4.3 – Comparison of 3D simulation results: average composition, liquid fraction and temperature at $t=3000$ s for *Tsolver* and *Hsolver*.

phase rather than the ferrite phase. The carbide phase can form with the austenite phase at some locations.

Solidification ends at around 2475 s, the last liquid solidifying at the cylinder's top surface, where the average composition reaches a maximum of Fe-2.151 wt.% C-30.633 wt.% Cr, i.e. a relative positive macrosegregation, $(\langle w_i \rangle - \langle w_i \rangle_0) / \langle w_i \rangle_0$, of 7.5% for carbon and 2.1% for chromium. The fact that the maximum average composition is observed at the top, is verified in [fig. 4.4](#) which shows the composition map in a 2D vertical slice through the longitudinal axis of the cylinder. We can also see it in [fig. 4.6](#) where relative composition profiles are plotted at the end of the cooling process along the longitudinal cylinder axis Z-Z' and along the axis of the segregated channel, F-F'. Segregation becomes more and more negative up to 1 cm from the chill, corresponding to solute depletion caused by the first solid formation. Subsequent solidification enriches further the liquid; hence the solid composition also increases.

The composition evolution trend for both solutes is similar: an overall rise until positive segregation is achieved above 5 cm from the chill on ZZ' in [fig. 4.6](#). The positive macrosegregation intensifies when the profile is chosen at the center of the segregated channel, negative segregation then becoming less pronounced.

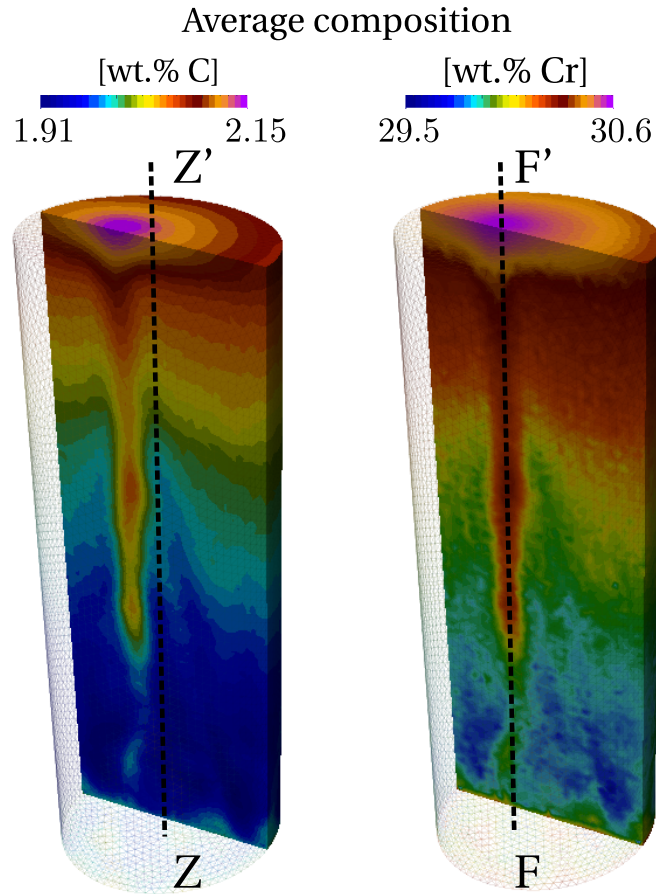


Fig. 4.4 – Average composition map on a vertical section inside the sample, along two vertical lines: the cylinder revolution axis and another axis parallel to the latter but passing through a segregated solidified channel.

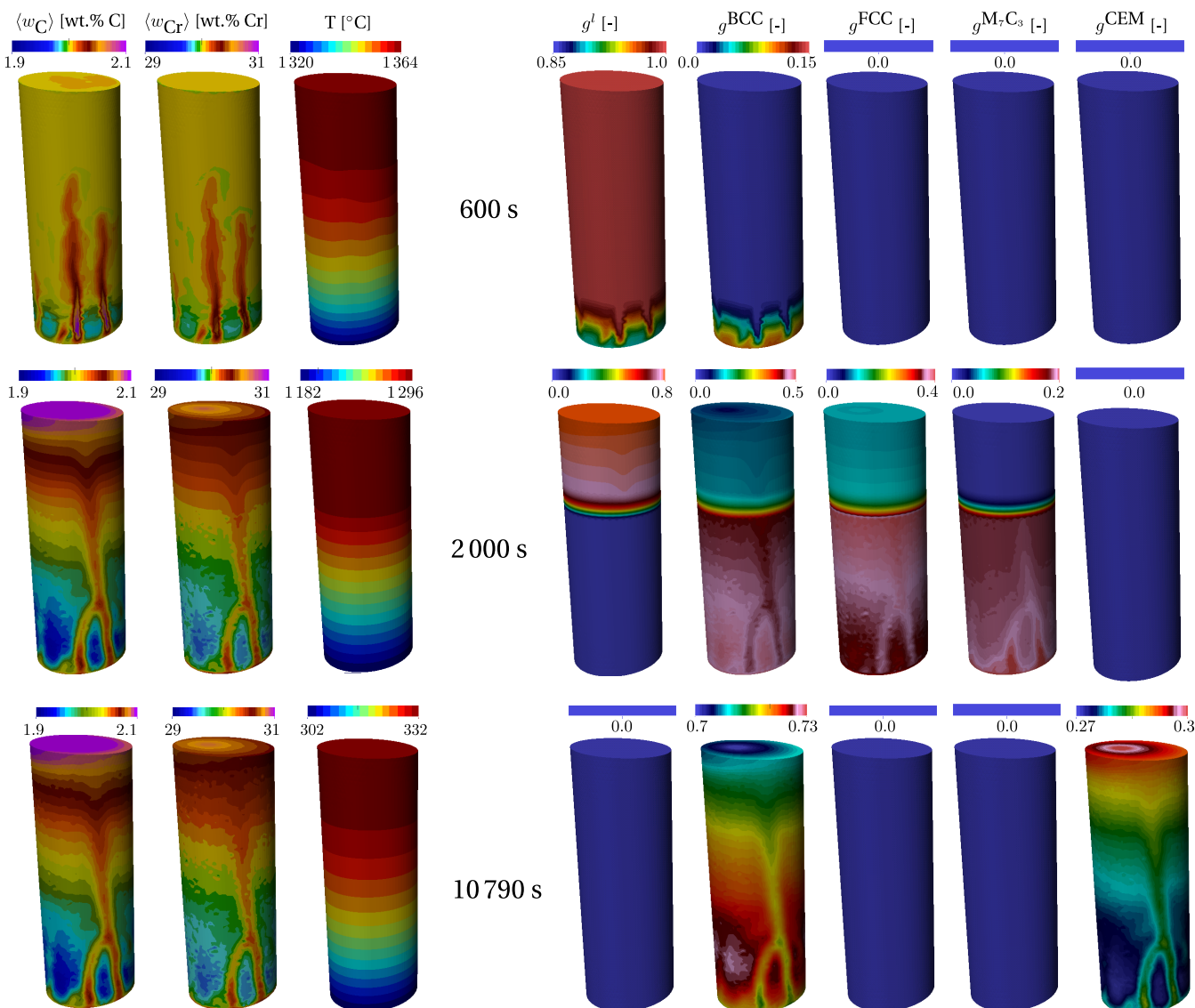


Fig. 4.5 – Upward solidification of a cylinder rod at 3 stages showing the metallurgical consequences of macrosegregation Fe-2 wt.% C-30 wt.% Cr. The left columns show the average composition and temperature distribution, while the right columns show the phase fractions.

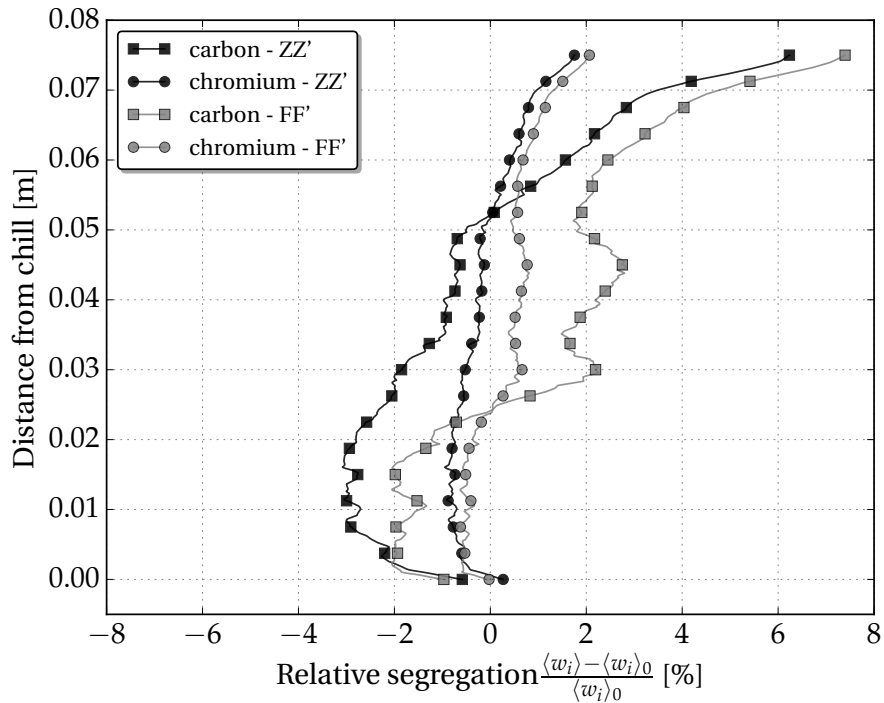


Fig. 4.6 – Relative macrosegregation profiles along the vertical revolution axis.

Beyond 2475 seconds, no variations of the average composition maps are observed since solidification is complete. Nonetheless, as temperature decreases, solid-state transformations are still possible as for the case with no macrosegregation. The formation of a cementite phase begins at the cylinder base at 8843 s with a temperature of 496.9 °C. At about 9293 s, the isotherm 488.5 °C reaches the top surface. This temperature value is the local cementite solvus temperature. The difference in the solvus temperature between the bottom and top surfaces is due to macrosegregation. Macrosegregation also explains the variation in the cementite content. The solid state transformation ends shortly before 10 500 s.

Comparing figs. 3.9 and 4.5, the influence of the solidification process is clear on the final macrosegregation pattern, hence the final phase distribution. This is better illustrated by drawing the time evolution of phase fractions at the center of the bottom and top surfaces of the cylinder in fig. 4.7. With no macrosegregation, in fig. 4.7a, the final distribution of the phases is the same at time 12 000 s, while in the presence of macrosegregation, as shown in fig. 4.7b, variations of the cementite and ferrite are revealed. The segregated channels inside the cylinder and on the boundary, often lead to *freckles*, where they consist of visible equiaxed grains [Copley et al. 1970]. This defect is marked by a noticeable gradient of composition and phase fractions, possibly changing the mechanical properties in the channels, hence the overall mechanical behaviour of the cast part. The coupling of the *Tsolver* with thermodynamic tabulations is thus demonstrated. It shows the ability to predict complex transformation paths, even if only at equilibrium. As for the computation time, the *Tsolver* resolution performed better: 500 seconds of solidification required 6 hours 14 minutes compared to 8 hours 6 minutes spent by the enthalpy resolution with 12 cores on the same machine. The gain factor is about 22%.

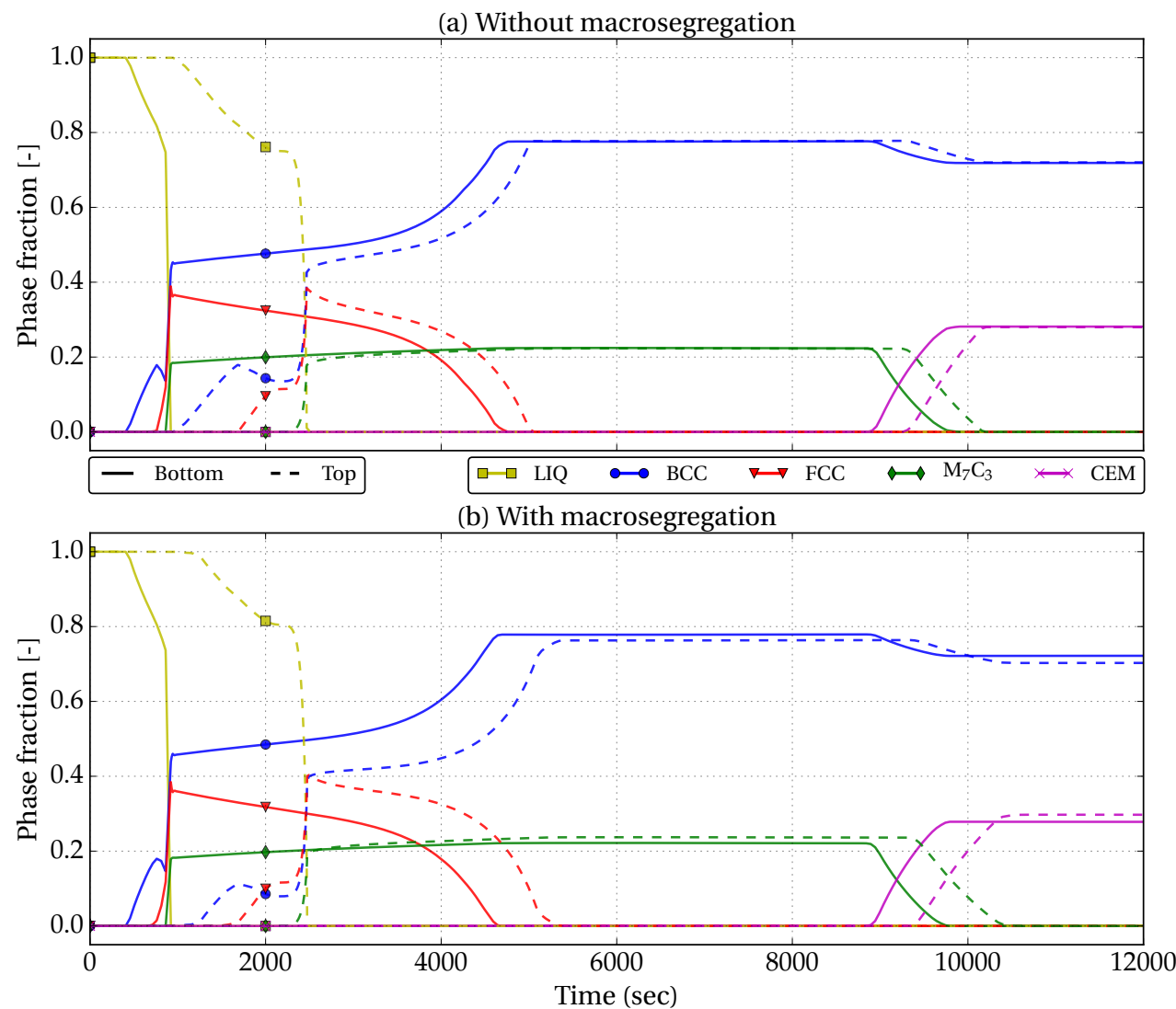


Fig. 4.7 – History of phase fraction (a) without macrosegregation and (b) with macrosegregation at the center of the bottom (solid lines) and top (dashed lines) of the cylinder surfaces. These plots are extracted from simulations displayed in (a) [fig. 3.9](#) and (b) [fig. 4.5](#).

4.5 Macroscopic prediction of channel segregates

4.5.1 Introduction

We have seen in the previous multicomponent solidification test case, a formation of segregated channels in the cylinder. This defect manifests itself as a composition inhomogeneity that is highly non-isotropic. A typical description of its morphology would consider a channel with a diameter proportional to few primary dendrite arm spacing and a length that could vary from millimeters to centimeters. These “worm”-like shapes may form during directional solidification of cast parts designed for engine applications, particularly in nickel-base superalloys [Giamei and Kear 1970; Beckermann et al. 2000; Genereux and Borg 2000; Schneider et al. 1997]. In the latter situation, the channels are often filled with a chain of small equiaxed crystals, thus referring to the term “freckle”. In large steel ingots, these channel defects are also related to A- and V-segregates [Pickering 2013].

Considering a binary alloy with a partition coefficient less than unity and having a negative liquidus slope, channel segregates may form by the following mechanisms: i) solute partitioning occurs at the scale of dendrite arms and solute is rejected in the melt, ii) local composition gradients are intensified resulting in an increase of the solutal buoyancy force in the mushy zone, iii) solute-rich pools are formed, causing segregation chimneys and convective plumes in the melt, iv) which lead to partial remelting and transport of dendrites, continuous solute feeding and locally delayed solidification, and finally v) accumulation of fragments and/or equiaxed crystals in the chimneys before the end of solidification.

Because it is of prime importance to control the occurrence of channel segregation, several attempts have been made from the late 1960’s [Flemings and Nereo 1967; Flemings et al. 1968; Flemings and Nereo 1968] to the early 2000’s [Ramirez and Beckermann 2003] to understand it and characterise it by deriving freckling criteria. These studies are summarized in [Auburtin 1998]. One of the reasons for only considering freckling criteria is that direct realistic simulations of the formation of freckles in a casting geometry are still difficult. It is indeed not crucial for industrial applications, as freckles cannot be cured and lead systematically to part rejection, except for casting ingots, where channel segregation cannot be avoided.

Experimental observations show that it requires a satisfying description of the microstructure together with the 3D convective flow controlled by the cooling conditions of the complete cast part [Shevchenko et al. 2013]. Such information is not accessible yet. Only simulations in representative simple cuboid or cylindrical domains are usually achieved [Felicelli et al. 1991; Felicelli et al. 1998; Kohler 2008; Guo and Beckermann 2003], except when considering small volume casting [Desbiolles et al. 2003]. They are usually limited to unstable thermosolutal convection without or with little regard to the microstructural features. Considering the spatial resolution of the defect, being for example of the order of the primary dendrite arm spacing, a fluid flow computation in the 3D casting part is also very demanding and not common in the literature. Among other criteria, the dimensionless Rayleigh number has been identified as a good indicator for the occurrence of segregation channels and freckle defects. The dependence of freckling tendency on the Rayleigh number has been studied numerically and compared to experimental observations, as done by [Ramirez and Beckermann 2003].

4.5.2 Experimental work

An interesting experimental work on directional solidification of In-75 wt.% Ga featuring in-situ X-ray monitoring has been recently carried out by [Shevchenko et al. \[2013\]](#) at Dresden's Helmholtz institute. We give here a detailed description of their experimental setup, as this experimental work has been used as a reference to test the performance of our numerical simulations. This was done through a collaboration resulting in the joint publication [\[Saad et al. 2015\]](#). The comparison with numerical modelling is paramount for two main reasons: firstly, the in-situ technique allows to follow solidification in real-time and offers visual description of the system behaviour: grain morphology, composition evolution, effect on fluid flow in the mushy zone and chimney initiation, as well as other modelling input data such as dendritic and eutectic nucleation undercooling; secondly, an indium-gallium system is more representative of metallic alloy solidification than the widely used organic systems, e.g. the succinonitrile-acetone mixture that exhibits alloy-like dendritic formation in its growth stage. Further information with respect to the experimental hardware, procedure and data analysis can be found in [\[Boden et al. 2008; Shevchenko et al. 2013\]](#).

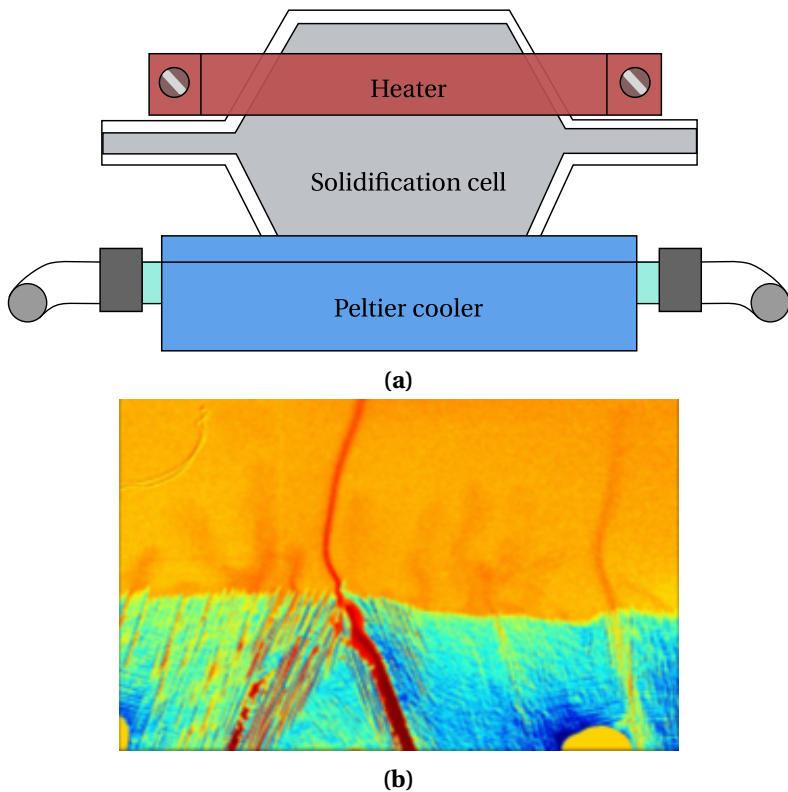


Fig. 4.8 – Illustration of the benchmark experiments for in-situ observation of segregated channels formation using X-Ray radiography with (a) a schematic of the cell and (b) a typical image of the microstructure formed during directional solidification of an In-75 wt.% Ga alloy.

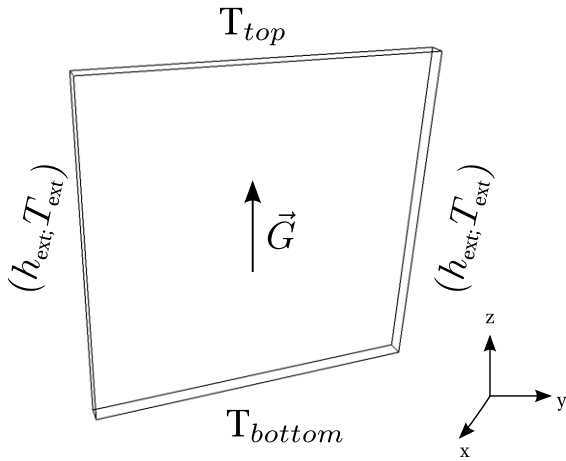


Fig. 4.9 – Computational geometry used for simulating channel segregation phenomena, along with top and bottom imposed boundary temperatures, T_{Top} and T_{Bottom} , and lateral Fourier cooling fluxes using a heat transfer coefficient and an external temperature, h_{ext} and T_{ext} . The resulting temperature gradient, G , is parallel to the vertical z-axis.

4.5.3 Macroscopic scale simulations

Configuration

The focus of this section is on qualitative comparison between numerical simulation and the previously mentioned experiment.

To qualitatively replicate this effect while simplifying the cell geometry, a cuboid cell measuring $22 \text{ mm} \times 22 \text{ mm} \times 1 \text{ mm}$ is considered. On the lateral vertical side surfaces, small cooling fluxes are imposed, after being computed from a constant heat transfer coefficient, h_{ext} , and a constant external temperature, T_{ext} , as shown in [fig. 4.9](#). On the same figure, temperatures at the bottom and top surfaces, respectively T_{Top} and T_{Bottom} , are imposed in a way to maintain a constant vertical gradient, G , thus linearly decreasing over time with the same cooling rate R . Both square faces of the geometry, having an area of $22 \text{ mm} \times 22 \text{ mm}$, are adiabatic. In spite of taking cell dimensions similar to benchmark experiments presented above, the cell thickness is increased from $150 \mu\text{m}$ to 1 mm . In general, a minimum of 5 to 8 elements is practically needed to get a better representation of the fluid motion. When the domain thickness is $150 \mu\text{m}$, imposing 8 elements in the thickness results in a huge homogeneous isotropic mesh containing about 10^9 elements, the mesh size being equal to 0.018 mm . This leads to slower simulations and therefore more complicated analysis with the large data files. Instead, we choose to keep the same number of thickness elements, but increase the thickness instead. That way, the resulting isotropic mesh would reduce to 2.5×10^4 elements. Therefore, we keep the latter thickness as the current study is limited to qualitative comparisons, but the mesh size is imposed to about $2\lambda_2=140 \mu\text{m}$, and the fixed finite element grid contains around 2×10^6 elements and 3×10^5 degrees of freedom.

Initial and boundary conditions are given in [table 4.1](#) while materials properties are provided in [table 4.2](#). A series of computations is performed to understand the influence of process parameters on the final macrosegregation pattern. In directional growth, the main parameters are the vertical temperature gradient, G , and the cooling rate, R , since they control the isotherms

Table 4.1 – Summary of the simulations and the corresponding parameters for the FE cases, where a purely macroscopic model is used. Parameters are varied from (G1) low to (G2) high gradient and (L0) no, to (L1) low lateral cooling.

Case	Vertical gradient $\ G\ $ [K mm $^{-1}$]	Cooling rate R [K s $^{-1}$]	Lateral cooling L (h_{ext} , T_{ext}) [W m $^{-2}$ K $^{-1}$, °C]	Initial temperature (T_{top} , T_{bottom}) [°C]
FE-G1R1L0	G1:0.2	R1:-0.01	L0:(0,0)	(29.75, 25.25)
FE-G1R1L1	G1:0.2	R1:-0.01	L1:(20,0)	(29.75, 25.25)
FE-G2R1L1	G2:1.5	R1:-0.01	L1:(20,0)	(58.25, 25.25)

speed. However, the effect of a higher lateral cooling is also considered below by increasing the heat transfer coefficient, h_{ext} .

The computation cases used in this study are presented in [table 4.1](#). The label of each case allows direct access to the simulation parameters as explained in the table caption. Values for these parameters are inspired from the above experiments ([section 4.5.2](#)). Initial conditions consider a quiescent liquid at uniform composition given by the nominal alloy composition w_0 . The temperature field is also initially uniform at a temperature averaged between the top and bottom initial values provided in [table 4.1](#). It has been checked that a uniform temperature gradient is swiftly reached, and that the unsteady regime to settle a vertical temperature gradient does not affect the phenomena studied.

The liquid fraction is determined directly from temperature and average composition fields which are deduced from the FE solution, assuming a linear phase diagram, i.e. linear liquidus with full thermodynamic equilibrium between phases or lever rule approximation. This linear approximation is made available by the dotted line provided in [fig. 4.10](#). Note that this line defines a phase diagram that seems very different from the correct one. However, this linear fit is only used in a composition region located around the nominal composition of the alloy. It is also worth noticing that the eutectic microstructure is expected to appear at 15.3 °C. Nevertheless, experimental observations revealed that large eutectic nucleation undercooling was reached, so the eutectic solidification was not reported in the experiments studied by [Shevchenko et al. \[2013\]](#). Consequently, the solidification path is computed without accounting for the eutectic microstructure in the present simulations, thus extending the liquidus and solidus lines below the eutectic temperature as sketched with the linear approximations in [fig. 4.10](#).

Results

The first case labeled FE-G1R1L0 is a reference case that features a low gradient (G1), low cooling rate (R1), and without any lateral cooling (L0), ensuring that isotherms retain a planar shape. These simulation parameters defined in [table 4.1](#), result in a negligible fluid flow reaching a maximum velocity of 4×10^{-8} mm s $^{-1}$ in the bulk. Accordingly, the solidification front remains stable and follows the planar isotherms; no convective plumes are observed. The average composition field is thus only little modified in the mushy zone as shown in [fig. 4.11a](#) (mind the values of the scale limits).

It is concluded that velocity in the bulk is not high enough to initiate instabilities. In the next case, FE-G1R1L1, a cooling flux with a constant and very low value of the heat transfer coefficient is imposed on both vertical lateral surfaces to initiate a downward fluid flow due to

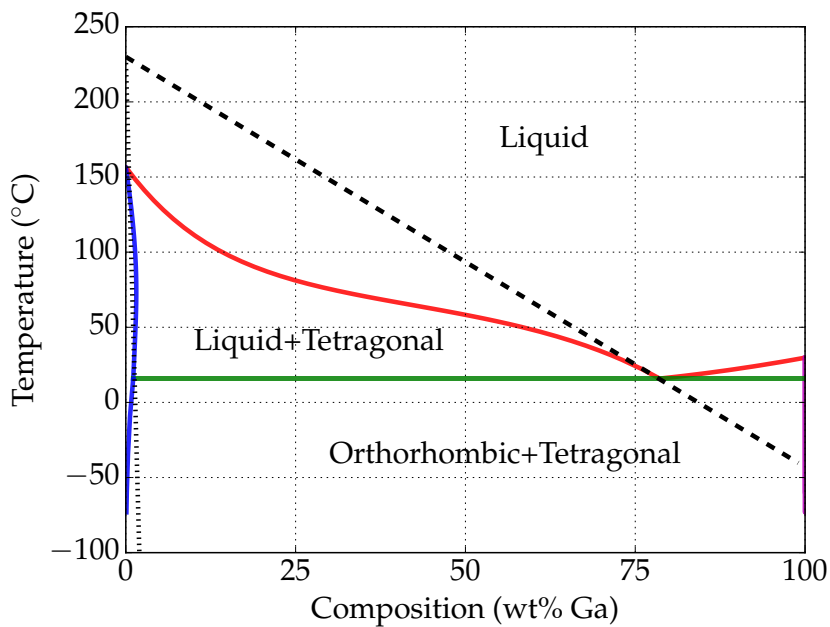


Fig. 4.10 – Binary phase diagram of the In-Ga system [Andersson et al. 2002; TCBIN 2006] and its approximation for solidification studies with an In-75 wt.% Ga alloy. The dashed and dotted lines are linear liquidus and solidus approximations near the nominal composition.

thermal buoyancy. Once solidification starts, solute-rich regions start to appear on the sides of the domain. Despite the visible concentration difference between these lateral regions and the central mush seen in fig. 4.11b, their diffuse and uniform aspect indicates no resemblance to channel segregations. We keep the same configuration but increase the vertical gradient from 0.2 K mm^{-1} (G1) to 1.5 K mm^{-1} (G2) in the case FE-G2R1L1.

The isotherms become closer to each other hence reducing the depth of the mushy zone for the same time increment compared to the preceding case. The rejected gallium solute locally accumulates at several different positions in the mushy zone, stemming from the base of the cell, with a maximum of 0.7 wt.%Ga above nominal composition. This is the consequence of segregation of gallium rich liquid being lighter than the above liquid bulk and creating an upward buoyancy force. A positive segregation and subsequent Ga-rich chimneys then rise up with an upward velocity component slightly greater than 1 mm s^{-1} .

Figure 4.12 gives a series of snapshots for case FE-G2R1L1 at three different times. Among the two clear distinct plumes that are visible at 250 s in fig. 4.11c, only one has led to the formation of a segregated channel that remains in fig. 4.12 at 500 s. In fact, an animation between 250 s and 500 s (not shown here) reveals that one plume vanishes, thus permitting the first one to further develop. A second segregated channel is also seen on the left hand side of the cell. These two channels are stable for a long time since they remain at time 1000 s. However, the left side channel develops further to become the main one at 1500 s, while the mid-width channel decreases in intensity, changes orientation and subsequently disappears (not shown here). Thus, the birth and death of very few channels is observed in this simulation, mainly due to solutal instability, as the temperature field shown in fig. 4.12 clearly remains stable despite the low lateral heat flux. As shown in fig. 4.11, instability is still required to create solutal plumes. Here, it is created by a very small lateral heat flow but other sources of instability could be

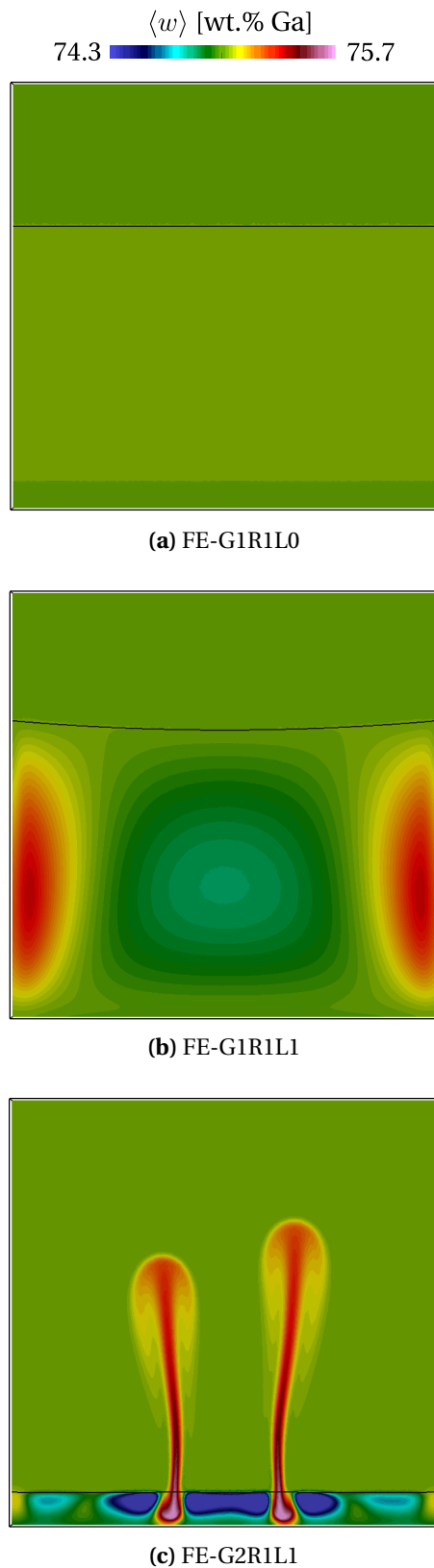


Fig. 4.11 – Average Ga composition field at 250 s for the 3 FE cases showing the influence of process parameters on the tendency to form channel segregation and convective plumes. The black line represents the liquidus isotherm given in [table 4.2](#).

4.5. Macroscopic prediction of channel segregates

Table 4.2 – Material parameters for In-75 wt.% Ga and numerical parameters.

Parameter	Symbol	Value	Unit
Nominal composition	w_0	75	wt.%
Liquidus temperature	T_L	25.25	°C
Segregation coefficient	k	0.0165	
Liquidus slope	m_L	-2.73	K wt.% ⁻¹
Gibbs-Thomson coefficient	Γ_{GT}	2×10^{-7}	K m ⁻¹
Heat capacity	c_p	380.74	J kg ⁻¹ K ⁻¹
Enthalpy of fusion	l_f	8.02×10^{-4}	J kg ⁻¹
Diffusion coefficient of Ga in liquid In	$\langle D \rangle^l$	1.525×10^{-9}	m ² s ⁻¹
Dynamic viscosity	μ^l	2×10^{-3}	Pa s
Thermal expansion coefficient	β_T	0.0978×10^{-3}	K ⁻¹
Solutal expansion coefficient	$\beta_{\langle w \rangle^l}$	1.44×10^{-3}	wt.% ⁻¹
Thermal conductivity in the solid	$\langle \kappa \rangle^s$	40	W m ⁻¹ K ⁻¹
Thermal conductivity in the liquid	$\langle \kappa \rangle^l$	28	W m ⁻¹ K ⁻¹
Dendrite arm spacing	λ	60×10^{-6}	m
Density	ρ_0^l	6725	kg m ⁻³
Reference composition	w_0^l	75	wt.%
Reference temperature	T_0	25.25	°C
CA cell size		30×10^{-6}	m
FE mesh size		140×10^{-6}	m
Time step	Δt	0.1	s

involved, as shown with the grain structure in the next section.

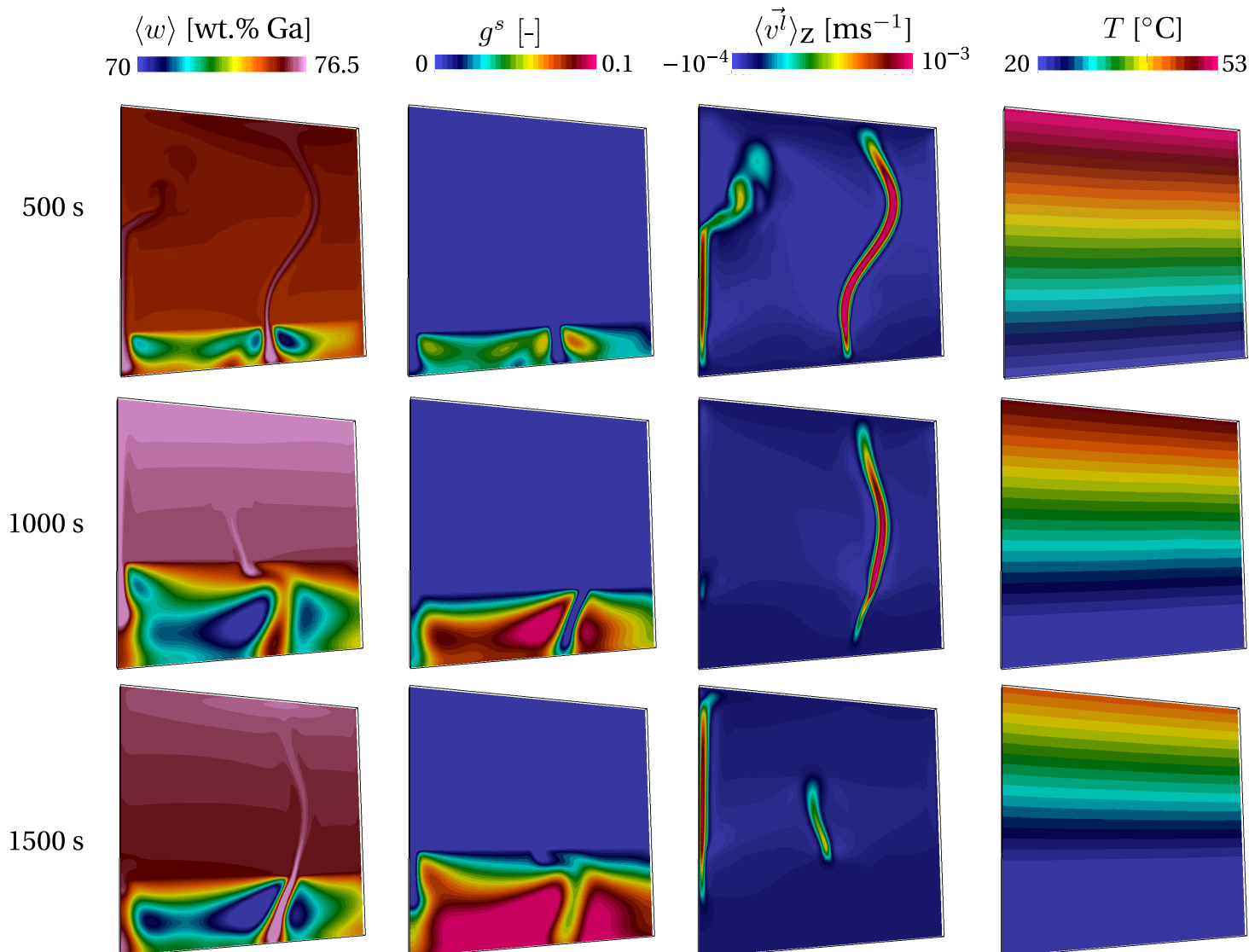


Fig. 4.12 – Simulation results for case FE-G2R1L1 showing maps of the average composition in gallium, the solid fraction, the vertical component (z-axis) of the superficial velocity field and the temperature, on a cut plane at the center of the cell at 500 s, 1000 s and 1500 s.

Discussion

In section 4.5.1, we have introduced some successful attempts of channel segregation predictions. The authors tackled the problem from a qualitative perspective. To our knowledge, the closest work to quantitative prediction of segregated channels in solidification literature was done by Ramirez and Beckermann [2003]. They attempted to draw a correlation (*freckling* criterion) between the process parameters and the occurrence of segregated channels, without any size or shape constraints, i.e. any flow instability that may appear and form the smallest channel segregate is considered. To accomplish this, they took a number of experiments done independently by Pollock and Murphy [1996] and Auburtin et al. [2000] where the casting parameters vary one at a time: casting speed (R), thermal gradient (G), angle (θ) with respect to vertical orientation and nominal composition (w_0), giving a database for 6 different superalloys. The experimental results were compared to a modified Rayleigh number that accounts for the various parameters. It allowed them to define a threshold for the formation of channel segregation in nickel-base superalloys, as well as in Pb-Sn alloys. Other contributions by Yuan and Lee [2012] (Pb-Sn alloy) and Karagadde et al. [2014] (In-Ga alloy) relied on a Cellular Automata Finite Difference (CAFD) model developed by Lee et al. [2002], which solves the dendrite tip growth kinetics at the solid-liquid interface together with macroscopic conservation equations. The authors compared simulation results to experimental findings obtained by Shevchenko et al. [2013]. However, their simulation follow solidification in a small volume that contains a few dendrites with interdendritic liquid, therefore limited as far as to predict the liquid behaviour outside the mushy zone.

On another hand, experimental observations reveal a great deal of information regarding solute redistribution, first in the chimneys that wash the dendrites in their way and then convective plumes that expel chemical species outside the mush, resulting in a global complex phenomenon. In order to capture simultaneously the interaction between the mushy zone and the free liquid, we use the Cellular Automata Finite Element (CAFE) method to combine the macroscopic and mesoscopic length scales and predict more realistic channel segregation in the next section.

4.6 Meso-Macro prediction of channel segregates

4.6.1 Numerical method

Microscopic scale

The CAFE model introduces a grid of regular and structured cubic cells, with a constant size in all space directions, referred to as the cellular automaton (CA) grid. It is different from the unstructured finite element mesh previously mentioned for the solution of the average conservation equations. A typical CA step dimension is smaller than the smallest FE mesh size. The CA grid serves to represent solidification phenomena including nucleation, growth and remelting of the envelope of the primary dendritic grains. Details about the CAFE model can be found in [Carozzani et al. 2012; Carozzani et al. 2013; Carozzani et al. 2014]. Cell information, such as the temperature, the average composition or the velocity of the liquid phase, is interpolated from the nodes of the FE mesh. State indices are also defined for each CA cell, providing the presence of liquid or solid phases.

Nucleation

Initially, cells are in a fully liquid state. In the present situation, random nucleation sites are chosen based on a nucleation density, n_{\max} (expressed in surface density inverse m⁻²), at the bottom surface of the geometry in contact with the cooler. Nucleation occurs in a cell only if the latter contains a nucleation site, and when the local undercooling of the cell reaches the critical nucleation undercooling given as input by a Gaussian distribution of mean undercooling ΔT_N with a standard deviation ΔT_σ . The crystallographic orientation of each grain newly nucleated is also randomly chosen using values of the Euler angles to fully define the three rotations that transform the reference frame to the ⟨100⟩ directions that define the main growth axes of the dendrite trunks and arms. Grain selection is therefore solely controlled by growth competition.

Growth

Dendrite growth is driven by the chemical supersaturation, Ω_{sat} , which is a dimensionless number proportional to the difference between the liquid composition at the dendrite tip and the melt composition far away from the tip, scaled by the composition jump at the interface. The higher the supersaturation, the faster the dendrite tip velocity. However, in the presence of a convective fluid, the chemical supersaturation is highly influenced by the intensity and the direction of the flow with respect to the growth direction of the dendrites. In the current model, convection is central in studying the formation of channel segregation. Therefore, the purely diffusive Ivantsov relation used to determine the Peclet number Pe as function of the supersaturation, is replaced by a modified relation using a boundary layer correlation model that accounts for both the intensity and the misorientation of the liquid velocity with respect to the growth direction of the dendrites [Gandin et al. 2003]. The main parameters for this growth kinetics models are the Gibbs Thomson coefficient, Γ_{GT} , and the diffusion coefficient for Ga in In, $\langle D \rangle^l$, all given in [table 4.2](#).

Solidification path

The CA model gives the presence of the grains in the liquid as well as its growth undercooling. For coupling with macroscopic scale modelling, the fraction of phases needs to be fed back to the FE model. This is done by accounting for the information provided by the CA model. Thus, the fraction of solid is no longer the consequence of a simple conversion of the temperature and composition assuming thermodynamic equilibrium. It also includes the solidification delay due to the kinetics of the development of the grains as detailed in the work of Carozzani et al. [2013].

Numerical method

Both the finite element mesh and the cellular automaton grid play a role in predicting channel segregation inasmuch as this type of defect originate from interplays between hydrodynamic instabilities on the scale of the dendrites and macroscopic flows defined by the geometry of the experimental cell [Shevchenko et al. 2013]. One has to respect a small maximum FE mesh size, comparable to the dendrite arm spacing. With such an element size, composition gradients giving rise to solutal buoyancy forces can be captured. This limits consequently the CA cell size, as a minimum number of cells is required in each finite element. In the array of simulations

that will be presented in the next section, the value of λ_2 was considered. We have chosen a fixed mesh element size of $2\lambda_2$ and a CA cell size of $\lambda_2/2$. An average of 4 CA cells per unit length of a finite element is enough to accurately compute the development of the grain envelopes together with the solutal, thermal and mechanical interactions. Values are given in ??.

4.6.2 Configuration

Knowing that the configuration in FE-G2R1L1 produces segregated channels, the same set of parameters is first used for case CAFE-G2R1L1 by adding the effect of the grain structure using the CAFE model. Results are accessible in [fig. 4.14](#) for comparison with [fig. 4.12](#). A striking difference is seen: the composition maps become more perturbed as shown by the formation of numerous plumes when coupling with grain structure is active. The growing front displayed on the grain structure at the right most column of [fig. 4.14](#) dictates the leading position of the mushy zone shown in the third column. Note that each color corresponds to one grain, with 17 grains having nucleated at the cell's bottom surface. However, comparison of the solid fraction maps between [fig. 4.12](#) and [fig. 4.14](#) at the same times reveals a delay in the growing front position.

Values of the nucleation parameters in [table 4.3](#) are such that few grains rapidly form below the nominal liquidus isotherm. The delay is therefore not due to the nucleation undercooling but to the growth undercooling of the dendrite tips. It should be noticed that, the growth front driven by undercooling in [fig. 4.14](#) also forms with a higher initial solid fraction and hence larger solute segregation occurs at the front. This effect, together with instabilities of the composition field, is caused by a more perturbed fluid flow and more plumes as observed in CAFE-G2R1L1 compared to FE-G2R1L1. Such observations fit to the complicated fluid and solute flow patterns typically occurring in the experiments as shown in [fig. 4.15](#). It becomes obvious that the consideration of grain structure and growth undercooling are vital to accurately simulate chimney formation in these experiments. The reasons for the instabilities are discussed hereinafter.

In the present 3D CAFE simulation, each grain shown in [fig. 4.13](#) is associated with a crystallographic orientation. The growth kinetics is only given for the $\langle 100 \rangle$ crystallographic directions at the grain boundaries with the liquid. The CA growth model is based on the hypothesis that, in a quiescent liquid of uniform temperature distribution and composition, the grain envelop should reproduce an octahedral grain shape with main directions given by the six $\langle 100 \rangle$ directions.

In the present situation where complicated fields are present for temperature, composition and liquid velocity, each grain envelope with different crystallographic orientation adapts differently to its local environment. Thus, the local undercooling of the front varies everywhere. Such variations are within few degrees here, but this is sufficient to create irregularities on the growth front, as seen on the grain structure in [fig. 4.13](#). Apart from that, these variations are linked to the position of the instabilities for the chemical and liquid velocity fields, thus demonstrating the full coupling between the CA and FE models.

Table 4.3 – Summary of the simulations and the corresponding parameters for the CAFE cases, coupling macroscopic model with the grain structure model. Parameters are varied from (G1) low to (G2) high gradient, (R1) low to (R2) high cooling rate and (L0) no, (L1) low and (L2) high lateral cooling.

Case	Vertical gradient $\ G\ $ [K mm ⁻¹]	Cooling rate R [K s ⁻¹]	Lateral cooling L (h _{ext} , T _{ext}) [W m ⁻² K ⁻¹ , °C]	Initial temperature (T _{top} , T _{bottom}) [°C]	Nucleation (n _{max} , ΔT _N , ΔT _σ) [m ⁻² , °C, °C]
CAFE-G2R1L1	G2:1.5	R1:-0.01	L1:(20,0)	(58.25, 25.25)	(10 ⁶ , 1, 0.2)
CAFE-G1R1L1	G1:0.2	R1:-0.01	L1:(20,0)	(29.75, 25.25)	(10 ⁶ , 1, 0.2)
CAFE-G1R1L2	G1:0.2	R1:-0.01	L2:(500,0)	(29.75, 25.25)	(10 ⁶ , 1, 0.2)
CAFE-G1R2L1	G1:0.2	R2:-0.05	L1:(20,0)	(29.75, 25.25)	(10 ⁶ , 1, 0.2)

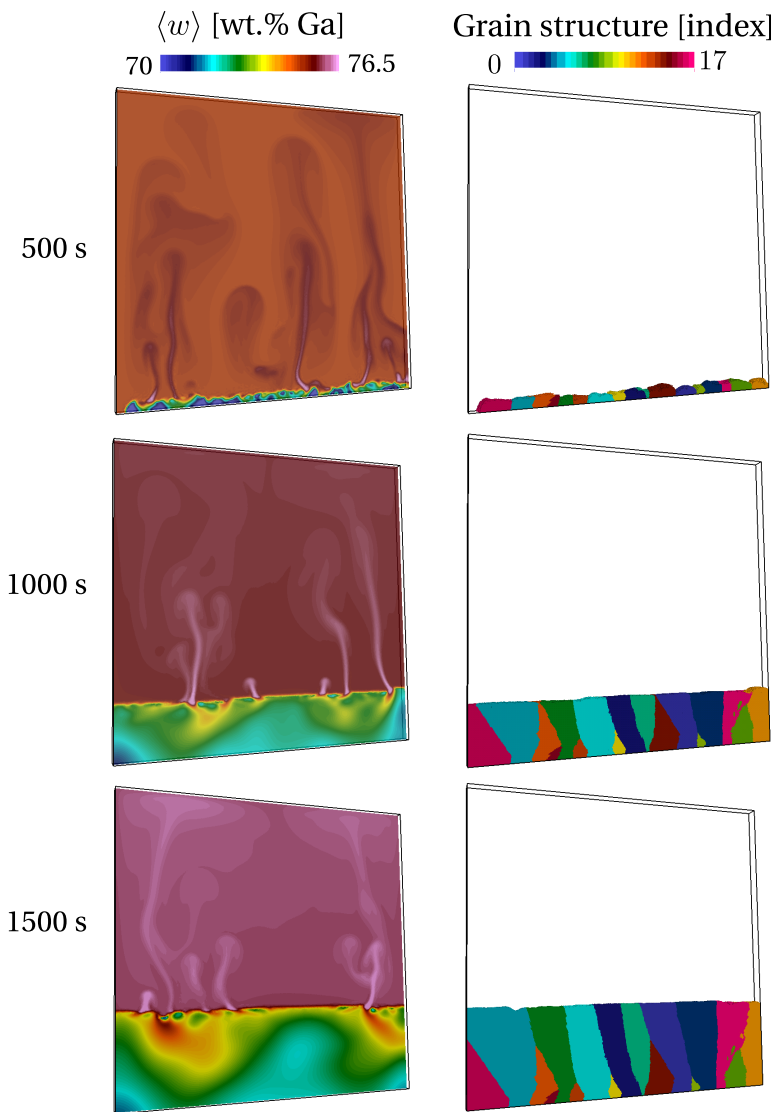


Fig. 4.13 – Simulation results the predicted of mushy grain structure with the corresponding composition maps, at 500 s, 1000 s and 1500 s.

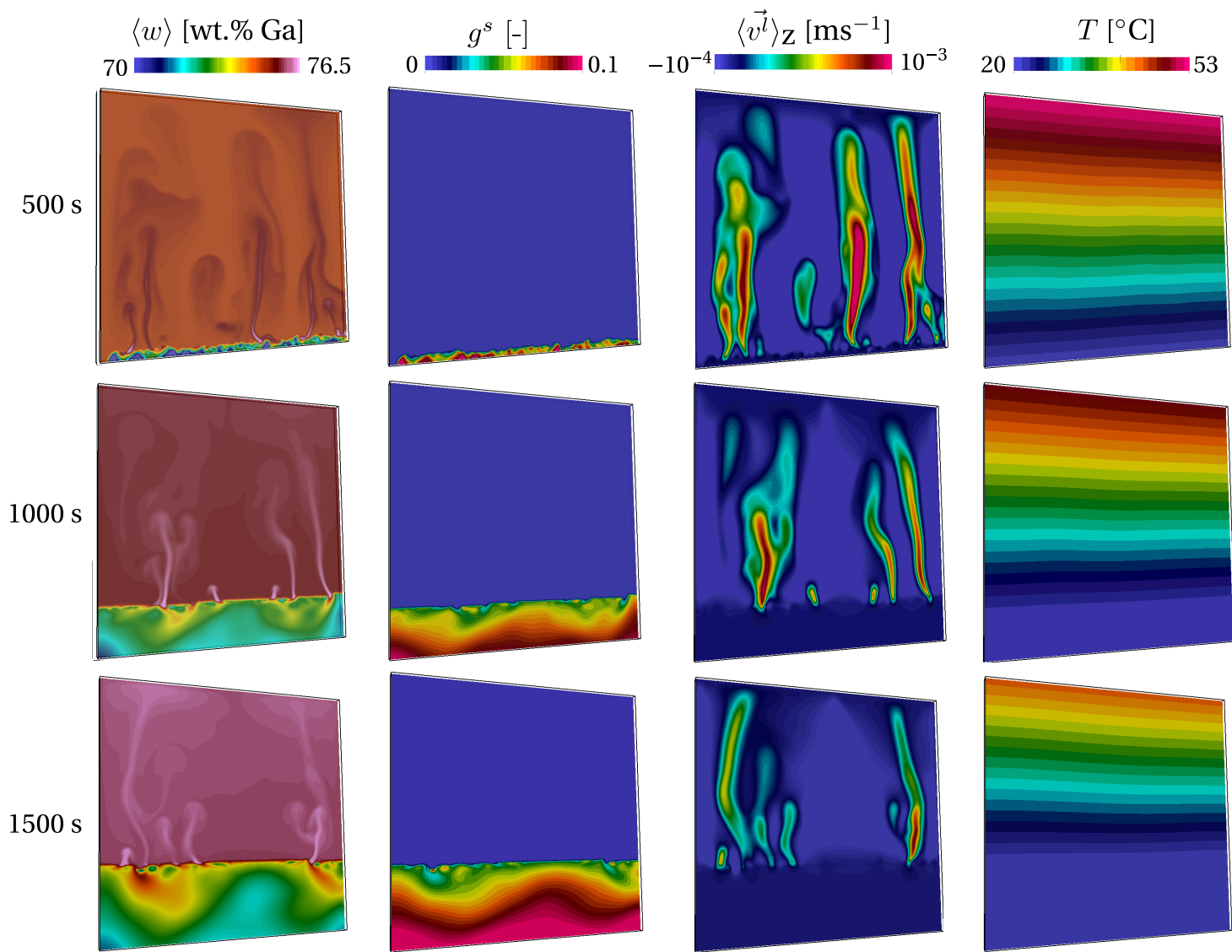


Fig. 4.14 – Simulation results for case CAFE-G2R1L1 showing maps of the average composition in gallium, the solid fraction, the vertical component (z-axis) of the superficial velocity field and the temperature, on a cut plane at the center of the cell at 500 s, 1000 s and 1500 s.

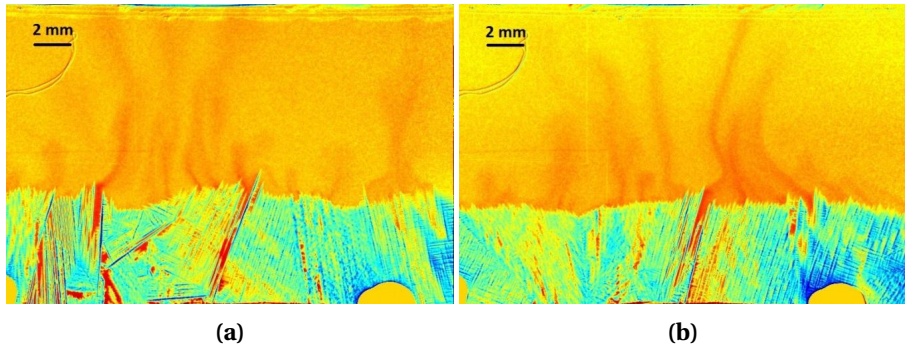


Fig. 4.15 – Snapshots of dendritic structure and composition field obtained from two solidification experiments at a cooling rate $R=-0.01 \text{ K s}^{-1}$ and temperature gradients of (a) $\|G\|=1.1 \text{ K mm}^{-1}$ and (b) $\|G\|=1.3 \text{ K mm}^{-1}$ [Shevchenko et al. 2013].

4.6.3 Effect of vertical temperature gradient

The influence of diverse process parameters can now be considered in the context of the grain structure. The effect of the vertical temperature gradient is shown by comparing the previous case CAFE-G2R1L1 with case CAFE-G1R1L1. The temperature gradient is decreased about 7 times here, from $G_2=1.5 \text{ K mm}^{-1}$ to $G_1=0.2 \text{ K mm}^{-1}$. In fact, both cases share almost all traits with respect to flow patterns and velocity magnitude in the bulk. Main differences are yet seen regarding the dynamics of the plumes shown in fig. 4.16.

In the case of a low temperature gradient (G_1), the solidification front cannot maintain a shape as smooth as for the case of a large temperature gradient (G_2): the solute gradient in the liquid of the mushy zone (basically following the lever rule approximation for a given temperature) decreases, leading to a lower gradient of the solutal buoyancy force. In turn, more solute accumulates close to the front and locally reduces the growth velocity, thus creating larger “valleys” or steps with higher solute content. The irregular geometry of the front is also influenced by the dendrite tip growth kinetics model. The velocity of the isotherms is the ratio of the cooling rate, R , to the temperature gradient, G . Consequently, the isotherm velocity in case G1 is larger than in G2, since cooling rate, R_1 , is the same in both cases. Moreover, because the dendrite tip velocity is a monotonously increasing function with the undercooling [Gandin et al. 2003], the latter for CAFE-G1R1L1 is larger than for CAFE-G2R1L1. Height differences of the growth front are proportional to the variations of the undercooling by the temperature gradient. Therefore, this forms larger steps on the growth front for case G1 compared to G2.

The chimney extends deeper in the mushy zone when the temperature gradient increases. This is confirmed by both the simulation results shown in fig. 4.16 as well as the experimental observations. Another remarkable phenomenon is also observed in the low gradient case: a “pulsing” mechanism in CAFE-G1R1L1 where a series of solute rich liquid pockets are observed one above the other. This corresponds to a repeated and localized strong spatial variation of the liquid velocity field outside the mushy zone, regularly thrusting away small plumes. These pulses are roughly similar to each other in size and exit speed, creating thus a very regular pattern during some time.

In the case of a high temperature gradient (case CAFE-G2R1L1) this phenomenon is barely seen. In fact, the pattern shown in fig. 4.16 is more typical, with continuous plume rising from

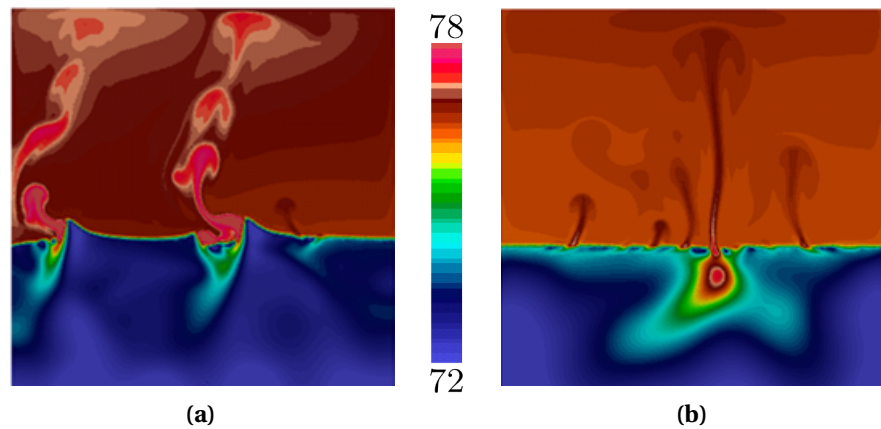


Fig. 4.16 – Average composition maps for CAFE-G1R1L1 at time 1060 s and CAFE-G2R1L1 at time 1845 s.

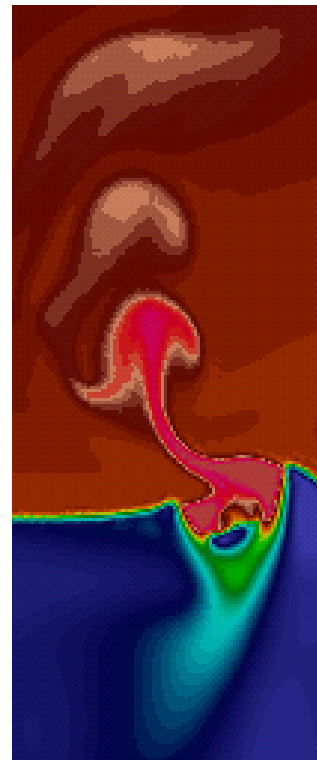


Fig. 4.17 – Snapshot of the pulsing mechanism coming from a groove shape in the mushy (check animation in the PDF file).

the mushy zone and reaching the top of the domain. However, such regular plume is the initial and final pattern seen for low gradient before the pulsing regime. Similar observations have been made in the experiments too. Figure 4.18a displays the phenomenon of the “pulsing” plumes, which could be explained by the following mechanisms. The permeability of the mushy zone and the narrow gap of the solidification cell obstruct the feeding of the plumes by solute. A critical solute concentration has to be accumulated at a specific location in order to trigger the formation of a rising plume. An interim drop of the solute concentration below such a threshold would interrupt the plume. Flow instabilities can be another reason for the peculiar shape of the plumes. Figure 4.18b shows a pronounced continuous plume. The same plume can be seen a few seconds later in fig. 4.18c. The plume structure becomes unstable; one can observe an indentation of streamlines followed by a mixing of rising solute-rich liquid with descending In-rich fluid. This mechanism also causes a non-continuous structure of the plumes.

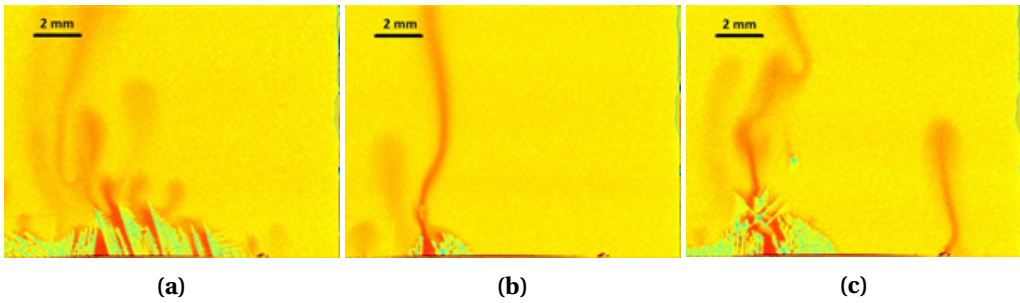


Fig. 4.18 – Snapshots of dendrite structure and composition field from two solidification experiments conducted at a cooling rate $R=-0.01 \text{ K s}^{-1}$ and a temperature gradient $\|G\|=1 \text{ K mm}^{-1}$: (a) “pulsing” plumes, (b) continuous plume, (c) upcoming plume instability [Shevchenko et al. 2013].

4.6.4 Effect of cooling rate

The next parameter studied is the cooling rate, corresponding to case CAFE-G1R2L1. A snapshot of the composition map and the corresponding vertical component of the velocity field are given in fig. 4.19. We see a similarity with case CAFE-G1R1L1 in fig. 4.16a with respect to the buckled interface between the liquid and the mushy zone as well a plume pulsing effect when a low temperature gradient is applied. On the other hand, segregation inside the mush is more irregular with more pronounced patterns reaching a larger depth.

One could distinguish alternating V-shapes and A-shapes patterns in the mushy zone. As for case CAFE-G1R1L1, these patterns are created by a network of pulsing plumes formed by the steps created on the delocalized growth front due to the low temperature gradient. However, these considerations are not sufficient to explain the shape of the growth front. The reason for the protuberances created at the tips of the V-shape is the presence of a descending bulk liquid with a low composition seen by the growth front. It infers that favorable growth conditions are created for a higher working temperature since the dendrite tip undercooling decreases for facing liquid flow and a lower composition; the growth rate is given by the isotherm velocity. The growth front thus adjusts its position to catch up with the corresponding isotherm, the latter being located at the tips of the V-shape, i.e. the outmost advanced position of the growth front. It also means that the V-shape angle depends on the size and intensity of the convection

loops above the front. When the steps are formed on the growth front, the plumes exiting the mushy zone follow a direction normal to the front. They are inclined towards each other above the V-shape. As a result, they may join and form a larger plume as seen in CAFE-G1R1L1 (fig. 4.16a), thus forming larger and more stable chimneys. The other observation in fig. 4.19 is the existence of stable regions of the growth front. For instance, this is seen in between the two V-shape forming or on the right hand side of the cell.

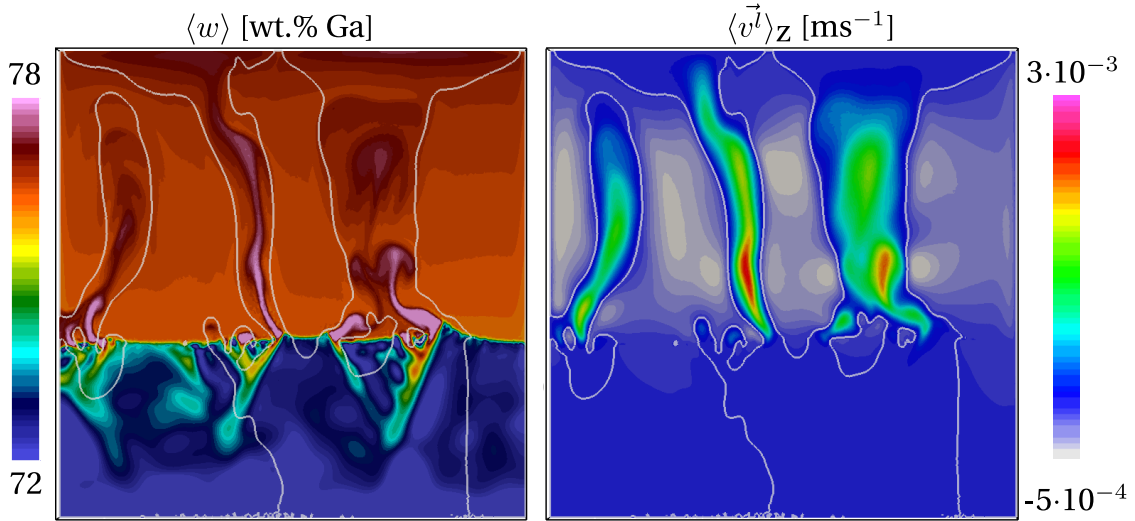


Fig. 4.19 – Average fields inside the cell for case CAFE-G1R2L1 at 350 s. The white contour identifies the zero velocity limit for the vertical component (z-axis) of the velocity field .

The reason for this stability is the inversion of the composition gradient located ahead. Animation shows that solute coming from the top of the cell is responsible for this accumulation, creating a layering that provides a stabilization effect above the mushy zone. This is verified by the vertical component of the average velocity also made available in fig. 4.19.

It is negative outside the path of the plumes. A resulting concurrent effect is the formation of the A-shape segregates in between the V-shape patterns seen in fig. 4.19. Finally, it can be observed that these patterns are sustained longer compared to fig. 4.16 CAFE-G1R1L1 because, at high cooling rate, the flow in the mushy zone is decreased due to a faster solidification. This is the same effect as described for the large gradient configuration in CAFE-G2R1L1 (fig. 4.16b). It is not clear how these observations could be compared with the A-shapes and V-shapes segregates reported for steel ingots [Pickering 2013]. Despite the fact that macrosegregation is the main phenomenon leading to these patterns, there has not been a clear explanation yet in the literature for their formation. However, for steel casting, the A and V patterns are believed to form simultaneously. Further investigations would thus be required to quantify the consequences of thermosolutal instabilities simulated here for an In-75 wt.% Ga alloy and check their possible correlation with experimental observations in steel casting.

4.6.5 Effect of lateral temperature gradient

The previous simulations show the effect of cooling rate and temperature gradient on the survival of segregation patterns deep in the mushy zone. Another simulation is performed by increasing the cooling rate using higher heat flux extracted from the vertical side boundaries.

This is achieved in case CAFE-G1R1L2 where the heat transfer coefficient reaches $500 \text{ W m}^{-2} \text{ K}^{-1}$. As a consequence of the large cooling from the sides, the temperature gradient is no longer vertical. A distinct flow due to thermal buoyancy is created, driving a cold liquid downwards near the sides of the cell. Under the influence of these two main convection loops, all segregation plumes tend to regroup in the middle of the domain, forming a larger central plume, as seen in the composition map at 450 s in [fig. 4.20](#). However, this regime occurs at times earlier than 500 s, where the effect of thermally induced buoyancy forces is prevailing, feeding the convection loops. Approximately 500 s later, the mushy zone has extended, favouring the segregation mechanical forces i.e. $\rho_{\text{ref}} (1 - \beta_{\langle w \rangle^l} \Delta \langle w \rangle^l) g$, rather than the thermal mechanical forces, $\rho_{\text{ref}} (1 - \beta_T \Delta T) g$.

[Figure 4.20](#) shows the corresponding composition maps with stable segregated channels at about 1000 s that also remain at 1500 s. The solidification front then tends to form a concave shape at the center of the cell, thus partially revealing the form of the isotherms toward the cell center. The stable pattern in the center is similar to the plateau seen at the center, between the A-shapes in [fig. 4.16](#) and [fig. 4.19](#). As stated before, it is an inactive region with respect to plume initiation due to the inversion of the solute composition gradient. In other words, the high gallium concentration at the top of cell causes indium, which is the heavier species, to accumulate and be partially trapped between the mushy walls, thus creating a stable flow configuration.

Outside of the plateau, two plumes are observed from the prominent instabilities of the growth front, adopting diverging directions. This is also observed at the center of the cell in [fig. 4.19](#) on each side of the A-shape segregate. These plumes in [fig. 4.20](#) lead to the formation of two stable channels. The corresponding situation in the experiment is shown in [fig. 4.21](#). The chimneys on both sides and the plateau in between can be clearly recognised.

The additional cooling at the side walls produces two flow vortices between the side wall and the strong convective plumes above the chimneys. The central part of the sample remains almost unaffected by the additionally driven thermal convection. This area is characterised by the occurrence of a number of smaller convective plumes.

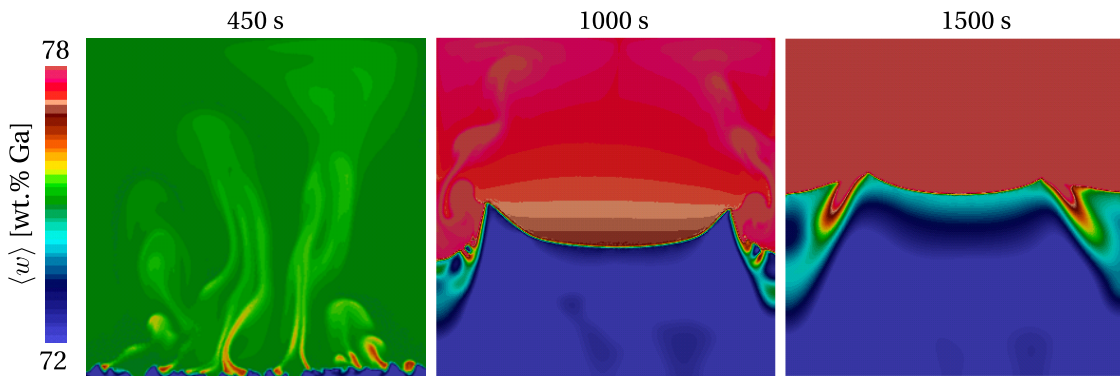


Fig. 4.20 – 2D cut plane of the average composition inside the cell for case CAFE-G1R1L2 at the following time increments: 450 s, 1000 s and 1500 s.

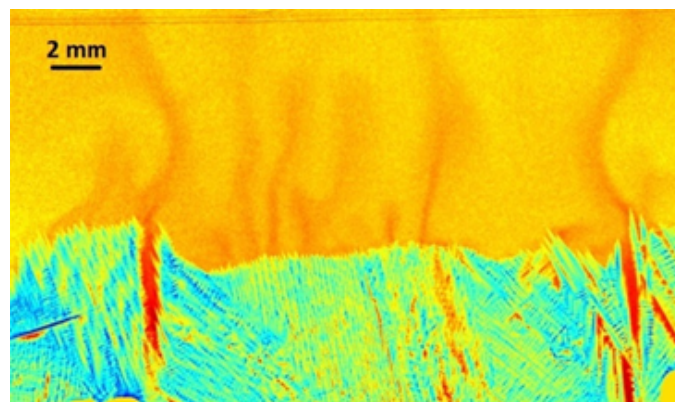


Fig. 4.21 – Snapshot of dendritic structure and composition field from a solidification experiment recorded at 1000 s for a cooling rate $R=-0.01 \text{ Ks}^{-1}$ and a temperature gradient $\|G\|=1 \text{ Kmm}^{-1}$ [Shevchenko et al. 2013].

Résumé chapitre 4

Ce 4^e chapitre est dédié à la macroségrégation induite par le mouvement de la phase liquide par convection thermosolutale, à solide fixe et en absence de retrait à la solidification ($\langle \rho \rangle^s = \langle \rho \rangle^l$). Pour cela, nous introduisons dans un premier temps les principaux schémas de résolution des équations Navier-Stokes selon la façon dont ils répondent aux critères de stabilité de Babuška-Brezzi : les éléments finis mixtes et la méthode multi-échelles variationnelle (Variational MultiScale).

En choisissant la seconde méthode, nous donnons les détails de la formulation éléments finis correspondante qui régit les écoulements dans la phase liquide loin du front de solidification, ainsi qu'au sein de la zone dendritique pâteuse. Le principal moteur de mouvement liquide est la convection thermosolutale. Celle-ci est générée par la densité du liquide qui varie à la fois avec la température et la composition intrinsèque de la phase liquide, contribuant ainsi à la redistribution des éléments d'alliage. On s'intéresse à ce type de méso-macroségrégation en montrant une application de solidification dirigée, traitée dans le chapitre 3 en diffusion pure. Nous montrons qu'en fin de solidification, les écoulements créent des canaux à forte ségrégation positive en peau et dans le cœur de la pièce.

L'investigation de ce défaut fait ensuite l'objet d'une confrontation qualitative entre la simulation et une expérience de solidification. Cette dernière consiste en un banc de solidification dirigée d'un alliage d'indium-gallium à bas point de fusion. Un suivi en caméra rapide permet de suivre la formation de la microstructure en fonction du temps. Par le biais de la simulation, on teste d'abord la performance du modèle purement macroscopique, i.e. avec suivi indirect des structures et phases via leur fraction volumique. Les résultats montrent que les canaux de ségrégation sont visibles mais sont moins nombreux et moins stables que l'on prédit expérimentalement.

Ensuite, on rajoute au modèle précédent une couche de modélisation à l'échelle mésoscopique pour suivre directement les enveloppes des grains. Cette fois, la comparaison avec l'expérience montre que nous prédisons mieux qualitativement l'interaction complexe entre structure de solidification, l'écoulement au sein de la zone pâteuse et la ségrégation conséquente. Une étude paramétrique permet après d'étudier la sensibilité de l'occurrence et la forme des canaux ségrégés par rapport aux différents paramètres de contrôle du procédé.

Chapter 5

Macrosegregation with changing metal volume

Contents

5.1	Solidification shrinkage	96
5.2	Choice of boundary tracking	96
5.3	Multidomain formalism	98
5.3.1	Assumptions	98
5.3.2	Metal-Air boundary definition	100
5.4	FE partitioned model	101
5.4.1	In the metal	101
5.4.2	In the air	104
5.5	FE monolithic model	106
5.5.1	Mass and momentum conservation	106
5.5.2	Energy conservation	108
5.5.3	Species conservation	109
5.6	1D application: solidification with inverse segregation	111
5.6.1	Geometry and boundary conditions	111
5.6.2	Shrinkage without macrosegregation	112
5.6.3	Shrinkage with macrosegregation	120
5.7	2D application: controlled solidification benchmark	132
5.7.1	Computational configuration	132
5.7.2	Results	134
5.7.3	Mass conservation	136
5.8	3D application: reduced-gravity solidification	141
5.8.1	Previous work	141
5.8.2	Computational configuration	143
5.8.3	Texus binary alloy	149
5.8.4	Texus ternary and quaternary alloys	155

5.1 Solidification shrinkage

Solidification shrinkage is, by definition, the effect of relative density change between the liquid and solid phases. In general, it results in a progressive volume change during solidification, until the phase change has finished. The four stages in [figs. 5.1a](#) to [5.1d](#) depict the volume change with respect to solidification time. First, at the level of the first solid crust, near the local solidus temperature, the solid forms with a density greater than the liquid. The subsequent volume decrease forces the fluid to be sucked in the direction of the volume change (cf. [fig. 5.1b](#)). When this sucking becomes impossible due to a low permeability of the mush, voids may appear. As a direct result of the inward feeding flow, the ingot free surface with the air tends to gradually deform to follow the feeding direction, forming the so-called *shrinkage pipe*, shown in [fig. 5.2](#). Since the mass of the alloy and its chemical species is conserved, a density difference between the phases ($\langle \rho \rangle^l < \langle \rho \rangle^s \implies \frac{\langle \rho \rangle^l}{\langle \rho \rangle^s} < 1$) eventually leads to a different overall volume ($V^s < V^l$) once solidification is complete, as confirm the following mass conservation equations, from initial (LHS term) to final (RHS term) state:

$$\langle \rho \rangle^l V^l = \langle \rho \rangle^s V^s \quad (5.1a)$$

$$V^s = \frac{\langle \rho \rangle^l}{\langle \rho \rangle^s} V^l \quad (5.1b)$$

Solidification shrinkage is not the only factor responsible for volume decrease. Shrinkage due to temperature and composition variations in both solid and liquid phases, are also common causes in a casting process. Thermal shrinkage is very important to apprehend in steel casting, as the temperature decrease usually exceeds a 1000 °C between the solidus and ambient temperature. This causes substantial density variations.

5.2 Choice of boundary tracking

In chapter 2, several methods of boundary tracking/capturing methods were presented along with their similarities and differences. In the case of solidification shrinkage, the metal-air boundary can be tracked with any method from the previously mentioned. However, several reasons motivate us to settle on the level set method. First, the easiest solution is testing a method which already exists in the *CimLib* library. The level set method was implemented as a framework for monolithic resolution. Since this work, the method has been extensively used and improved in several projects mainly for multiphase flows, which is the main competence of the Computing and FLuids (C.FL.) group at CEMEF. Another motivation is the compatibility between *CimLib* and *THERCAST®*, where the latter is the final destination of the code developed during this Ph.D. thesis. In its recent versions, *THERCAST®* handles laminar and turbulent ingot filling where the level set method is used to capture the free surface of the molten metal. Aside from the practical motivations, some technical aspects of the level set method make it very attractive to address macroscopic surface tracking (in contrast to microscopic interface tracking, for instance the solid-liquid interface), such as topological properties that are readily available (e.g. curvature) and accurate position compared to volume-based methods like VOF [[Sethian 1999](#)].

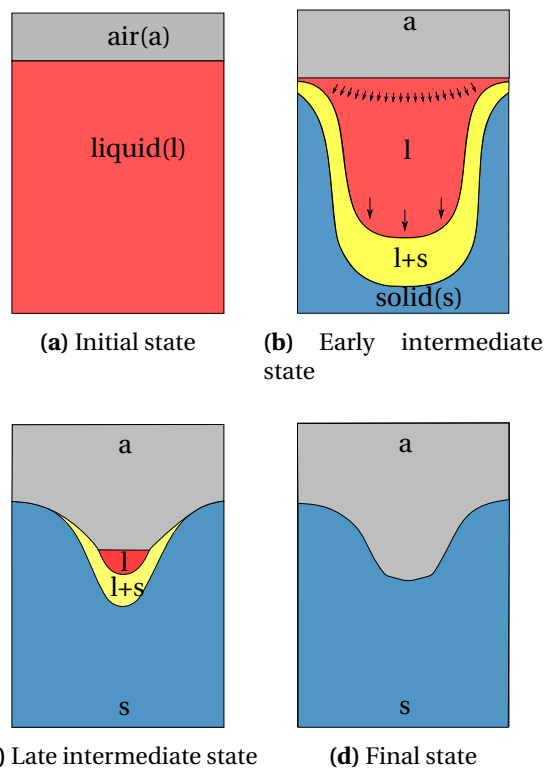


Fig. 5.1 – Schematic of the main cooling stages of an ingot against side and bottom mould walls (not shown)

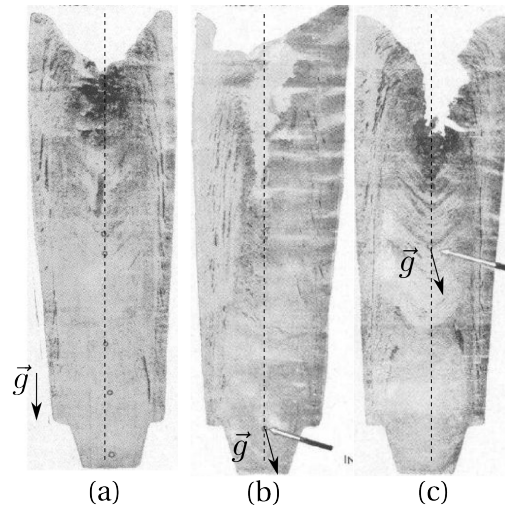


Fig. 5.2 – Sulphur prints of three low-carbon steel ingots showing pipe formation at the top as a result of solidification shrinkage, marked with dark areas corresponding to higher sulphur content, while varying ingot inclination during casting. Ingot orientation changes from (a) vertical position to (b) 25°-inclination after 34 minutes of vertical (dashed line) casting and finally (c) 25°-inclination after 3 hours of vertical casting. The white arrow indicates the inclination onset [Onodera and Arakida 1959]. The black arrow indicates the gravity direction.

5.3 Multidomain formalism

In the previous chapters, we considered in our simulations the metallic alloy as a saturated mixture of solid and liquid during solidification. It means that no gas phase was supposed to appear during the process. Additionally, we ignored shrinkage and expansion effects. These considerations resulted in a fixed interface between the free surface of the liquid metal and the surrounding air. As a consequence, air was not considered in the model. The reason is that we chose to describe our model in Eulerian description, for which we have considered a fixed grid to discretise the averaged conservation equations governing the phase change between the liquid and solid phases. With the introduction of shrinkage, an increase in global density of the metallic alloy means that a gas phase should enter the domain to replace the shrunk volume. At this point, several interfaces may be distinguished: liquid-solid ($l-s$), liquid-air ($l-a$) and solid-air ($s-a$), where we defined 2 phases (l and s) belonging to the "Metal" domain denoted M , while the "Air" domain, denoted A , is made up of a unique gas phase, (a), with the same name. As a standard for this formalism, we consider that upper case letters are used for domains, while lower case letters are used for phases.

The main idea behind the multidomain formalism is to go from the classic conservations equations introduced by volume averaging in chapter 2 in the context of a solidifying two-phase system to generalise it by taking into account a third gas phase, such as:

$$V^l + V^s + V^a = V_E \quad (5.2)$$

$$g^l + g^s + g^a = 1 \quad (5.3)$$

where g^ϕ is the volume fraction of each phase $\phi = [l, s, a]$. Then, one is free to choose a suitable numerical method to define and track the physical interfaces between the several phases. In our macroscale applications, we are particularly interested in keeping an indirect representation of the $l-s$ interface (dotted line in [fig. 5.3](#)) using the volume averaging theory, while employing a different method to track the metal-air ($M-A$) boundary ($l-a$ and $s-a$ interfaces, represented by dashed lines in [fig. 5.3](#)) with the level set method. This allows switching to the latter method in a physically representative manner.

In this context, each domain can be seen as a material having a physical interface with the other domains. As a consequence of our interpretation, the gas phase should not exist in the metal, which may naturally occur if the thermodynamic conditions are in favour of nucleating and growing a new phase, or in the case of a gas that was trapped inside mould grooves.

5.3.1 Assumptions

Each phase in the system has its own velocity, $\langle v \rangle^l$, $\langle v \rangle^s$ and $\langle v \rangle^a$, while the respective interfaces $l-s$, $l-a$ and $s-a$ have different and independent velocities, represented by v^{l-s} , v^{l-a} and v^{s-a} . Note that the solid-liquid interface velocity was denoted v^* in the previous chapters as no more than two phases were considered.

The first major assumption is that the solid phase, once formed from the liquid, is fixed and rigid, hence $\langle v \rangle^s = 0$. It means that no subsequent deformation or contraction/expansion of the solid phase ($\langle \rho \rangle^s = \text{constant}$) may occur and therefore v^{s-a} reduces to vector zero. Moreover, we use the already introduced volume averaging principles to write locally for any quantity

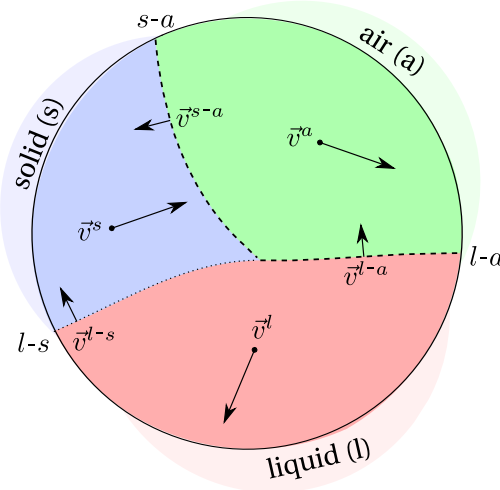


Fig. 5.3 – Schematic of a representative volume element containing 3 phases with distinct velocities, separated by 3 interfaces. The dotted line is the indirectly tracked solid-liquid interface while the other dashed lines, air-liquid and air-solid interfaces, are directly tracked.

ψ :

$$\langle \psi \rangle = \langle \psi^l \rangle + \langle \psi^s \rangle + \langle \psi^a \rangle \quad (5.4a)$$

$$= g^l \psi^l + g^s \psi^s + g^a \psi^a \quad (5.4b)$$

where volume fractions, g^ϕ , for each phase ϕ were used. Rappaz et al. [2003] define the volume fraction by writing a general expression inside the representative volume V_E :

$$g^\phi = \frac{1}{V_E} \int_{V_E} \chi^\phi(x, t) d\Omega = \langle \chi^\phi \rangle \quad (5.5)$$

where the integrated quantity is an indicator (or presence) function relative to phase ϕ , defined in chapter 2 by eq. (2.9).

Any phenomenon that may displace an interface, whether by phase change or a phase motion, is mathematically translated by variations of the presence function, such that its total derivative for each phase satisfies the following:

$$\frac{d\chi^\phi}{dt} = \frac{\partial \chi^\phi}{\partial t} + \mathbf{v}^* \cdot \nabla \chi^\phi = 0 \quad (5.6)$$

If we consider the liquid phase for instance, the variations of any quantity ψ are given by:

$$\langle \frac{\partial \psi^l}{\partial t} \rangle = \frac{\partial \langle \psi^l \rangle}{\partial t} - \frac{1}{V_E} \int_{\Gamma_{l-a}} \psi^l \mathbf{v}^{l-a} \cdot \mathbf{n}^{l-a} dA - \frac{1}{V_E} \int_{\Gamma_{l-s}} \psi^l \mathbf{v}^{l-s} \cdot \mathbf{n}^{l-s} dA \quad (5.7)$$

$$\langle \nabla \psi^l \rangle = \nabla \langle \psi^l \rangle + \frac{1}{V_E} \int_{\Gamma_{l-a}} \psi^l \mathbf{n}^{l-a} dA + \frac{1}{V_E} \int_{\Gamma_{l-s}} \psi^l \mathbf{n}^{l-s} dA \quad (5.8)$$

$$\langle \nabla \cdot \psi^l \rangle = \nabla \cdot \langle \psi^l \rangle + \frac{1}{V_E} \int_{\Gamma_{l-a}} \psi^l \cdot \mathbf{n}^{l-a} dA + \frac{1}{V_E} \int_{\Gamma_{l-s}} \psi^l \cdot \mathbf{n}^{l-s} dA \quad (5.9)$$

So far, we know that eq. (5.6) allows transporting an interface between 2 phases, or a more

generally a boundary between multiphase domains. We also know that [eqs. \(5.7\) to \(5.9\)](#) allow computing temporal and spatial variations of any physical quantity related to a phase or more generally a multiphase domain. To avoid ambiguity, we still have to establish a definition for the boundary between the metal and the air, i.e. which interfaces should be accounted for when considering the transport of the metal-air boundary.

5.3.2 Metal-Air boundary definition

In reality, between the metal and the air, two boundaries exist, as explained by [Niane \[2004\]](#). The liquid-air interface exists at early stages of solidification where only the free surface of the liquid is in contact with the air, as shows stage 1 in [fig. 5.4](#).

Stage 2 in [fig. 5.4](#) shows that the mushy zone boundary delimited by dendrite tips reaches the free liquid surface. Upon subsequent solidification, two distinct boundaries are created: a first boundary separating interdendritic liquid from the air, and a second boundary that separates the dendrite tips from the air, as illustrated in stage 3 of [fig. 5.4](#). In other words, a porous medium made up of solid+air settles between the mushy zone (solid+liquid) and the air domain. The lower part of the this porous medium is defined by the *l-a* interface and is driven by solidification shrinkage, as it was already the case during stages 1 and 2. Therefore, its real microscopic velocity is equal to the interdendritic liquid velocity, $\langle v \rangle^l$. According to [Dantzig and Rappaz \[2009\]](#), this velocity is constant when the solidification shrinkage and the isotherms velocity v_T are constant, as states the equation:

$$\langle v \rangle^l = -\beta_{SS} v_T \quad (5.10)$$

As for the upper part of porous medium, delimited by the *s-a* boundary, its motion could be induced by a mechanical deformation of the solid phase either due to thermal shrinkage/expansion or external mechanical stresses. The first factor is ubiquitous in any solidification process, while the second factor is process-dependent.

In the present work, we remind that the solid phase is assumed fixed and rigid, therefore we consider dendrites to be undeformable during their growth. Unfortunately, this assumption is contradictory with our current situation where the metal keeps shrinking, until an overlap of the transition zone (intersection of both domains, identified by H^{tr}) and the mushy zone takes place, as shown in [fig. 5.4](#) (second row, stage 3). At this point, both interfaces define the *M-A* boundary. Although it is necessary to track the *s-a* boundary also, the present work limited to considering the *l-a* interface as fully defining the metal-air boundary. Tracking the *s-a* interface adds complexity as an additional tracking method has to be used like a new level set with distinct numerical properties. This assumption will have some influence regarding the overall simulation performance, as some errors are induced, as the porous medium is not properly accounted for. Further discussions about the outcomes of our definition of the metal-air boundary are given in the 1D application section. With the previous definitions, [eq. \(5.6\)](#) can be recast with the level set method by using the smoothed Heaviside function in the metal:

$$\frac{dH^M}{dt} = \frac{\partial H^M}{\partial t} + \mathbf{v}^{M-A} \cdot \nabla H^M = 0 \quad (5.11a)$$

$$\frac{dH^M}{dt} = \frac{\partial H^M}{\partial t} + \mathbf{v}^{l-a} \cdot \nabla H^M = 0 \quad (5.11b)$$

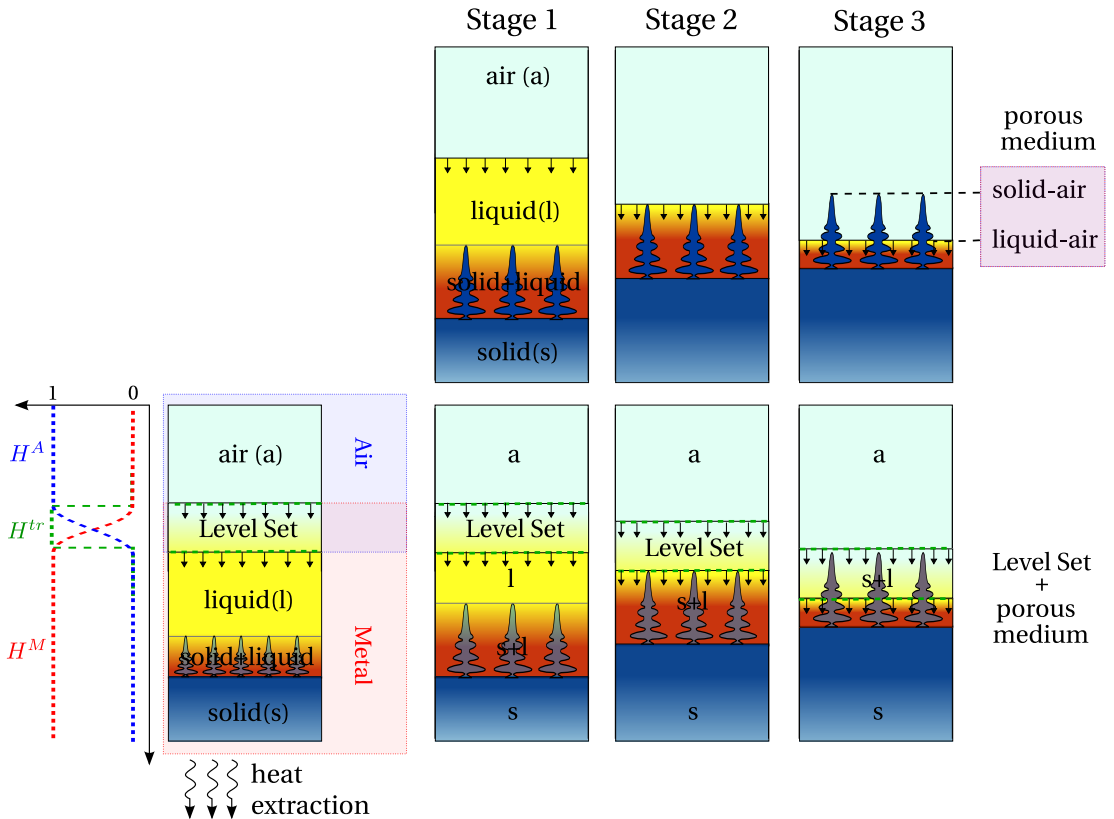


Fig. 5.4 – Schematic describing (first row) the physical solidification process and (second row) its numerical treatment of moving the boundary between air and metal domains, at three intermediate stages of solidification. H^M , H^A and H^{tr} are respectively the Heaviside functions for the metal, the air and the transition zone between both domains.

5.4 FE partitioned model

In this section, we start from the monodomain finite element model presented in [section 2.1.1](#) that was relevant to the metal only, referred to by the superscript M , then present the essential assumptions and formulations that allow predicting solidification shrinkage in a Eulerian context that introduces another domain, the air, referred to by the superscript A .

5.4.1 In the metal

Mass and momentum conservation

By assuming a fixed solid phase ($\langle v \rangle^s = 0$), i.e. a constant density for the solid phase without any transport of this phase, the average velocity in the metal reduces only to liquid's average velocity.

Therefore, we can write:

$$\langle v \rangle^M = \langle v^l \rangle + \langle v^s \rangle = g^l \langle v \rangle^l + g^s \langle v \rangle^s \quad (5.12)$$

With eq. (5.12), the mass balance in the metal writes:

$$\frac{\partial \langle \rho \rangle^M}{\partial t} + \nabla \cdot (\rho \mathbf{v})^M = 0 \quad (5.13a)$$

$$\frac{\partial \langle \rho \rangle^M}{\partial t} + \nabla \cdot (g^l \langle \rho \rangle^l \langle \mathbf{v} \rangle^l) = 0 \quad (5.13b)$$

$$\frac{\partial \langle \rho \rangle^M}{\partial t} + \langle \rho \rangle^l \nabla \cdot (g^l \langle \mathbf{v} \rangle^l) + g^l \langle \mathbf{v} \rangle^l \cdot \nabla \langle \rho \rangle^l = 0 \quad (5.13c)$$

$$\nabla \cdot \langle \mathbf{v}^l \rangle = -\frac{1}{\langle \rho \rangle^l} \left(\frac{\partial \langle \rho \rangle^M}{\partial t} + \langle \mathbf{v}^l \rangle \cdot \nabla \langle \rho \rangle^l \right) \quad (5.13d)$$

Equation (5.13d) explains the flow due to shrinkage. A negative divergence term means that a liquid feeding is necessary to compensate for a density increase upon solidification, where $\langle \rho \rangle^s > \langle \rho \rangle^l$ in the transient term, hence acting as a flow driving force in the melt. The second RHS term accounts for the volume change due to heat and species variations in the liquid. When the metal's density was considered constant during solidification, the assumption of an incompressible system made it possible to use the Boussinesq approximation. However, in the case of solidification shrinkage, the average density $\langle \rho \rangle^M$ varies, as it depends on the solidification path as well as on $\langle \rho \rangle^s$ and $\langle \rho \rangle^l$ which are not equal nor constant. Therefore, the incompressibility condition is no more applicable. In such case, the earlier given system eq. (2.45) is reformulated without any reference value for density and assuming a fixed solid phase:

$$\begin{cases} \rho_0^l \left(\frac{\partial \langle \mathbf{v}^l \rangle}{\partial t} + \frac{1}{g^l} \nabla \cdot (\langle \mathbf{v}^l \rangle \times \langle \mathbf{v}^l \rangle) \right) = \\ -g^l \nabla p^l - 2\mu^l \nabla \cdot (\bar{\nabla} \langle \mathbf{v}^l \rangle + \bar{\nabla}^t \langle \mathbf{v}^l \rangle) - g^l \mu^l \mathbb{K}^{-1} \langle \mathbf{v}^l \rangle + g^l \langle \rho \rangle^l \mathbf{g} \\ \nabla \cdot \langle \mathbf{v}^l \rangle = -\frac{1}{\langle \rho \rangle^l} \left(\frac{\partial \langle \rho \rangle^M}{\partial t} + \langle \mathbf{v}^l \rangle \cdot \nabla \langle \rho \rangle^l \right) \end{cases} \quad (5.14)$$

Energy conservation

In the energy equation, a volumetric source term accounts for the heat dissipation caused by the shrinking metal volume. Before writing the new equation, we make the following assumptions:

- consequence of the static solid phase: $\langle \rho h \mathbf{v} \rangle^M = g^l \langle \rho \rangle^l \langle h \rangle^l \langle \mathbf{v} \rangle^l + \underline{g^s \langle \rho \rangle^s \langle h \rangle^s \langle \mathbf{v} \rangle^s}$,
- the heat generated by mechanical deformation, $\mathbb{S} : \dot{\epsilon}$, is neglected.

The unknowns in the energy conservation are the average volumetric enthalpy $\langle \rho h \rangle^M$ and temperature T . The energy conservation equation writes:

$$\frac{\partial \langle \rho h \rangle^M}{\partial t} + \nabla \cdot (\rho \mathbf{v})^M = \nabla \cdot (\langle \kappa \rangle^M \nabla T) \quad (5.15a)$$

$$\frac{\partial \langle \rho h \rangle^M}{\partial t} + \nabla \cdot (g^l \langle \rho \rangle^l \langle h \rangle^l \langle \mathbf{v} \rangle^l) = \nabla \cdot (\langle \kappa \rangle^M \nabla T) \quad (5.15b)$$

$$\frac{\partial \langle \rho h \rangle^M}{\partial t} + \langle \mathbf{v}^l \rangle \cdot \nabla (\langle \rho \rangle^l \langle h \rangle^l) = \nabla \cdot (\langle \kappa \rangle^M \nabla T) - \langle \rho \rangle^l \langle h \rangle^l \nabla \cdot \langle \mathbf{v}^l \rangle \quad (5.15c)$$

$$\frac{\partial \langle \rho h \rangle^M}{\partial t} + \langle \mathbf{v}^l \rangle \cdot \nabla (\langle \rho \rangle^l \langle h \rangle^l) = \nabla \cdot (\langle \kappa \rangle^M \nabla T) + \langle h \rangle^l \left(\frac{\partial \langle \rho \rangle^M}{\partial t} + \langle \mathbf{v}^l \rangle \cdot \nabla \langle \rho \rangle^l \right) \quad (5.15d)$$

The second term in the RHS of eq. (5.15d) is a heat power (of unit Wm^{-3}) that adds to the system in the liquid phase (if $\langle \rho \rangle^l$ is not constant) as well as in the mushy zone (if $\langle \rho \rangle^l$ and $\langle \rho \rangle^s$ are not equal). This term is proportional to the solidification rate and expresses the heat generated in regions where the average density is changing and/or a gradient of liquid density is being advected.

Species conservation

The last conservation principle is applied to the chemical species or solutes. This principle allows predicting macrosegregation when applied to a solidification system, along with the mass, momentum and energy balances. However, the conservation equation should be reformulated in the case of a melt flow driven by shrinkage. Considered assumptions are:

- the solidification path is tabulated using thermodynamic data at equilibrium,
- the macroscopic solute diffusion coefficient D^s in the solid phase is neglected in the mass diffusive flux term,
- consequence of the static solid phase: $\langle \rho w \mathbf{v} \rangle^M = g^l \langle \rho \rangle^l \langle w \rangle^l \langle \mathbf{v} \rangle^l + \cancel{g^s \langle \rho \rangle^s \langle w \rangle^s \langle \mathbf{v} \rangle^s}$.

The species conservation presents similarities with the energy conservation formulated in the previous section. The main difference is the breakup of the volumetric variable $\langle \rho w \rangle^M$ into a product of density $\langle \rho \rangle^M$ and the mass composition $\langle w \rangle^M$ in the transient term.

For a binary alloy, we write:

$$\frac{\partial \langle \rho w \rangle^M}{\partial t} + \nabla \cdot (\rho w \mathbf{v})^M - \nabla \cdot (\langle \langle D \rangle^l \rangle \nabla (\langle \rho \rangle^l \langle w \rangle^l)) = 0 \quad (5.16a)$$

$$\langle \rho \rangle^M \frac{\partial \langle w \rangle^M}{\partial t} + \langle w \rangle^M \frac{\partial \langle \rho \rangle^M}{\partial t} + \nabla \cdot (g^l \langle \rho \rangle^l \langle w \rangle^l \langle \mathbf{v} \rangle^l) - \nabla \cdot (g^l \langle D \rangle^l \nabla (\langle \rho \rangle^l \langle w \rangle^l)) = 0 \quad (5.16b)$$

$$\begin{aligned} \langle \rho \rangle^M \frac{\partial \langle w \rangle^M}{\partial t} + \langle w \rangle^M \frac{\partial \langle \rho \rangle^M}{\partial t} &+ (\langle \rho \rangle^l \langle w \rangle^l) \nabla \cdot \langle \mathbf{v}^l \rangle + \langle \mathbf{v}^l \rangle \cdot \nabla (\langle \rho \rangle^l \langle w \rangle^l) \\ &- \nabla \cdot (g^l \langle D \rangle^l \nabla (\langle \rho \rangle^l \langle w \rangle^l)) = 0 \end{aligned} \quad (5.16c)$$

The mass balance, eq. (5.13d), gives the following relation when the liquid density is constant:

$$\nabla \cdot \langle \mathbf{v}^l \rangle = -\frac{1}{\langle \rho \rangle^l} \left(\frac{\partial \langle \rho \rangle^M}{\partial t} \right) \quad (5.17)$$

If we use the result of eq. (5.17) in eq. (5.16c), then we get the following equation:

$$\langle \rho \rangle^M \frac{\partial \langle w \rangle^M}{\partial t} + \langle w \rangle^M \frac{\partial \langle \rho \rangle^M}{\partial t} = \langle w \rangle^l \frac{\partial \langle \rho \rangle^M}{\partial t} - \langle \mathbf{v}^l \rangle \cdot \nabla (\langle \rho \rangle^l \langle w \rangle^l) + \nabla \cdot (g^l \langle D \rangle^l \nabla (\langle \rho \rangle^l \langle w \rangle^l)) \quad (5.18)$$

Applying Voller-Prakash [Voller et al. 1989] variable splitting, the system ends up with only one variable, $\langle w \rangle^M$. The splitting is done as follows:

$$\langle w \rangle^l = (\langle w \rangle^l)^t + \langle w \rangle^M - (\langle w \rangle^M)^t \quad (5.19)$$

where the superscript t refers to the previous time step, and the absence of this superscript corresponds to the unknown variable at the next time step. The chemical species conservation writes, still assuming a constant liquid density:

$$\begin{aligned} & \cancel{\langle \rho \rangle^M \frac{\partial \langle w \rangle^M}{\partial t}} + \cancel{\langle w \rangle^M \frac{\partial \langle \rho \rangle^M}{\partial t}} = \\ & \cancel{\langle w \rangle^M \frac{\partial \langle \rho \rangle^M}{\partial t}} - \langle \rho \rangle^l \langle \mathbf{v}^l \rangle \cdot \nabla \langle w \rangle^M + \nabla \cdot (g^l \langle \rho \rangle^l \langle D \rangle^l \nabla \langle w \rangle^M) \\ & + \frac{\partial \langle \rho \rangle^M}{\partial t} \left[(\langle w \rangle^l)^t - (\langle w \rangle^M)^t \right] - \langle \rho \rangle^l \langle \mathbf{v}^l \rangle \cdot \nabla \left((\langle w \rangle^l)^t - (\langle w \rangle^M)^t \right) \\ & - \nabla \cdot \left[g^l \langle \rho \rangle^l \langle D \rangle^l \nabla \left((\langle w \rangle^M)^t - (\langle w \rangle^l)^t \right) \right] \end{aligned} \quad (5.20)$$

$$\begin{aligned} & \langle \rho \rangle^M \frac{\partial \langle w \rangle^M}{\partial t} + \langle \rho \rangle^l \langle \mathbf{v}^l \rangle \cdot \nabla \langle w \rangle^M - \nabla \cdot (g^l \langle \rho \rangle^l \langle D \rangle^l \nabla \langle w \rangle^M) = \\ & - \frac{\partial \langle \rho \rangle^M}{\partial t} \left[(\langle w \rangle^M)^t - (\langle w \rangle^l)^t \right] \\ & + \langle \rho \rangle^l \langle \mathbf{v}^l \rangle \cdot \nabla \left((\langle w \rangle^M)^t - (\langle w \rangle^l)^t \right) - \nabla \cdot \left[g^l \langle \rho \rangle^l \langle D \rangle^l \nabla \left((\langle w \rangle^M)^t - (\langle w \rangle^l)^t \right) \right] \end{aligned} \quad (5.21)$$

It is noted that eq. (5.21) is valid only if both densities $\langle \rho \rangle^l$ and $\langle \rho \rangle^s$ are constant but have different values. Since density changes are incorporated in this equation, inverse segregation following solidification shrinkage could be predicted. For the case where macrosegregation is solely due to fluid flow generated by natural or forced convection, i.e. no shrinkage occurs whether due to thermal-solutal contraction or phase change, the overall volume remains constant, hence density will be constant.

5.4.2 In the air

The presence of an air domain in our approach is important to follow the free surface of the solidifying metal. For this particular reason, some assumptions are introduced and explained in this section in order to limit unnecessary treatment within the air, since it does not undergo phase change. It should be reminded that we consider air as a single-phase system, hence superscripts A and a are interchangeably used.

Mass and momentum conservation

To simplify fluid flow resolution in the air, we consider it as incompressible. Therefore, the free metal surface is not disturbed by air flow in its vicinity, but only by shrinkage flow in the liquid metal. With the incompressibility of air, we are saying that any deformation of the free surface is solely due to an air mass increase, coming from the system boundaries. The mass balance hence writes:

$$\nabla \cdot \langle v \rangle^A = \nabla \cdot \langle v \rangle^a = 0 \quad (5.22)$$

The air flow is governed by time-dependent incompressible Navier-Stokes equations, as previously done for the metal:

$$\begin{cases} \langle \rho \rangle^a \left(\frac{\partial \langle v \rangle^a}{\partial t} + \nabla \cdot (\langle v \rangle^a \times \langle v \rangle^a) \right) = \\ - \nabla p^a - 2\mu^a \nabla \cdot (\bar{\nabla} \langle v \rangle^a + \bar{\nabla}^t \langle v \rangle^a) + \langle \rho \rangle^a g \\ \nabla \cdot \langle v \rangle^a = 0 \end{cases} \quad (5.23)$$

The air density $\langle \rho \rangle^a$ is considered constant along the casting process, therefore thermal gradients in the air that arise due to the low thermal conductivity, do not generate any flow, i.e. no Boussinesq approximation is made on the term $\langle \rho \rangle^a g$ in [eq. \(5.23\)](#).

Energy conservation

It was mentioned in the introduction of the current section that air is a single-phase system that cannot undergo any phase change. Therefore, heat transfer in this domain simplifies to thermal convection and thermal conduction with a low thermal conductivity coefficient, $\langle \kappa \rangle^a$, for a single gas phase. The energy balance governs the air enthalpy $\langle \rho h \rangle^A$ (which is equal to $\langle \rho \rangle^a \langle h \rangle^a$ in the current context) as follows:

$$\frac{\partial \langle \rho h \rangle^A}{\partial t} + \nabla \cdot \langle \rho h v \rangle^A = \nabla \cdot (\langle \kappa \rangle^A \nabla T) \quad (5.24a)$$

$$\frac{\partial \langle \rho h \rangle^A}{\partial t} + \nabla \cdot (\langle \rho \rangle^a \langle h \rangle^a \langle v \rangle^a) = \nabla \cdot (\langle \kappa \rangle^a \nabla T) \quad (5.24b)$$

$$\frac{\partial \langle \rho h \rangle^A}{\partial t} + \langle v \rangle^a \cdot \nabla (\langle \rho \rangle^a \langle h \rangle^a) = \nabla \cdot (\langle \kappa \rangle^a \nabla T) \quad (5.24c)$$

Species conservation

The composition of alloying elements is a crucial quantity to predict in this work. Nevertheless, such prediction is only relevant with metallic species, even if the air is also made up of other chemical species (e.g. nitrogen, oxygen ...). While the other conservation equations (energy, mass and momentum) are important to be solved in the air, the species conservation equation brings no added value to the model when solved in this domain. It may even cause the composition values (i.e. the equation solution) to be unstable near the *M-A* boundary, where mixed properties may lead to unwanted solute transport in both directions across the boundary, hence causing cumulative errors. Therefore, we leave the species resolution in the air to be

included in the final monolithic model.

5.5 FE monolithic model

The monolithic model combines all conservation equations derived for metal and air in a unique set of equations, to be solved on a Eulerian mesh. This is done by multiplying each conservation equation relative to a domain, obtained in the previous section, by the corresponding Heaviside function then summing all terms, finally using the mixed properties to simplify notations. For each conservation equation, these mixed properties will be properly defined before writing the final monolithic equation.

5.5.1 Mass and momentum conservation

We define the metal+air average system velocity, $\langle v^F \rangle$, as an arithmetic mixing between each domain's relative average fluid velocity, i.e. the domain's own relative fluid phase velocity with respect to solid phases. In parallel, we also define $\langle v \rangle^F$ as the system's fluid intrinsic velocity, obtained by an arithmetic mixing between intrinsic velocities of domain fluids. In the present context, the metal domain consists of a single fluid phase (liquid) and solid phases that form in fixed and rigid structures (assuming that solidification results in undeformable columnar structures, without any free-to-move equiaxed structure). The air domain entirely consists of a fluid phase. With this notation, we express the monolithic mass balance as:

$$\nabla \cdot \langle v^F \rangle = \nabla \cdot (H^M \langle v \rangle^M + H^A \langle v \rangle^A) \quad (5.25)$$

$$\nabla \cdot \langle v^F \rangle = H^M \nabla \cdot \langle v \rangle^M + H^A \cancel{\nabla \cdot \langle v \rangle^A} + \cancel{\nabla H^M \cdot (\langle v \rangle^M - \langle v \rangle^A)} \quad (5.26)$$

$$\nabla \cdot \langle v^F \rangle = H^M \nabla \cdot \langle v^l \rangle \quad (5.27)$$

where we used the relation [eq. \(5.12\)](#) in the case of a fixed rigid solid to obtain [eq. \(5.27\)](#). As for the second term in [eq. \(5.26\)](#), we have made the assumption that air is incompressible, hence $\nabla \cdot \langle v \rangle^A = 0$. Therefore any volume variation of the metal domain, will trigger an air inflow or suction effect through the surface boundaries of the air domain. The third and last term in the same equation expresses a velocity jump at the interface. In our case, we neglect this contribution by assuming that both velocities tend to be equal when the interface thickness tends to zero.

Finally, using the monolithic mass balance [eq. \(5.13d\)](#), we get:

$$\nabla \cdot \langle v^F \rangle = H^M \left(-\frac{1}{\langle \rho \rangle^l} \left(\frac{\partial \langle \rho \rangle^M}{\partial t} + \langle v^l \rangle \cdot \nabla \langle \rho \rangle^l \right) \right) \quad (5.28)$$

In order to derive the monolithic momentum balance, we first define a fluid fraction, g^F , as an arithmetic mixing between liquid and air fractions across the interface:

$$g^F = H^M g^l + H^A g^a = H^M g^l + H^A \quad (5.29)$$

This quantity will be essential for the monolithic Darcy term. We have seen in the previous chapter that adding the Darcy term for the metallic alloy momentum equation modifies the shape of the latter, dividing all terms by the liquid fraction, g^l . The presence of this dissipation

term in one domain, obliges us to keep it in both domains but "deactivate" it where it is useless, i.e. in the air. This is done by computing a fictitious permeability in the air as function of the air fraction using the Carman-Kozeny model, as used previously for the metal in [eq. \(1.3\)](#). We may speak of level set mixing for the Darcy term. It has a double advantage:

1. the consistency in shape is kept between both domains equations, thus easily deriving the monolithic system;
2. since the monolithic system retains the shape of the monodomain equation, the VMS solver does not require further implementation updates and subsequent validation.

The first point implies that the Darcy term should also be added in the the air's momentum balance, but remains inactive by imposing a high permeability in the air, while having realistic values where needed, namely in the metal domain. The modified permeability, \tilde{K} , depends on the fluid fraction ([eq. \(5.29\)](#)) as follows:

$$\tilde{K} = \frac{\lambda_2^2 g^F}{180(1-g^F)^2} \quad (5.30)$$

Depending on the values of this quantity, the extent to which the Darcy becomes imposing in Navier-Stokes varies as follows:

- $\tilde{K}^{-1} \rightarrow 0$ (completely permeable), then Darcy's term is negligible in Navier-Stokes resolution,
- $\tilde{K}^{-1} > 0$ (slightly permeable), then fluid flow is greatly dissipated due to a decreasing permeability,
- $\tilde{K}^{-1} \rightarrow \infty$ (non permeable), then no fluid flow may exist.

These 3 cases are graphically represented in [fig. 5.5](#), showing the different values along with the transitions with respect to phases and domains distribution.

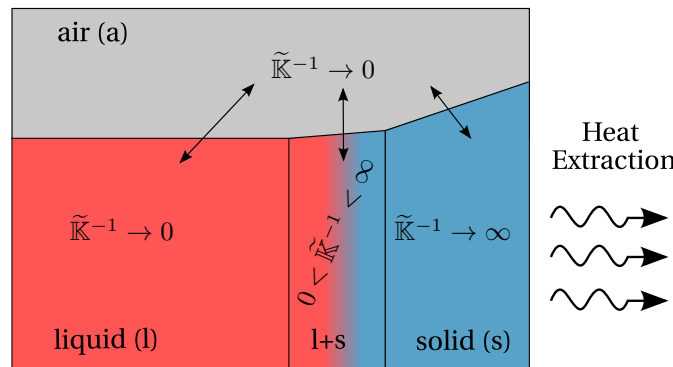


Fig. 5.5 – Schematic representation of an ingot undergoing solidification while shrinking. The inverse of the modified permeability, \tilde{K}^{-1} , falls to zero in the air and liquid phases, indicating that the Darcy term is only activated in the solid and liquid+solid regions. The arrows indicate three different transitions of the Darcy term between the air and metal domains.

As for the weight force in both domains, it is taken into account via [eq. \(5.33\)](#). The phase densities may vary as functions of other parameters such as temperature or phase composition ($\langle \rho \rangle^l$ depends on both), creating buoyancy forces of convection inside the fluid.

In our approach, since we are only interested in liquid's flow, we keep the air phase density $\langle \rho \rangle^a$ constant, so as to prevent a mixture of forces around the level set, which helps stabilise the fluid flow resolution. The mechanical properties are mixed as follows:

$$\text{Fluid density : } \widehat{\rho^F} = H^M \langle \rho \rangle^l + H^A \langle \rho \rangle^a \quad (5.31)$$

$$\text{Dynamic viscosity : } \widehat{\mu} = H^M \mu^l + H^A \mu^a \quad (5.32)$$

$$\text{Weight force : } \widehat{\rho g g} = H^M g^l \langle \rho \rangle^l \mathbf{g} + H^A g^a \langle \rho \rangle^a \mathbf{g} = H^M g^l \langle \rho \rangle^l \mathbf{g} + H^A \langle \rho \rangle^a \mathbf{g} \quad (5.33)$$

The momentum balance can now be obtained from $H^M \times \text{eq. (5.14)} + H^A \times \text{eq. (5.23)}$, after adapting [eq. \(5.23\)](#) to account for a fictitious Darcy term :

$$\left\{ \begin{array}{l} \widehat{\rho^F} \left(\frac{\partial \langle \mathbf{v}^F \rangle}{\partial t} + \frac{1}{g^F} \nabla \cdot (\langle \mathbf{v}^F \rangle \times \langle \mathbf{v}^F \rangle) \right) = \\ - g^F \nabla p - 2\widehat{\mu} \nabla \cdot \left(\overline{\nabla} \langle \mathbf{v}^F \rangle + \overline{\nabla^t} \langle \mathbf{v}^F \rangle \right) - g^F \widehat{\mu} \widetilde{\mathbb{K}}^{-1} \langle \mathbf{v}^F \rangle + \widehat{\rho g g} \\ \nabla \cdot \langle \mathbf{v}^F \rangle = H^M \left(-\frac{1}{\langle \rho \rangle^l} \left(\frac{\partial \langle \rho \rangle^M}{\partial t} + \langle \mathbf{v}^l \rangle \cdot \nabla \langle \rho \rangle^l \right) \right) \end{array} \right. \quad (5.34)$$

5.5.2 Energy conservation

To write the monolithic energy conservation equation, we are interested in [eqs. \(5.15d\)](#) and [\(5.24c\)](#). Mixed quantities from these equations are defined by:

$$\text{Total enthalpy : } \widehat{\langle \rho h \rangle} = H^M \langle \rho h \rangle^M + H^A \langle \rho h \rangle^A \quad (5.35)$$

$$\text{Fluid phases enthalpy : } \widehat{\langle \rho h \rangle^F} = H^M \langle \rho \rangle^l \langle h \rangle^l + H^A \langle \rho \rangle^a \langle h \rangle^a \quad (5.36)$$

$$\text{Average thermal conductivity : } \widehat{\langle \kappa \rangle} = H^M \langle \kappa \rangle^M + H^A \langle \kappa \rangle^A \quad (5.37)$$

$$\text{Fluid heat change due to shrinkage : } \widehat{\Phi^F} = H^M \langle \rho \rangle^l \langle h \rangle^l \nabla \cdot \langle \mathbf{v}^l \rangle \quad (5.38)$$

where [eq. \(5.35\)](#) will be used to predict the transient change in the system's global enthalpy, [eq. \(5.36\)](#) for the fluid-transported enthalpy in both domains while [eq. \(5.37\)](#) expresses the global energy conduction in the system. The last equation, [eq. \(5.38\)](#), is only present in the domain whose volume is changing, that is the metal in our case. Using the mixed thermophysical properties, [eqs. \(5.15d\)](#) and [\(5.24c\)](#) can now be mixed to obtain:

$$\frac{\partial \widehat{\langle \rho h \rangle}}{\partial t} + \langle \mathbf{v}^F \rangle \cdot \nabla \widehat{\langle \rho h \rangle^F} = \nabla \cdot \left(\widehat{\langle \kappa \rangle} \nabla T \right) + \widehat{\Phi^F} \quad (5.39)$$

The solution of [eq. \(5.39\)](#) is $\widehat{\langle \rho h \rangle}$, a mixed field between both domains average volumetric enthalpies.

Using the current approach for the energy, any motion of the *M-A* boundary is energetically translated into a phase change between the air phase on one side and the metallic phases on the other side. [Chen \[2014\]](#) tackled this problem by reformulating the energy equation with the smoothed Heaviside functions in order to prevent this purely numerical phenomenon. However in the current work, we prefer avoiding this numerical artefact by using the same tabulated phase enthalpy properties (or specific heat if the tabulation approach is not used)

for the air and the liquid phase. This assumption made on only for the *l-a* is compatible with definition of the mobile *M-A* boundary made in [section 5.3.2](#).

5.5.3 Species conservation

Unlike monolithic energy conservation which applies to whole metal+air system, the monolithic species conservation equation is dedicated to the transport of *metallic* chemical species, meaning that the air does not contain any metallic species to be transported. This physical specificity leaves us with two main resolution strategies:

Monolithic strategy: we combine two species conservation equations into a single monolithic equation. We compute the conservation of chemical species in both the metal and the air, considering the latter as a *fictitious metal*. We apply the same mixing technique used to formulate [eq. \(5.39\)](#), based on the monodomain species conservation equation used without level set, [eq. \(2.30\)](#). The relevant mixed quantities are defined as follows:

$$\text{Fluid phases composition : } \widehat{(\rho w)^F} = H^M \langle \rho \rangle^l \langle w \rangle^l + H^A \langle \rho \rangle^a \langle w \rangle^a \quad (5.40)$$

$$\text{Average solute diffusion : } \widehat{\langle D \rangle^F} = H^M g^l \langle D \rangle^l + H^A g^a \langle D \rangle^a \quad (5.41)$$

$$\text{Fluid composition change due to shrinkage : } \widehat{\Psi^F} = H^M \langle \rho \rangle^l \langle w \rangle^l \nabla \cdot \langle v^l \rangle \quad (5.42)$$

The corresponding monolithic equation is given by:

$$\widehat{\langle \rho \rangle} \frac{\partial \widehat{\langle w \rangle}}{\partial t} + \langle v^F \rangle \cdot \nabla \widehat{(\rho w)^F} = \nabla \cdot \left(\widehat{\langle D \rangle^F} \nabla \widehat{(\rho w)^F} \right) + \widehat{\Psi^F} \quad (5.43)$$

where $\widehat{\langle w \rangle}$ is the mixed average composition solution for the whole domain.

Then, we control solute transport between both domains by proposing two monolithic resolution techniques, based on the treatment of solute diffusive and advective transport in the air domain:

1. **Monolithic with low solute diffusion (MD):** a very low macroscopic solute diffusion coefficient is used, at most a thousand times less than its value in the melt, $\langle D \rangle^a \ll \langle D \rangle^l$. The low solute diffusion in the air may not completely ensure a zero solute flux at the *M-A* boundary, but it helps maintaining a weak diffusive transport,
2. **Monolithic with low solute diffusion and low solute advection (MDA):** the computed fluid velocity, $\langle v^F \rangle$, is post-processed to be zero in the species equation for the air, thus suppressing the advective solute transport term influence which can be more important than the diffusive transport.

In both cases, the initial air average composition (which is equal to the composition of the air phase in our case) should normally be set to zero. However, this initialisation creates a composition gradient across the *M-A* boundary, creating a driving force for diffusion. Another option would be initialising both domains to the same value, $\langle w_0 \rangle^M = \langle w_0 \rangle^A$. This has the advantage of keeping solutal gradients to the lowest during the boundary motion and delaying as much as possible the occurrence of artificial solute transport, until the *s-a* interface forms gradually.

Non-monolithic (NM) strategy: this strategy aims to avoid the difficulty of dealing with a *fictitious* solute equation for the air. This is done by considering only the metal's species conservation equation, [eq. \(5.21\)](#). The solution of the latter is the metal's average composition, $\langle w \rangle^M$. From this solution, we determine the monolithic composition value, $\widehat{\langle w \rangle}$, :

$$\widehat{\langle w \rangle} = H^M \langle w \rangle^M + H^A \langle w_0 \rangle^M \quad (5.44)$$

where we directly initialise the composition in the air to the metal's nominal composition. This strategy has the advantage of being simpler, especially that we do not have to deal with density terms (which can be seen for example in [eq. \(5.21\)](#)) as dictates the previous monolithic strategy, knowing that air density remains constant in this work.

In the next section, we present a simple 1D solidification case with solidification shrinkage, in which we test the segregation results given by each strategy.

5.6 1D application: solidification with inverse segregation

5.6.1 Geometry and boundary conditions

A simple but very efficient way of analysing the model is to test it through a 1D flow configuration with energy and species conservation. For this purpose, we take an aluminium-silicon alloy with the properties shown in [table 5.1](#).

Table 5.1 – Parameters for the 1D inverse segregation test case with a binary Al-7 wt.% Si alloy.

Parameter	Symbol	Value	Unit
Nominal composition	w_0	7	wt.%
Liquid density	$\langle \rho \rangle^l$	2600	kg m^{-3}
Solid density	$\langle \rho \rangle^s$	2800	kg m^{-3}
Air density	$\langle \rho \rangle^a$	1.3	kg m^{-3}
Liquid viscosity	μ^l	10^{-3}	Pa s
Air viscosity	μ^a	10^{-4}	Pa s
Liquid heat capacity	c_p^l	1000	$\text{J kg}^{-1} \text{K}^{-1}$
Solid heat capacity	c_p^s	928.57	$\text{J kg}^{-1} \text{K}^{-1}$
Air heat capacity	c_p^a	1000	$\text{J kg}^{-1} \text{K}^{-1}$
Enthalpy of fusion	l_f	365 384	J kg^{-1}
Thermal conductivity	κ	70	$\text{W m}^{-1} \text{K}^{-1}$
Heat transfer coefficient	h_{ext}	500	$\text{W m}^{-2} \text{K}^{-1}$
External temperature	T_{ext}	100	$^{\circ}\text{C}$
Initial temperature	T_0	800	$^{\circ}\text{C}$
FE mesh size		table 5.2	m
Time step	Δt	table 5.3	s
Convergence criterion (residual)	ε_R	10^{-5}	—
Convergence criterion (temperature)	ε_T	10^{-2}	K

The rectangular 2D mesh having the dimensions $0.14 \text{ m} \times 0.001 \text{ m}$, consists of metal and air. Initially the air column's height is only 0.04 m and the remainder of the length is the metal. [Figure 5.6](#) shows the geometry and boundary conditions used for the simulations in this section. In the same figure, the thermal and mechanical boundary conditions are shown. In the latter, velocity-slip conditions were imposed on the lateral boundaries while a no-slip was used at the bottom where heat is extracted, and a free-velocity condition is set at the top of the domain, to ensure a 1D air flow from the top air inlet.

In this case, imposing slip conditions on lateral sides is two-fold: on one hand, we need to ensure that the fluid flow solution remains one-dimensional, hence symmetry on the boundaries solves the issue, while on the other hand during solidification, the resulting feeding flow should be able to transport the interface intersecting with boundary nodes. If boundary velocities are zero, then the interface transport will face problems at these boundary nodes. This is indeed an important and relevant point in the next 2D test case.

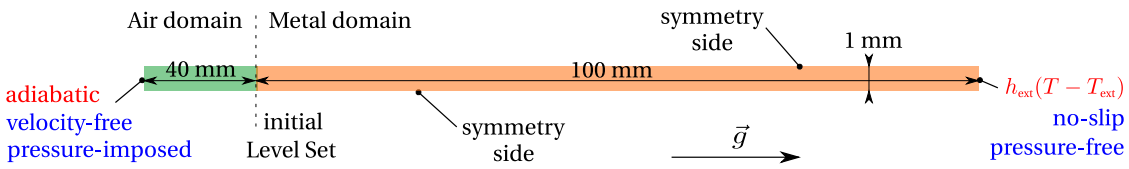


Fig. 5.6 – Computational configuration for the 1D inverse segregation case showing the domain geometry with the applied boundary conditions to it as well as the gravity vector. The symmetry sides represent the following set of boundary conditions: adiabatic, zero normal velocity, free tangential velocity and pressure-free. The boundary pressure of the air domain is imposed to atmospheric pressure.

5.6.2 Shrinkage without macrosegregation

The first simulation is for solidification without any segregation, hence a unique solidification path is considered at $w_0 = 7$ wt.%, shown in [fig. 5.8](#). This case is interesting as a reference case, where we can study volume shrinkage and level set behaviour in a simple segregation-free configuration. We first use a homogeneous isotropic mesh of constant size $h = 200 \mu\text{m}$ then the domain is remeshed before any resolution, as shown in [fig. 5.7](#). The remeshing parameters are given in [table 5.2](#). The liquid and solid phase densities are assumed constant.

Before solidification onset, almost no fluid flow occurs in the liquid metal, while air enter and leaves the domain without changing the level set position. As soon as solidification takes place, the average metal density increases, hence the metal volume starts decreasing by a downward level set motion. In the metal, a unidirectional flow results from the suction effect in the mushy zone. Results show however that the interface stability is compromised by a chosen time step for a given mesh size, and that the interface dynamics requires attention even before investigating the feeding flow created by solidification. As a demonstration, [fig. 5.9](#) shows the effect of different time steps with the same adaptive meshing parameters. For time steps greater than 0.01 s, Navier-Stokes computations did not converge resulting in a high artificial flow quickly destabilising the interface. It should be noted that the frame corresponding to 0.02 s was taken at an earlier time than the two other frames.

Table 5.2 – Summary of the mesh parameters used to generate an adaptive anisotropic mesh, along with the level set mixing thickness, ε . Refer to [section 2.6.2](#) for the definition of each mesh parameter.

Mesh parameter	Value
ε	$2.5 \times 10^{-4} \text{ m}$
h_n	$2.5 \times 10^{-5} \text{ m}$
h_τ	$2 \times 10^{-4} \text{ m}$
h_M	$1.5 \times 10^{-4} \text{ m}$
h_A	$2.5 \times 10^{-4} \text{ m}$
Remeshing frequency	0.1 s
Number of nodes	$\approx 7 \times 10^3$
Number of elements	$\approx 10^4$

Although no solidification has yet started at 100 s, a two-dimensional flow is observed around the interface, and tends to 10^{-8} m s^{-1} elsewhere in the ingot. [Figure 5.9](#) confirms that this flow is still predicted at smaller time steps. This flow seems like a pure numerical response to the

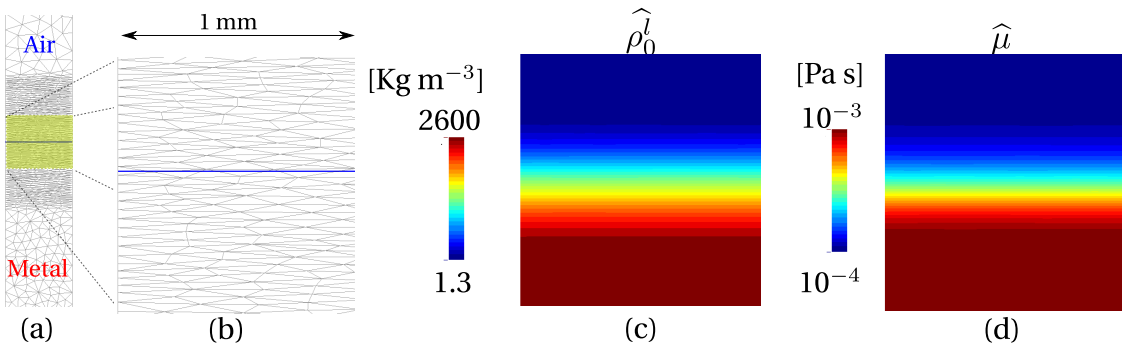


Fig. 5.7 – Snapshots of (a,b) the initial adapted mesh around the interface with different mesh sizes in the air and the metal. The adapted region is stretched beyond the level set mixing thickness to ensure better interpolation around the interface, in case of emergence of diffusion instabilities. To the right, (c) the reference fluid density and (d) viscosity are plotted in the transition zone. The thick blue line represents the zero iso-value of the distance function.

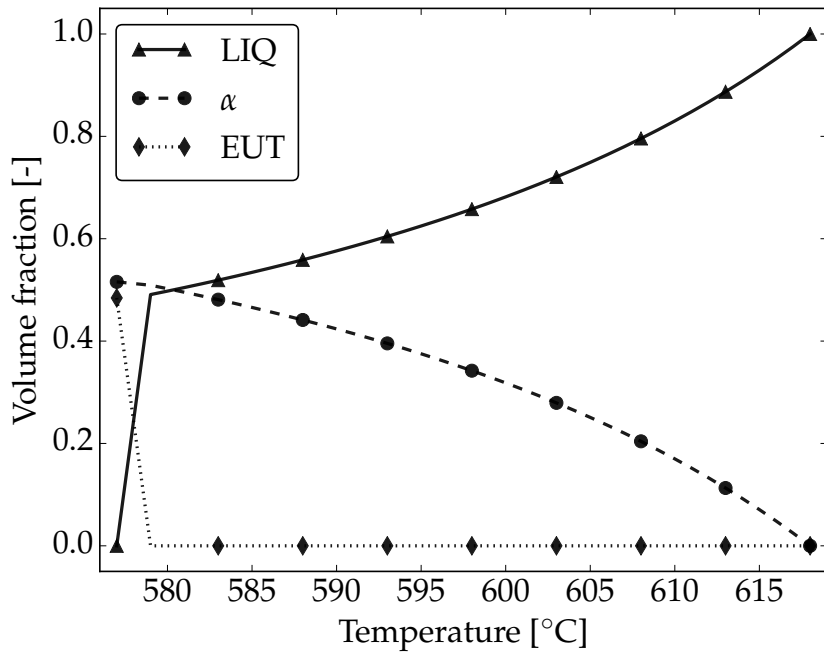


Fig. 5.8 – Unique solidification path at nominal composition for the shrinkage case without macrosegregation in Al-7 wt.% Si, showing the liquid phase, an aluminium-rich α phase (dendritic structure) and the eutectic structure.

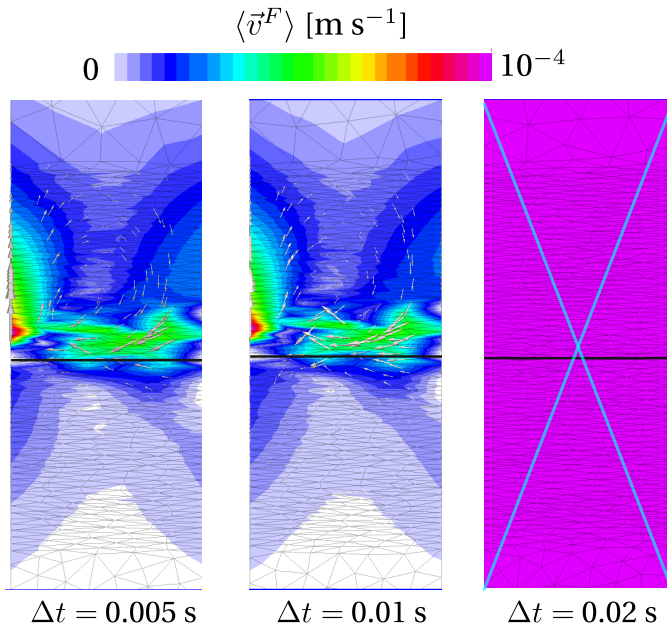


Fig. 5.9 – Three average fluid velocity frames at different time steps: 0.005 s, 0.01 s and 0.02 s. The first and second frame are taken after 50 seconds of cooling while for the last frame, the frame was taken after only 1 second of cooling, thus it is crossed to show non-convergence. The thick black line represents the zero isovalue of the distance function. Properties are given in [tables 5.1](#) and [5.3](#) under case “R”.

properties jump across the interface, namely density and dynamic viscosity. It is also noted that the interface position is not modified by the neighbouring currents, that reach a maximum magnitude of 10^{-4} m s^{-1} . Therefore, the optimal time step for this simulation is set to 0.01 s, and we refer to it as case R, which stands for "real" air.

The fact that properties transition is crucial in the solution stability, is investigated by 2 reference cases, having equal properties (density and dynamic viscosity) but with different time steps, 0.01 (case A1) and 0.1 s (case A2), where "A" stands for artificial. All simulation cases are grouped in [table 5.3](#).

Table 5.3 – Summary of the comparative shrinkage simulations without macrosegregation.

Case	Air viscosity [Pa s]	Air density [kg m^{-3}]	Time step [s]
R	10^{-4}	1.3	0.01
A1	10^{-3}	2600	0.01
A2	10^{-3}	2600	0.1

When the air domain is given the metal's properties, it becomes denser and more viscous by several orders of magnitude. [Figure 5.10](#), in which cases A1 and A2 are compared, shows no noticeable sign of velocity instability near the interface before 200 s. It can be explained by the fact that the air behaves mechanically like a fluid metal given similar properties, therefore no steep transitions are computed at the interface. However, it is interesting to compare results of [fig. 5.10a](#) and [fig. 5.10b](#) at 600 s. For case A1, the interface is slightly skewed due to slower flow at the left side of the interface, while for case A2, the flow disturbs the interface deforming it until the end of solidification, as seen at 1000 s. This shows the importance of the chosen time

step in the Navier-Stokes solver.

In contrast, [fig. 5.11b](#) shows more viable results as far as the level set transport is concerned. From 200 s to 800 s, the local flow instability (discussed earlier in [fig. 5.9](#)) is sustained, even until after solidification is complete. However, in regions of 100% metal and 100% air the computed velocity is nearly the same order of magnitude as predicted for all three simulations. Finally, in [fig. 5.11b](#), we notice a recirculating air flow in the vicinity of the interface as no metal shrinkage may further occur once solidification is complete, thus air flows freely in and out of the upper boundary with a very low magnitude ($\approx 10^{-7} \text{ m s}^{-1}$), while impinging on the metal-air surface. Regarding the CPU times, cases A1 ran for 14 hours, case A2 took only 2 hours while case R ran for 23.3 hours.

To summarise, we can see conclude from the previous results, the following points:

1. Greater differences in mechanical properties of fluids across the level set impose using smaller time steps,
2. When real properties are used, smaller time steps are needed to capture the variations across the moving level set, hence inducing longer simulation time,
3. In a situation where the flow dynamics in the non-metallic (gas) domain is not a primary objective, one can use artificial properties instead of the real values, hence gaining in computation time at the expense of the flow prediction accuracy.

Mass conservation study

In order to get a better idea about the performance of our model, a mass conservation study is performed hereafter. We define the metal's mass as a function of the metal's average density and the Heaviside function relative to the metal domain, as follows:

$$m^M = \int_{\Omega} H^M \langle \rho \rangle^M d\Omega \quad (5.45)$$

Then, the mass conservation can be monitored by processing [eq. \(5.45\)](#) at each time step, and computing the relative mass change by writing:

$$m_{\%}^M = \frac{m^M - m_0^M}{m_0^M} \times 100 \quad (5.46)$$

The relative mass change gives us information on the level set transport. As the current case is 1D and phase densities are constant throughout the simulation, mass conservation can be checked in a much simpler approach than by checking [eq. \(5.46\)](#). Since we know the initial metal's column length, l_0^M , and the expected solidification shrinkage is 7.14 %, we should expect a final length of $l_f^M = (1 - \beta_{SS}) l_0^M = 92.86 \text{ mm}$. In the previous section, we observed M-A boundary instability problems taking place around 400 s of cooling, where the flow begins slightly losing its one-dimensional shape. Although it was clearly seen in [fig. 5.10b](#), it applies for both cases, whether air properties are equal to (cases A1 and A2) or different than (case R) the liquid's properties across the interface. The mass variation plots in [fig. 5.12](#) confirm these observations, since the metal's mass does not remain constant during simulations. Indeed, in both cases A1 and R, the mass variation curves shown in [fig. 5.12](#) reveal a general behaviour of increase then decrease below zero. The increase corresponds to gain in metal mass. Such gain

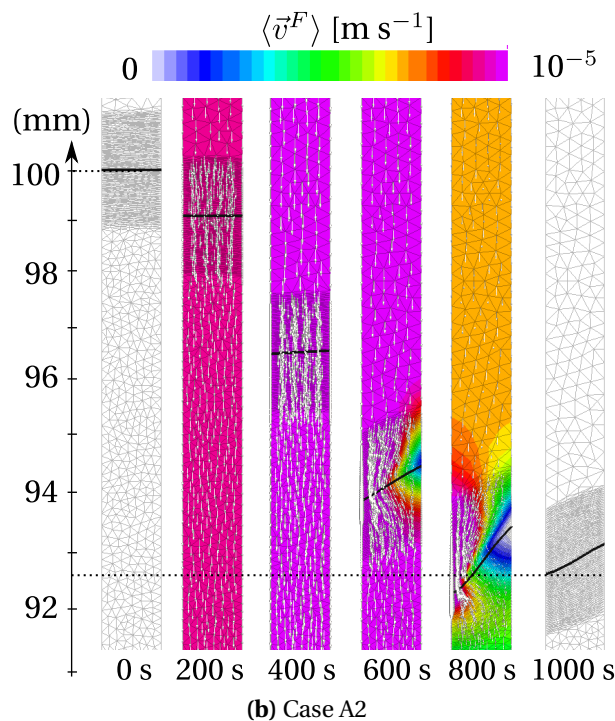
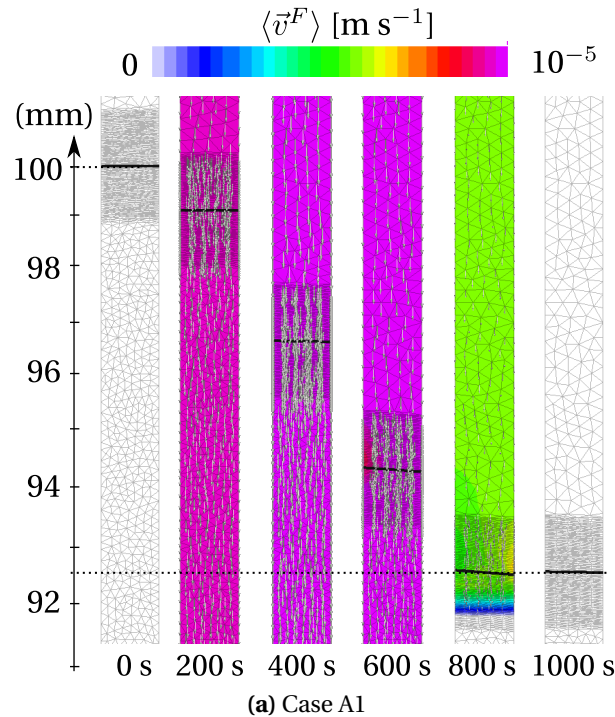


Fig. 5.10 – Comparison of two simulations at several stages of solidification ending shortly after 800 s. The results shows the influence of density and viscosity properties across the level set interface. The plotted field is the average fluid velocity, on which the corresponding nodal vectors are superimposed, mainly pointing downwards, i.e. towards the solidification front. The thick black line represents the zelue of the distance function. Properties are given in [tables 5.1 to 5.3](#).

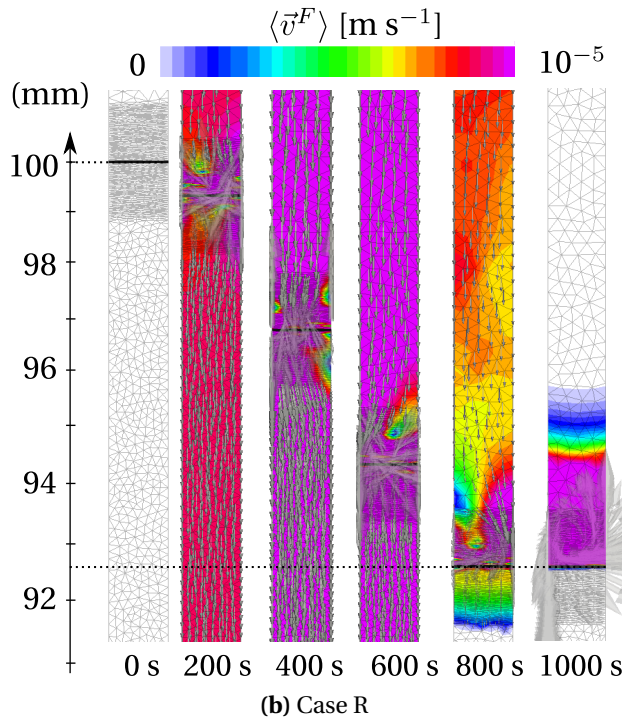
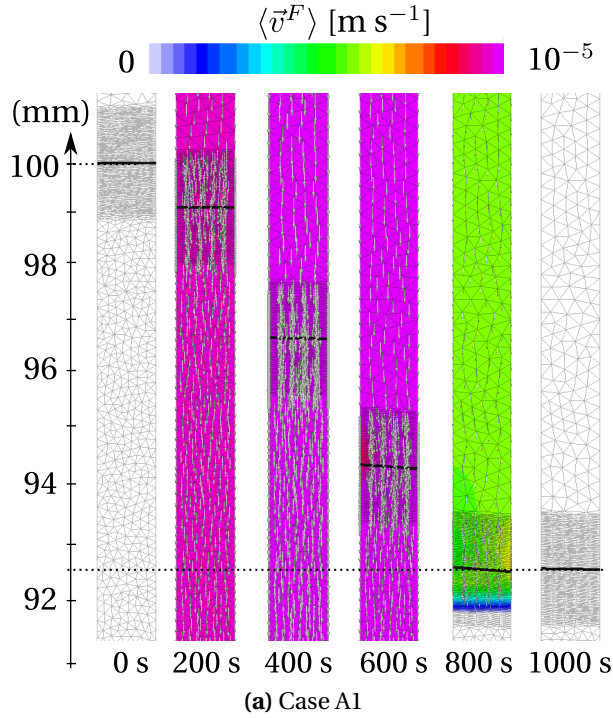


Fig. 5.11 – Comparison of two simulations at several stages of solidification ending shortly after 800 s. The results shows the influence of density and viscosity properties across the level set interface. The plotted field is the average fluid velocity, on which the corresponding nodal vectors are superimposed, pointing towards the solidification front. Properties are given in [tables 5.1](#) to [5.3](#).

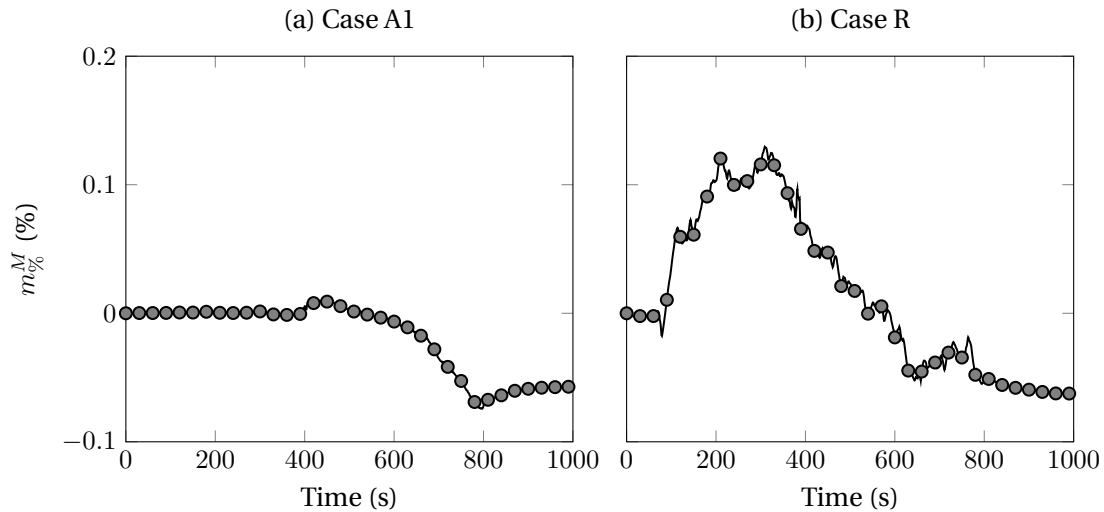


Fig. 5.12 – Variation of the metal's mass versus solidification time in cases A1 and R.

is the result of a limited motion of the level set while the metal density is increasing and the latter needs to shrink even more. The cause leading to the limited motion is not identified, no further testing was made. On the other hand, the decrease corresponding to a mass loss can be attributed to the contact between the mushy zone and the level set boundary. We showed in the introduction of this chapter that the *M-A* boundary actually consists of several interfaces, and when the mushy zone overlaps with the level set mixing zone, we cannot track the boundary between the porous medium (described in [fig. 5.4](#)), which induces concept errors.

In the light of these facts, we can try to limit as much as possible the motion of the porous medium boundaries, once the mushy zone has reached the level set mixing zone, and test the influence on mass conservation. To do so, we firstly advise to keep a very small thickness interface, in order to delay the previously explained overlap. Moreover, we deducing the transport velocity, used in the level set transport equation ([eq. \(2.60\)](#)), at each node as follows:

$$v = \begin{cases} \langle v^l \rangle & \text{if } g^l > g_{BL}^l \\ 0 & \text{otherwise} \end{cases} \quad (5.47)$$

where g_{BL}^l is the threshold for the liquid fraction, below which we consider that the interface should not be transported.

[Figure 5.13](#) shows the mass variation for three blocking fractions: 0, 50, 75 and 99 percent. The first value corresponds the case where the Navier-Stokes solution is directly passed to the transport solver, corresponding to the previously presented result in [fig. 5.12b](#). For the last value, we consider that as soon as a portion of the *M-A* boundary becomes in contact with the low solid fraction part, the liquid in the mushy zone becomes immobile. It is clearly seen that the consequence on the mass conservation is not good, as the mass increases up to 3% while the eutectic front is consuming the liquid within the mushy zone, and no further shrinkage is allowed. We conclude that this strategy adds metal mass in the system, unlike the initial strategy with $g_{BL}^l = 0\%$ that removes mass.

In [fig. 5.14](#), we plot again the same curves as in [fig. 5.13](#), but keeping the values of $g_{BL}^l=0\%$ and $g_{BL}^l=50\%$. We notice that both values produce the same results until about 300 s. Then,

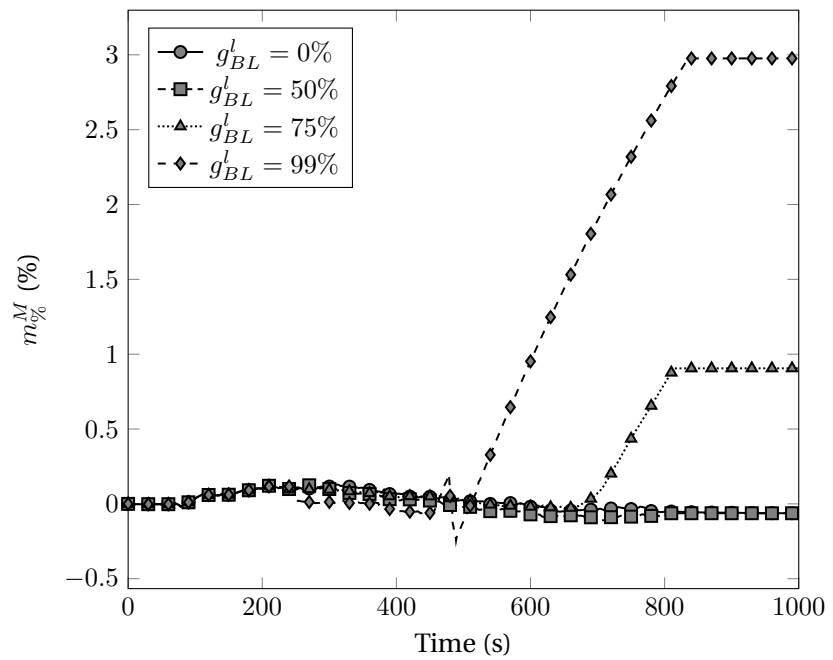


Fig. 5.13 – Relative mass change versus time for different blocking fractions g_{BL}^l in the transport solver.

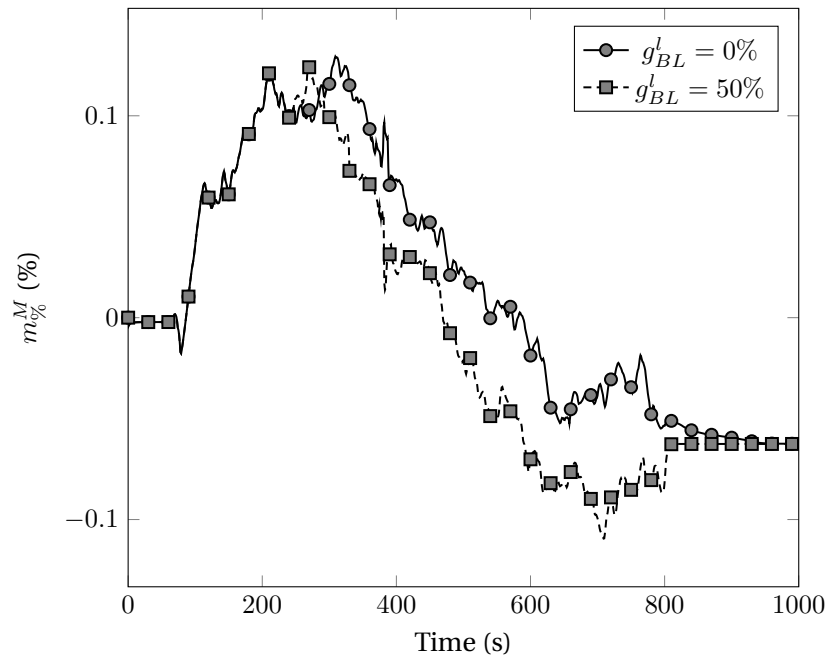


Fig. 5.14 – Relative mass change versus time only for 0% and 50% blocking fractions.

when the mushy zone reaches the interface region, differences appear as a consequence of the reduced transport for the higher blocking fraction. However, it should be pointed out that the differences between 300 s and 800 s are not important because the permeability predicted by the Carman-Kozeny model, falls to zero quickly for liquid fractions less than about 60%. In the current application, it is not clear whether the idea of the blocking fraction is useful or not, since the feeding flow occurs in a single direction and solidification takes place far from the interface. Since the results obtained zero blocking fraction were better than with increasing values of g_{BL}^l , further simulations will adopt this strategy.

5.6.3 Shrinkage with macrosegregation

In this section, we consider species conservation equation, in addition to energy conservation and fluid momentum conservation equations, studied in the previous section to predict solidification shrinkage. The interesting point here is to study the formation of macrosegregation in a one-dimensional configuration and the effect of solidification shrinkage on it. As shown in chapter 2, our approach to solve the energy equation relies on tabulations of various solidification paths. In this case, we will generate a simple tabulation based on a phase diagram with linear liquidus and solidus lines, whose properties are reminded in [table 5.4](#).

Table 5.4 – Main properties of the linearised phase diagram for Al-Si alloys.

Parameter	Symbol	Value	Unit
Nominal composition	w_0	7	wt.%
Liquidus temperature	T_L	618	°C
Eutectic temperature	T_E	577	°C
Segregation coefficient	k	0.13	–
Liquidus slope	m_L	-6.5	Kwt.% ⁻¹

Using the values from [table 5.4](#), a python program generates a *CimLib* -compatible tabulation assuming lever rule as microsegregation law, with a 0.1 wt.% step for average composition within an offset of 20% around the nominal value, i.e. 29 composition values within the interval [5.6,8.4]wt.%Si. For temperature, a range between $T_E=577$ °C and 630 °C is considered with a step of 1 °C, corresponding to 54 values. It is noted that for this application, the phase enthalpies are deduced from constant specific heat of each phase as well as constant latent heat, given in [table 5.1](#).

In order to understand better the effect of shrinkage combined with macrosegregation, we plot in [fig. 5.15](#), the cooling curves from 4 different simulations:

- Grey curve - case G0: pure diffusion solidification with $\langle \rho \rangle^l = \langle \rho \rangle^s$ (no level set) used previously in chapter 2 for validation; we use it as a reference case,
- Green curve - case G: convection-diffusion solidification with $\langle \rho \rangle^l = \langle \rho \rangle^s$ (with level set) at a constant average composition
- Blue curve - case B: convection-diffusion solidification with $\langle \rho \rangle^l \neq \langle \rho \rangle^s$ (with level set) at a constant average composition; this curve is plotted in [fig. 5.15a](#) and [fig. 5.15b](#),
- Red curve - case R (not to be confused with case R defined in the previous section): convection-diffusion solidification with $\langle \rho \rangle^l \neq \langle \rho \rangle^s$ (with level set) and macrosegregation.

Shrinkage effect on temperature

If we focus first on [fig. 5.15a](#), we first compare solidification cases G and G0, both with equal phase densities, hence no shrinkage. This first comparison shows that the introduction of the level set method, compared to a monodomain configuration, heats up the overall sample temperature by about 4 °C (difference between green and grey curves), causing solidification to finish a few seconds later than predicted in case G0. This is because we set a very high initial temperature in the air, 800 °C, to prevent a brutal diffusive flux that may lead to surface solidification in the metal. As the sample cools down, the air conductivity ($10^{-2} \text{ W m}^{-1} \text{ K}^{-1}$) is not low enough to prevent a small diffusion flux in the metal's direction. However, since in both cases the cooling trend is predicted, we will keep the same thermal diffusion properties in the air, so as not to use unreal conductivity values, but we keep in mind that the current approach delays the solidification.

The second comparison is done between cases G and B, both using the level set approach but only case B considers solidification shrinkage. We notice that blue curve temperature of the sixth Eulerian sensor rises steadily from 180 s to 600 s reaching a constant temperature of 800 °C, the air's temperature. This rise confirms the metal has shrunk in length (volume in 3D), becoming less than 10 cm, hence replaced by air that entered through the open top boundary. The 6th sensor (at 100 mm) was initially on the metal-air boundary, then later relocated in the air after shrinkage. The sensors at 12 cm and 14 cm are not shown in this figure as the simulation done for the pure diffusion without level set, the air domain does not exist.

Another interesting difference resulting from shrinkage is that solidification ends sooner by about 70 s, compared to the pure diffusion case. As mass is almost perfectly conserved in both cases, cooling flux is the only factor that may accelerate the cooling. The imposed cooling boundary condition is a Fourier-type with the same heat transfer coefficient h_{ext} in both cases. However, a shrinkage flow transports energy in its direction, i.e. towards the solidification front, and thus raising slightly the temperature in regions close to the cool wall. Therefore, the Fourier flux proportional to the local temperature increase and the sample solidifies earlier.

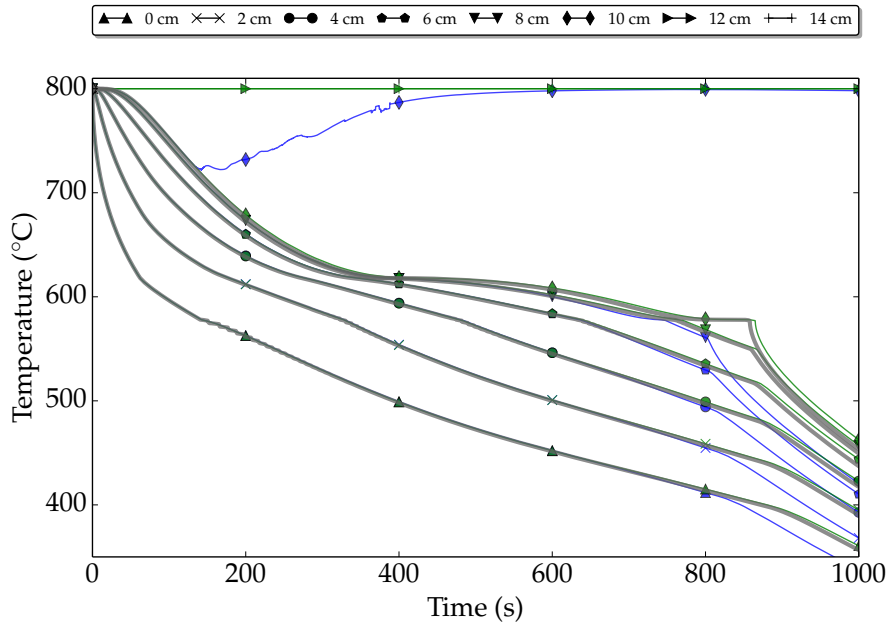
Finally, [fig. 5.15b](#) compares cases B and R, both with unequal phase densities but also predicting macrosegregation in the latter case. Differences are not striking, as temperatures along the metal sample are the same.

Shrinkage effect on average composition

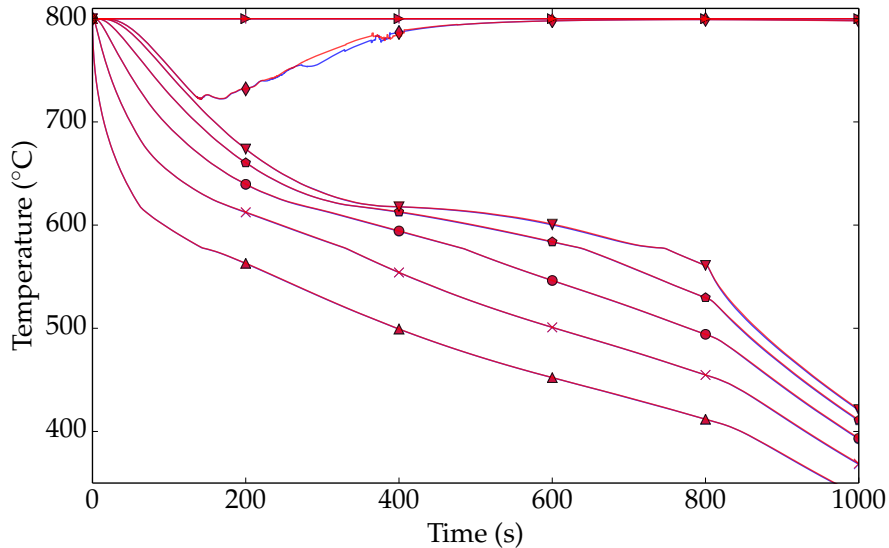
In this section, we shall test the strategies regarding modelling the species conservation in a level set context. Therefore, we summarise in [table 5.5](#) the approaches along with the most important values.

Table 5.5 – Summary of simulation configurations that are performed showing the different modelling strategies to account for metallic species transport in the air domain: monolithic strategy with low species diffusion in the air (MD), monolithic strategy with low species diffusion and advection in the air (MDA) and non monolithic strategy with composition reinitialisation in the air (NM).

Configuration	Diffusion in air [$\text{m}^2 \text{ s}^{-1}$]	Advection in air [m s^{-1}]	Composition reinitialisation
MD	1.5×10^{-12}	$\langle \mathbf{v}^F \rangle$	-
MDA	1.5×10^{-12}	0	-
NM	$\langle D \rangle^l$	$\langle \mathbf{v}^F \rangle$	$\widehat{\langle w \rangle} = H^M \langle w \rangle^M + H^A \langle w_0 \rangle^M$



(a) Solidification shrinkage effect: grey curves correspond to a pure diffusion in a metal monodomain case, green curves consider the latter case but with level set (metal and air domains) while blue curves correspond to a shrinkage-driven flow case. All cases are solved without macrosegregation.



(b) Macrosegregation effect: blue curves represent the same simulation corresponding to the shrinkage-driven flow without macrosegregation, while the red curves correspond to a simulation of shrinkage-driven flow with macrosegregation.

Fig. 5.15 – Cooling curves at different fixed positions from 0 to 14 cm. where we show (a) the effect of solidification shrinkage on temperature history without any macrosegregation and show (b) the effect of macrosegregation on temperature in the presence of solidification shrinkage. Initial M-A boundary: 10 cm.

[Figure 5.16](#) shows snapshots at different times of the shrinkage flow from a MD simulation, caused by the density difference between liquid and solid phases. By solid phases, we mean the primary solid phase assumed as a dendritic structure, then the primary and secondary solid phases forming together the eutectic that we see starting at 150 s in [fig. 5.16](#). We can see that almost no solute segregation has yet taken place in the mushy zone at 100 s. Then at 150 s, the average composition reaches a positive peak of $\langle w \rangle = \text{Al-7.4 wt.\% Si}$ at the closest nodes to the chill. This is triggered by the progression of the eutectic front. The sudden transformation of the remaining liquid in the mushy zone into eutectic solid, triggers a local velocity increase (real intrinsic velocity). This is made possible near the eutectic temperature (T_E) where density varies abruptly from $\langle \rho \rangle^M = g^E \langle \rho \rangle^l + (1 - g^E) \langle \rho \rangle^s$ to $\langle \rho \rangle^s$ in a single time step, g^E being the volume fraction of eutectic.

The velocity increase causes species transport in the opposite direction of solidification, hence solute "freezes" in the eutectic structure leading to positive macrosegregation in the first solidified nodes. This phenomenon is better known as inverse segregation. As the transport continues in the same direction, solute is progressively depleted in the remaining liquid, causing negative macrosegregation at nodes located between 2 cm and 7 cm from the chill.

[Figure 5.16](#) shows only the first 1.5 cm of the solidifying sample, therefore a complete segregation profile is plotted along the sample length in [fig. 5.17](#). Three curves are plotted in the latter figure: the first curve, [fig. 5.17a](#), uses the monolithic species conservation ([section 5.5.3](#)) with limited diffusion in the air, the second curve [fig. 5.17b](#) employs the same strategy but with both limited diffusion and advection in the air, and finally [fig. 5.17c](#) is given by the non monolithic strategy for species conservation. We look first at [fig. 5.17a](#) showing the negative macrosegregation between 2 cm and 7 cm from the chill, as previously explained. However, from 7 cm to the M-A boundary, the average composition rises. This tendency was also found by [Niane \[2004\]](#). It corresponds to the liquid freezing due to the eutectic reaction, with no solute feeding in the mushy zone, near the end of solidification, i.e. when the mushy zone has reached the M-A boundary. Also, an unexpected composition profile is seen surrounding this boundary. By comparing with [fig. 5.17b](#), where the input velocity field is set to zero in the air domain before solving the monolithic species conservation equation, resulting in limited species transport in the air as well as within the M-A boundary vicinity. The numerical anomaly seen in the previous composition plot is reduced. This comparison confirms the fact that macrosegregation is mainly promoted by advective transport rather than diffusion, and therefore controlling the velocity field in the air greatly reduced the sharp composition decrease in the boundary vicinity.

The last plot, [fig. 5.17c](#), shows the segregation result obtained by the non monolithic strategy presented previously to solve the species conservation equations in the air and the metal. Two comments can be made on the latter result: first, the concentration *valley* effect surrounding the M-A boundary seen in [fig. 5.17b](#) has shrunk even more, and is now restricted to a very small thickness spanning on one or two elements around the boundary. On the air side, the decreasing composition trend has also disappeared, and is now replaced by a sharp transition, as an effect of the explicit reinitialisation of the composition solution. The second comment is about the instability amplitude: it is still better than the first result ([fig. 5.17a](#)) but worse than the second result ([fig. 5.17b](#)).

To conclude on the effect of shrinkage on macrosegregation, we may say that the non monolithic gives the best compromise in terms of composition solution quality. We may also conclude that the mesh should remain fine around the level set boundary, in order to prevent any

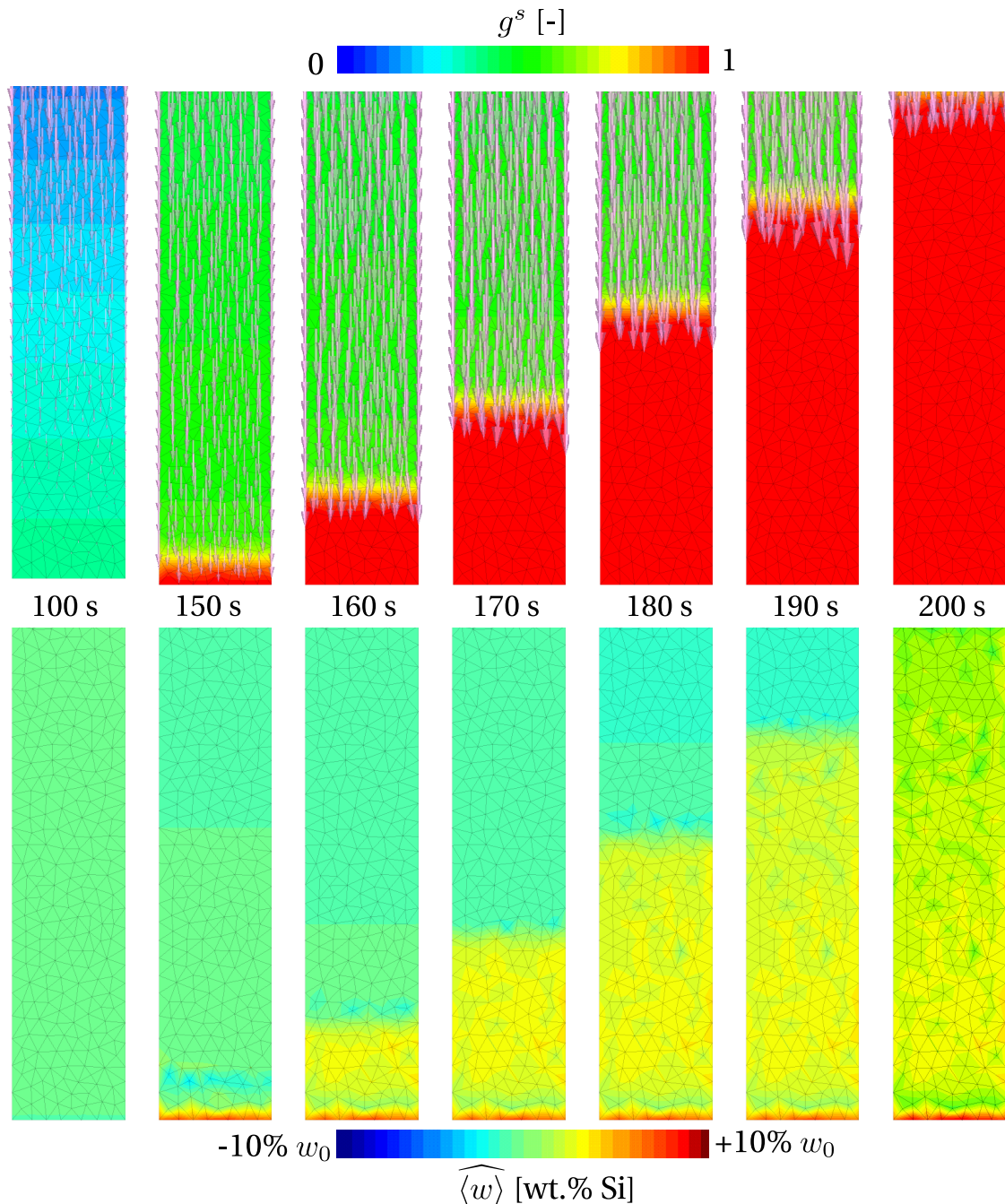


Fig. 5.16 – Zoom on the lower part, approximately 0.5 cm of the alloy close to the cooling boundary condition. The upper row of figures shows the evolution of volume fraction of solid, when eutectic transformation takes place. The vectors represent the direction of the average velocity field, with a length proportional to the magnitude. The lower row of figures shows for the same time increments, the solute redistribution, clearly changing behind the eutectic front.

composition instability from spanning on larger distances and destabilising the computation. We continue our analysis on the link between macrosegregation and solidification shrinkage by plotting in [fig. 5.18](#) important quantities at different times of the simulation corresponding to the MD strategy.

The first column in [fig. 5.18](#) shows the evolution of the average composition in the metal+air system (same plot as in [fig. 5.17a](#)), as well as the solid (primary and eutectic) and liquid phase compositions. At 200 s, classic segregation takes place governed by the alloy properties defined in [table 5.4](#), where we can see that the eutectic had already reached almost 0.6 cm from the chill (as previously seen in [fig. 5.16](#)), forcing the liquid composition to drop to zero locally. Later at 600 s, the mushy zone reaches the *M-A* boundary, causing the instability to begin. This instability is identified by a decrease in average composition, forming the *valley* effect. Shortly before solidification ends at 800 s, the instability had already reached its minimum peak, due to neglecting to porous medium boundaries.

The second column in [fig. 5.18](#) shows mixed average density plots during solidification. From 200 s to 600 s, we can identify the extent of the mushy zone, as previously discussed for the phase compositions. We assume that the primary and eutectic solids have the same phase density, $\langle \rho \rangle^s$. The density graphs show only values in the interval [2550, 2850] kg m⁻³, and therefore we cannot see that in the air domain, the mixed average density drops to $\langle \rho \rangle^a$.

Finally, the third column of [fig. 5.18](#) describes the temporal evolution of mixed fluid velocity solutions, namely the average fluid velocity, $\langle v^F \rangle$, and the intrinsic average fluid velocity, $\langle v \rangle^F$. At 200s, we see that the suction effect created by the density change in the mushy zone creates a unidirectional flow of constant velocity, in both the liquid and air, with a magnitude of about 0.9×10^{-5} m s⁻¹. At the *M-A* boundary, we see a velocity jump caused by the ratio of metal density to air density. Closer to the chill, we can distinguish average and intrinsic velocity profiles in the mushy zone. The latter decreases more slowly than the former and showing a slight sharp increase in magnitude (not very visible on the plot) when at the intersection between the mushy zone and the eutectic front. In previous solidification shrinkage studies carried by [Niane \[2004\]](#), the author showed a similar effect caused by the instantaneous eutectic solidification of the remaining liquid. However in our simulations, this effect is less prominent, possibly because of the mesh size . Later from to 600 s to 800 s, we notice a relatively turbulent flow in the air, compared to its behaviour in the remaining liquid. Another remarkable phenomenon, is the increase in velocity magnitude, almost a hundred times after solidification is finished. We may see this as a numerical response to the modelled physics, which vary before and after solidification.

At this stage, it is interesting to conduct the same investigation done for [fig. 5.18](#) but changing the species resolution strategy to NM, whose results are plotted in [fig. 5.20](#). We have already seen the difference in the average composition plot, which is the same in [fig. 5.17c](#). However, the liquid composition shows a peak value when meeting the *M-A* boundary at 800 s. The mixed density does not show noticeable differences, as the predicted phase fractions are the same, regardless of the species resolution strategy. The last column in [fig. 5.20](#) shows a much better flow behaviour compared to the results seen in [fig. 5.18](#). The velocity plots show also lower magnitudes than the MD strategy plots, while still predict a more prominent effect of local intrinsic velocity increase near the eutectic front at 200 s.

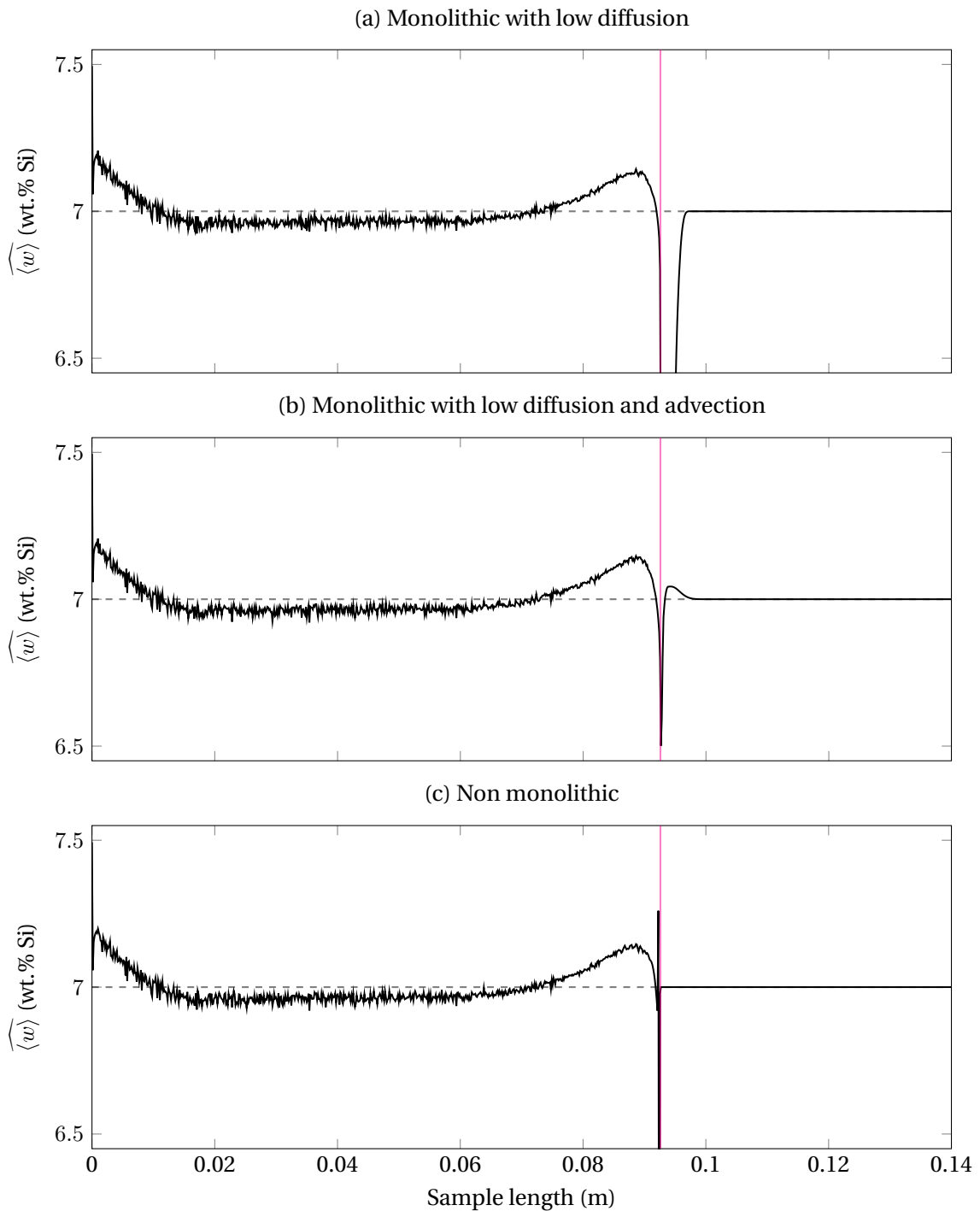


Fig. 5.17 – Plot of the average composition as function of length, along a vertical line passing through the centre of the sample at 1000 s, while varying the modelling strategy to account for species conservation in the air by considering (a) the MD configuration (b) the MDA configuration (c) the NM configuration. These configurations are defined in [table 5.5](#). The solid magenta line shows the position of the interface while the black dashed line shows the nominal average composition of the alloy.

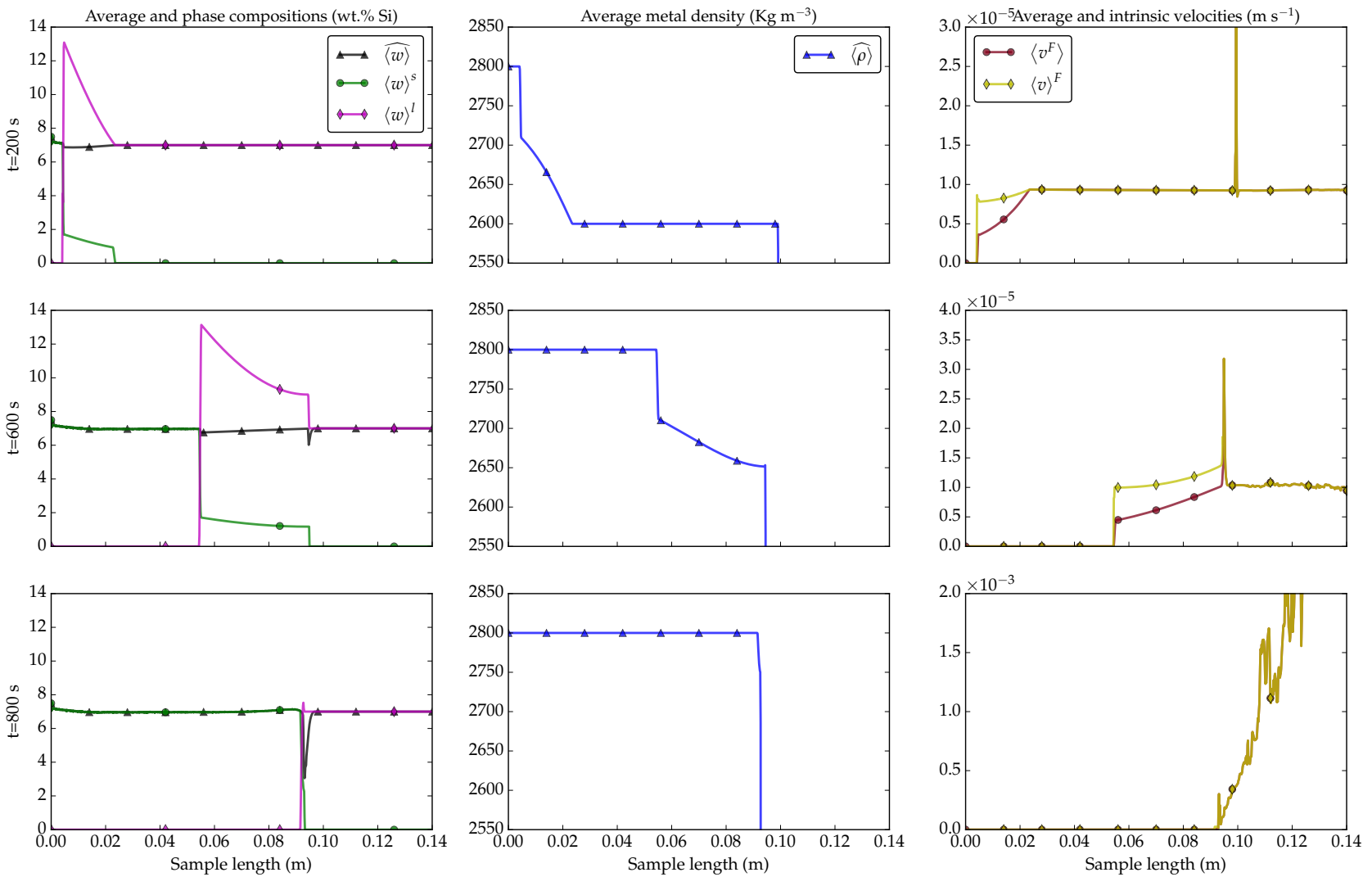


Fig. 5.18 – Group of plots where each row is a given time increment ($t=200$ s, $t=600$ s and $t=800$ s) of the 1D solidification shrinkage simulation with macrosegregation applying the **MD strategy** (fig. 5.17a). Physical quantities are plotted along a line passing through the centre of the sample and parallel to the gravity vector.

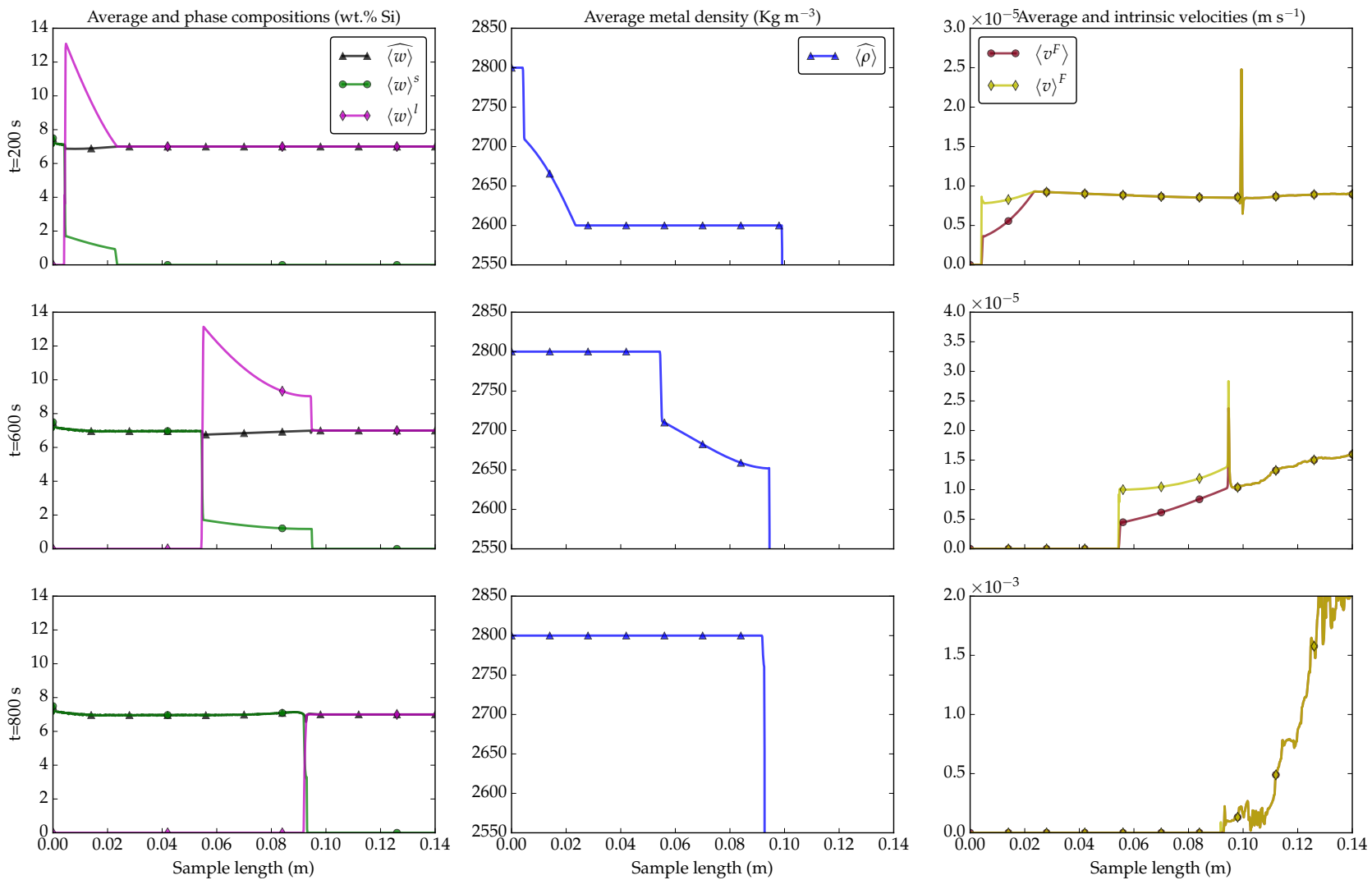


Fig. 5.19 – Group of plots where each row is a given time increment ($t=200$ s, $t=600$ s and $t=800$ s) of the 1D solidification shrinkage simulation with macrosegregation applying the MDA strategy (fig. 5.17b). Physical quantities are plotted along a line passing through the centre of the sample and parallel to the gravity vector.

5.6. 1D application: solidification with inverse segregation

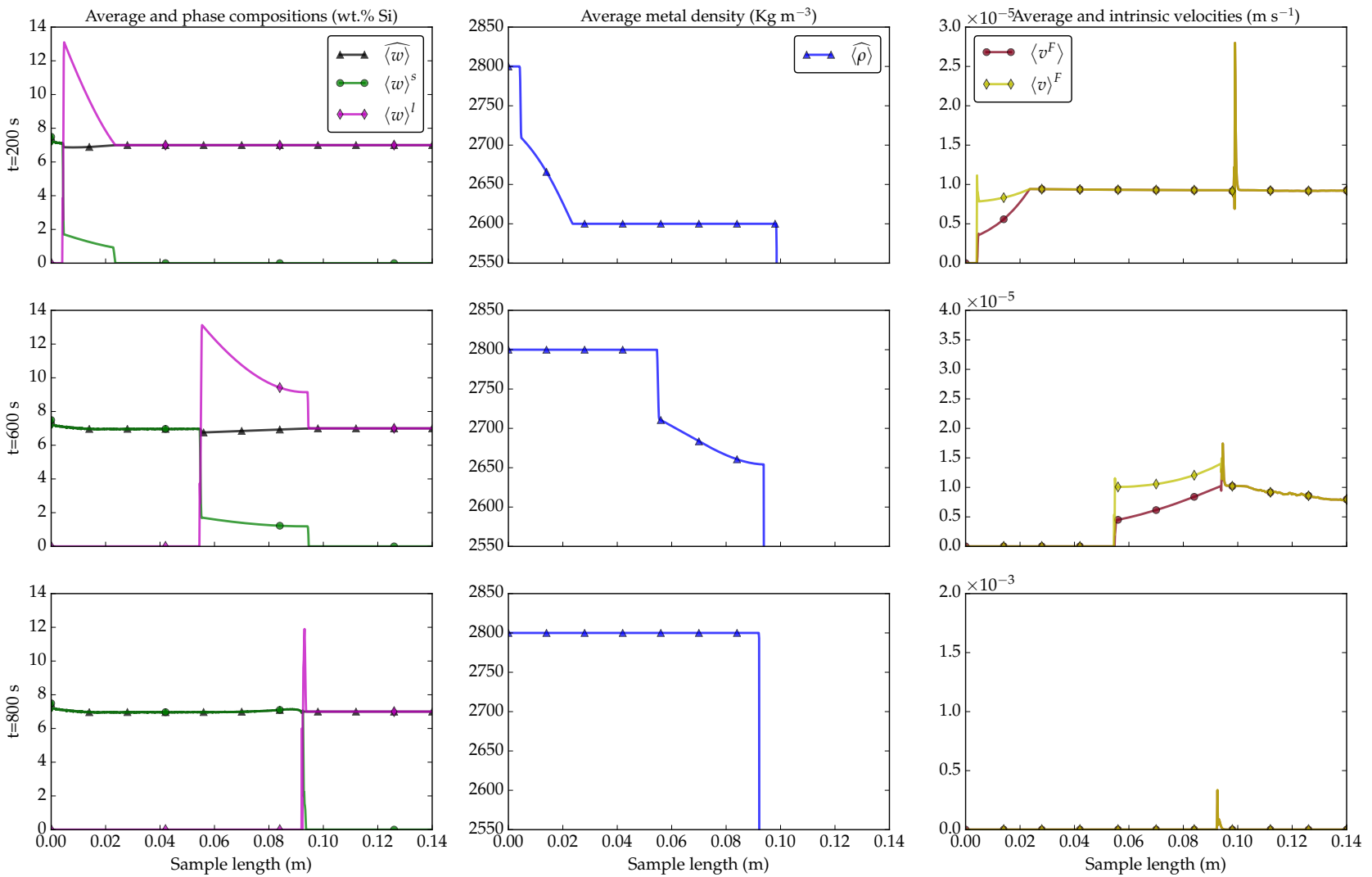


Fig. 5.20 – Group of plots where each row is a given time increment ($t=200$ s, $t=600$ s and $t=800$ s) of the 1D solidification shrinkage simulation with macrosegregation applying the NM strategy (fig. 5.17c). Physical quantities are plotted along a line passing through the centre of the sample and parallel to the gravity vector.

Solute mass conservation

The mass conservation for the metal and the metallic species is discussed in this section. [Figure 5.21](#) shows the relative mass variation of the metal and the silicon species for each of the previously defined and used modelling strategies. The solute mass variation is computed, similarly to the metal ([eq. \(5.46\)](#)), as follows:

$$m_{\%}^{\text{sp}} = \frac{m^{\text{sp}} - m_0^{\text{sp}}}{m_0^{\text{sp}}} \times 100 \quad (5.48)$$

where m_0^{sp} is the initial solute mass (“sp” stands for species, silicon in this case), knowing that m^{sp} is computed using the average composition as follows:

$$m^{\text{sp}} = \int_{\Omega} H^M \widehat{\langle w \rangle} \langle \rho \rangle^M d\Omega \quad (5.49)$$

It is important to analyse the metal mass variation together with the species mass variation because a gain or loss in the metal’s mass is directly reflected on the mass of the metallic species. However, the latter may also be subject to variations depending on the configuration of the simulation: resolution technique, time step, boundary conditions ... In our case, we first compared the mass conservation for the metal with all three methods for species conservation: MD (monolithic with low diffusion), MDA (monolithic with low diffusion and advection) and last NM (non monolithic). We cannot see a noticeable difference when comparing mass analysis for all three techniques, as shown by the dotted lines in [fig. 5.21](#). This conclusion goes for both the metal and its species. Nevertheless, we see the main behaviour discussed earlier in [fig. 5.12](#) regarding the increase then decrease of the metal mass. As for the species mass, it can be lost due to 2 causes mainly: the species mass is computed from the volume of the metal, and therefore any changes in the metal volume are directly reflected on metallic species. The other cause is the species resolution equation which gradually loses mass of species during the simulation, possibly leading to negative composition in some cases. The solute rise observed in the same figure ([fig. 5.12](#)) for all three strategies is the result of taking into account some solute in the air which may slightly transported from the air into the metal. We may think of a competition between the species mass increase due a damped level set motion and a species mass decrease due to the previously explained reason. Changing the species resolution strategy affects only the area surrounding the M - A boundary (as earlier seen in [fig. 5.17](#)) and thus the predicted average composition varies. The latter variation impacts the phase fractions, namely the liquid, which is an input of the fluid fraction used to evaluate the transport velocity in Navier-Stokes. The predicted transport velocities in [figs. 5.18](#) and [5.20](#) show that the flow reaches high magnitude during solidification time (from 200 s to 800 s) thus causing the level set to move further but on

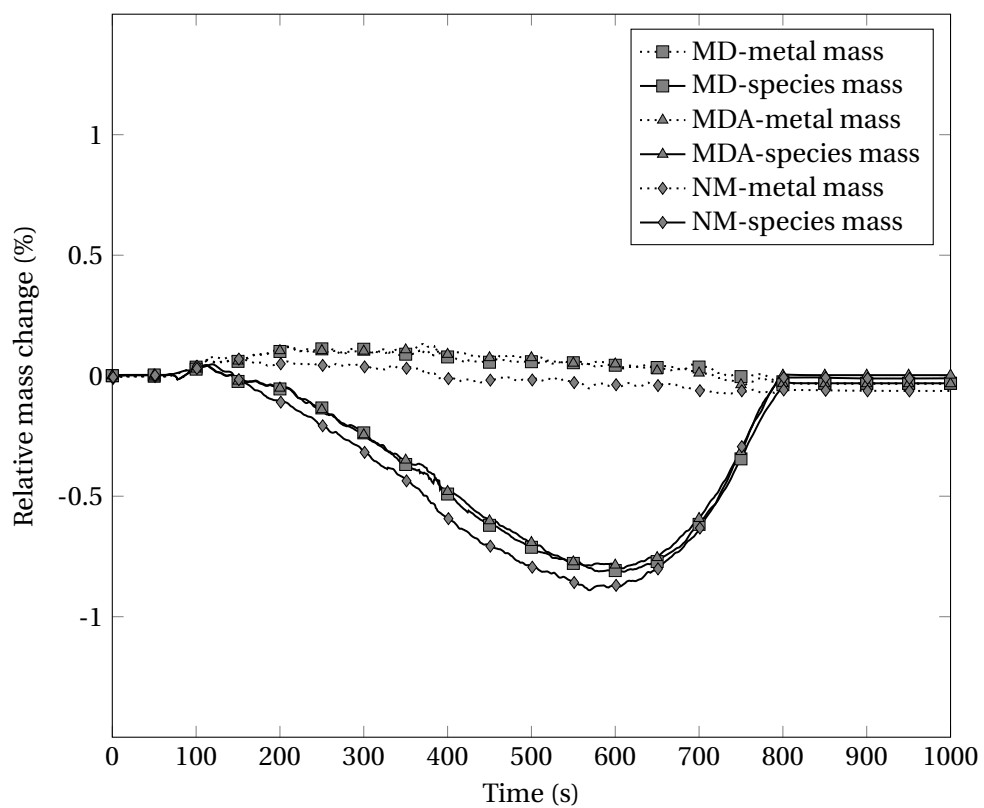


Fig. 5.21 – Mass variation plots for the metal and its chemical species, considering three different strategies to account for the species conservation in the air domain.

5.7 2D application: controlled solidification benchmark

In this application, we aim at predicting macrosegregation produced by liquid convection, in the presence of solidification shrinkage. The simulation is the same performed in [section 4.4](#) but now the level set approach is added. The importance of the experiment lies in the thermal convection forces arising from temperature gradients, but also solutal buoyancy forces arising from liquid concentration gradients. The final macrosegregation pattern strongly depends on density variations caused by each chemical species, but also on the experimental conditions like the lateral thermal gradients as well the cooling rate, as shown in [fig. 5.22](#). [Hebditch and Hunt \[1974\]](#) suggested one of the first experiments working on Sn-Zn and Sn-Pb alloys. More recently, an experimental benchmark was performed by [Hachani et al. \[2012\]](#) to obtain more accurate composition results with various Sn-Pb and Pb-Sn alloys. In the current section, we are interested in the latter experiment with Sn-3 wt.% Pb especially in the prediction of the metal's shrunk surface together with the final macrosegregation.



Fig. 5.22 – Final ingot shape with grain structure at mid-width obtained experimentally by solidifying a Sn-3 wt.% Pb alloy [[Carozzani et al. 2013](#)].

5.7.1 Computational configuration

Mesh and adaptive remeshing

The case considers a 2D geometry having equivalent dimensions to the 3D case performed earlier (sample of 10 cm in length and 6 cm in height). To accommodate the air domain, an extra 2 cm are added to sample's height, which finally reaches 8 cm, thus the interface has an initial elevation of 6 cm. The initial mesh consists of three different mesh sizes: isotropic meshes in the air and the metal, having respectively a uniform size of 2 mm and 1 mm. Regarding the interface, an anisotropic mesh adapts to the *M-A* boundary with a mesh size of 0.1 mm in the normal direction to the interface. The thickness of the anisotropic mesh spans 0.5 mm from each side of the interface, hence ensuring an initial resolution of almost 10 elements in the interfacial transition zone.

To adapt the mesh during convection and subsequent solidification, we use the *Remesh4* adaptive technique to maintain accurate predictions for velocity and interface transport. After performing some tests, it has been concluded that the remeshing frequency should vary depending on the convection regime which pilots the flow velocity. For this simulation, we adopted a fast

adaptation technique in the high convection regime then later we reduce the pace by a factor of 5. The frequency values are included in [table 5.6](#). Regarding the transition between high and low convection regimes, we did not conduct detailed analysis using known non-dimensional numbers (e.g. Reynolds number), but rather rely on direct inspection of the results while changing the remeshing frequency to check if they are satisfactory. We chose 2800 s as an optimal transition time between these high and low convection regimes.

However as solidification proceeds, we also need to keep a relatively small mesh size in regions with noticeable composition gradients. Although possible to achieve with the *Remesh4* technique, it is still difficult to maintain a fine mesh size throughout the metal, especially in areas where solidification is almost complete and where the velocity field has a low magnitude. These areas are interesting as they represent potential sites where segregated channels may form. If a low mesh size is not maintained, these channels may numerically disappear.

To avoid such unwanted effects, we use another uniform isotropic grid, named *grid B*, having a constant mesh size of 0.3 mm, that is a good compromise between the finer interface elements and the coarser air low-velocity elements in the original adapted, named *grid A*. These grids are shown in [fig. 5.23](#). The strategy consists of scanning the liquid fraction of each node in *grid A*, if its value is located between 30% and 70%, then we consider that region of interest, since the flow velocity is still not zero and a relatively fine mesh is locally obtained. We consequently transport the average composition field exclusively for these nodes from *grid A* to *grid B*, keeping for all other nodes their respective average composition values. It should be noted that this transport is only one-way, hence no information feedback from *grid B* to *grid A*.

Table 5.6 – Summary of the mesh parameters used to generate an adaptive mesh. Refer to [section 2.6.3](#) for the definition of each mesh parameter.

Mesh parameter	Value
ε	5×10^{-4} m
h_{\min}	10^{-5} m
Remeshing frequency	0.2 s ($t \leq 3000$ s) 1 s ($t > 3000$ s)
ε_{er}	500
Remeshing criteria	$\ \langle \mathbf{v}^F \rangle\ , \langle \mathbf{v}^F \rangle_x, \langle \mathbf{v}^F \rangle_y, \alpha, g^F$
Number of nodes (<i>Grid A</i>)	$\approx 10^4$
Number of elements (<i>Grid A</i>)	$\approx 2 \times 10^4$
Number of nodes (<i>Grid B</i>)	$\approx 10^5$
Number of elements (<i>Grid B</i>)	$\approx 2 \times 10^5$

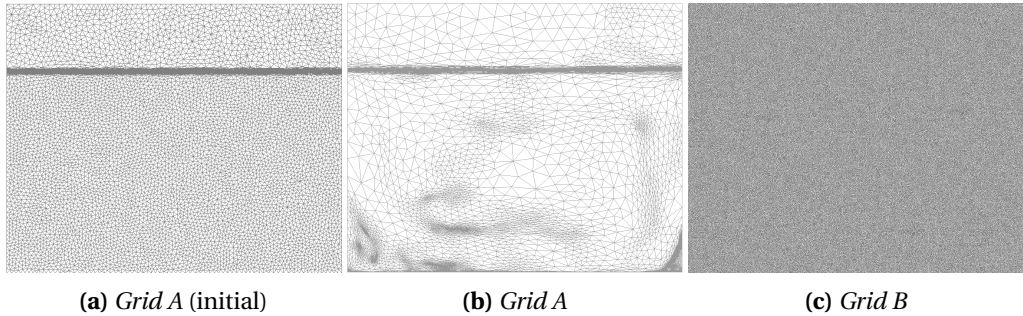


Fig. 5.23 – Snapshots of (a) the initial adaptive anisotropic *grid A* then (b) the same grid but at a given time increment with (c) the corresponding fixed isotropic *grid B* at the same time increment, used to record the average composition for $g^s > 0.7$.

Initial and boundary conditions

The air initial temperature is set the same as the initial liquid. This is only a hypothesis to prevent steep temperature gradients at the interface, which may lead to surface solidification. The initial and boundary thermal conditions used to cool down the metal are defined in chapter 4, given by the experimental data of Hachani et al. [2012]. For the mechanical properties, the top wall allows free inflow/outflow of the air in all directions at an imposed atmospheric pressure. This allows the air to follow any volume changes in the metal upon solidifying and shrinking. The geometry and boundary conditions are given in [fig. 5.24](#). Regarding the species conservation in the presence of the level set, the non monolithic strategy proved to be good in limiting the composition instability surrounding the *M-A* boundary, and hence it will be used for this 2D simulation. All simulation related parameters are shown in [table 5.7](#).

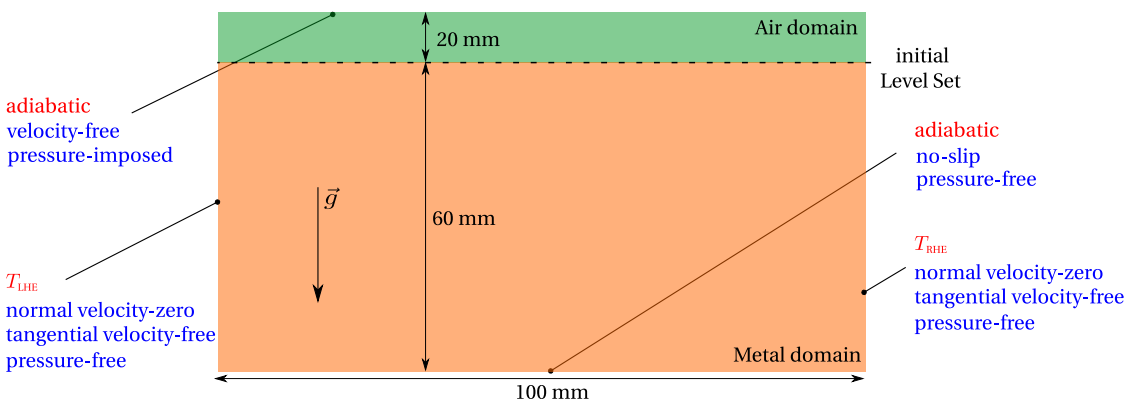


Fig. 5.24 – Computational configuration for the 2D inverse segregation case showing the domain geometry with the applied boundary conditions to it as well as the gravity vector. The pressure of top boundary is imposed to atmospheric pressure. The left heat exchanger (LHE) and right heat exchanger (RHE) temperatures are given in [Hachani et al. 2012].

5.7.2 Results

The results are recorded at two intermediate solidification stages, at 3050 s and 3550 s, knowing that solidification onset is around 1920 s. First, we look to the results in [fig. 5.25](#) at 3050 s. The

Table 5.7 – Parameters for the 2D simulation of the solidification benchmark performed by Hachani et al. [2012].

Parameter	Symbol	Value	Unit
Nominal composition	w_0	3	wt.%
Liquidus temperature	T_L	tabulations ([Carozzani et al. 2013])	°C
Segregation coefficient	k	tabulations ([Carozzani et al. 2013])	—
Liquidus slope	m_L	tabulations ([Carozzani et al. 2013])	K wt.% ⁻¹
Liquid density	$\langle \rho \rangle^l$	7130	kg m ⁻³
Solid density	$\langle \rho \rangle^s$	7530	kg m ⁻³
Air density	$\langle \rho \rangle^a$	1.3	kg m ⁻³
Liquid viscosity	μ^l	10 ⁻³	Pas
Air viscosity	μ^a	10 ⁻⁴	Pas
Air thermal conductivity	κ^a	0.01	W m ⁻¹ K ⁻¹
Liquid thermal conductivity	κ^l	33	W m ⁻¹ K ⁻¹
Solid thermal conductivity	κ^s	55	W m ⁻¹ K ⁻¹
Solute diffusion in the liquid	$\langle D \rangle^l$	1.7 × 10 ⁻⁹	m ² s ⁻¹
Solute diffusion in the solid	$\langle D \rangle^s$	0	m ² s ⁻¹
Solute diffusion in the air	$\langle D \rangle^a$	(non monolithic)	m ² s ⁻¹
Initial temperature	T_0	240	°C
Time step	Δt	0.01	s
Convergence on residual	ε_R	10 ⁻⁵	—
Convergence on temperature)	ε_T	10 ⁻²	K

original average composition field obtained by *grid A*, shown in [fig. 5.25a](#), is almost free of composition gradients except for one segregated channel rising from the bottom by the action of thermal convection. On the other hand, the average composition transport from the adaptive grid to the fixed one, allows recording macrosegregation onto the latter at nodes where the volume fraction of solid is greater than 70%, depicted by the yellow region in [fig. 5.25c](#). This is why we observe in [fig. 5.25b](#) a number of channel segregates which are richer in Pb species with respect to the surrounding solid. The solid fraction distribution is shown in [fig. 5.25d](#), along with the flow pattern. Local vortices are observed in the metal, probably due to considering only a 2D geometry instead of the complete 3D, and this alters the computation stability by ignoring the boundary layers in the sample thickness, obtained otherwise in 3D. Nevertheless, the overall flow is driven by a thermosolutal driving force, with a compatible flow in the air side. We can observe how the solid fraction is modified in the segregated channel, as a result of macrosegregation. At this stage of solidification, the interface movement is still difficult to see, but 500 s later it becomes more visible.

We look now at [fig. 5.26d](#) at 3550 s, and the decreasing left heat exchanger temperature has just went below the local liquidus, triggering solidification from the left side. The average composition field presents noticeable differences between the adaptive *grid A* and the fixed *grid B*. The weak macrosegregation observed in [fig. 5.25a](#) are now lost in [fig. 5.26a](#), as the mesh got coarser

on the metal's solidified right side. Fortunately, the macrosegregation distribution is stored in the fixed grid ([fig. 5.26b](#)) and shows more details with the advancement of solidification. The shrinkage due to phase density difference, is now clearly visible judging from interface shape, which still almost planar above the last liquid pool.

At the end of solidification, the ingot top surface has shrunk, showing greater boundary displacement in the last liquid region to solidify, as shown in [fig. 5.27](#). In this figure, it is interesting to compare the final experimental shape ([fig. 5.27](#)) to the numerical one ([fig. 5.27c](#)), while comparing the final obtained segregation maps ([fig. 5.27b](#)) to the numerical result of ([fig. 5.27c](#)).

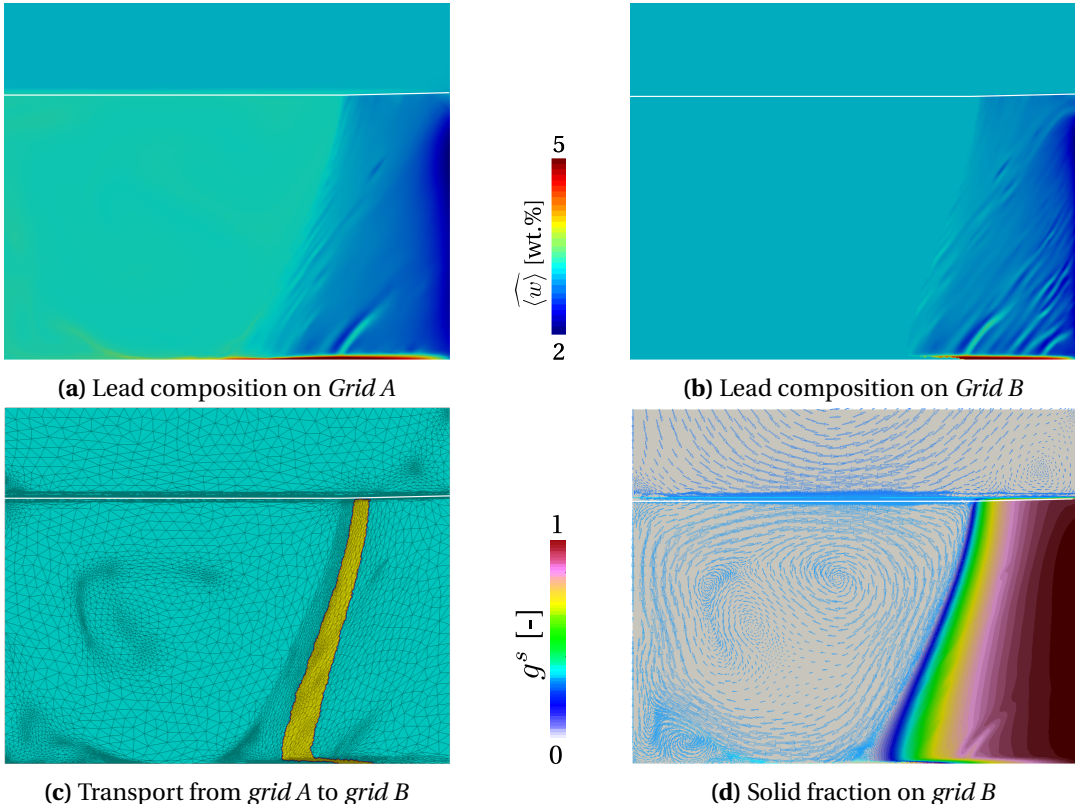


Fig. 5.25 – Snapshots at 3050 s of the average composition field shown on (a) *grid A* where the mesh gets coarser in fully solidified regions near the right side while and then on (b) *grid B* where the uniform fine mesh predicts a smoother composition field (line indicates the current interface level). The increased number of segregated channels on the right side of the metal is obtained by the successive transport operations performed in (c) a restricted area (yellow colour) based on the nodal values of (d) the solid fraction field. The white line represents the zero isovalue of the level set function.

5.7.3 Mass conservation

All mass and volume data related to both air and metal are plotted in [fig. 5.28a](#). The main reason for grouping all plots in a single is to be able to analyse the mass variations as function of the solidification advancement, which can be tracked by volume changes.

We see in the figure that no mass/volume variations are detected before 1900 s, seconds before solidification onset. Once the phase change starts, the average metal density decreases. Since

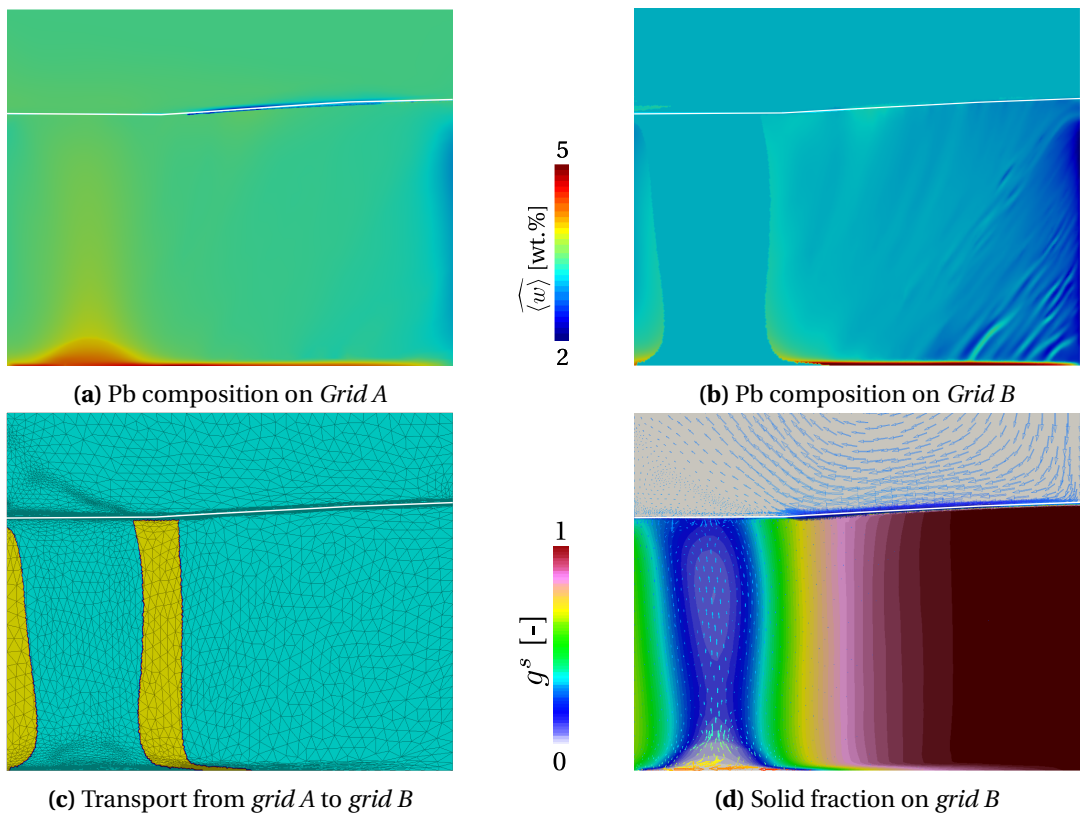
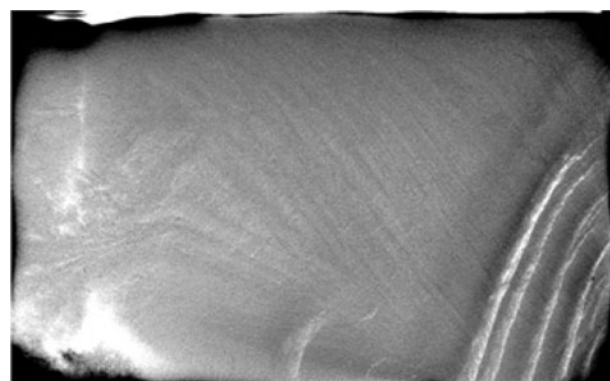


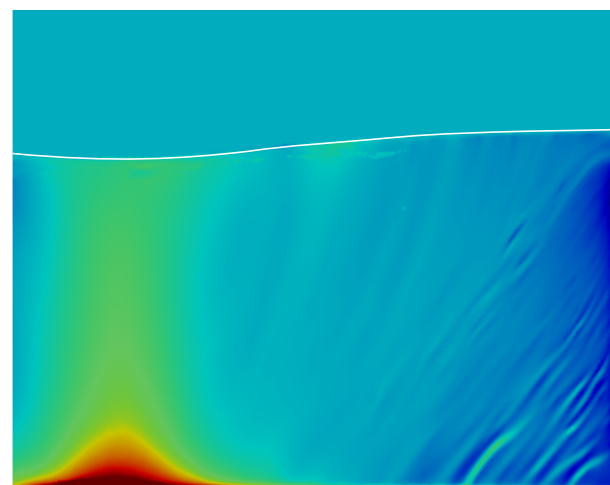
Fig. 5.26 – Snapshots at 3550 s of (a) the average composition result obtained on *grid A*, compared to (b) the composition field obtained on *grid B*, (c) after being transported in (c) a restricted area (**yellow** colour) based on the nodal values of (d) the solid fraction field. The white line represents the zero isovalue of the level set function.



(a)



(b)



(c)



Fig. 5.27 – (a) Final ingot shape with grains structure with (b) experimental macrosegregation patterns showing the positively segregated channels within negative segregation areas to the right, while on the left the last liquid to solidify forms a recognisable pipe shrinkage and a positively segregated region underneath it as predicted by (c) the corresponding simulation.

air is incompressible, it is sucked towards the shrinking metallic front. With our free velocity boundary condition, an air intake thus takes place, which is confirmed by the green curve corresponding to the relative air volume variation, starting from 2400 s. However between 1900 s and 2400 s, an unexpected slight volume increase of the metal takes place, although it should be decreasing under the action of the decreasing average density by solidification. This behaviour can be attributed to the competition between the flow due to thermosolutal convection and another flow due to shrinkage, and obviously the former is more imposing than the latter. Therefore, it forces the level set to slightly move upwards, letting the metal gain some volume at the expense of air, whose volume is seen temporarily decreasing between 1900 s and 2500 s. The metal's mass curve confirms also a positive variation, which is also reflected on the solute mass. After 2500 s, we can see that the metal volume is beginning its descent until it reaches the final volume corresponding to -6% of the initial volume. This value can also be deduced from the solidification shrinkage coefficient, β_{SS} , deduced from $\langle \rho \rangle^l$ and $\langle \rho \rangle^s$ included in [table 5.7](#). However between 2500 s and 3000 s, the metal and species mass do not show any sign of stability, but still rising. Until around 3200 s, both mass percentages decrease again as expected. While the metal's mass and volume follow the same trend after 3200 s, they are not really correlated. The mass is supposed to remain relatively unchanged until the final volume is reached. Therefore this means that the *M-A* is moving towards the metal, with a greater speed than it should have. At about 3800 s, solidification is almost complete, and the remaining liquid is not capable of inducing a significant boundary.

The other unexpected profile is the solute mass from 3600 s to 3800 s, where the ingot is almost completely solidified but still features species transport. It can be explained by the new quantities

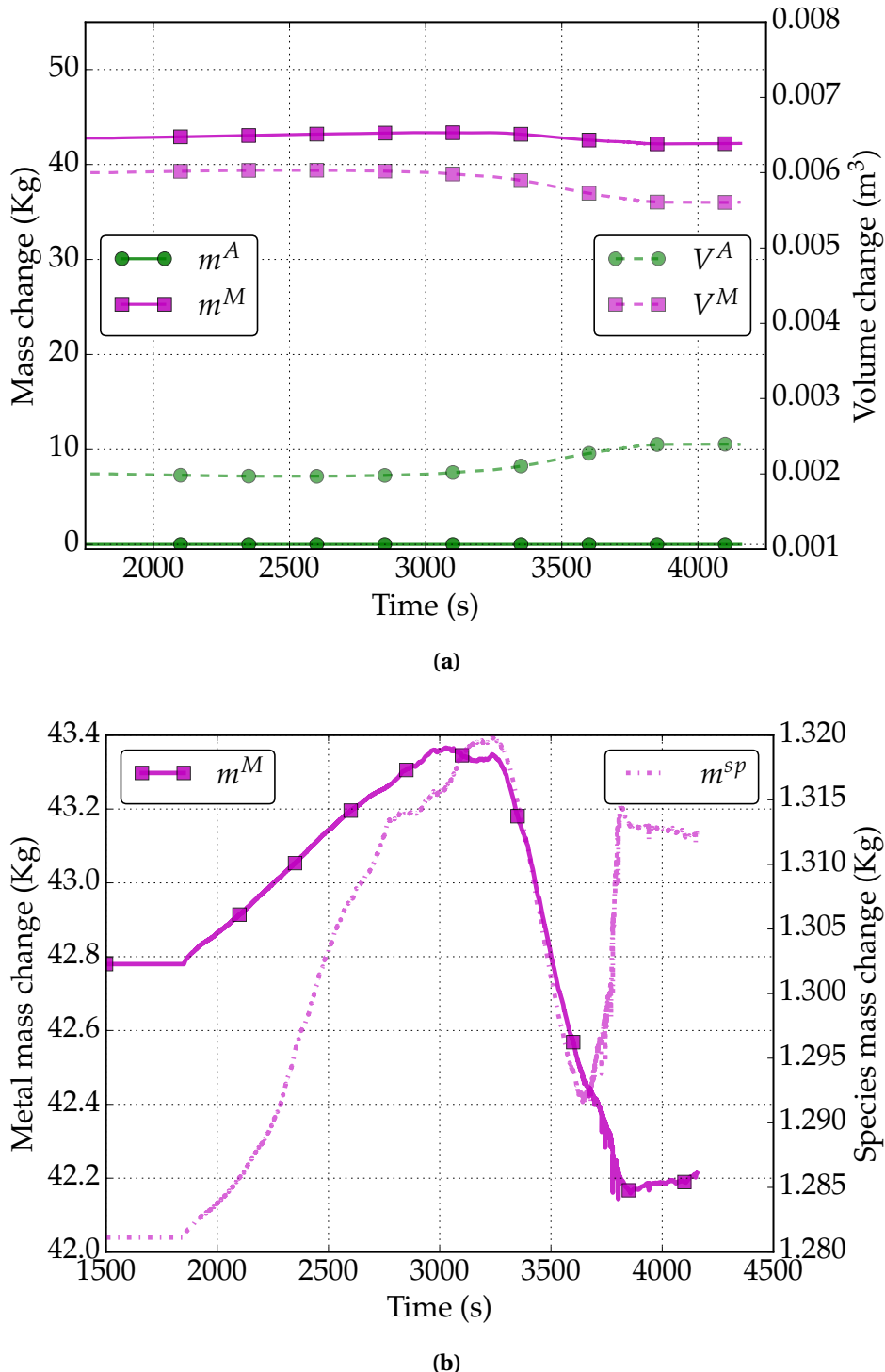


Fig. 5.28 – Global plots showing (a) global system of metal and air mass (left y-axis) and volume (right y-axis) variation with time and (b) the metal's mass (left y-axis) along with the mass of its metallic species (right y-axis). The thickness dimension of the 2D domain is assumed to be 1 m, hence the use of 3D units.

5.8 3D application: reduced-gravity solidification

As presented in the introductory chapter, the aim of the CCEMLCC project is to "reach a better understanding of surface defects formed during processing of steels from the liquid state" [Gandin 2014]. Among the several scientific topics being studied, the interaction between skin macrosegregation and thermomechanical deformation is investigated through chill cooling experiments. The idea is to have the molten steel in a containerless environment, which could be done by several ways: electromagnetic levitation, on-board parabolic flights or sounding rockets and finally in a real microgravity context as in the ISS. Heat is extracted from the sample by contact with a ceramic (Si_3N_4) substrate at room temperature (hence the term "chill cooling"), that collides into the alloy at a controlled speed. This contact situation generating a high thermal gradient is comparable to casting processes between the molten alloy and the moulds. For ground-based experiments, EML was used to achieve chill cooling of samples without using moulds. However, levitation induces currents in the spherical sample, generated by means of electromagnetic stirring (Lorentz forces) but also by thermal and solutal convection on the other hand. In reduced-gravity conditions, the dynamics of the phenomena behind fluid motion are less significant. The current modelling is therefore compared to chill cooling experiments performed in parabolic flights and sounding rockets with reduced gravitational forces ($\|g\| \in [10^{-5}; 10^{-1}] \text{ m s}^{-2}$).

5.8.1 Previous work

TEXUS sounding rocket

TEXUS-46 is the name of the sounding rocket mission that carries the experimental setup, but for simplicity we will refer to the latter as being the TEXUS experiment. The setup is shown in fig. 5.29. The main difference with respect to parabolic flight experiments, TEXUS features solidification in near-zero gravitational fields and for extended periods of time (3 minutes). We do not have an exact measurement of the gravitational field magnitude, but it is several orders less than Earth's gravity magnitude ($\|g\| \in [10^{-5}; 10^{-8}] \text{ m s}^{-2}$). It should be mentioned that the experimental setup is comparable between parabolic flights and sounding rocket experiments. That is to say that the dimensions of the steel sample, the substrate and the container are almost the same. Nevertheless, different steel compositions were considered in each type of experiment.

TEMPUS experiment for parabolic flight campaigns

The TEMPUS experiment came as a first alternative for EML experiments on ground during which accurate thermophysical and rheological characterisation were difficult to achieve. Each flight consists of several cycles of free fall, a reduced-gravity environment is hence created, allowing to use only a single radio frequency (RF) coil to stabilise the position of the droplet, while the substrate comes into contact with the molten sample from above it. An axial pyrometer measures the sample temperature during the process. Also, a high-speed camera records the solidification process, producing frames as shown in fig. 5.30. This is useful to measure the front growth speed. Each parabola cycle lasts for 50 s, offering an effective low gravity ($\|g\| \approx 10^{-1} \text{ m s}^{-2}$) for about 20 s.

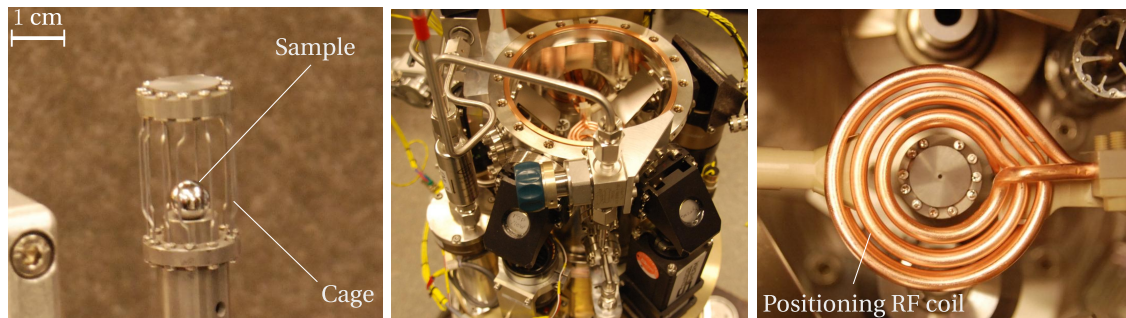


Fig. 5.29 – Three frames describing the experimental setup used to achieve reduced-gravity solidification on-board a sounding rocket flight, showing the initial alloy sample, the cage and the positioning coil. The setup is similar to the one used for TEMPUS experiments.

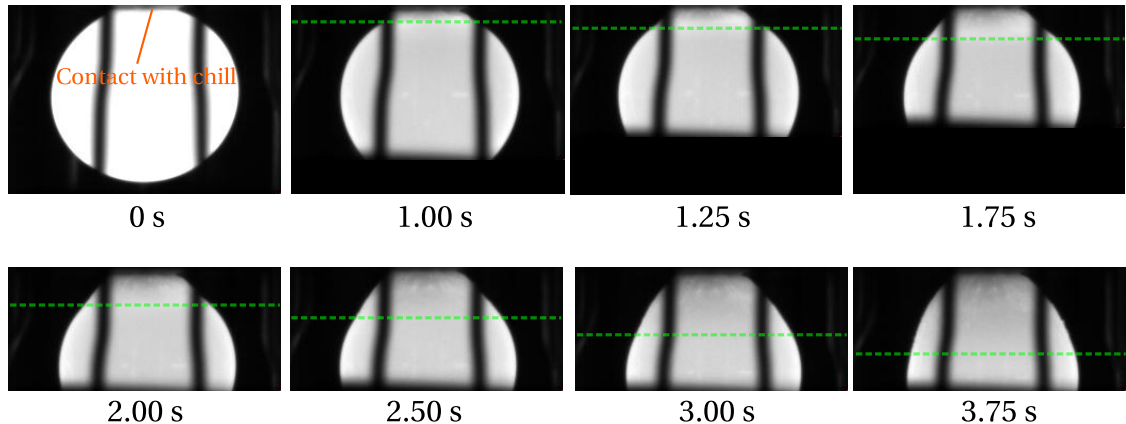


Fig. 5.30 – Image sequence given by a high speed camera on-board a TEMPUS parabolic flight (parabola #14 Oct 2014), showing the solidification progress between 0 s (when contact with the chill is initiated) to 3.75 s in a Fe-0.9 wt.% C-0.2 wt.% Si steel droplet. The progress of the solidification front is marked by the green dashed line. In some frames, the droplet is partially hidden by the narrow opening of the sample holder facing the camera.

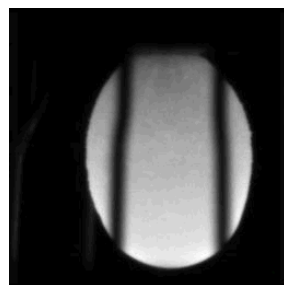


Fig. 5.31 – Camera image from the TEMPUS 2014 experiment, showing the fully solidified droplet with a deformed shape after 10 s.

Numerical contribution

A former numerical contribution was done by [Rivaux \[2011\]](#) at CEMEF, as mentioned in the first chapter. His model considered both the steel droplet and the ceramic chill in a Lagrangian formulation, i.e. each object is modelled using a separate mesh. Conservation equations of mass, energy, chemical species and momentum were solved in the metal domain, while the energy conservation was the sole equation solved on the chill mesh. The mechanical problem was divided into two parts: fluid mechanics and solid mechanics. For the first part, the momentum conservation in the liquid phase was solved using an incompressible P1/P1 SUPG-PSPG formulation of Navier-Stokes equations, i.e. without any contraction for the liquid phase neither solidification shrinkage at the solid-liquid interface. The second part, solid mechanics, was solved using P1+/P1 formulation to predict solid deformation caused by the solid's thermal contraction as well as solidification shrinkage, using an elastic-viscoplastic behaviour.

The simulation results showed that the total droplet deformation that has been observed in the experiments is not primarily due to solid deformation. The density jump between the solid and liquid phases at the solidification front is actually predominant. High speed camera images shown in [figs. 5.30](#) and [5.31](#) endorse this observation, where the droplet underwent a continuous spherical-to-elliptic shape change while the solidification front travelled away from the contact point. Another interesting point to comment is the computation of solidification shrinkage in the solid resolution, although this type of shrinkage does not generate stresses in the solidifying alloy, compared to thermal contraction for instance.

Thermal contraction and strains in the solid phase were computed and coupled with fluid mechanics but hardly managed to retrieve the final shape of the droplet reported in the experiment, as revealed in [fig. 5.30](#).

5.8.2 Computational configuration

Geometry and mesh

The simulation considers only 1/4 of the droplet-gas system, given the axial symmetry of the problem. Furthermore, the substrate is implicitly taken into account via a boundary condition, as explained in the next section. This is sufficient in the current context, because we are only interested in the energy transfer from the droplet to the substrate.

The steel sample is not perfectly spherical initially as surface oscillations perturb the equilibrium shape. Such perturbations may be attributed to Lorentz forces created by the positioning coil. The droplet hence is compared to an ellipsoid having a vertical minor axis of 5.68 mm and a horizontal major axis of 6.6 mm [[Rivaux 2011](#)], as shown in [fig. 5.32](#). The top is a planar surface (diameter of 2 mm), where the contact is initiated. Also in [fig. 5.32](#), the alloy is immersed in a gas medium (argon), such that both domains form together 1/4 of a cylinder having 8 mm in radius and 8 mm in height.

The mesh is then automatically adapted to the moving interface using *Remesh2*. We adopt the same remeshing strategy applied for computations shown in [figs. 5.10b](#) and [5.11b](#), whereby a fixed mesh size, h_M , is imposed in the metal domain, another fixed size, h_A , for the argon domain, while the interface is remeshed using anisotropic elements. All remeshing parameters are found in [table 5.8](#). The corresponding parameters are given by [table 5.8](#). Remeshing is performed each second.

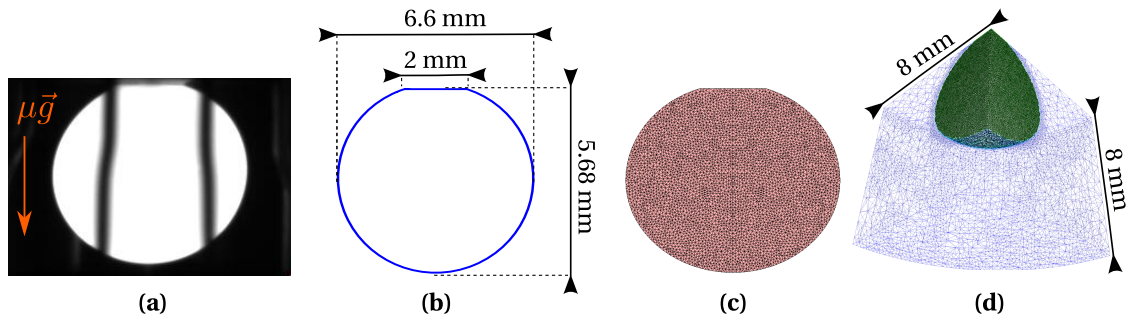


Fig. 5.32 – (a) The camera frame before the onset of solidification gives the essential information to (b) rebuild the droplet geometry then (c) a standalone 2D mesh used to obtain (d) the final immersed 3D mesh corresponding to time 0 s in [fig. 5.30](#).

Table 5.8 – Summary of the mesh parameters used to generate an adaptive mesh, along with the level mixing thickness, ε . Refer to [section 2.6.2](#) for the definition of each mesh parameter.

Mesh parameter	Value
ε	1.5×10^{-4} m
$h_n = h_\tau$	2×10^{-5} m
h_M	1×10^{-4} m
h_A	6×10^{-4} m
Remeshing frequency	1 s
Number of nodes	$\approx 10^5$
Number of elements	$\approx 5 \times 10^5$

Initial and boundary conditions

The thermal boundary conditions are set as follows: heat loss by radiation is not considered in our model, hence all boundaries are considered adiabatic, except for the metal-substrate contact area which is substituted by an equivalent convection boundary condition.

For the velocity-pressure boundary conditions, [fig. 5.33](#) shows that a no-slip condition is imposed on the droplet-substrate surface, since this area solidifies first without further fluid motion, as shows [fig. 5.30](#). It is noted that the first solidified shell may experimentally deform under thermal contraction stresses, but we do not consider it hereafter, unlike what was done by [Rivaux \[2011\]](#). For the rest of the domain, we impose the normal velocity component to zero on both symmetry faces, while keeping free tangential components. The remaining boundaries, namely the top and the outer lateral surface of the argon gas, have free velocity components. However, such condition may cause instability in the level set transport solver. This problem has been reported by [\[Basset 2006\]](#), showing a limitation in the imposed boundary conditions between Navier-Stokes solver and level set transport. Therefore, we limit these instabilities by imposing a no-slip condition, thus allowing the argon to flow in the computational domain through the outer lateral surface. The cylinder height was taken big enough to prevent any flow damping near the droplet's north pole, which may spuriously alter its final shape. The pressure condition for the argon gas is left free for all boundaries. The adopted time step is 0.01 s.

Choice of alloy

Various steel grades were considered in the CCEMLCC project, depending on whether the considered alloy will be used for parabolic flights or sounding rocket missions. A medium-carbon steel, Fe-0.9 wt.% C-0.2 wt.% Si, was affected for TEMPUS parabolic flights. For TEXUS missions, the sample is a low-carbon steel and the grade is designated as "*b1*" alloy. Its nominal composition is given in [table 5.9](#).

As our approach relies on thermodynamic tabulations, we show in the next section that we can take into account the multicomponent alloy to predict segregation, by considering first only one species, hence a binary Fe-C alloy, refer to as *b1Bin* alloy. In a later step, we consider a ternary Fe-C-Si alloy, *b1Tern*. Finally, we consider a quaternary Fe-C-Mn-Si alloy, *b1Quat*.

By performing the same reduced-gravity simulation while varying the alloy from binary to quaternary, we can study how the varying solidification paths (as a consequence of macrosegregation) may affect the final droplet shape, as the shrinkage profile is directly related to the solid fraction and its evolution with time.

Table 5.9 – Nominal composition (wt.%) of the experimental *b1* steel and its binary, ternary and quaternary alloys approximations, respectively *b1Bin*, *b1Tern* and *b1Quat*.

Alloy	C	Si	Mn	Al	S	P
<i>b1</i>	0.105	0.268	0.636	0.0067	0.009	0.0189
<i>b1Bin</i>	0.105	-	-	-	-	-
<i>b1Tern</i>	0.105	0.268	-	-	-	-
<i>b1Quat</i>	0.105	0.268	0.636	-	-	-

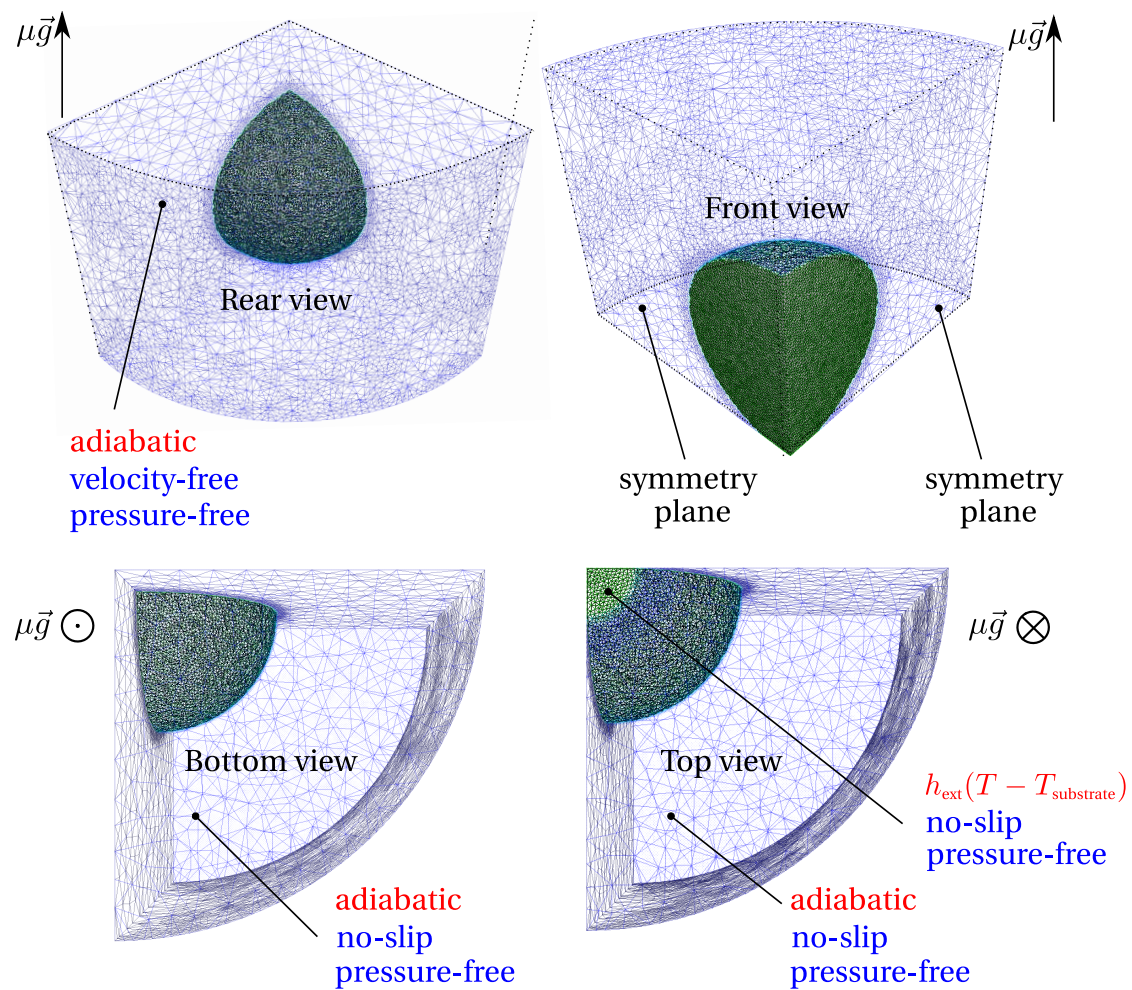


Fig. 5.33 – 3D views showing the thermal (in red) and mechanical (in blue) boundary conditions used in reduced-gravity simulations. The symmetry planes represent the following set of boundary conditions: adiabatic, zero normal velocity, free tangential velocity and pressure-free.

Parametric study: final shape prediction

In this subsection, we focus on obtaining a comparable finale shape of the droplet between the experiment and simulation. To do so, we study the variations of 2 main important parameters: first, the heat transfer coefficient of the metal-substrate contact surface that controls the heat extraction and hence the solidification rate. The second parameter is the magnitude if the gravitational field, which has a great influence on the fluid flow inside the molten droplet. The importance of this parametric study is two-fold:

1. in our model, the energy equation solved with the level set methodology considers only heat conduction and advection in the gas A, hence no account for the heat dissipated by radiation. Therefore a trial-and-error strategy is necessary to determine an optimal value of h_{ext} to ensure that the solidification rate is comparable to the experimental measurements,
2. from a hydrodynamics perspective, a containerless molten droplet levitated under reduced-gravity conditions is maintained nearly spherical under the action of surface tension forces. Other forces due to tangential surface tension gradients (Marangoni force) or Lorentz force may also exist. Although possible to implement by the CSF method, accounting numerically for surface tension adds complexity to the model by imposing a time step constraint. However, if we neglect this force, the droplet will tend to collapse if gravity acceleration is fast enough. Consequently, a parametric study helps us determine this gravity threshold, while neglecting surface tension and Lorentz forces.

A series of test simulations were launched in the aim of getting comparable results with the experiment. Several values of h_{ext} were tested in the interval $[10^2; 10^6] \text{ W m}^{-2} \text{ K}^{-1}$, while the gravity acceleration influence was tested for values lying in the interval $[10^{-6}; 10^{-2}] \text{ m s}^{-2}$. To demonstrate the effect of varying these parameters, we present a parametric study in [table 5.10](#), where only the most relevant cases are studied with a binary alloy, Fe-0.105 wt.% C.

Table 5.10 – Summary of the parametric study for the conductive heat transfer coefficient (H) and the magnitude of the gravity vector (G, not to be confused with thermal gradient). The cases are defined by fixing each parameter to a reference value then varying the latter parameter. The reference values, $H_0 = 6 \times 10^4 \text{ W m}^{-2} \text{ K}^{-1}$ and $G_0 = 5 \times 10^{-5} \text{ m s}^{-2}$, ensure a good compromise when compared to the experimental solidification rate and final droplet shape.

Case	$h_{\text{ext}} [\text{W m}^{-2} \text{ K}^{-1}]$	$\ g\ [\text{m s}^{-2}]$
H1G0	10^3	5×10^{-5}
H2G0	10^4	5×10^{-5}
H3G0	10^5	5×10^{-5}
H4G0	10^6	5×10^{-5}
H0G1	6×10^4	10^{-3}
H0G2	6×10^4	10^{-4}
H0G3	6×10^4	10^{-5}
H0G4	6×10^4	10^{-6}

We start the analysis by observing the results in [fig. 5.35](#), where the parameter h_{ext} increases from case H1G0 to H4G0, while maintaining a constant gravity acceleration at $5 \times 10^{-5} \text{ m s}^{-2}$. In the first case, H1G0, the heat coefficient is at its lowest between the droplet and the chill. As

this contact is the only way to dissipate heat from the droplet, a low heat exchange coefficient means a slow cooling. Therefore, contact area of the droplet solidifies first. As we consider a fixed solid in our model, any solidified part can no longer move or deform. As time passes, solidification is slow, such that the droplet starts collapsing at about 10 sec, undergoing a significant shape change under the gravity's action. It is not clear if such microgravity conditions are sufficient to deform the droplet as simulated in case H1G0. In fact, surface tension forces might play a central role in stabilising the sample shape by minimising its surface energy. As we neglect it in our simulations, the droplet naturally deforms in the direction of the gravity vector. We can make the same conclusion for case H2G0, while taking note of a thicker solid shell base in the horizontal direction, featuring also necking around the droplet axis mid-height. It should be noted that in both cases H1G0 and H2G0, solidification is not complete at 15 s.

More interesting results are obtained in case H3G0 where the heat coefficient is two orders of magnitude higher than that in the first case. The high solidification rate allows the mushy front to propagate further before deformation occurs by gravity. We see a global deformation which is qualitatively comparable to the experimental results: an ellipsoidal form with a longer vertical axis (i.e. in the direction of the microgravity vector) with respect to the initial shape, while the horizontal axis decreases compared to the original sample diameter. Finally, we observe the same deformation tendency if we compare cases H3G0 and H4G0. The latter becomes closer to a situation of pure shrinkage flow. Consequently, its final shape corresponds to a global shrinkage of the initial one.

In order to have a clear idea on the effect of varying the cooling rate parameter on mass conservation, we plot in fig. 5.34a the mass variation versus time for all four cases. We can notice that mass variation for case H4G0 occurs between 2% and -1% near the solidification end, recording the least variations compared to other cases. On the other hand, cases H1G0 and H2G0 show an important mass loss before solidification comes to end, reaching -11%. We are particularly interested in case H3G0, which shows a good compromise between the deformation magnitude and mass loss, the latter being at -3% of metal mass.

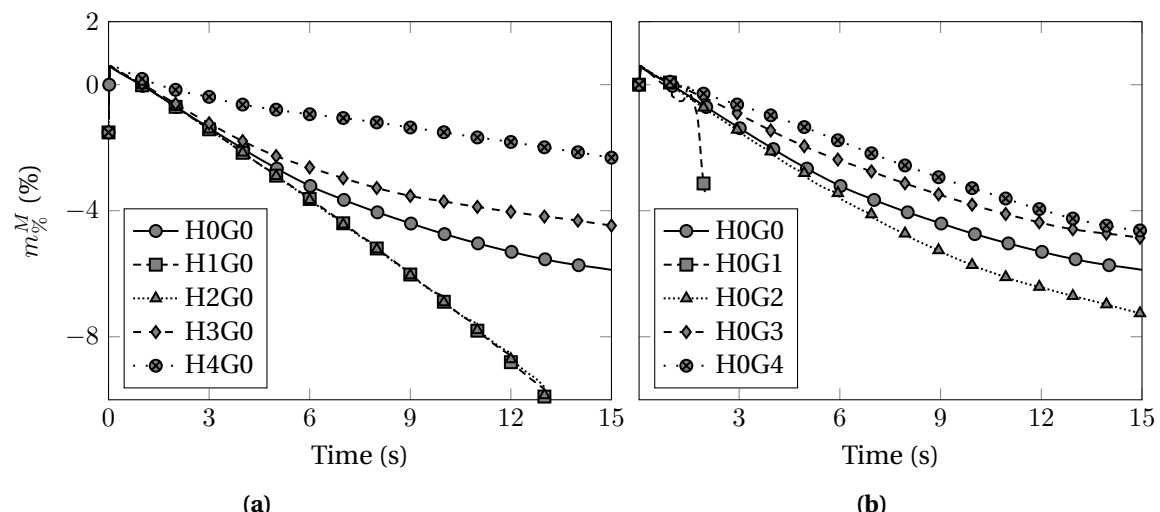


Fig. 5.34 – Mass conservation analysis for (a) cases H0G0 (reference) and HxG0 ($x=1,2,3,4$) and (b) cases H0G0 (reference) and H0Gx ($x=1,2,3,4$), where Hx increases for an increasing x , while G decreases for increasing x . All values are defined in table 5.10.

Now, we study the effect of varying the gravity parameter and its influence on the final deformation. We observe first the results for case H0G1 where gravity magnitude is about four orders less than the Earth gravity at zero altitude. While the base solidifies, the remaining part falls down deforming severely by its weight and leading to a non-converging level set transport. The last recorded time is 1.75 s. For case H0G2, the droplet is less solicited by its weight, and therefore solidifies while having a vertically elongated shape. It should be reminded that in the current global numerical model does not account for the metal's surface tension, which may clearly have a drastic influence on the final shape, especially at higher gravity magnitudes, such as for cases H0G1 and H0G2. Moving on to cases H0G3 and H0G4, the weight driving force becomes negligible compared to the shrinkage driving force. Therefore, the sample shows little lateral deformation, while in the central vertical plane of the droplet, the droplet has shrunk when compared to the initial profile. This is more visible in case H0G4, where the final shape is overall smaller than the initial volume, which is not the same as found in cases H3G0 and H4G0. The mass conservation analysis corresponding to the gravity magnitude variation are plotted in [fig. 5.34b](#). The plots show, as expected, better mass conservation for decreasing gravity acceleration, i.e. from case H0G1 to H0G4. We think however that surface tension would change this analysis, and non-convergence obtained in case H0G1 may be prevented.

5.8.3 Texus binary alloy

Optimal configuration

This contact surface between the droplet and the chill is modelled by a Fourier condition with $T_{ext}=25\text{ }^{\circ}\text{C}$ and an effective exchange coefficient h_{ext} of $6 \times 10^4 \text{ W m}^{-2} \text{ K}^{-1}$. The h_{ext} coefficient's value has been determined by running multiple simulations with different values in the aim of predicting a front speed as closer as possible to the experimental measurements plotted in [fig. 5.37](#). The best match for the final shape while preserving a front propagation speed close to 0.7 mm s^{-1} , was obtained by setting simultaneously $h_{ext} = 6 \times 10^4 \text{ W m}^{-2} \text{ K}^{-1}$ and $\|g\| = 5 \times 10^{-5} \text{ m s}^{-2}$. These values are included in [table 5.11](#) along with the other simulation parameters. It is reminded that for the species conservation, the non monolithic strategy is used. The optimal computational configuration is now known, thus we proceed to simulate the solidification of the binary alloy given previously in [table 5.9](#).

Results

The nominal composition for this alloy is Fe-0.105 wt.% C. In order to obtain accurate segregation results, a fine resolution mapping was performed from equilibrium calculations, using 20 values of composition between a minimum of 0.01 wt.% and 1 wt.%. This is equivalent for a composition step of 0.0495 wt.%, with a temperature step of 1 °C varying in the interval [20 °C; 1600 °C]. The importance of choosing small steps in composition and temperature is to predict accurate solidification paths during macrosegregation (relative to the droplet scale), which is the main input of solidification shrinkage. Therefore, less accurate mappings may result in false shrinkage profile prediction, as will be shown henceforth.

Using the initial and boundary conditions defined earlier, 15 seconds of simulation give the final shrinkage profile shown in [fig. 5.38](#). We notice that the predicted overall deformation of the droplet is in a good agreement with the experimental shape after solidification. This agreement is still not perfect as some key input parameters are still missing in the model, namely the real

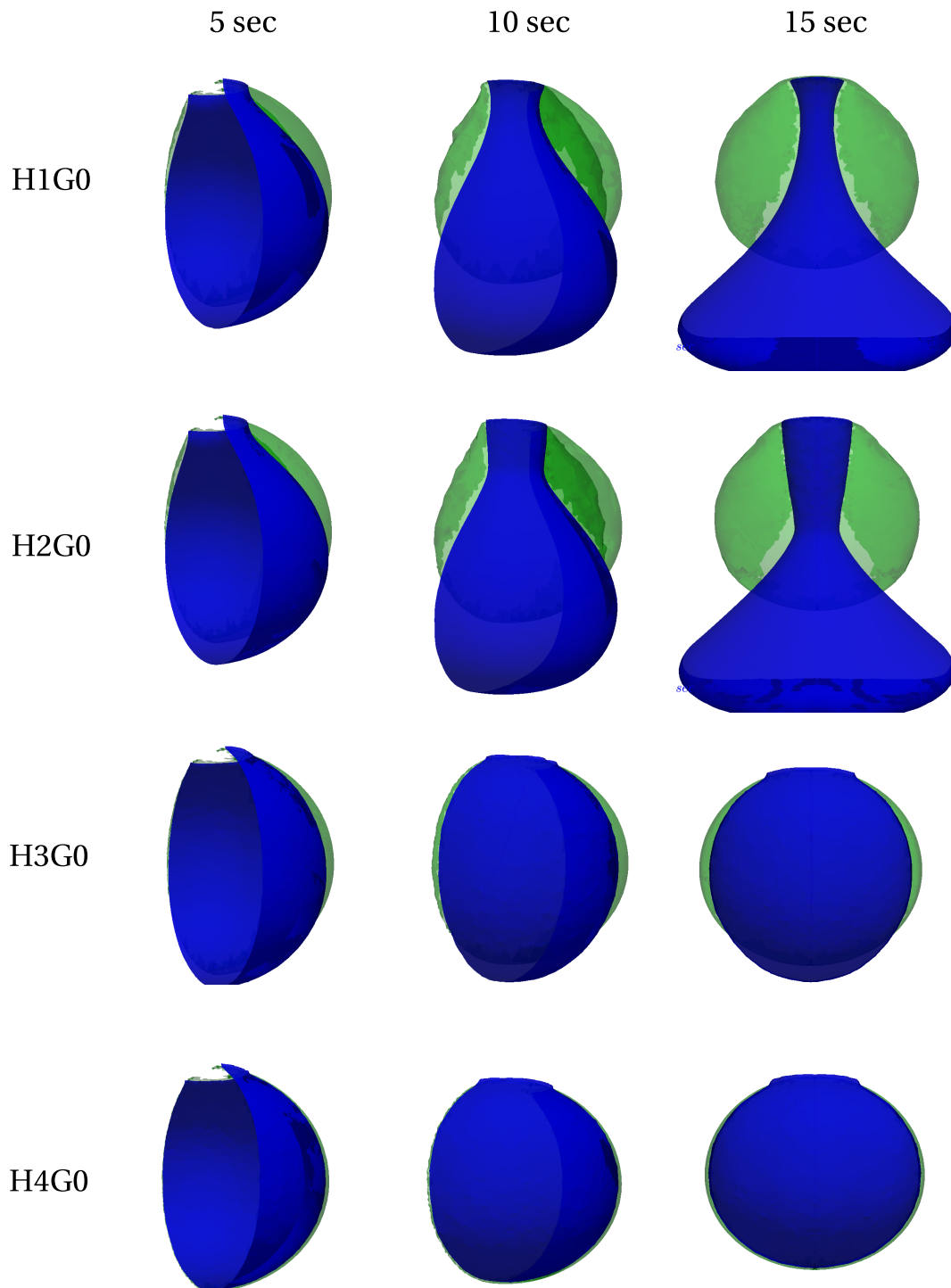


Fig. 5.35 – 3D snapshots of a droplet (only half shown for symmetry) undergoing solidification shrinkage where the heat exchange coefficient increases from H1 to H4 according to [table 5.10](#). The green surface is the initial droplet profile while the blue surface is the deforming droplet profile. The camera rotation over time allows observing deformation from different angles. The gravity vector points downwards.

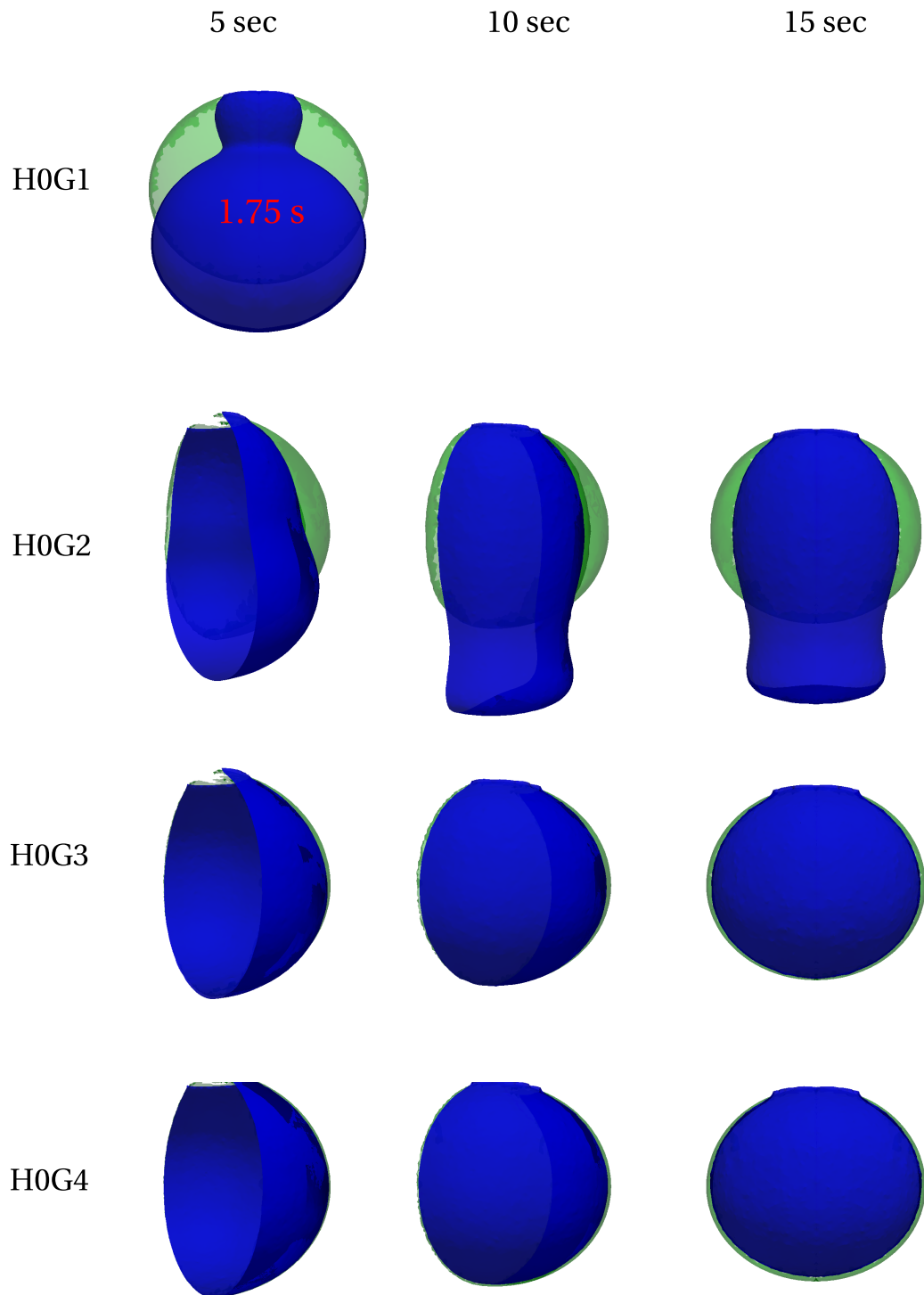


Fig. 5.36 – 3D snapshots of a droplet (only half shown for symmetry) undergoing solidification shrinkage where the magnitude of the gravitational field decreases from G1 to G4 according to [table 5.10](#). The green surface is the initial droplet profile while the blue surface is the deforming droplet profile. The camera rotation over time allows observing deformation from different angles. The gravity vector points downwards.

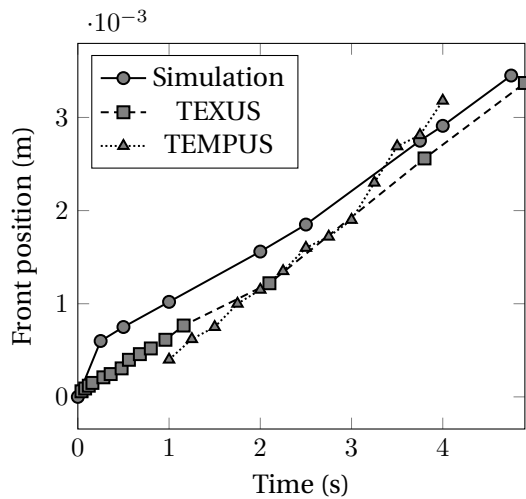


Fig. 5.37 – Position of solidification front versus time for the binary alloy simulation compared to the experimental findings of the TEXUS-46 flight in 2009 and TEMPUS 2014 measurements [Gandin 2014].

gravity acceleration on-board the TEXUS sounding rocket missions and the correct heat flux between the sample and the substrate. It is emphasized that for higher gravity accelerations or lower heat transfer, surface tension is of central importance since it counters the gravitational force by stabilising the *M-A* boundary.

Three solid phases are considered for the *b1Bin* alloy: a primary BCC phase, a peritectic FCC phase and a cementite phase. The latter can be obtained by cooling the sample at low temperatures to achieve solid-state transformation. The next point to discuss is segregation and fluid flow. With the chosen gravity acceleration, the liquid metal moves in the downward direction when the ceramic substrate comes from above the droplet. As soon as solidification takes place right after the metal-substrate contact, a BCC-rich mushy zone forms near the contact surface. The abrupt phase change imposes a fast shrinkage rate, which tends to straighten the interface near the substrate, as we can observe in [fig. 5.38](#). A part of the flow thus deviates towards the solid front to compensate for the density increase, as shown in [fig. 5.39](#). This flow pattern in the sample shows distinct regions: at 0.25 s and 1 s in the previous figure, upward flow driven by solidification shrinkage contributes to a slight enrichment by inverse segregation, while a downward flow driven by gravity redistributes species in the containerless melt. Upon completely solidifying, the droplet forms a rigid and fixed solid, surrounded by natural argon flow.

The fluid flow is behind the reduced-gravity segregation shown at different stages in [fig. 5.40](#). As earlier mentioned, a restricted region of positive segregation settles at the contact area with the substrate, from the first second after the contact. Later, between 2 s and 8 s, the solid front advances in the melt, creating a noticeable negatively segregated area, about 4% less than the nominal composition, just below the positive segregation zone. Normally, we would expect that the composition decreases gradually once the solid front advances in time, as confirm the 1D segregation profiles in [fig. 5.17](#). To interpret this unusual observation, we refer to the fluid flow shown earlier in [fig. 5.39](#). At 0.25 s, a velocity zero-level isovolume (i.e. depicting a volume with null velocity magnitude) forms between the two distinct regions of upward and downward flow. The strong negative divergence that settles in this area results in solute depletion in the

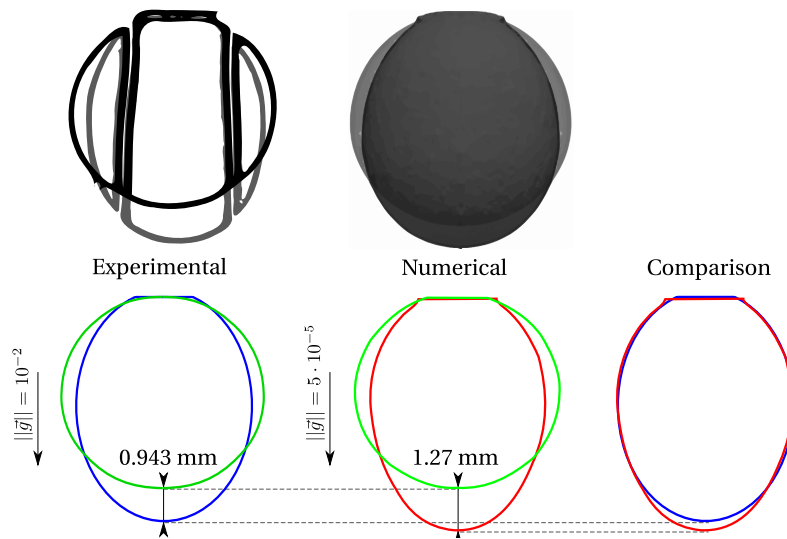


Fig. 5.38 – Comparison of experimental (blue) and numerical (red) shrinkage profiles, compared to their respective initial shapes (green). An image processing algorithm is used to extract the droplet outlines from the experimental images. The experimental displacement of the droplet was estimated by scaling the initial numerical profile to the initial experimental profile, and then comparing the final profiles. The gravitational field points downwards, depicted by the arrow (note that the vector length is not scaled to its magnitude).

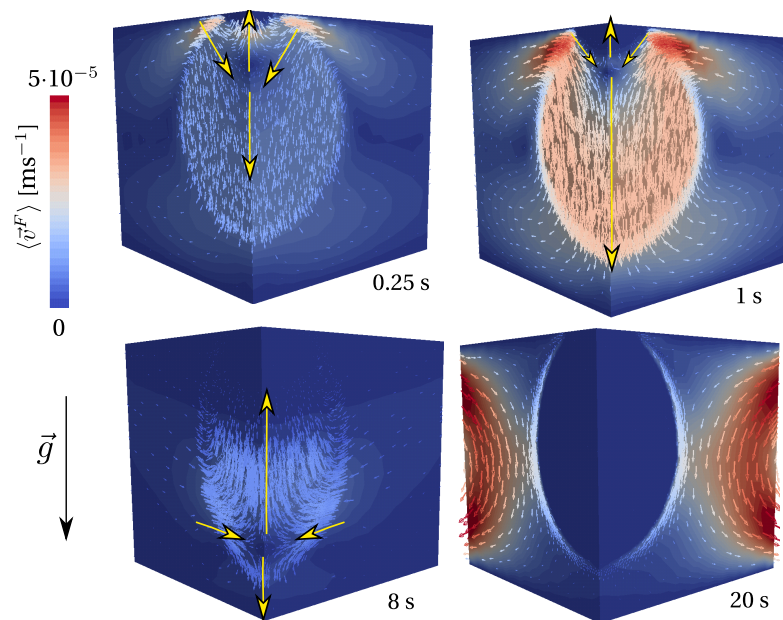


Fig. 5.39 – Flow patterns in reduced-gravity solidification with shrinkage: deviation towards the solidification front at 0.25 s and 1 s, contributing to solute transport in gravity's opposite direction. At 8 sec, the mushy zone reaches the droplet vertex marking a flow pattern change. At 20 s, the argon flows freely in the domain around the completely solidified and rigid sample. Yellow arrows help visualise the directions of the velocity field. Please note that the scale of latter snapshot has a maximum magnitude of 10^{-6} m s^{-1} , not shown for illustrative simplicity.

Table 5.11 – Parameters for the 3D simulation of the TEXUS droplet solidification under microgravity conditions.

Parameter	Symbol	Value	Unit
Nominal composition	w_0	0.105	wt.%
Segregation coefficient	k	Tabulations ([Andersson et al. 2002])	–
Liquidus slope	m_L	Tabulations ([Andersson et al. 2002])	K wt.% ⁻¹
Liquid density	$\langle \rho \rangle^l$	Tabulations ([Andersson et al. 2002])	kg m ⁻³
Solid density	$\langle \rho \rangle^s$	2800	kg m ⁻³
Air density	$\langle \rho \rangle^a$	1.3	kg m ⁻³
Liquid viscosity	μ^l	10 ⁻³	Pa s
Air viscosity	μ^a	10 ⁻⁴	Pa s
Air thermal conductivity	κ^a	0.01	W m ⁻¹ K ⁻¹
Liquid thermal conductivity	κ^l	42	W m ⁻¹ K ⁻¹
Solid thermal conductivity	κ^s	42	W m ⁻¹ K ⁻¹
Solute diffusion in the liquid	$\langle D \rangle^l$	1 × 10 ⁻⁹	m ² s ⁻¹
Solute diffusion in the solid	$\langle D \rangle^s$	0	m ² s ⁻¹
Solute diffusion in the air (fictitious)	$\langle D \rangle^a$	(Non monolithic)	m ² s ⁻¹
Gravity acceleration	$\ g\ $	5 × 10 ⁻⁵	m s ⁻²
Heat transfer coefficient	h_{ext}	6 × 10 ⁴	W m ⁻² K ⁻¹
External temperature	T_{ext}	25	°C
Time step	Δt	0.01	s
Convergence criterion (residual)	ε_R	10 ⁻⁴	–
Convergence criterion (temperature)	ε_T	10 ⁻¹	K

two directions and due to the various driving forces.

However, at 1 s, the zero isovolume clearly shrinks in a matter of only 0.75 s. That is because the initial temperature gradient is the highest during the process, then it decreases gradually. Since a higher temperature gradient produces a greater cooling flux according to the Fourier model, solidification is faster in the beginning and the volume shrinkage is fast, hence the shrinkage flow coexists with the gravity flow. As the transformation progresses, shrinkage flow becomes insignificant compared to the latter, therefore the negative segregation intensity decreases gradually from 2.2 mm to 4.3 mm from the chill, corresponding to the first seconds of contact ($t < 8$ s). This result is also shown in fig. 5.42 where we plot the relative segregation profile along the vertical rotation axis of the droplet. At 8 s, fig. 5.39 shows the zero-velocity isovolume moved down the vertical revolution axis by following the solidification front, then vanishing at about 10 s. It means that from this point in time, the flow is so dissipated by the mushy zone's low permeability, hence the low-magnitude shrinkage flow dominates again. We may correlate this flow pattern once again to the segregation profile in fig. 5.42: As of 4.3 mm and down to the tip of the deformed sample, we observe a steady rise in solute content caused by the shrinkage-dominated flow between dendrites compensating for density differences.

In fig. 5.42, the final phase distribution along the vertical revolution axis is plotted. The plots

show that in the upper part of the droplet close to the chill, a eutectoid product (we may not speak of eutectoid microstructure as the current approach is only macroscopic, without information on the smaller scale) that results from the hypoeutectoid composition, consisting of 98% of α -BCC phase together and 2% of CEM between 0 and 2.9 mm away from the substrate. Beyond this point, the austenitic γ -FCC phase is gradually replaced by α -BCC, which represents the proeutectoid α phase, taking place before temperature reaches the eutectoid isotherm at 727 °C.

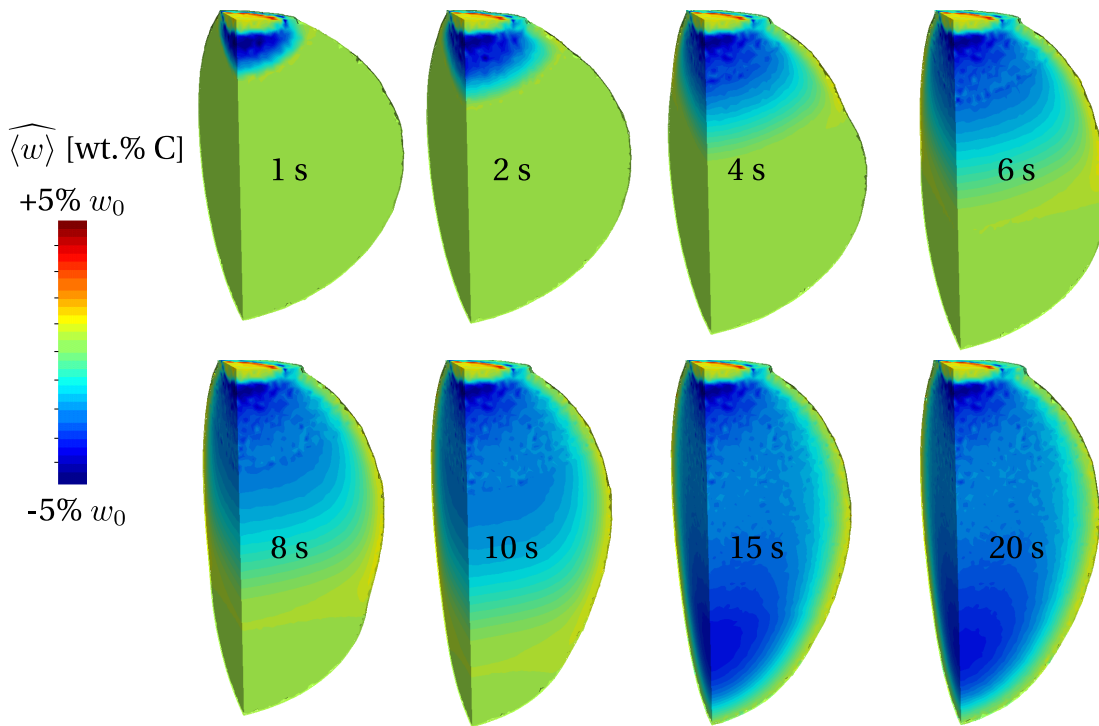


Fig. 5.40 – Evolution of the average composition with solidification time, showing evidence of segregation and shape deformation between 0 s and 20 s. (check animation in the PDF file).

A better global visualisation of the transformation is given in [fig. 5.41](#), at different time stages. Each column depicts a definite time with temperature and phase distribution.

5.8.4 Texus ternary and quaternary alloys

In this section, the aim is to predict macrosegregation in reduced-gravity solidification of the *b1* alloy, the latter being considered as a ternary and then as a quaternary alloy (cf. [table 5.9](#)). We want to show that, on the one hand our model handles multicomponent alloys (based on equilibrium conditions), while on the other hand, how transformation paths vary by adding additional components, thus changing the shrinkage kinetics, hence the final sample shape. The first visible sign of different paths during solidification is given in [fig. 5.43](#). We can see that upon adding additional chemical species while applying the same cooling conditions, a different liquid fraction remains after 15 s, showing evidence of slower solidification as we go from binary to quaternary. Also, with multicomponent alloys like *b1Tern* and *b1Quat*, an additional solid phase may appear, that is the M_7C_3 carbide. Slower cooling rates result in more

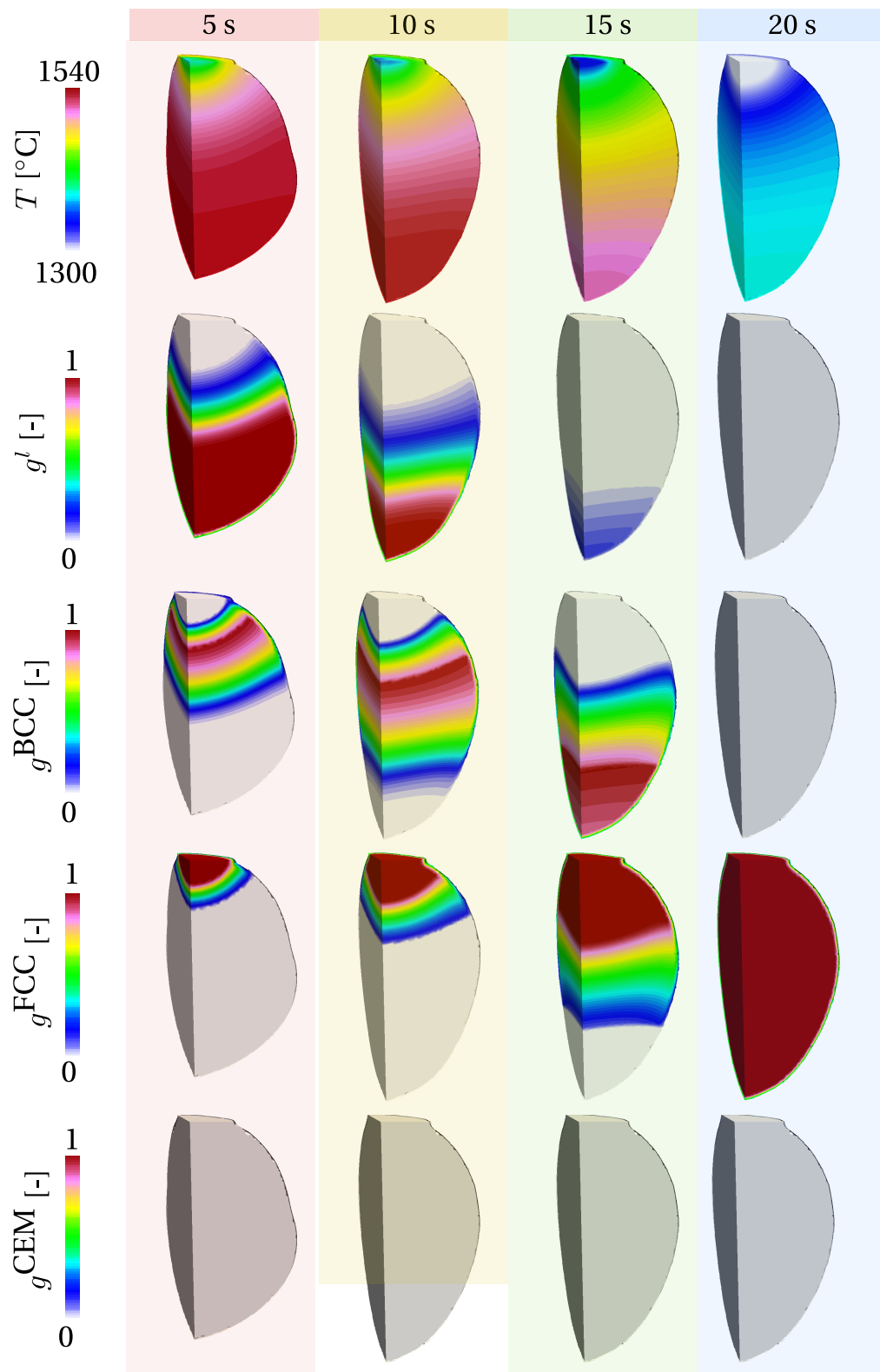


Fig. 5.41 – Solidification progress at 5, 10, 15 and 20 s showing the effect of segregation on the transformation paths, from liquid to solid and solid-state.

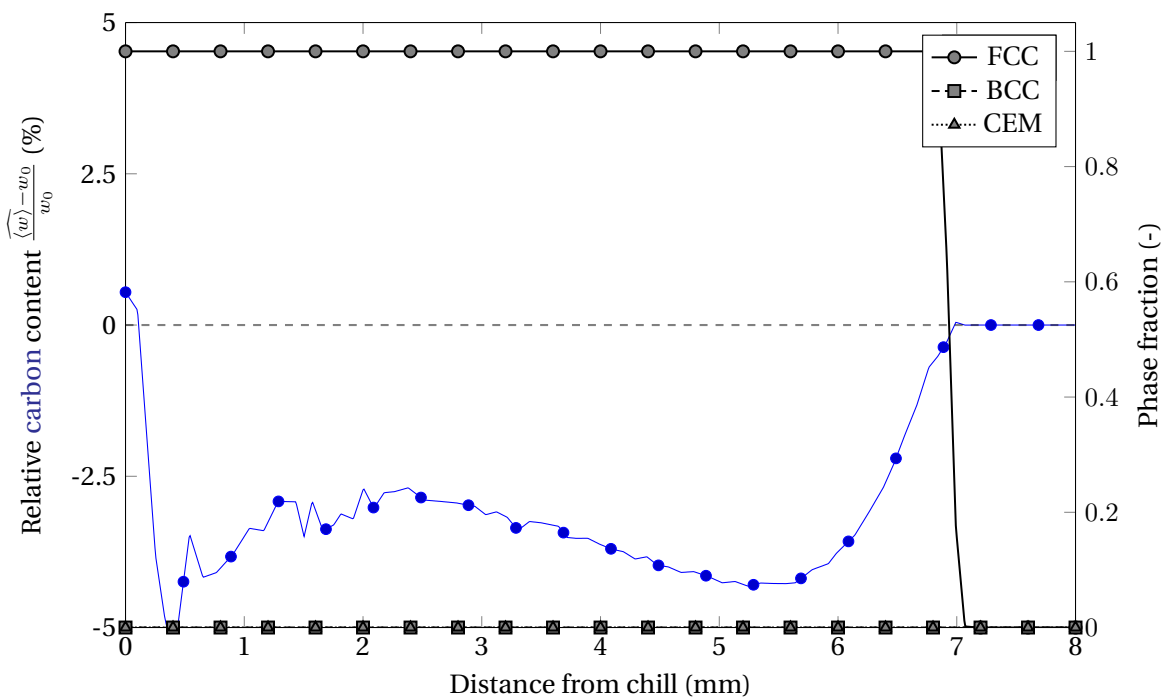


Fig. 5.42 – Relative segregation profile in percent with respect to the nominal composition, along the vertical revolution axis of the solidified sample at a temperature lower than 1100 °C. Phase fractions are superimposed on the same graph and their values are read on the right y-axis.

elongated droplet shapes due to weight force, whereas shrinkage forces tend to counter this effect. Therefore the final predicted shape is different, as shown earlier in the parametric study. In fig. 5.44, we focus on the final droplet profile caused by varying the number of solute elements. We clearly notice that the multicomponent solidification results in a slightly more elongated shape. All cases were obtained using the optimal simulation parameters determined previously by the parametric study, i.e. thermal exchange coefficient, h_{ext} , of $6 \times 10^4 \text{ W m}^{-2} \text{ K}^{-1}$ and a gravitational acceleration, $\|g\|$, of $5 \times 10^{-5} \text{ m s}^{-2}$. The clear difference in solidification paths requires to do the same parametric study to get better simulation-vs-experiment prediction. However, as we have shown earlier the effect of varying these parameters on the final profile, we do not perform parametric studies for *b1Tern* and *b1Quat* alloys.

The vertical elongation obtained by the *b1Tern* sample is slightly different than the *b1Bin* result, as shown in fig. 5.44. Moreover, the final ternary and quaternary profiles are almost overlapping, indicating that the prediction accuracy is very close for these alloys. This reveals the importance of simulating solidification processes with real alloy compositions instead of binary simplifications where the transformation path is not complex as a result of the smaller number of phases forming at equilibrium.

Nevertheless, it should be mentioned that the mapping resolution plays an important role in the accuracy of thermodynamic conversions. Therefore, tabulations size easily increases with the increasing number of solute elements, because of the greater number of temperature-composition combinations to scan while computing equilibrium. To test the effect of changing the mapping resolution, we repeated the binary sample solidification but with a composition step of 0.0495 wt.% instead of 0.0052 wt.% used for the *b1Bin* sample, i.e. about 10 times

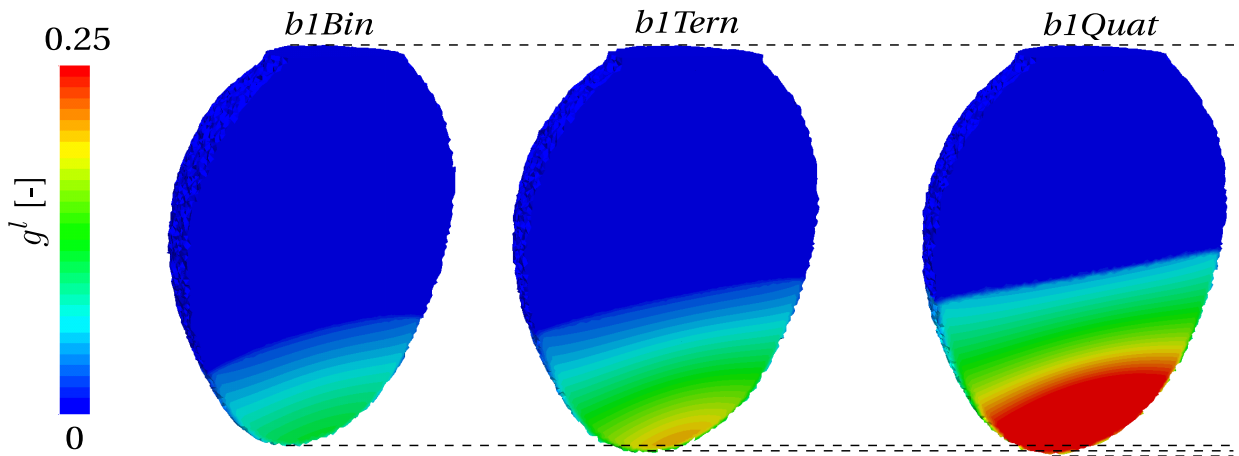


Fig. 5.43 – Snapshots showing the remaining volume fraction of liquid at 15 s in each sample of the binary, ternary and quaternary *b1* alloy. The dashed lines delimit the upper and lower limits of the droplets in the vertical direction.

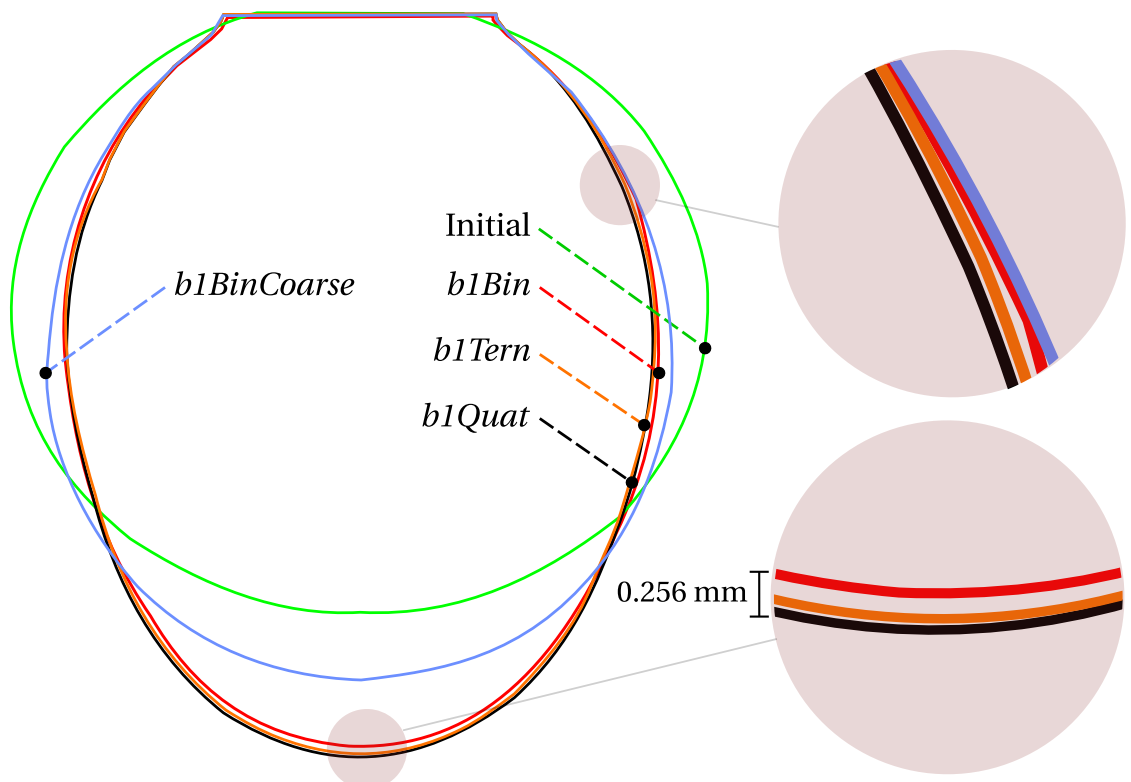


Fig. 5.44 – Comparison of final droplet profiles obtained by solidifying *b1Bin*, *b1Tern* and *b1Quat* samples, with respect to the initial profile. The *b1BinCoarse* sample is obtained using coarser composition steps.

coarser. The corresponding profile in [fig. 5.44](#), *b1BinCoarse*, shows less vertical elongation than predicted by the finer *b1Bin* tabulation. This is clearly due to inaccurate calculation of the solidification path, revealing the importance of mappings accuracy in predicting transformation-related physics.

In order to test the effect of the tabulation file size on computation time, we simulate again the quaternary solidification case but this time with a lightweight tabulation where all successive line with similar phase fractions outside the solidification range are deleted, giving what we call *b1QuatLite*. The resulting file is three time smaller than the original tabulation file. Surprisingly, the computation time for *b1QuatLite* shows no significant acceleration compared to *b1Quat*. The file size, proportional to the number of tabulated lines, is important as it causes a search overhead each time the conversion module is called. However, [table 5.12](#) reveals that the multi-variable interpolation overhead is even more important, resulting in longer computation times. This may be considered as a limitation of the thermodynamic mapping approach.

Table 5.12 – Information table showing the tabulations size for each alloy obtained by the same mapping resolution for temperature and composition, depending on the number of solute elements and phases. The temperature step is 1 °C and the range is the range is [20-1620]°C for all four cases . The computation time corresponds to the CPU time of a simulation running on 20 cores.

Alloy	Nb solutes	Composition range (wt.%)	Composition step (wt.%)	Nb phases	Tabulation lines	Size (MB)	Computation time (s)
<i>b1Bin</i>	1	C: [0.0945-0.1155]	0.00525	4	185 010	4.37	59 461.5
<i>b1Tern</i>	2	C: [0.0945-0.1155] Si: [0.2412-0.2948]	0.00525 0.0134	5	220 250	10.18	62 644.4
<i>b1Quat</i>	3	C: [0.0945-0.1155] Mn: [0.5724-0.6996] Si: [0.2412-0.2948]	0.00525 0.0318 0.0134	5	1 101 250	66.89	85 476.7
<i>b1QuatLite</i>	3	C: [0.0945-0.1155] Mn: [0.5724-0.6996] Si: [0.2412-0.2948]	0.00525 0.0318 0.0134	5	326 014	20.93	84 104.8

Finally we are interested in comparing the macrosegregation levels obtained in all three solidification cases. Segregation maps are presented in [fig. 5.45](#) on a symmetry plane section. First, we compare the carbon segregation as it is the common species among the presented alloys. The first difference is a remarkable positive macrosegregation of 3.5% at the chill contact of the *b1Tern* and *b1Quat* samples, while being less prominent for *b1Bin*.

As we explained earlier, this positive macrosegregation taking place at the beginning of solidification is related to the shrinkage flow (cf. [fig. 5.39](#)) created by the strong thermal gradient in the contact zone. As the thermal gradient in this zone is almost the same for all three cases at solidification onset, the higher velocity which is responsible for the noticeable positive macrosegregation in both multicomponent samples, is related to the solidification path varying with the number of species. Two regions of negative macrosegregation are observed across the samples, with various amplitudes. The first region lies just below the chill contact. It corresponds to the solute depletion caused by an upward shrinkage flow and a downward gravity flow. With the advancement of the solidification front, the gravity flow dominates forcing the remaining liquid to fall down while dragging the species from the sides of the droplet to the centre. This creates a radial negative segregation pattern, as seen in [fig. 5.45](#).

The last result regarding the multicomponent solidification application in reduced-gravity

conditions is a composition plot in [fig. 5.46](#) for each species in the solidified samples. This is basically similar to the analysis we made for [fig. 5.45](#), but this plot show the composition profile along the revolution axis.

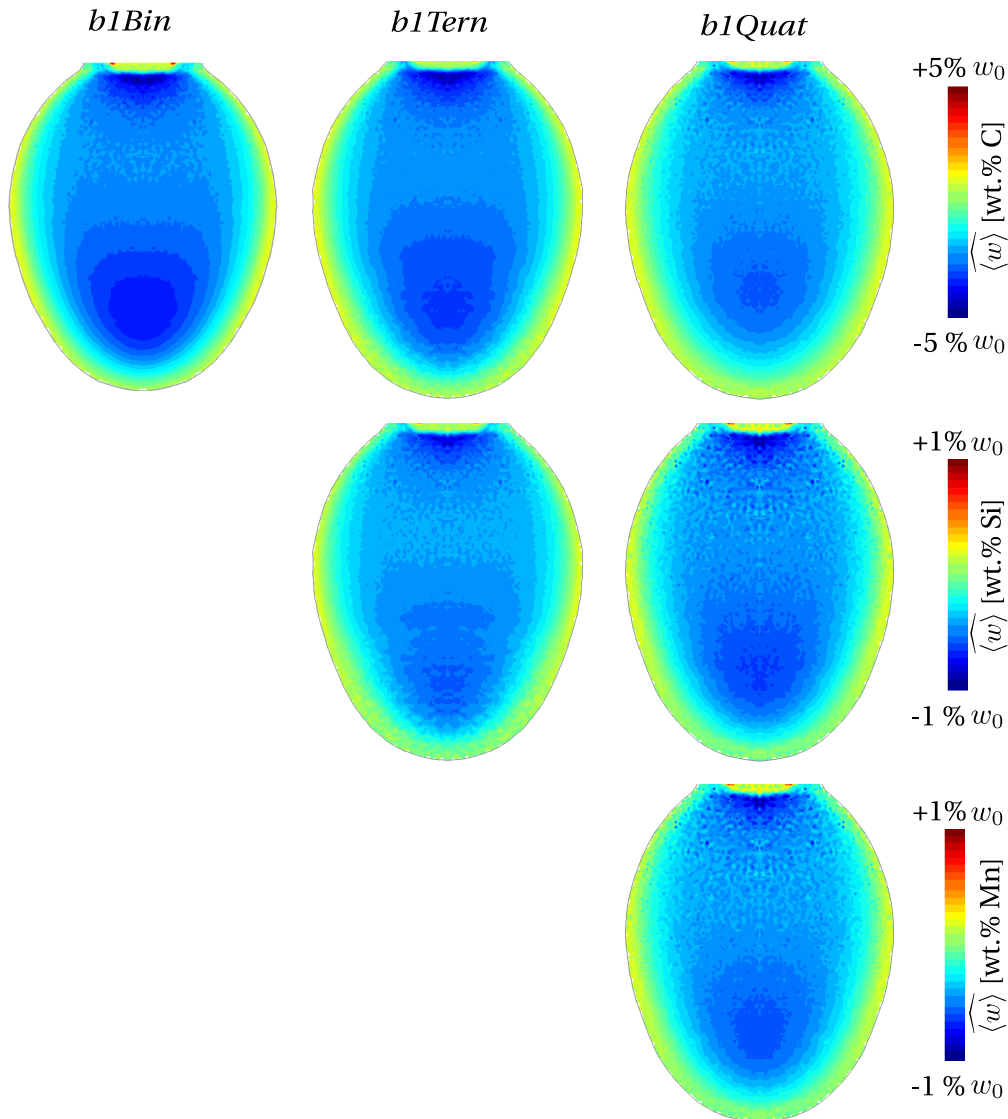


Fig. 5.45 – Segregation maps relative to each alloy, showing positive and negative mesosegregation of each chemical species for *b1Bin*, *b1Tern* and *b1Quat* samples.

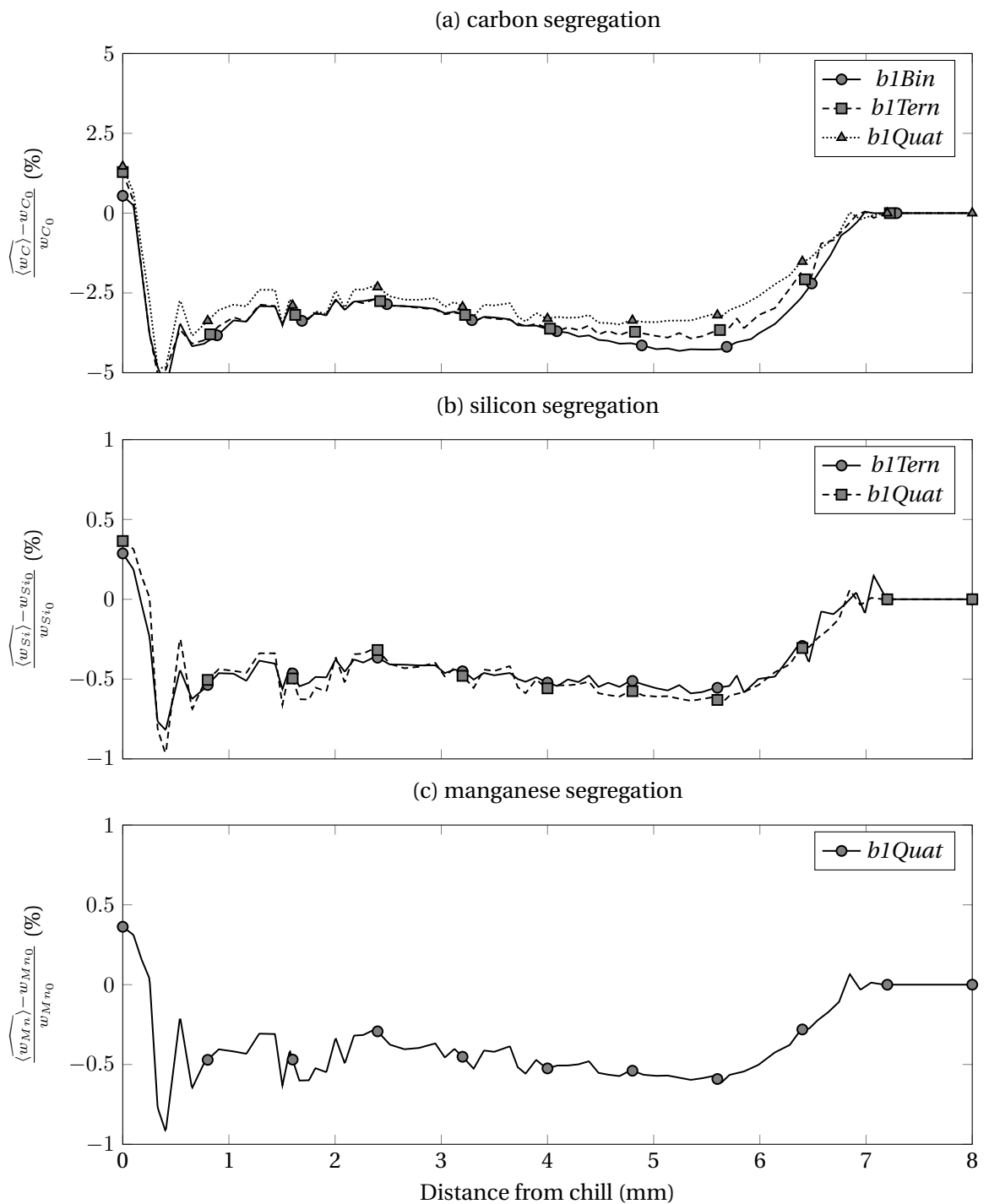


Fig. 5.46 – Relative macrosegregation profiles as functions of the distance from the chill, plotted for (a) carbon (b) silicon and (c) manganese elements along the vertical revolution axis of the solidified sample.

Résumé chapitre 5

Ce dernier chapitre est dédié à la prise en compte du retrait à la solidification à l'origine de la déformation de la surface libre métal-air, en présence des phénomènes de ségrégation. Pour ce faire, le modèle de solidification utilisé précédemment pour prédire la macroségrégation induite par convection thermosolutale en monodomaine, est enrichi par une méthode de suivi direct d'interface, la level set. Les équations du modèle sont alors reformulées dans un contexte eulérien multidomaine-multiphasé, i.e. où deux domaines mutliphasés sont séparés par une interface mobile, l'aspect mutliphasé dans chaque domaine étant géré par la méthode de prise de moyenne volumique.

Un premier cas d'application 1D est ensuite présenté. C'est un cas qui avait fait l'objet de validation du *Tsolver* dans le chapitre 3, et qui est refait avec des masses volumiques solide et liquide différentes. Cette application simple permet toutefois de comprendre le phénomène de ségrégation inverse résultant de l'écoulement du liquide vers le front de solidification pour compenser la différence des masses volumiques des phases, ce qui enrichit en solutés la partie du métal en contact avec le refroidisseur. Ce phénomène est souvent observé en surfaces des lingots en contact avec les moules. Des courbes de refroidissement ainsi qu'un bilan de conservation de masse de métal sont présentés pour permettre de comprendre l'effet de l'introduction de la méthode level set sur la physique de la solidification.

La seconde application est aussi un cas de validation utilisé dans un chapitre précédent, issu d'une simulation sans retrait présente dans la littérature [CAROZZANI et al. 2013]. Cependant, le but en est maintenant de tester la robustesse du modèle en présence de convection naturelle, d'origine thermique dans l'air et thermosolutale dans le métal, avec suivi de déformation de l'interface par retrait à la solidification. Nous utilisons une méthode de remaillage adaptatif basée sur la projection sur les arêtes [COUPEZ et HACHEM 2013], permettant d'avoir une résolution de maillage fine autour des zones d'intérêt, notamment l'interface décrite par level set, le vecteur vitesse et la concentration moyenne. Ce couplage de techniques numériques permet de déterminer à la fois la retassure en surface du lingot et la macroségrégation, présente également sous forme de canaux.

Dans le dernier cas, il s'agit de la solidification d'une goutte d'acier en microgravité. Des essais expérimentaux de solidification déclenchée par contact avec un substrat sont présentés avec la forme finale de la goutte. Pour pouvoir prédire la déformation de la goutte en présence de ségrégations, nous considérons trois nuances issues du même alliage : un binaire (*b1Bin*) Fe-C, un ternaire (*b1Tern*) Fe-C-Si et finalement un quaternaire (*b1Quat*) Fe-C-Mn-Si. D'abord, une étude paramétrique est faite en se servant de l'alliage binaire, dans le but de déterminer les paramètres optimaux de vitesse de refroidissement et d'accélération gravitationnelle, pour se rapprocher du profil expérimental de la goutte déformée en fin de solidification. Ensuite, nous simulons la solidification de chaque alliage en montrant la déformation finale ainsi que la distribution finale des espèces chimiques.

Conclusion and Perspectives

The current thesis proposes a numerical model to predict macrosegregation in different contexts: without or with overall metal volume change. The first case considers no average density change during solidification, assuming that the liquid and solid phases in the metal have the same density. On the other hand, the second case considers that the difference in metallic phase densities causes the average density to change, causing the metal's volume to change concurrently.

Temperature resolution compatible with thermodynamic mapping: In this thesis, we have introduced and validated a finite element method to solve energy conservation with phase change, based on thermodynamic data mapping and having the temperature as a main variable (*Tsolver*). The algorithm proved to be faster for several computations shown in chapters 3 and 4, when compared to the enthalpy-based method (*Hsolver*). The approach is also well suited to predict macrosegregation of both binary and multicomponent alloys. Some limitations are met nevertheless. It is important to have prior knowledge of composition variations during solidification in order to adapt to limit the mapping size while also keeping fine composition and temperature steps. Finer steps ensure more accurate transformation paths. We may also conclude that this thermodynamic mapping approach is still to equilibrium assumptions (full equilibrium or solid-liquid interface equilibrium). [Tourret et al. \[2011\]](#) proposed a similar solution but supports more than just a lever rule for microsegregation, by allowing input of diffusion coefficients.

Channel segregation: Using our energy solver, the Navier-Stokes solver and species conservation solver, we attempted modelling an experimental benchmark of directional (upward) In-75 wt.% Ga solidification. Some of the experimental data was used to get a closer numerical configuration to the experiment. Two scales of modelling were considered, a purely macroscopic finite-element (FE) approach and a coupled mesoscopic-macroscopic approach relying on cellular automata (CA) for the small scales and also on FE for the greater scales, hence the approach name CAFE. The pure FE model considers only average macroscopic conservation equations (mass, energy, species and liquid momentum) on a finite-element grid, with a constant volume for the metal, i.e. no shrinkage is possible. The FE approach resulted in either no channel segregation at all at low temperature gradients, or a limited number of channels when the temperature gradient was increased. These numerical observations reveal however discrepancy in the general fluid flow behaviour and subsequent formation of segregation channels, when qualitatively compared to experimental findings. This is where the CAFE model is introduced to show the advantage of nurturing the FE scale with feedback information coming from the lower scale CA grid, where nucleation and growth of grain envelopes are

systematically solved. Indeed, CAFE predictions showed a noticeable difference with respect to the pure FE approach. The overall fluid flow pattern is much more complicated and random, many convective plumes form mainly at grain boundaries as a result of solute enrichment inside the mushy zone (solutal convection), powered also by the temperature gradient (thermal convection). The comparison between the experimental data and numerical predictions is only qualitative, due to the lack of an array of crucial data, such as the nuclei positions, the undercooling, magnitude of fluid flow inside the rising convective plumes and others. In order to conduct a quantitative comparison, such data may be very useful to calibrate the CAFE model. The second limitation in this comparison is the difficulty of simulating the real solidification cell with a thickness of 150 µm. Therefore, the simulations considered an alternate thickness of 1 mm, due to the huge FE mesh that would be obtained if we want at least 5 elements in the thickness to correctly predict the flow. Using adaptive remeshing could be a solution, but should be used with care since small elements are almost needed everywhere in the mushy zone where thermosolutal convection is initiated. It is interesting to model the entire thin solidification cell for future research. In addition, it is interesting to compare simulation results with real single grain casting experiments, which allow to understand better the basic mechanisms of channel segregation, which could precede the formation of freckle defects.

Solidification shrinkage: To model this phenomenon, we go from the previous FE model, and reformulate the conservation equations to be compatible with the level set method, which helps us track the boundary between the metal and a surrounding gas domain. The presence of the latter is important as its volume should compensate for the metal's volume shrinkage. A detailed analysis is given to explain the various interfaces which form the metal-air boundary in reality along with the necessary assumptions to get the equivalent definition in the model. The monolithic energy, fluid momentum and species conservation equations incorporate the volume change in the metal by using the mass balance. A modified Darcy was defined to account for the presence of the gas domain in the monolithic fluid momentum equation. Regarding species conservation, three modelling strategies were introduced: if we consider that the gas domain contains fictitious metallic species, then we may define a monolithic strategy with limited solute diffusion known as MD, and a monolithic strategy with limited diffusion and advection in the gas known as MDA. The third strategy consists of solving for species conservation in the metal while completely disregarding the gas domain, then making the necessary correction.

Three applications cases are presented in the increasing order of modelling dimension: 1D, 2D and 3D. The first application shows the performance of the model applied to one-dimensional solidification shrinkage configuration without then with macrosegregation, using each of the 3 proposed strategies. The results show an instability in the predicted average composition field surrounding the metal-air boundary, where a positive segregation peak is seen in the air domain. This peak amplitude is reduced when the MDA strategy is used, and almost disappears with the NM strategy. A full analysis made for each strategy reveals that the latter species conservation strategy performs better than the former two, without having a bad effect on species mass conservation and metal mass conservation.

The 2D application is based on a comparison with a Sn-3 wt.% Pb solidification benchmark that simulates the configuration of [Hebditch and Hunt \[1974\]](#) experiments. The experiment

was simulated by [Carozzani et al. \[2013\]](#) assuming a constant volume for the metal. In this work, the level set context allows predicting the final ingot shape once completely solidified. The added value of this result with respect to previous simulation attempts is the prediction of mesosegregation and macrosegregation trends in the shrunk ingot, which is closer to the experimental results. As future work, it may be interesting to couple the work done by [Chen et al. \[2014\]](#) for grain structure prediction in an increasing metal volume using the level set context with the current developments in order to get more accurate predictions compared to the experiment. Knowing that all the previous suggestions are made in the context of a fixed and rigid solid phase, it is also interesting to continue research in the direction of coupling the fluid and solid mechanics in the same simulation.

The 3D application simulates solidification of a small steel droplet in a reduced-gravity environment, as an extension to the work of [Rivaux \[2011\]](#). A parametric study is performed to determine the best heat transfer coefficient values of the contact surface with the ceramic chill, and the magnitude of the microgravity vector resulting. The optimal values were used to simulate solidification of the steel droplet, but approximating the composition by a binary equivalent. Segregation and subsequent phase distributions analysis is given. The final droplet shape is compared to the experimental observation obtained with a high speed camera, by image processing the latter then scaling the initial experimental and numerical profiles, and finally comparing the fully solidified profiles. The agreement is acceptable. However, it is useful to accurately compare in the future the simulation performance to the experiment by physically processing the solidified sample to obtain the final length and chemical composition. These data are still not made available. Later, the same simulation is conducted but considering ternary and quaternary approximations of the same steel. Segregation profiles do not reveal high segregation intensities due to the limited flow under reduced gravity. An analysis of the competition of fluid motion between microgravity forces and suction to shrinkage inside the droplet is given.

Bibliography

[Andersson et al. 2002]

Andersson, J.-O., Helander, T., Höglund, L., Shi, P., and Sundman, B. (2002). "Thermo-Calc & DICTRA, computational tools for materials science". *Calphad*, 26 (2), pp. 273–312. URL: <http://www.sciencedirect.com/science/article/pii/S0364591602000378> (cited on pages 52, 54, 55, 79, 154).

[Arnold et al. 1984]

Arnold, D. N., Brezzi, F., and Fortin, M. (1984). "A stable finite element for the stokes equations". *CALCOLO*, 21 (4), pp. 337–344. URL: <http://link.springer.com/article/10.1007/BF02576171> (cited on page 62).

[Auburtin et al. 2000]

Auburtin, P., Wang, T., Cockcroft, S. L., and Mitchell, A. (2000). "Freckle formation and freckle criterion in superalloy castings". *Metallurgical and Materials Transactions B*, 31 (4), pp. 801–811. URL: <http://link.springer.com/article/10.1007/s11663-000-0117-9> (cited on page 83).

[Auburtin 1998]

Auburtin, P. B. L. (1998). "Determination of the influence of growth front angle on freckle formation in superalloys". PhD thesis. Vancouver, BC, Canada: University of British Columbia. URL: https://circle.ubc.ca/bitstream/handle/2429/8676/ubc_1998-345084.pdf?sequence=1 (cited on page 75).

[Babuška 1971]

Babuška, I. (1971). "Error-bounds for finite element method". *Numerische Mathematik*, 16 (4), pp. 322–333. URL: <http://link.springer.com/article/10.1007/BF02165003> (cited on page 62).

[Barbosa and Hughes 1991]

Barbosa, H. J. C. and Hughes, T. J. R. (1991). "The finite element method with Lagrange multipliers on the boundary: circumventing the Babuška-Brezzi condition". *Computer Methods in Applied Mechanics and Engineering*, 85 (1), pp. 109–128. URL: <http://www.sciencedirect.com/science/article/pii/004578259190125P> (cited on page 62).

[Basset 2006]

Basset, O. (2006). "Simulation numérique d'écoulements multi-fluides sur grille de calcul". PhD Thesis. École Nationale Supérieure des Mines de Paris. URL: <https://tel.archives-ouvertes.fr/tel-00376484> (cited on pages 30, 145).

[Beckermann 2002]

Beckermann, C. (2002). "Modelling of macrosegregation: applications and future needs". *International Materials Reviews*, 47 (5), pp. 243–261. URL: <http://www.maneyonline.com/doi/abs/10.1179/095066002225006557> (cited on page 7).

[Beckermann et al. 1999]

Beckermann, C., Diepers, H. J., Steinbach, I., Karma, A., and Tong, X (1999). "Modeling Melt Convection in Phase-Field Simulations of Solidification". *Journal of Computational Physics*, 154 (2), pp. 468–496. URL: <http://www.sciencedirect.com/science/article/pii/S0021999199963234> (cited on pages 24, 26).

[Beckermann et al. 2000]

Beckermann, C., Gu, J. P., and Boettinger, W. J. (2000). "Development of a freckle predictor via rayleigh number method for single-crystal nickel-base superalloy castings". *Metallurgical and Materials Transactions A*, 31 (10), pp. 2545–2557. URL: <http://link.springer.com/article/10.1007/s11661-000-0199-7> (cited on pages 69, 75).

Bibliography

[Bellet et al. 2009]

Bellet, M., Combeau, H., Fautrelle, Y., Gobin, D., Rady, M., Arquis, E., Budenkova, O., Dussoubs, B., Duterrail, Y., Kumar, A., Gandin, C. A., Goyeau, B., Mosbah, S., and Založník, M. (2009). "Call for contributions to a numerical benchmark problem for 2D columnar solidification of binary alloys". *International Journal of Thermal Sciences*, 48 (11), pp. 2013–2016. URL: <http://www.sciencedirect.com/science/article/pii/S129007290900177X> (cited on page 40).

[Bernacki et al. 2007]

Bernacki, M., Digonnet, H., Resk, H., Coupez, T., and Logé, R. (2007). "Development Of Numerical Tools For The Multiscale Modelling Of Recrystallization In Metals, Based On A Digital Material Framework". *AIP Conference Proceedings*. Vol. 908. AIP Publishing, pp. 375–380. URL: <http://scitation.aip.org/content/aip/proceeding/aipcp/10.1063/1.2740840> (cited on page 35).

[Boden et al. 2008]

Boden, S., Eckert, S., Willers, B., and Gerbeth, G. (2008). "X-Ray Radioscopic Visualization of the Solutal Convection during Solidification of a Ga-30 Wt Pct In Alloy". *Metallurgical and Materials Transactions A*, 39 (3), pp. 613–623. URL: <http://link.springer.com/article/10.1007/s11661-007-9462-5> (cited on page 76).

[Boettinger et al. 2002]

Boettinger, W. J., Warren, J. A., Beckermann, C., and Karma, A. (2002). "Phase-Field Simulation of Solidification". *Annual Review of Materials Research*, 32 (1), pp. 163–194. URL: <http://dx.doi.org/10.1146/annurev.matsci.32.101901.155803> (cited on page 24).

[Bogno et al. 2013]

Bogno, A., Nguyen-Thi, H., Reinhart, G., Billia, B., and Baruchel, J. (2013). "Growth and interaction of dendritic equiaxed grains: In situ characterization by synchrotron X-ray radiography". *Acta Materialia*, 61 (4), pp. 1303–1315. URL: <http://www.sciencedirect.com/science/article/pii/S1359645412008026> (cited on page 5).

[Brackbill et al. 1992]

Brackbill, J. U., Kothe, D. B., and Zemach, C (1992). "A continuum method for modeling surface tension". *Journal of Computational Physics*, 100 (2), pp. 335–354. URL: <http://www.sciencedirect.com/science/article/pii/002199919290240Y> (cited on page 26).

[Brezzi 1974]

Brezzi, F. (1974). "On the existence, uniqueness and approximation of saddle-point problems arising from lagrangian multipliers". *ESAIM: Mathematical Modelling and Numerical Analysis - Modélisation Mathématique et Analyse Numérique*, 8 (R2), pp. 129–151. URL: <https://eudml.org/doc/193255> (cited on page 62).

[Brody and Flemings 1966]

Brody, H. D. and Flemings, M. C. (1966). "Solute redistribution in denritic solidification". *AIME Met. Soc. Trans.*, 236, p. 615 (cited on page 17).

[Brooks and Hughes 1982]

Brooks, A. N. and Hughes, T. J. R. (1982). "Streamline upwind/Petrov-Galerkin formulations for convection dominated flows with particular emphasis on the incompressible Navier-Stokes equations". *Computer Methods in Applied Mechanics and Engineering*, 32 (1–3), pp. 199–259. URL: <http://www.sciencedirect.com/science/article/pii/0045782582900718> (cited on page 29).

[Buffet et al. 2010]

Buffet, A., Nguyen-Thi, H., Bogno, A., Schenk, T., Mangelinck-Noël, N., Reinhart, G., Bergeon, N., Billia, B., and Baruchel, J. (2010). "Measurement of Solute Profiles by Means of Synchrotron X-Ray Radiography during Directional Solidification of Al-4 wt% Cu Alloys". *Materials Science Forum*, 649, pp. 331–336. URL: <http://www.scientific.net/MSF.649.331> (cited on page 5).

[Carlson et al. 2002]

Carlson, K. D., Lin, Z., Hardin, R. A., and Beckermann, C. (2002). "Modeling Of Porosity Formation And Feeding Flow In Steel Casting". *Proceedings of the 56th SFSA Technical and Operating Conference*. Steel Founders' Society of America. URL: <http://goo.gl/p9ftCp> (cited on page 8).

[Carozzani et al. 2012]

Carozzani, T., Digonnet, H., and Gandin, C.-A. (2012). "3D CAFE modeling of grain structures: application to primary dendritic and secondary eutectic solidification". *Modelling and Simulation in Materials Science and Engineering*, 20 (1), p. 015010. URL: <http://iopscience.iop.org/0965-0393/20/1/015010> (cited on page 83).

[Carozzani et al. 2014]

Carozzani, T., Gandin, C.-A., and Digonnet, H. (2014). "Optimized parallel computing for cellular automaton-finite element modeling of solidification grain structures". *Modelling and Simulation in Materials Science and Engineering*, 22 (1), p. 015012. URL: <http://iopscience.iop.org/0965-0393/22/1/015012> (cited on page 83).

[Carozzani 2012]

Carozzani, T. (2012). "Développement d'un modèle 3D Automate Cellulaire-Éléments Finis (CAFE) parallèle pour la prédiction de structures de grains lors de la solidification d'alliages métalliques". PhD Thesis. Ecole Nationale Supérieure des Mines de Paris. URL: <http://pastel.archives-ouvertes.fr/pastel-00803282> (cited on page 11).

[Carozzani et al. 2013]

Carozzani, T., Gandin, C.-A., Digonnet, H., Bellet, M., Zaidat, K., and Fautrelle, Y. (2013). "Direct Simulation of a Solidification Benchmark Experiment". *Metallurgical and Materials Transactions A*, 44 (2), pp. 873–887. URL: <http://link.springer.com/article/10.1007/s11661-012-1465-1> (cited on pages 40, 68, 83, 84, 132, 135, 162, 165).

[Chen et al. 1997]

Chen, S., Merriman, B., Osher, S., and Smereka, P. (1997). "A Simple Level Set Method for Solving Stefan Problems". *Journal of Computational Physics*, 135 (1), pp. 8–29. URL: <http://www.sciencedirect.com/science/article/pii/S0021999197957211> (cited on page 24).

[Chen 2014]

Chen, S. (2014). "Three dimensional Cellular Automaton - Finite Element (CAFE) modeling for the grain structures development in Gas Tungsten / Metal Arc Welding processes". PhD thesis. Ecole Nationale Supérieure des Mines de Paris. URL: <https://pastel.archives-ouvertes.fr/pastel-01038028/document> (cited on pages 24, 108).

[Chen et al. 2014]

Chen, S., Guillemot, G., and Gandin, C.-A. (2014). "3D Coupled Cellular Automaton (CA)-Finite Element (FE) Modeling for Solidification Grain Structures in Gas Tungsten Arc Welding (GTAW)". *ISIJ International*, 54 (2), pp. 401–407 (cited on page 165).

[Choudhary and Ganguly 2007]

Choudhary, S. K. and Ganguly, S. (2007). "Morphology and Segregation in Continuously Cast High Carbon Steel Billets". *ISIJ International*, 47 (12), pp. 1759–1766. URL: https://www.jstage.jst.go.jp/article/isijinternational/47/12/47_12_1759/_article (cited on page 2).

[Clyne and Kurz 1981]

Clyne, T. W. and Kurz, W. (1981). "Solute redistribution during solidification with rapid solid state diffusion". *Metallurgical Transactions A*, 12 (6), pp. 965–971. URL: <http://link.springer.com/article/10.1007/BF02643477> (cited on page 17).

[Combeau et al. 1996]

Combeau, H., Drezet, J.-M., Mo, A., and Rappaz, M. (1996). "Modeling of microsegregation in macrosegregation computations". *Metallurgical and Materials Transactions A*, 27 (8), pp. 2314–2327. URL: <http://link.springer.com/article/10.1007/BF02651886> (cited on page 17).

[Combeau et al. 2009]

Combeau, H., Založník, M., Hans, S., and Richy, P. E. (2009). "Prediction of Macrosegregation in Steel Ingots: Influence of the Motion and the Morphology of Equiaxed Grains". *Metallurgical and Materials Transactions B*, 40 (3), pp. 289–304. URL: <http://link.springer.com/article/10.1007/s11663-008-9178-y> (cited on page 2).

[Copley et al. 1970]

Copley, S. M., Giamei, A. F., Johnson, S. M., and Hornbecker, M. F. (1970). "The origin of freckles in unidirectionally solidified castings". *Metallurgical Transactions*, 1 (8), pp. 2193–2204. URL: <http://link.springer.com/article/10.1007/BF02643435> (cited on page 73).

[Coupez 2011]

Coupez, T. (2011). "Metric construction by length distribution tensor and edge based error for anisotropic adaptive meshing". *Journal of Computational Physics*, 230 (7), pp. 2391–2405. URL: <http://www.sciencedirect.com/science/article/pii/S002199911000656X> (cited on page 35).

Bibliography

[Coupez and Hachem 2013]

Coupez, T. and Hachem, E. (2013). "Solution of high-Reynolds incompressible flow with stabilized finite element and adaptive anisotropic meshing". *Computer Methods in Applied Mechanics and Engineering*, 267, pp. 65–85. URL: <http://www.sciencedirect.com/science/article/pii/S0045782513002077> (cited on page 162).

[Coupez 1991]

Coupez, T. (1991). *Grandes transformations et remaillage automatique*. EMP. URL: <http://www.theses.fr/1991ENMP0615> (cited on page 33).

[Coupez 2000]

Coupez, T. (2000). "Génération de maillage et adaptation de maillage par optimisation locale". *Revue Européenne des Éléments*, 9 (4), pp. 403–423. URL: <http://www.tandfonline.com/doi/abs/10.1080/12506559.2000.10511454> (cited on page 33).

[Coupez et al. 2013]

Coupez, T., Jannoun, G., Veysset, J., and Hachem, E. (2013). "Edge-Based Anisotropic Mesh Adaptation for CFD Applications". *Proceedings of the 21st International Meshing Roundtable*. Ed. by X. Jiao and J.-C. Weill. DOI: 10.1007/978-3-642-33573-0_33. Springer Berlin Heidelberg, pp. 567–583. URL: http://link.springer.com/chapter/10.1007/978-3-642-33573-0_33 (cited on pages 35, 36).

[Courtois et al. 2014]

Courtois, M., Carin, M., Masson, P. L., Gaied, S., and Balabane, M. (2014). "A complete model of keyhole and melt pool dynamics to analyze instabilities and collapse during laser welding". *Journal of Laser Applications*, 26 (4), p. 042001. URL: <http://scitation.aip.org/content/lia/journal/jla/26/4/10.2351/1.4886835> (cited on page 24).

[Dantzig and Rappaz 2009]

Dantzig, J. A. and Rappaz, M. (2009). *Solidification*. EPFL Press (cited on pages 4, 8, 17, 18, 21, 100).

[Darcy 1856]

Darcy, H. (1856). *Les fontaines publiques de la ville de Dijon : exposition et application des principes à suivre et des formules à employer dans les questions de distribution d'eau*. V. Dalmont (Paris). URL: <http://gallica.bnf.fr/ark:/12148/bpt6k624312> (cited on page 5).

[Desbiolles et al. 2003]

Desbiolles, J.-L., Thévoz, P., Rappaz, M., and Stefanescu, D. (2003). "Micro-Macrosegregation Modeling in Casting: A Fully Coupled 3D Model". TMS Publ., pp. 245–252 (cited on page 75).

[Desmaison et al. 2014]

Desmaison, O., Bellet, M., and Guillemot, G. (2014). "A level set approach for the simulation of the multipass hybrid laser/GMA welding process". *Computational Materials Science*, 91, pp. 240–250. URL: <http://www.sciencedirect.com/science/article/pii/S092702561400278X> (cited on page 24).

[Digonnet et al. 2007]

Digonnet, H., Silva, L., and Coupez, T. (2007). "Cimlib: A Fully Parallel Application For Numerical Simulations Based On Components Assembly". *AIP Conference Proceedings*. Vol. 908. AIP Publishing, pp. 269–274. URL: <http://scitation.aip.org/content/aip/proceeding/aipcp/10.1063/1.2740823> (cited on page 12).

[Dijkstra 1959]

Dijkstra, E. W. (1959). "A note on two problems in connexion with graphs". *Numerische Mathematik*, 1 (1), pp. 269–271. URL: <http://link.springer.com/article/10.1007/BF01386390> (cited on page 32).

[DLR 2014]

DLR (2014). *ElectroMagnetic Levitation*. <http://goo.gl/e5JhiA> (cited on page 11).

[Doré et al. 2000]

Doré, X., Combeau, H., and Rappaz, M. (2000). "Modelling of microsegregation in ternary alloys: Application to the solidification of Al–Mg–Si". *Acta Materialia*, 48 (15), pp. 3951–3962. URL: <http://www.sciencedirect.com/science/article/pii/S1359645400001774> (cited on page 40).

[Du et al. 2007]

Du, Q., Eskin, D. G., and Katgerman, L. (2007). "Modeling Macrosegregation during Direct-Chill Casting of

- Multicomponent Aluminum Alloys". *Metallurgical and Materials Transactions A*, 38 (1), pp. 180–189. URL: <http://link.springer.com/article/10.1007/s11661-006-9042-0> (cited on page 40).
- [Du et al. 2001]**
Du, Q., Li, D., Li, Y., Li, R., and Zhang, P. (2001). "Simulating a double casting technique using level set method". *Computational Materials Science*, 22 (3–4), pp. 200–212. URL: <http://www.sciencedirect.com/science/article/pii/S0927025601001902> (cited on page 24).
- [Easton et al. 2011]**
Easton, M., Davidson, C., and StJohn, D. (2011). "Grain Morphology of As-Cast Wrought Aluminium Alloys". *Materials Transactions*, 52 (5), pp. 842–847 (cited on page 5).
- [El Jannoun 2014]**
El Jannoun, G. (2014). "Space-Time accurate anisotropic adaptation and stabilized finite element methods for the resolution of unsteady CFD problems". Theses. Ecole Nationale Supérieure des Mines de Paris. URL: <https://pastel.archives-ouvertes.fr/tel-01146245> (cited on page 35).
- [Ettrich et al. 2014]**
Ettrich, J., Choudhury, A., Tschukin, O., Schoof, E., August, A., and Nestler, B. (2014). "Modelling of transient heat conduction with diffuse interface methods". *Modelling and Simulation in Materials Science and Engineering*, 22 (8), p. 085006. URL: <http://iopscience.iop.org/0965-0393/22/8/085006> (cited on page 28).
- [Felicelli et al. 1991]**
Felicelli, S. D., Heinrich, J. C., and Poirier, D. R. (1991). "Simulation of freckles during vertical solidification of binary alloys". *Metallurgical Transactions B*, 22 (6), pp. 847–859. URL: <http://link.springer.com/article/10.1007/BF02651162> (cited on pages 6, 75).
- [Felicelli et al. 1998]**
Felicelli, S. D., Poirier, D. R., and Heinrich, J. C. (1998). "Modeling freckle formation in three dimensions during solidification of multicomponent alloys". *Metallurgical and Materials Transactions B*, 29 (4), pp. 847–855. URL: <http://link.springer.com/article/10.1007/s11663-998-0144-5> (cited on page 75).
- [Ferreira et al. 2004]**
Ferreira, I. L., Garcia, A., and Nestler, B. (2004). "On macrosegregation in ternary Al–Cu–Si alloys: numerical and experimental analysis". *Scripta Materialia*, 50 (4), pp. 407–411. URL: <http://www.sciencedirect.com/science/article/pii/S1359646203007346> (cited on page 6).
- [Ferreira et al. 2009]**
Ferreira, I., Moutinho, D., Gomes, L., Rocha, O., and Garcia, A. (2009). "Modeling and experimental analysis of macrosegregation during transient solidification of a ternary Al–6wt%Cu–1wt%Si alloy". *Philosophical Magazine Letters*, 89 (12), pp. 769–777. URL: <http://dx.doi.org/10.1080/09500830903292320> (cited on page 6).
- [Flemings and Nereo 1967]**
Flemings, M. C. and Nereo, G. E. (1967). "Macrosegregation: Part I". *Transactions of the Metallurgical Society of AIME*, 239, pp. 1449–1461 (cited on pages 6, 75).
- [Flemings and Nereo 1968]**
Flemings, M. C. and Nereo, G. E. (1968). "Macrosegregation: Part III". *Transactions of the Metallurgical Society of AIME*, 242, pp. 50–55 (cited on pages 6, 75).
- [Flemings et al. 1968]**
Flemings, M. C., Mehrabian, R., and Nereo, G. E. (1968). "Macrosegregation: Part II". *Transactions of the Metallurgical Society of AIME*, 242, pp. 41–49 (cited on pages 6, 75).
- [Gada and Sharma 2009]**
Gada, V. H. and Sharma, A. (2009). "On Derivation and Physical Interpretation of Level Set Method-Based Equations for Two-Phase Flow Simulations". *Numerical Heat Transfer, Part B: Fundamentals*, 56 (4), pp. 307–322. URL: <http://dx.doi.org/10.1080/10407790903388258> (cited on page 26).
- [Gandin 2000]**
Gandin, C. A. (2000). "From constrained to unconstrained growth during directional solidification". *Acta Mater*

Bibliography

rialia, 48 (10), pp. 2483–2501. URL: <http://www.sciencedirect.com/science/article/pii/S1359645400000707> (cited on pages 48, 60).

[Gandin 2014]

Gandin, C.-A. (2014). *Project ESA-MAP CCEMLCC phase #2 – Final Report* (cited on pages 141, 152).

[Gandin et al. 2003]

Gandin, C. A., Guillemot, G., Appolaire, B., and Niane, N. T. (2003). “Boundary layer correlation for dendrite tip growth with fluid flow”. *Materials Science and Engineering: A*, 342 (1–2), pp. 44–50. URL: <http://www.sciencedirect.com/science/article/pii/S0921509302002617> (cited on pages 84, 88).

[Genereux and Borg 2000]

Genereux, P. D. and Borg, C. A. (2000). “Characterization of Freckles in a High Strength Wrought Nickel Superalloy”. Warrendale, PA: K.A. Green, M. McLean, S. Olson, J.J. Schirra, TMS (The Minerals, Metals, and Materials Society), pp. 19–27. URL: http://www.tms.org/superalloys/10.7449/2000/Superalloys_2000_19_27.pdf (cited on page 75).

[Giamei and Kear 1970]

Giamei, A. F. and Kear, B. H. (1970). “On the nature of freckles in nickel base superalloys”. *Metallurgical Transactions*, 1 (8), pp. 2185–2192. URL: <http://link.springer.com/article/10.1007/BF02643434> (cited on pages 8, 75).

[Gibou et al. 2003]

Gibou, E., Fedkiw, R., Caflisch, R., and Osher, S. (2003). “A Level Set Approach for the Numerical Simulation of Dendritic Growth”. *Journal of Scientific Computing*, 19 (1–3), pp. 183–199. URL: <http://link.springer.com/article/10.1023/A%3A1025399807998> (cited on page 24).

[Gouttebroze 2005]

Gouttebroze, S. (2005). “Modélisation 3d par éléments finis de la macroségrégation lors de la solidification d’alliages binaires”. PhD thesis. École Nationale Supérieure des Mines de Paris. URL: <https://pastel.archives-ouvertes.fr/pastel-00001885/document> (cited on pages 11, 66).

[Gruau and Coupez 2005]

Gruau, C. and Coupez, T. (2005). “3D tetrahedral, unstructured and anisotropic mesh generation with adaptation to natural and multidomain metric”. *Computer Methods in Applied Mechanics and Engineering*, Unstructured Mesh Generation 194 (48–49), pp. 4951–4976. URL: <http://www.sciencedirect.com/science/article/pii/S0045782505000745> (cited on page 33).

[Guo and Beckermann 2003]

Guo, J. and Beckermann, C. (2003). “Three-Dimensional Simulation of Freckle Formation During Binary Alloy Solidification: Effect of Mesh Spacing”. *Numerical Heat Transfer, Part A: Applications*, 44 (6). <http://dx.doi.org/10.1080/716100512>, pp. 559–576. URL: <http://user.engineering.uiowa.edu/~becker/documents.dir/GuoFreckle.pdf> (cited on page 75).

[Hachani et al. 2012]

Hachani, L., Saadi, B., Wang, X. D., Nouri, A., Zaidat, K., Belgacem-Bouzida, A., Ayouni-Derouiche, L., Raimondi, G., and Fautrelle, Y. (2012). “Experimental analysis of the solidification of Sn–3 wt.%Pb alloy under natural convection”. *International Journal of Heat and Mass Transfer*, 55 (7–8), pp. 1986–1996. URL: <http://www.sciencedirect.com/science/article/pii/S0017931011007009> (cited on pages 6, 68, 132, 134, 135).

[Hachem et al. 2010]

Hachem, E., Rivaux, B., Kloczko, T., Digonnet, H., and Coupez, T. (2010). “Stabilized finite element method for incompressible flows with high Reynolds number”. *Journal of Computational Physics*, 229 (23), pp. 8643–8665. URL: <http://www.sciencedirect.com/science/article/pii/S0021999110004237> (cited on page 64).

[Hachem 2009]

Hachem, E. (2009). “Stabilized finite element method for heat transfer and turbulent flows inside industrial furnaces”. PhD Thesis. École Nationale Supérieure des Mines de Paris. URL: <https://tel.archives-ouvertes.fr/tel-00443532> (cited on page 63).

[Harlow and Welch 1965]

Harlow, F. H. and Welch, J. E. (1965). “Numerical Calculation of Time-Dependent Viscous Incompressible Flow

- of Fluid with Free Surface". *Physics of Fluids* (1958-1988), 8 (12), pp. 2182–2189. URL: <http://scitation.aip.org/content/aip/journal/pof1/8/12/10.1063/1.1761178> (cited on page 24).
- [Hebditch and Hunt 1974]**
Hebditch, D. J. and Hunt, J. D. (1974). "Observations of ingot macrosegregation on model systems". *Metallurgical Transactions*, 5 (7), pp. 1557–1564. URL: <http://link.springer.com/article/10.1007/BF02646326> (cited on pages 6, 68, 132, 164).
- [Hirt 1971]**
Hirt, C. W. (1971). "An arbitrary Lagrangian-Eulerian computing technique". *Proceedings of the Second International Conference on Numerical Methods in Fluid Dynamics*. Ed. by M. Holt. Lecture Notes in Physics 8. Springer Berlin Heidelberg, pp. 350–355. URL: http://link.springer.com/chapter/10.1007/3-540-05407-3_50 (cited on page 23).
- [Hirt and Nichols 1981]**
Hirt, C. W and Nichols, B. D (1981). "Volume of fluid (VOF) method for the dynamics of free boundaries". *Journal of Computational Physics*, 39 (1), pp. 201–225. URL: <http://www.sciencedirect.com/science/article/pii/0021999181901455> (cited on page 24).
- [Hitti 2011]**
Hitti, K. (2011). "Direct numerical simulation of complex Representative Volume Elements (RVEs): Generation, Resolution and Homogenization". PhD thesis. École Nationale Supérieure des Mines de Paris. URL: <https://pastel.archives-ouvertes.fr/pastel-00667428/document> (cited on page 35).
- [Hysing et al. 2009]**
Hysing, S., Turek, S., Kuzmin, D., Parolini, N., Burman, E., Ganesan, S., and Tobiska, L. (2009). "Quantitative benchmark computations of two-dimensional bubble dynamics". *International Journal for Numerical Methods in Fluids*, 60 (11), pp. 1259–1288. URL: <http://onlinelibrary.wiley.com/doi/10.1002/fld.1934/abstract> (cited on page 30).
- [Jannoun 2014]**
Jannoun, G. E. (2014). "Space-Time accurate anisotropic adaptation and stabilized finite element methods for the resolution of unsteady CFD problems". PhD thesis. Ecole Nationale Supérieure des Mines de Paris. URL: <https://pastel.archives-ouvertes.fr/tel-01146245/document> (cited on page 33).
- [Karagadde et al. 2014]**
Karagadde, S., Yuan, L., Shevchenko, N., Eckert, S., and Lee, P. D. (2014). "3-D microstructural model of freckle formation validated using in situ experiments". *Acta Materialia*, 79, pp. 168–180. URL: <http://www.sciencedirect.com/science/article/pii/S1359645414004984> (cited on page 83).
- [Karma and Rappel 1996]**
Karma, A. and Rappel, W.-J. (1996). "Phase-field method for computationally efficient modeling of solidification with arbitrary interface kinetics". *Physical Review E*, 53 (4), R3017–R3020. URL: <http://link.aps.org/doi/10.1103/PhysRevE.53.R3017> (cited on page 24).
- [Kobayashi 1988]**
Kobayashi, S. (1988). "Solute redistribution during solidification with diffusion in solid phase: A theoretical analysis". *Journal of Crystal Growth*, 88 (1), pp. 87–96. URL: <http://www.sciencedirect.com/science/article/pii/S0022024898900100> (cited on page 17).
- [Kohler 2008]**
Kohler, F. (2008). "Peritectic solidification of Cu-Sn alloys: microstructure competition at low speed". PhD Thesis. EPFL (cited on page 75).
- [Koshikawa et al. 2014]**
Koshikawa, T., Gandin, C.-A., Bellet, M., Yamamura, H., and Bobadilla, M. (2014). "Computation of Phase Transformation Paths in Steels by a Combination of the Partial- and Para-equilibrium Thermodynamic Approximations". *ISIJ International*, 54 (6), pp. 1274–1282 (cited on page 59).
- [Lee et al. 2002]**
Lee, P. D., Atwood, R. C., Dashwood, R. J., and Nagaumi, H. (2002). "Modeling of porosity formation in direct chill cast aluminum-magnesium alloys". *Materials Science and Engineering: A*, 328 (1–2), pp. 213–222. URL: <http://www.sciencedirect.com/science/article/pii/S0921509301016872> (cited on page 83).

Bibliography

[Lesoult 2005]

Lesoult, G. (2005). "Macrosegregation in steel strands and ingots: Characterisation, formation and consequences". *Materials Science and Engineering: A*, International Conference on Advances in Solidification Processes 413–414, pp. 19–29. URL: <http://www.sciencedirect.com/science/article/pii/S0921509305010063> (cited on pages 3, 6).

[Lesoult et al. 2001]

Lesoult, G., Albert, V., Appolaire, B., Combeau, H., Daloz, D., Joly, A., Stomp, C., Grün, G. U., and Jarry, P. (2001). "Equi-axed growth and related segregations in cast metallic alloys". *Science and Technology of Advanced Materials*, 2 (1), p. 285. URL: <http://iopscience.iop.org/1468-6996/2/1/A55> (cited on page 6).

[Liu 2005]

Liu, W. (2005). "Finite Element Modelling of Macrosegregation and Thermomechanical Phenomena in Solidification Processes". PhD thesis. École Nationale Supérieure des Mines de Paris. URL: <http://pastel.archives-ouvertes.fr/pastel-00001339> (cited on pages 11, 66).

[Ludwig et al. 2012]

Ludwig, A., Mogeritsch, J., Kolbe, M., Zimmermann, G., Sturz, L., Bergeon, N., Billia, B., Faivre, G., Akamatsu, S., Bottin-Rousseau, S., and Voss, D. (2012). "Advanced Solidification Studies on Transparent Alloy Systems: A New European Solidification Insert for Material Science Glovebox on Board the International Space Station". *JOM*, 64 (9), pp. 1097–1101. URL: <http://link.springer.com/article/10.1007/s11837-012-0403-4> (cited on page 6).

[Maitre 2006]

Maitre, E. (2006). "Review of numerical methods for free interfaces". Les Houches, France. URL: <http://gogl/Re6f3a> (cited on page 24).

[Martorano et al. 2003]

Martorano, M. A., Beckermann, C., and Gandin, C.-A. (2003). "A solutal interaction mechanism for the columnar-to-equiaxed transition in alloy solidification". *Metallurgical and Materials Transactions A*, 34 (8), pp. 1657–1674. URL: <http://link.springer.com/article/10.1007/s11661-003-0311-x> (cited on page 17).

[Mesri et al. 2009]

Mesri, Y., Digonnet, H., and Coupez, T. (2009). "Advanced parallel computing in material forming with CIMLib". *European Journal of Computational Mechanics/Revue Européenne de Mécanique Numérique*, 18 (7-8), pp. 669–694. URL: <http://www.tandfonline.com/doi/abs/10.3166/ejcm.18.669-694> (cited on page 12).

[Mosbah 2008]

Mosbah, S. (2008). "Multiple scales modeling of solidification grain structures and segregation in metallic alloys". PhD thesis. École Nationale Supérieure des Mines de Paris. URL: <https://tel.archives-ouvertes.fr/tel-00349885/document> (cited on page 11).

[Ni and Beckermann 1991]

Ni, J. and Beckermann, C. (1991). "A volume-averaged two-phase model for transport phenomena during solidification". *Metallurgical Transactions B*, 22 (3), pp. 349–361. URL: <http://link.springer.com/article/10.1007/BF02651234> (cited on pages 17–19).

[Niane 2004]

Niane, N. T. (2004). "Étude des macroségrégations induites par le retrait et la déformation thermomécanique lors de la solidification de la peau des produits sidérurgiques". PhD thesis. URL: <http://www.theses.fr/2004INPL088N> (cited on pages 100, 123, 125).

[Onodera and Arakida 1959]

Onodera, S. and Arakida, Y. (1959). "Effect of Gravity on the Macro-Segregation of Larger Steel Ingots", pp. 358–368. URL: <http://eprints.nmlindia.org/3079/1/358-368.PDF> (cited on page 97).

[Osher and Fedkiw 2003]

Osher, S. and Fedkiw, R. (2003). "Signed Distance Functions". *Level Set Methods and Dynamic Implicit Surfaces*. Applied Mathematical Sciences 153. Springer New York, pp. 17–22. URL: http://link.springer.com/chapter/10.1007/0-387-22746-6_2 (cited on page 33).

[Osher and Sethian 1988]

Osher, S. and Sethian, J. A. (1988). "Fronts propagating with curvature-dependent speed: Algorithms based

- on Hamilton-Jacobi formulations". *Journal of Computational Physics*, 79 (1), pp. 12–49. URL: <http://www.sciencedirect.com/science/article/pii/0021999188900022> (cited on page 24).
- [Peng et al. 1999]**
Peng, D., Merriman, B., Osher, S., Zhao, H., and Kang, M. (1999). "A PDE-Based Fast Local Level Set Method". *Journal of Computational Physics*, 155 (2), pp. 410–438. URL: <http://www.sciencedirect.com/science/article/pii/S0021999199963453> (cited on pages 26, 31).
- [Pickering 2013]**
Pickering, E. J. (2013). "Macrosegregation in Steel Ingots: The Applicability of Modelling and Characterisation Techniques". *ISIJ International*, 53 (6), pp. 935–949 (cited on pages 75, 91).
- [Poirier 1987]**
Poirier, D. R. (1987). "Permeability for flow of interdendritic liquid in columnar-dendritic alloys". *Metallurgical Transactions B*, 18 (1), pp. 245–255. URL: <http://link.springer.com/article/10.1007/BF02658450> (cited on page 6).
- [Pollock and Murphy 1996]**
Pollock, T. M. and Murphy, W. H. (1996). "The breakdown of single-crystal solidification in high refractory nickel-base alloys". *Metallurgical and Materials Transactions A*, 27 (4), pp. 1081–1094. URL: <http://link.springer.com/article/10.1007/BF02649777> (cited on page 83).
- [Prescott et al. 1994]**
Prescott, P. J., Incropera, F. P., and Gaskell, D. R. (1994). "Convective Transport Phenomena and Macrosegregation During Solidification of a Binary Metal Alloy: II—Experiments and Comparisons With Numerical Predictions". *Journal of Heat Transfer*, 116 (3), pp. 742–749. URL: <http://dx.doi.org/10.1115/1.2910930> (cited on page 6).
- [Prosperetti 2002]**
Prosperetti, A. (2002). "Navier-Stokes Numerical Algorithms for Free-Surface Flow Computations: An Overview". *Drop-Surface Interactions*. Ed. by M. Rein. CISM International Centre for Mechanical Sciences 456. Springer Vienna, pp. 237–257. URL: http://link.springer.com/chapter/10.1007/978-3-7091-2594-6_8 (cited on page 24).
- [Ramirez and Beckermann 2003]**
Ramirez, J. C. and Beckermann, C. (2003). "Evaluation of a rayleigh-number-based freckle criterion for Pb-Sn alloys and Ni-base superalloys". *Metallurgical and Materials Transactions A*, 34 (7), pp. 1525–1536. URL: <http://link.springer.com/article/10.1007/s11661-003-0264-0> (cited on pages 6, 75, 83).
- [Rappaz et al. 2003]**
Rappaz, M., Bellet, M., and Deville, M. (2003). *Numerical Modeling in Materials Science and Engineering*. Springer Series in Computational Mathematics. Springer Berlin Heidelberg (cited on pages 6, 41, 44, 99).
- [Resk et al. 2009]**
Resk, H., Delannay, L., Bernacki, M., Coupez, T., and Logé, R. (2009). "Adaptive mesh refinement and automatic remeshing in crystal plasticity finite element simulations". *Modelling and Simulation in Materials Science and Engineering*, 17 (7), p. 075012. URL: <http://stacks.iop.org/0965-0393/17/i=7/a=075012> (cited on page 35).
- [Rivaux 2011]**
Rivaux, B. (2011). "Simulation 3D éléments finis des macroségrégations en peau induites par déformations thermomécaniques lors de la solidification d'alliages métalliques". PhD Thesis. École Nationale Supérieure des Mines de Paris. URL: <http://pastel.archives-ouvertes.fr/pastel-00637168> (cited on pages 11, 64, 66, 143, 145, 165).
- [Saad et al. 2015]**
Saad, A., Gandin, C.-A., Bellet, M., Shevchenko, N., and Eckert, S. (2015). "Simulation of Channel Segregation during Directional Solidification of In – 75 wt.% Ga – Qualitative Comparison with In-Situ Observations". *accepted in Metallurgical Transactions A*, (cited on pages 9, 76).
- [Sarazin and Hellawell 1992]**
Sarazin, J. R. and Hellawell, A. (1992). "Studies of Channel-Plume Convection during Solidification". *Interactive Dynamics of Convection and Solidification*. Ed. by S. H. Davis, H. E. Huppert, U. Müller, and M. G. Worster.

Bibliography

NATO ASI Series 219. Springer Netherlands, pp. 143–145. URL: http://link.springer.com/chapter/10.1007/978-94-011-2809-4_22 (cited on pages 6, 9).

[Schneider et al. 1997]

Schneider, M. C., Gu, J. P., Beckermann, C., Boettinger, W. J., and Kattner, U. R. (1997). “Modeling of micro- and macrosegregation and freckle formation in single-crystal nickel-base superalloy directional solidification”. *Metallurgical and Materials Transactions A*, 28 (7), pp. 1517–1531. URL: <http://link.springer.com/article/10.1007/s11661-997-0214-3> (cited on pages 9, 75).

[Sethian 1996]

Sethian, J. A. (1996). “A fast marching level set method for monotonically advancing fronts”. *Proceedings of the National Academy of Sciences*, 93 (4), pp. 1591–1595. URL: <http://www.pnas.org/content/93/4/1591> (cited on page 32).

[Sethian 1999]

Sethian, J. A. (1999). *Level Set Methods and Fast Marching Methods: Evolving Interfaces in Computational Geometry, Fluid Mechanics, Computer Vision, and Materials Science*. Cambridge University Press (cited on page 96).

[Shah and Moore 1989]

Shah, N. A. and Moore, J. J. (1989). “Effect of thermal conditions and alloying constituents (Ni, Cr) on macrosegregation in continuously cast high-carbon (0.8 Pct), low-alloy steel”. *Metallurgical Transactions B*, 20 (6), pp. 893–910. URL: <http://link.springer.com/article/10.1007/BF02670195> (cited on page 6).

[Shakoor et al. 2015]

Shakoor, M., Scholtes, B., Bouchard, P.-O., and Bernacki, M. (2015). “An efficient and parallel level set reinitialization method - Application to micromechanics and microstructural evolutions”. *Applied Mathematical Modelling (submitted)*, (cited on page 33).

[Shevchenko et al. 2013]

Shevchenko, N., Boden, S., Gerbeth, G., and Eckert, S. (2013). “Chimney Formation in Solidifying Ga-25wt pct In Alloys Under the Influence of Thermosolutal Melt Convection”. *Metallurgical and Materials Transactions A*, 44 (8), pp. 3797–3808. URL: <http://link.springer.com/article/10.1007/s11661-013-1711-1> (cited on pages 75, 76, 78, 83, 84, 88, 90, 93).

[Stratos et al. 2008]

Stratos, G., Gavaises, M., Theodorakakos, A., and Bergeles, G. (2008). “Numerical investigation of the cooling effectiveness of a droplet impinging on a heated surface”. *International Journal of Heat and Mass Transfer*, 51 (19–20), pp. 4728–4742. URL: <http://www.sciencedirect.com/science/article/pii/S001793100800149X> (cited on page 28).

[Süli 2000]

Süli, E. (2000). *Lecture Notes on Finite Element Methods for Partial Differential Equations* (cited on page 44).

[Sun and Beckermann 2004]

Sun, Y. and Beckermann, C. (2004). “Diffuse interface modeling of two-phase flows based on averaging: mass and momentum equations”. *Physica D: Nonlinear Phenomena*, 198 (3–4), pp. 281–308. URL: <http://www.sciencedirect.com/science/article/pii/S0167278904003689> (cited on page 26).

[Sussman et al. 1994]

Sussman, M., Smereka, P., and Osher, S. (1994). “A Level Set Approach for Computing Solutions to Incompressible Two-Phase Flow”. *Journal of Computational Physics*, 114 (1), pp. 146–159. URL: <http://www.sciencedirect.com/science/article/pii/S0021999184711557> (cited on pages 30, 31).

[Suzuki and Miyamoto 1973]

Suzuki, K. and Miyamoto, T. (1973). “The Mechanism of Formation of the V Segregation in Steel Ingot”. *Tetsu-to-Hagane*, 59 (3), pp. 431–445 (cited on page 6).

[Swaminathan and Voller 1993]

Swaminathan, C. R. and Voller, V. R. (1993). “On The Enthalpy Method”. *International Journal of Numerical Methods for Heat & Fluid Flow*, 3 (3), pp. 233–244. URL: <http://www.emeraldinsight.com/journals.htm?articleid=1665561&show=abstract> (cited on page 40).

[Tan and Zabaras 2007]

Tan, L. and Zabaras, N. (2007). "A level set simulation of dendritic solidification of multi-component alloys". *Journal of Computational Physics*, 221 (1), pp. 9–40. URL: <http://www.sciencedirect.com/science/article/pii/S0021999106002737> (cited on page 24).

[TCBIN 2006]

TCBIN (2006). *TCBIN: TC Binary Solutions Database*. Stockholm, SE (cited on page 79).

[TCFE6 2010]

TCFE6 (2010). *TCFE6: a thermodynamic database for different kinds of steels and Fe-based alloys*. Stockholm, SE. URL: <http://goo.gl/qiD3kE> (cited on pages 52, 54, 55).

[Tezduyar et al. 1992]

Tezduyar, T. E., Mittal, S., Ray, S. E., and Shih, R. (1992). "Incompressible flow computations with stabilized bilinear and linear equal-order-interpolation velocity-pressure elements". *Computer Methods in Applied Mechanics and Engineering*, 95 (2), pp. 221–242. URL: <http://www.sciencedirect.com/science/article/pii/0045782592901416> (cited on pages 64, 66).

[Tezduyar and Osawa 2000]

Tezduyar, T. E. and Osawa, Y. (2000). "Finite element stabilization parameters computed from element matrices and vectors". *Computer Methods in Applied Mechanics and Engineering*, 190 (3–4), pp. 411–430. URL: <http://www.sciencedirect.com/science/article/pii/S0045782500002115> (cited on page 66).

[Thuillet and Combeau 2004]

Thuillet, L. and Combeau, H. (2004). "Prediction of macrosegregation during the solidification involving a peritectic transformation for multicomponent steels". *Journal of Materials Science*, 39 (24), pp. 7213–7219. URL: <http://link.springer.com/article/10.1023/B%3AJMSC.0000048734.34597.1e> (cited on page 40).

[Tiller et al. 1953]

Tiller, W. A., Jackson, K. A., Rutter, J. W., and Chalmers, B (1953). "The redistribution of solute atoms during the solidification of metals". *Acta Metallurgica*, 1 (4), pp. 428–437. URL: <http://www.sciencedirect.com/science/article/pii/0001616053901266> (cited on page 4).

[Tourret and Gandin 2009]

Tourret, D. and Gandin, C. A. (2009). "A generalized segregation model for concurrent dendritic, peritectic and eutectic solidification". *Acta Materialia*, 57 (7), pp. 2066–2079. URL: <http://www.sciencedirect.com/science/article/pii/S1359645409000184> (cited on page 17).

[Tourret et al. 2011]

Tourret, D., Gandin, C. A., Volkmann, T., and Herlach, D. M. (2011). "Multiple non-equilibrium phase transformations: Modeling versus electro-magnetic levitation experiment". *Acta Materialia*, 59 (11), pp. 4665–4677. URL: <http://www.sciencedirect.com/science/article/pii/S1359645411002552> (cited on pages 59, 163).

[Vigneaux 2007]

Vigneaux, P. (2007). "Méthodes Level Set pour des problèmes d'interface en microfluidique". PhD thesis. Université Sciences et Technologies - Bordeaux I. URL: <https://tel.archives-ouvertes.fr/tel-00189409/document> (cited on page 32).

[Ville et al. 2011]

Ville, L., Silva, L., and Coupez, T. (2011). "Convected level set method for the numerical simulation of fluid buckling". *International Journal for Numerical Methods in Fluids*, 66 (3), pp. 324–344. URL: <http://onlinelibrary.wiley.com/doi/10.1002/fld.2259/abstract> (cited on page 32).

[Voller et al. 1989]

Voller, V. R., Brent, A. D., and Prakash, C. (1989). "The modelling of heat, mass and solute transport in solidification systems". *International Journal of Heat and Mass Transfer*, 32 (9), pp. 1719–1731. URL: <http://www.sciencedirect.com/science/article/pii/0017931089900549> (cited on page 104).

[Wang and Beckermann 1993]

Wang, C. Y. and Beckermann, C. (1993). "A multiphase solute diffusion model for dendritic alloy solidification". *Metallurgical Transactions A*, 24 (12), pp. 2787–2802. URL: <http://link.springer.com/article/10.1007/BF02659502> (cited on page 17).

Bibliography

[Wanqi and Yaohe 1989]

Wanqi, J. I. E. and Yaohe, Z. (1989). "Formation of hot-top segregation in steel ingot and effect of steel compositions". *Metallurgical Transactions B*, 20 (5), pp. 723–730. URL: <http://link.springer.com/article/10.1007/BF02655930> (cited on page 6).

[WSA 2014]

WSA (2014). *World Steel Association: Statistics archive*. URL: <http://www.worldsteel.org/statistics/statistics-archive.html> (cited on page 9).

[Xu and Li 1991]

Xu, D. and Li, Q. (1991). "Gravity- and Solidification-Shrinkage-Induced Liquid Flow in a Horizontally Solidified Alloy Ingot". *Numerical Heat Transfer, Part A: Applications*, 20 (2), pp. 203–221. URL: <http://dx.doi.org/10.1080/10407789108944817> (cited on page 6).

[Yuan and Lee 2012]

Yuan, L. and Lee, P. D. (2012). "A new mechanism for freckle initiation based on microstructural level simulation". *Acta Materialia*, 60 (12), pp. 4917–4926. URL: <http://www.sciencedirect.com/science/article/pii/S1359645412003205> (cited on page 83).

[Zabaras and Samanta 2004]

Zabaras, N. and Samanta, D. (2004). "A stabilized volume-averaging finite element method for flow in porous media and binary alloy solidification processes". *International Journal for Numerical Methods in Engineering*, 60 (6), pp. 1103–1138. URL: <http://onlinelibrary.wiley.com/doi/10.1002/nme.998/abstract> (cited on page 67).

Modélisation par Level Set des macroségrégations induites par le retrait à la solidification

RESUME : La macroségrégation est un défaut connu dans les procédés de coulées industrielles. La genèse de ce défaut est la conséquence de l'interaction complexe entre la microségrégation ou la distribution des espèces chimiques à l'échelle de la microstructure et les mouvements des phases liquide et solides. Les hétérogénéités de concentration en solutés à l'échelle de la pièce peuvent être rédhibitoires vis-à-vis de la qualité du produit. Dans ce travail, on propose un modèle numérique pour simuler et prédire la formation des macroségrégations en cœur des pièces d'alliages multi-constitués, induites par des variations thermiques et solutales dans la phase liquide. Dans un premier temps, on considère que le métal solidifie à volume constant. Dans ce contexte, la convection thermosolutale est étudiée ainsi que son influence sur la formation des canaux ségrégés à différentes échelles de modélisation. Dans un deuxième temps, le modèle vise à prédire les macroségrégations en présence de changement de volume du métal, dont la cause principale est le retrait à la solidification, pouvant être à l'origine du phénomène de ségrégation inverse. La surface entre le métal et le gaz environnant au cours du retrait évolue pendant le retrait en fonction du chemin de solidification qui varie avec la macroségrégation. Cette évolution d'interface est suivie par la méthode Level set. Des prédictions de concentration moyenne, couplées aux bases de données thermodynamiques pour mieux prédire les chemins de solidification des alliages multi-constitués, sont analysées et comparées avec des résultats expérimentaux. Finalement, des calculs de solidification en microgravité sont présentées, simulant un essai expérimental dans le contexte du projet CCEMLCC lancé par l'Agence Spatiale Européenne. Les résultats en fin de solidification montrent un accord acceptable quant à la forme et l'elongation des échantillons solidifiés. Ces calculs sont faits avec des approximations binaire, ternaire et quaternaire d'une même nuance d'acier utilisée dans les essais en microgravité.

Mots clés : modélisation, solidification, ségrégation, Level Set, éléments finis, métallurgie

Numerical modeling of macrosegregation formed during solidification with shrinkage using a Level Set Approach

ABSTRACT : Macrosegregation is key defect in industrial casting processes. During solidification, solute redistribution at the scale of microstructure, also known as microsegregation, take place with complex interactions, in order to form one or more solid phases. These interactions between microsegregation and movements of liquid and solid phases may lead to macrosegregations. These solute heterogeneities spanning on a larger scale, may result in a bad casting quality. In this thesis, we propose a numerical model to simulate and predict macrosegregations occurring in the centre of multicomponent alloys, caused by thermal and solutal variations in the liquid phase. First, we assume that the metallic alloy solidifies with a constant volume. In this context, we study the influence of thermosolutal convection on the formation of channel segregations, at different modelling scales. The second part of this modelling work consider solidification while the metallic alloy's volume is decreasing, mainly due to overall density variation, also known as solidification shrinkage, possibly leading to the so-called inverse segregation phenomenon, appearing on the alloy's skin. In the context of solidification shrinkage, the shape of the metal's boundary with surrounding gases varies according to a constantly changing solidification path due to macrosegregation. The Level Set method is therefore used to track its evolution with time. Composition predictions, coupled with thermodynamic database mappings for more accurate multicomponent solidification paths, are analysed and compared to existing experimental setups. Finally, simulations of a reduced-gravity solidification cases are performed, mocking an experimental benchmark from the CCEMLCC project launched by the European Space Agency. The results show acceptable agreement for the final shape, compared to experimental results. These computations were performed with binary, ternary and quaternary approximations of the same steel grade which was used in reduced-gravity experiments.

Keywords : modélisation, solidification, segregation, Level Set, finite elements, metallurgy



